A seismic study of the crust in and around the gregory rift

Josiah Udemadu Chukudebelu

A SEISMIC STUDY OF THE CRUST IN AND AROUND THE GREGORY RIFT

by

Josiah Udemadu Chukudebelu

A thesis submitted for the degree of
Doctor of Philosophy at the University of Durham

Department of Geological Sciences

September, 1987

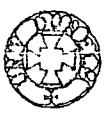

DECLARATION

I declare that this thesis is my own work. I further declare that this thesis is not substantially the same as any which has been previously submitted to this or any University.

September, 1987

ABSTRACT

Data used for the present study were recorded at the small aperture cross-linear array station which was installed at Kaptagat (in NW Kenya) by the University of Durham. The seismic array data from local earthquakes have been analysed by velocity/azimuth filtering technique. Apparent velocities and azimuths for first and later arrival phases were measured for local rift events from the immediate east, for local events from the south west and for more distant rift events to the north and south of Kaptagat.

Data from local rift events originating from the immediate east of Kaptagat were used in the present analysis to study the structure of the lithosphere beneath the Gregory rift at about 0.5°N latitude. The first arrival data (apparent velocities and azimuths) were determined to a high degree of accuracy. The first and later arrival data have been interpreted in terms of a simple two layer model with a horizontal refracting interface at a depth of 13 ± 5 km and having upper and lower layer uniform velocities of 5.8 ± 0.2 km/s and 7.2 ± 0.2 km/s respectively. The minimum lateral extent of the top surface of this refractor is estimated at about 30 km. A maximum dip of about 6° on the interface is allowed by the data.

In the preferred three layer model, a 10 km thick top horizontal layer of velocity 5.8 km/s overlies a 10 km thick intermediate layer in which velocity increases uniformly from 6.0 km/s at 10 km depth to 7.5 km/s at a depth of 20 km. The intermediate layer, in turn, overlies a 7.6 km/s refractor.

The models derived from the present data are consistent with the theory that upward perturbation of the lithosphere/asthenosphere boundary giving rise to domal uplift, lithospheric tension and magmatic activity, is the primary cause of rifting.

ACKNOWLEDGEMENTS

I thank Professor M.H.P. Bott and Dr. R.E. Long for the opportunity to work in the Department of Geological Sciences, University of Durham. I give special thanks to my supervisor, Dr. R. E. Long, for his patience, advice, guidance, encouragement and criticisms over these years.

I should also thank the Commonwealth Scholarship Scheme for financial support during the first part of my stay at Durham and the Federal Government of Nigeria for the scholarship that supported me during the remaining part of my stay.

My thanks also go to Drs. J.E.G. Savage and W.G. Rigden for their usefuld discussions and suggestions. I thank the staff of the Computer unit at Durham for helping with computing problems. To the staff of University of Durham Science Library, I am very grateful for the provision of workspace and other library facilities.

Finally I thank my wife, Ifeoma, whose care and firm support over these years have helped to sustain me.

CONTENTS

LIST OF FIGURES

LIST OF TABLES

CHAPTER 1

THE EAST AFRICAN RIFT SYSTEM

1.1 Introduction

The Afro-Arabian rift system (fig.1.1) includes the Gulf of Aden, the Red Sea and the East African rifts. These three rifts form a triple junction in the Afar region thus trisecting the Afro-Arabian plateau. The East African rift system is the world's largest and best exposed example of a continental rift system. It is apparently connected, via the Gulf of Aden, to the Carlesberg ridge of north west Indian ocean. Hence, unlike other continental rifts, it appears to be a continental extension of the global mid-ocean ridge system.

In the Red Sea and the Gulf of Aden, there has been complete separation of the continental lithosphere and the evolution of a new oceanic lithosphere by sea floor spreading. A thorough understanding of the magmatic and tectonic processes beneath the East African rift is required to establish whether the rift system is at the closing stages of a stalled evolution or is marking the initiation of an episode of lithospheric spreading.

1.2 The East African Rift System

The East African rift system extends southwards from Afar depression to Mozambique for a distance of about 3000 km (King, 1978). On a continental scale, the rift system is essentially a north-south trending feature although its

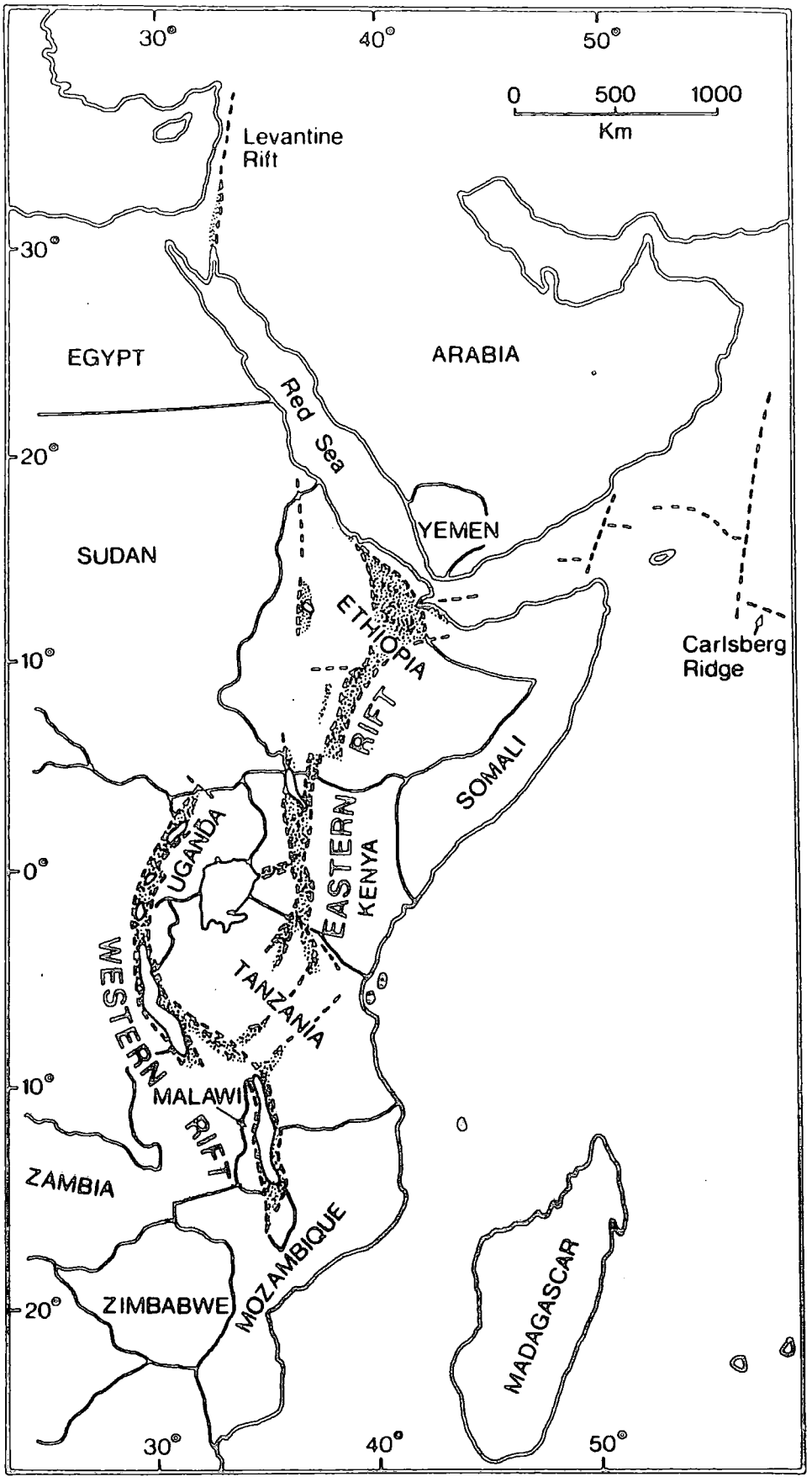

Fig. 1·1. The Afro-Arabian rift system.
(continental graben and depressions are shaded)

structural elements only exceptionally show this trend. Over much of the rift system a simple graben structure is expectional and the series of rifts are not continuously connected (Le Bas, 1971). The actual rift pattern is considered to be largely controlled by the influence of the pre-existing structures of the basement. Within Eastern Africa, the Tanganyika shield with east-west trends, appears to have acted as a resistant block deflecting the fault patterns to either side, thus forming the western and eastern rifts (fig. 1.1). These two branches appear to fringe the East African plateau on the west and east and cojoin through a broad zone of faults north of Lake Malawi at about latitude $8^{o}S$.

Apparent faulting ends in the neighbourhood of the Limpopo River (King, 1970). But heatflow and seismic data suggest that rifting may extend to as far south as $23^{o}S$ (Chapman and Pollack, 1975; Fairhead and Girdler, 1969). Seismicity studies suggest the existence of a tensile zone extending the eastern branch of the East African Rifts, on land, from North Tanzania divergence in a north-west to south-east direction to the Tanzanian coast-line at about $7^{o}S$. From there the eastern rift is further extended through northern Mozambique continental slope southwards along the Kerimbas and Lacarda deep grabens to as far south as about $17^{o}S$. Hence the Tanzanian rifts form a link between the eastern rift and the troughs along the Mozambique continental margin (Mougenot et al., 1986).

The East African rift system is a zone of normal faults indicating tensile stressfield (Heiskanem and Vening Meinesz, 1958; Fairhead and Girdler, 1971). It traverses two broad elongated domal uplifts, the Afro-Arabian (Ethiopian) dome in

Ethiopia and the Kenya dome further south in Kenya. The main Ethiopian rift, starting from Afar, traverses the crest of the Ethiopian dome and extends about 450 km south-south westward before dying out in a series of splayed tilted blocks (Shackleton, 1978). This splayed structure seperates the Ethiopian rift to the north from the Gregory rift to the south.

1.3 The Gregory Rift

The Gregory rift (fig. 1.2) is that part of the Eastern rift lying within Kenya and northern Tanzania. It bisects the Kenya domal uplift which is a second order structure and local culmination on the eastern rim of the more extensive East African plateau. The Kenya dome is elliptical in plan, about 1000 km long and 300 to 400 km wide (Logatchev et al, 1983). Elevations along both the shoulders and the floor of the rift rise towards the central sector of the dome. The dome may be, however, more a reflection of volcanic accumulation than of vertical uplift, which can only be judged from the displacement of levels of the basement (King, 1978).

The fault pattern in the Gregory rift has an element of symmetry about the minor (east-west) axis of this uplift while the main rift is located on the crest and major (north-south) axis. The Gregory rift approximates a discontinuous fault bounded graben for about 450 km between latitudes $2^{o}S$ and $2^{o}N$ along the major axis of the uplift (King, 1978) although later estimates suggest that the main axial depression is over 600 km in length (Logatchev et al,1983). Estimates for the overall width of the Gregory graben are all in the range 60-90 km (Baker et al., 1972; Longatchev et al,1983; King, 1978) while the width of the central graben is estimated at about 20-30 km (Baker and

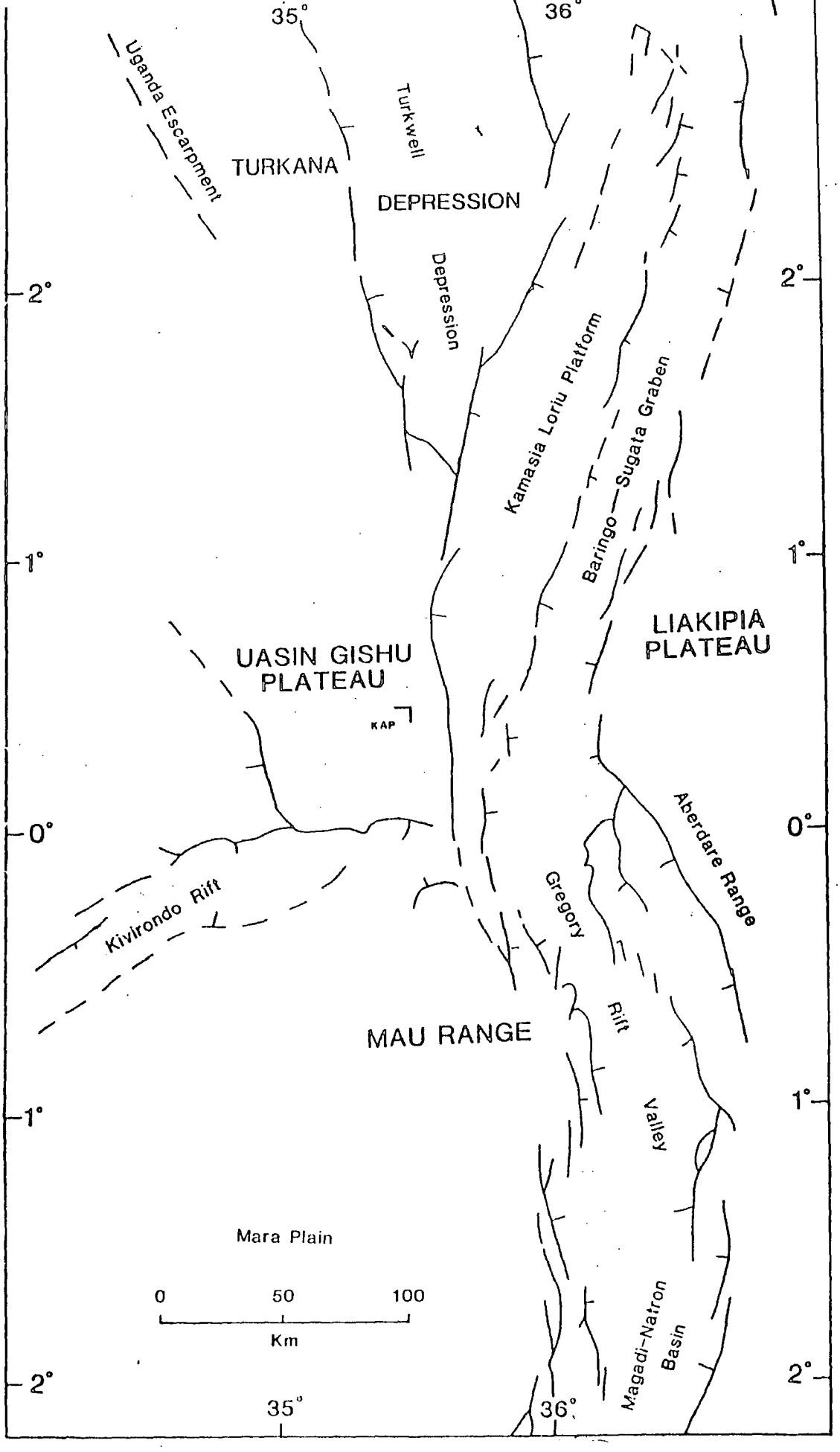

Fig 1.2 Major faults of the Gregory rift.

Wohlenberg, 1971). Generalised structural map of the Gregory rift shows a sinuous swing in trend between about 0^{o} and $1^{o}S$ latitude (fig. 1.2).

The faults are essentially normal dip-slip type and marginal faults have throws up to 4 km. Height of the fault escarpment in the central sector of the rift ranges up to 2000 m (Baker and Wohlenberg, 1971; King, 1978). Step faults and ramps lead from the margins to the central graben. The graben floor and step fault platforms are composed of Plio-Pleistocene volcanics cut by dense swarms of closely spaced sub-parallel faults. The faults on the rift floor are locally hidden by late Quaternary volcanic piles (McCall, 1968).

Northwards around Lake Turkana, by a succession of splay faults and downwarps the rift zone widens to an ill defined feature about 200 km across. This region separates the Gregory rift from the Ethiopian rift indicating that, at least superficially, the two rifts are not a single continuous feature. Southwards, too, in Tanzania, the Gregory rift widens by splay faulting and merges into a zone of tilted blocks (Baker et al.,1972).

The Kavirondo rift branches from the Gregory rift at the centre of the Kenya domal uplift and trends west and southwest, bisecting the highest part of the Western plateau and descending westward into Lake Victoria. Estimates for the width of the Kavirondo rift are in the range 15 to 30 km (Baker et al.,1972; King, 1978).

1.4 Evolution of the Gregory Rift

The Eastern rift and its associated uplifts are impressed on the late Precambrian - early Palaeozoic

Mozambique orogenic belt whose age is estimated to be in the range 835 to 400 my (Cahen and Snelling, 1966). During most of the Palaeozoic, Eastern Africa was occupied by fold mountains being eroded (Baker et al., 1972). Marine transgression started in the late Triassic - lower Jurassic in the Horn of Africa and extended westward to cover Somalia, NE Kenya, most of Ethiopia and SW Arabia by the end of the Jurassic. This marine transgression resulted from the opening Indian ocean (Shackleton, 1978). Downwarped sediments up to 2000 m thick in north central Ethiopia suggest that a subsiding trough lay along the future site of the Ethiopian rift as early as the Jurassic.

Regression of this sea began by the end of the Jurassic or early Cretaceous and continued with minor periods of transgression into the early Tertiary. The Cretaceous regression in eastern Africa may have been caused by continental epeirogeny (Baker et al., 1972). But evidence for localised differential uplifts in Ethiopia and Kenya are found in well preserved planar erosion surfaces (Saggerson and Baker, 1965). From these erosion surfaces it is inferred that uplift of central Kenya and Ethiopian domes took place in three synchronous pulses seperated by long periods of crustal stability and erosion. In both Kenya and Ethiopia, the three uplift stages are estimated as late Eocene, lower-middle Miocene and Plio-Pleistocene.

In central Kenya there was an uplift of about 500 m in the late Eocene and a further uplift of 300 m in the mid-Miocene. There was a major uplift of about

1500 m in central Kenya in the Plio-Pleistocene (Baker et al., 1972; Shackleton, 1978). The amount of each uplift decreased towards the east and was accompanied by flexuring and subsidence of the coastal region. The isobases of the sub-Miocene erosion surface is shown in fig. 1.3 which indicates that the sum of uplifts since the mid-Tertiary reached a maximum of 1800 m.

The upper Eocene uplift of the Afro-Arabian region marked the initiation of the Ethiopian domal uplift and of the eastern rift system. The uplift was preceded and accompanied by the outpouring of the Eocene-Oligocene Trap series fissure basalts (which cover most of Ethiopian and Somalian plateaux and the Yemen highlands of south-western Arabia) and axial downwarping in Ethiopia. The Trap series represent the largest single volcanic event in the history of the eastern rift and covered 750, 000 km^2 in Ethiopia and 30,000 km^2 in south west Arabia (Gass, 1970). Its estimated total thickness reaches 4 km in northern Ethiopia (Mohr, 1967). There was no equivalent Tertiary volcanism in Kenya (Logatchev, 1972).

By late Oligocene - early Miocene time, embroyonic troughs had formed along the present lines of the Red Sea and the Gulf of Aden. This mid-Tertiary phase of development extended southward through Afar and Ethiopia and was manifested by downflexing and faulting of the Turkana depression of northwest Kenya.

The formation of the Gregory rift started in the lower to middle Miocene (about 23-16 my ago) with the monoclinal upwarping of of the Kenya-Uganda border area

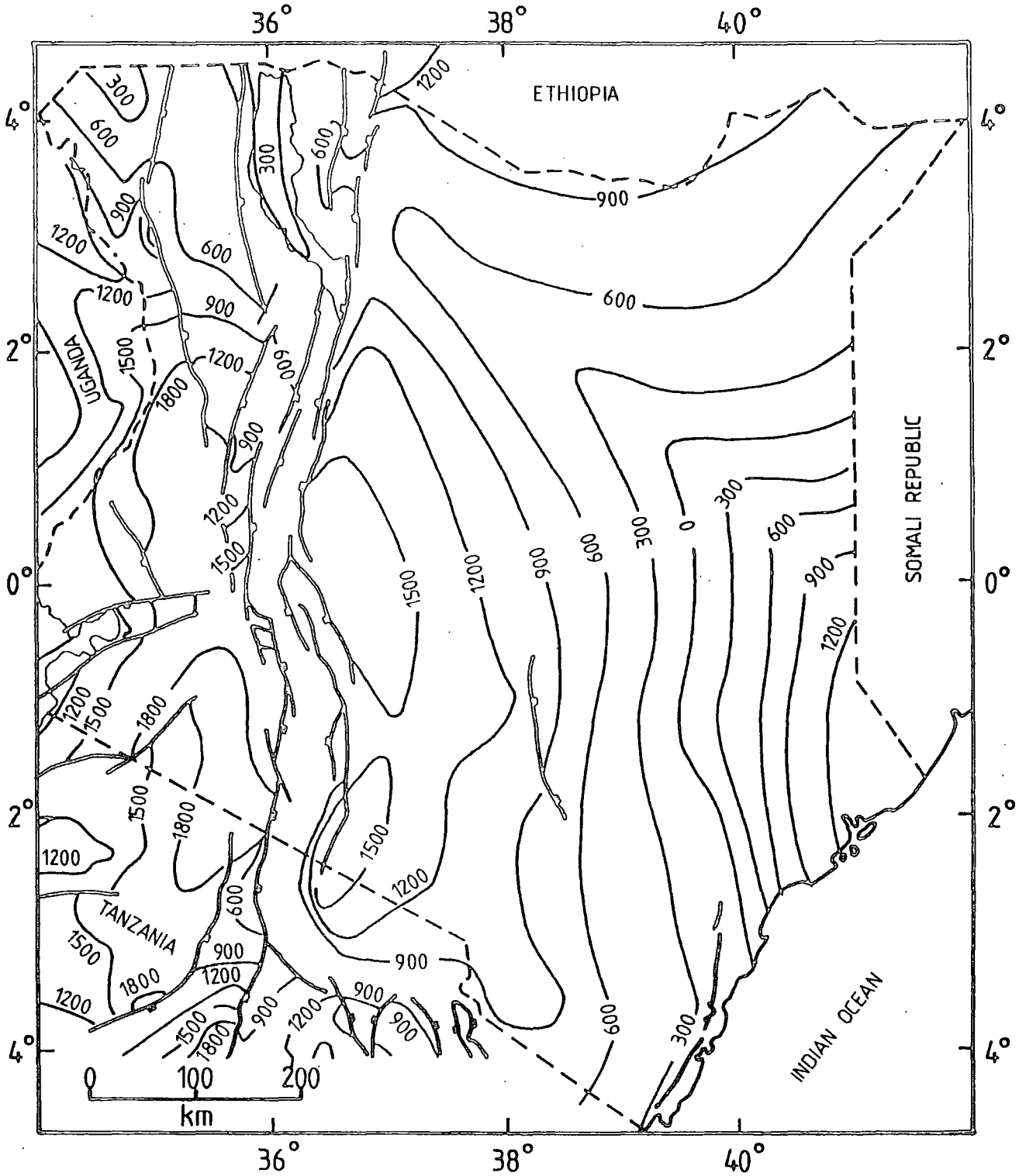

Fig 1.3. Isobases of the sub-Miocene erosion surface in Kenya. Present-day elevation of the surface given in metres

accompanied by downflexing of Turkana depression (Shackleton, 1978; King, 1978; Logatchev, 1972). During this period, alkaline carbonatite central volcanoes of eastern Uganda and of the future Kavirondo rift were formed on the uplifted area. In the complimentary Turkana depression, this was accompanied by massive fissure eruptions of basalts, mugearites and ryolites. The central rift area was uplifted about 300 m (Saggerson and Baker, 1965).

During the upper Miocene (about 13.5-12.0 my ago), the area of volcanic activity shifted to the Kenya domal uplift and lost its connection with the Ethiopian volcanic area. Immense fissure eruptions of phonolites and phonolithic trachytes occured through systems of fractures on the crest of the volcanic uplift along the strike of the future Gregory rift. Fissure eruptions dominated this stage which has the highest magmatic productivity in the whole history of the rift development. Estimate of the total volume of upper Miocene phonolites is 25,000-30,000 km^3 (Logatchev, 1972).

In the lower-middle Pliocene times (about 10 to 5 my ago), volcanic activity was restricted to a narrower zone but extended southwards beyond the limit of the plateau phonolites at the latitude of Lake Magadi. The mode of eruptions changed from mainly fissure to predominantly central. The numerous volcanoes were situated along the rift floor or over the scarps of the rift shoulders thus suggesting a connection with the future rift which at this time was still not defined as a real trough. At the same time, the

petrochemical composition of the volcanic rocks changed substantially from being strongly alkaline to being more variable. During this period, fault displacements took place along the Elgeyo escarpment and to the north of it within a flex ure zone seperating Turkana depression from the Eastern Uganda upwarped area. Marginal faults of the Kavirondo rift were possibly formed at this time (Logatchev et al. 1972).

On the western side of the rift zone vertical displacements embraced nearly the whole length of the structure from Kamasia range in the north to Crater Highlands in the south. Displacements on the eastern side occurred only in a limited section at the foot of the Aberdare range. Hence extensive rift faulting following Miocene uplift produced a meridional asymmetric trough faulted mainly on its western side. There was minor trachyte volcanism on the rift floor of this trough. This was followed by much more massive voluminous basaltic eruptions along nearly the whole length of the trough together with the formation of the dominantly basaltic Aberdare Central volcanic range.

The next stage in the rift development was in the upper Pliocene-Lower Pliestocene (about 5.0 to 2.0 my ago). In the upper Pliocene, massive eruptions of trachytic ignimbrites began in the central part of the rift floor locally filling the rift and overflowing its banks. The basalt series was formed mainly by fissure eruptions on the rift valley floor. Major upliftphase began which raised central Kenya by a further 1500 m.

This uplift was accompanied by major graben faulting along most of the Gregory rift at the end of the Pliocene. It was followed by mainly fissure trachyte volcanism which flooded most of the graben floor (Baker et al., 1972). At the end of this phase an outline of the Gregory rift was created as the shoulders were uplifted while the floor was downfaulted (King, 1978). Simultaneous with the immense basalt volcanic activity was the establishment of autonomous magma chambers to the east of the rift. These chambers started the formation of the gigantic volcanoes of Kenya and Kilimanjaro and probably Kulal (Logatchev, 1972). Volcanic activity to the west of the rift stopped completely at the start of the rift downfaulting. From that time on, volcanic activity was restricted to the regions within and to the east of the rift.

During the lower-middle Pleistocene times (about 2.0-0.7 my ago), the developing graben was partly filled by flood trachytes. This stage witnessed the formation of rift trough along the whole length of the Gregory rift. There were further local rejuvenations of the main graben and stepfaults which deepened the central sector of the rift. The graben floor was shattered by closely spaced minor faults which in some cases reach densities of 2 to 3 faults per km (Baker and Wohlenberg, 1971). Deepening of the rift valley and formation of stepfaults at its margins were produced by movement along these minor faults. The overall effect was to produce "rift in rift" structures with marginal platforms.

In the northern and southern ends of the rift valley there was intensive fracturing of the crust. In these regions, systems of splay faults formed with dominantly eastward dip-slip displacement of the blocks.

By the late Quaternary, from about 0.7 my ago to the present, fissure eruptions had stopped and widespread area of volcanity on the rift floor disintegrated into seperate areas of central volcanoes. Trachyte, basalt-trachyte and phonotite caldera volcanoes built up axially in the floor of the inner graben. The chemistry of the volcanics of the rift floor diversified. In areas well to the east of the rift there were extensive basaltic eruptions (Williams, 1969). Hence the eastward migration of magmatic activity, started in the upper Pliocene - lower Pleistocene continued into this period.

1.5 Petrochemistry

Basalts, phonolites and trachytes are prominent amongst Gregory rift volcanics. Basalts have been erupted repeatedly throughout the history of the Gregory rift and in total volume has been estimated at not less than 70,000 km^3 (Williams, 1972). The total volume of the Cenozoic volcanics is about 230,000 km^3 (King, 1978) which is higher than the previous estimates of about 150,000 km^3 (Baker et al., 1972; Williams, 1972). The thickness of the volcanics is estimated at about 2.5 km.

The volcanics of the Gregory rift can be divided into two geochemical series, one midly alkaline and the other strongly alkaline (Baker et al. 1972; King, 1978).

In the early stages of the rift development, from early Miocene to early Pliocene (about 25-5 my ago), the proportion of strongly alkaline rocks was 30-40% of the total volume of outflows. In the later stages, from early Pliocene to the present, the proportion of strongly alkaline rocks decreased to about 1% (Logatchev et al., 1983). Kenya basalts contain less SiO_2 and more CaO-MgO-FeO than Ethiopian basalts and this suggests a deeper origin for the Kenya rift basalts (Baker et al., 1972). The Miocene pre-rift flood basalts and the Quaternary flood basalts outside the rifts are more strongly alkaline than the Pliocene basalts of the rift floor. This suggests, as in Ethiopia, shallower melting under the rift than under the adjacent plateaux (Green and Ringwood, 1969).

Goles (1975) reached a similar conclusion from studies of Kenya basalts. He studied two suites of basalt, one from the Chyulu range, about 300 km to the south east of the culmination of the Kenya dome and the other from Olorgesailie, within the southern part of the rift. The Chyulu suite seems to have been derived from magma which equilibrated at a temperature of 1450^{o}C and pressures substantially less than 25 kbar (about 80 km depth). The Olorgesailie suite being more evolved and having equilibrated at shallower depth (1200^{o}C and 3-10 kbar pressures), is thought to be derived from a secondary magma chamber located within the crust. A series of such secondary magma chambers along the rift axis would give rise to the positive Bouguer anomaly

observed by Searle (1970).

Baker et al. (1972) from available geological data argue that "volcanism and tectonism are dual expressions of thermal events in the asthenosphere, along an uplifted zone of crustal dilatation." The geothermal gradient is lower under the eastern rift than under the mid ocean ridge. Consequently a greater depth of melting under the eastern rift compared with the oceanic spreading zones is indicated by abundance of strongly alkaline volcanism (Green and Ringwood, 1969). Furthermore, the long duration of alkaline magnatism is not consistent with the view that the African rifts simply represent embryonic stages of sea floor spreading (Murray, 1970; Le Bas, 1971). But contrary views are widely held.

1.6 Summary.

Formation of the Gregory rift started in the early Miocene. Volcanic activity was not in general restricted to the confines of the rift valley. Volcanic activity developed in the west in the Miocene and to the east in the Plio-Pleistocene to recent times. Within the rift, volcanism commenced in the north and extended to the south in the Pliocene (King, 1978).

The downwarping trough was largely or wholly filled with products of episodes of volcanism and sedimentation. Throws on the main faults range up to 4 km. Faulting has produced a graben about 80 km wide in places and about 450 km in length to the north and south of which the faults splay outwards over much broader zones.

King (1978) infers the presence of basement rocks beneath the volcanics in all parts of the Gregory rift. This suggestion is supported by other geological and geophysical data (Chapman et al., 1978; Swain et al., 1981). He therefore argues that although there is a possible crustal extension of about 8 km, there is no evidence for crustal seperation. Current centres of activity are along the rift axis and to the east.

1.7 Relevant previous Geophysical Work in Africa.

1.7.1 Africa Outside the Rift Zone.

Geophysical data indicate that, away from the rift zone, Africa has a structure similar to that found in stable shield areas.

Gumper and Pomeroy (1970) measured Rayleigh wave phase velocities in the period range 30 to 67s for paths from Helwan in Egypt to South Africa. They also determined Rayleigh and Love wave group velocities for the African continent utilizing all available data from WWSSN and LGO stations. These authors observed a similarity between their phase velocities and those obtained for the Canadian sheild by Brune and Dorman(1963).

Gumper and Pomeroy (1970) also obtained travel time data for paths traversing the African continent in the distance range 100 to 4700 km. A velocity of 8.07 km/s was found for P_n while S_n velocity varied from 4.55 to 4.72 km/s.

The mean structural model (AFRIC model) satisfying their seismic velocities was derived and compared with models for shield and continental regions (fig. 1.4). This comparison indicated that the structure for parts

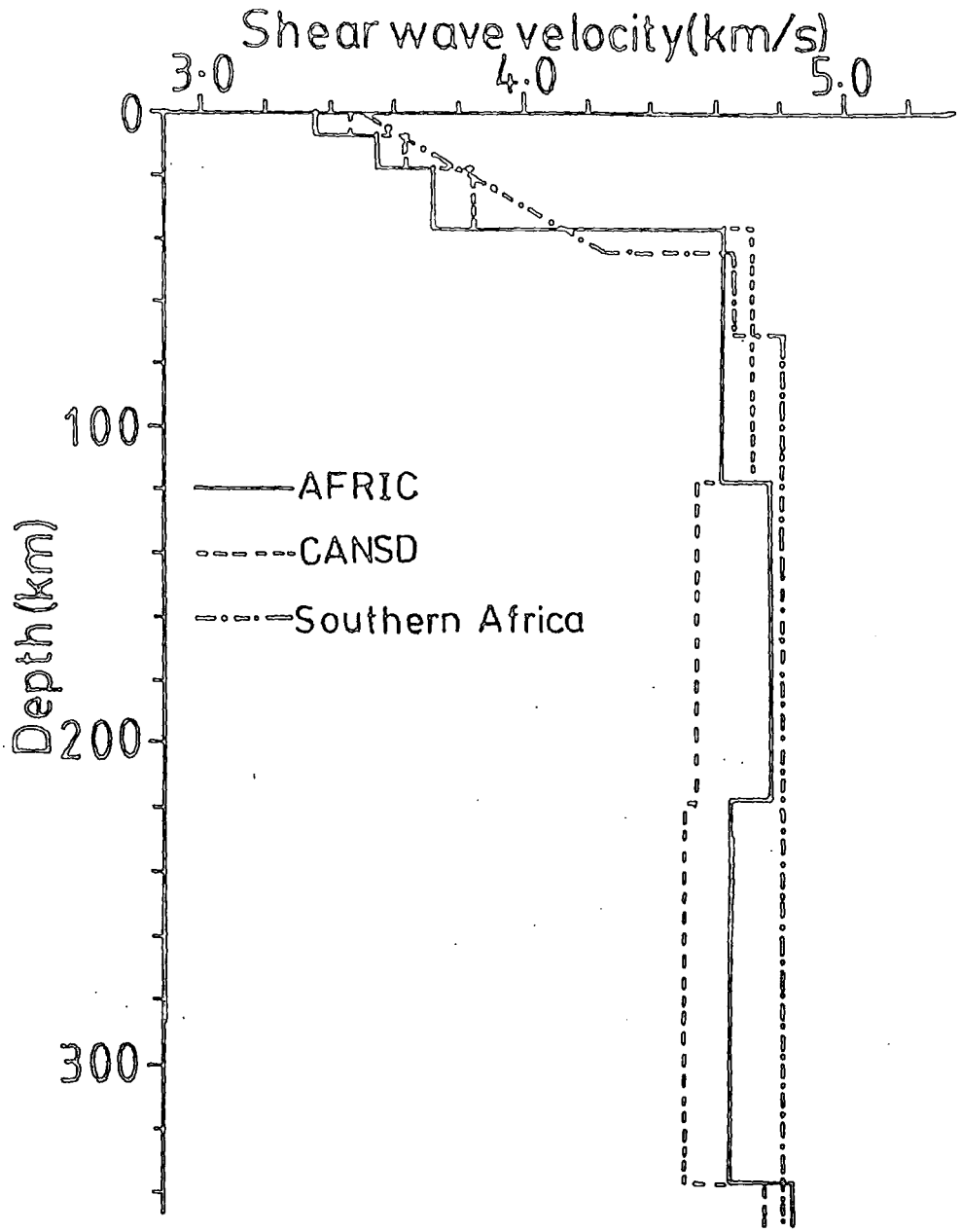

Fig 1.4 CANSD, AFRIC and South African shear wave models of the lithosphere.

of Africa away from the rift zone is similar to the structure associated with normal stable shield regions exemplified by the CANSD model of Brune and Dorman (1963).

Bloch et al (1969) determined Rayleigh wave phase velocities (in the period range 20-100s) from an array of stations located near Johannesburg, South Africa, and from WWSSN stations at Pretoria, Bulawayo and Windhoek. Multimode Rayleigh and Love wave group velocities from the records of a number of earthquakes originating near Kariba dam and in southern Malawi were also measured. The group velocities extended from the period range 2-40s for the fundamental mode and 2-12s for the higher modes.

The multimode dispersion data indicated that the crustal and upper mantle velocities to the east of a line through Pretoria and Bulawayo are higher than those to the west. The phase velocity and group velocity curves for the path Kariba-Pretoria were found to be similar to those for shield areas. The phase velocities obtained for the array area confirmed the high subcrustal shear velocities previously determined for southern Africa from refraction studies (Willmore et al, 1952; Gane et al., 1956; Hales and Sacks, 1959). The model derived from the data of Block et al, (1969) for South Africa matched closely the CANSD and AFRIC models. These models are illustrated in figure 1.4.

Details of crustal structure for southern Africa come from the refraction studies of Willmore et al,(1952), Gane et al. (1956) and Hales and Sacks (1959). Willmore et al. (1952) studied seismograms of the Witwaterstrand earth tremors at distances up to 500 km in Western Transvaal.

These tremors originated at depths between 1 and 2.5 km. Travel time data on 210 seismograms obtained from 150 tremors recorded on three component sets were interpreted in terms of a single layer crust with crustal and Moho velocities of 6.09 (3.68) and 8.27 (4.83) for P and (S) waves (fig. 1.5a). The depth to the Moho was estimated at 36 km.

These authors observed "clear second P phases" in the distance range 200 to 290 km. These phases were too early to be regarded as P_g. They could be headwaves from an intermediate layer within the crust. The data interpreted in terms of a two layer crust gave a model shown in figure 1.5b. This gives an average depth of about 39 km to the Moho and about 23 km to the top of the lower crustal layer. But because of possible uncertainty in the identification of the second P and S phases the authors did not push forward this two-layer model. They preferred an alternative interpretation of the data in terms of a single layer crust in which velocity increased uniformly with depth.

Gane et al.(1956) used seismograms from the Witwatersrand area around Johannesburg out to epicentral distances between 50 and 500 km at 25 km intervals. Tremors were of magnitude not exceeding 3.5 and have normal focal depth of 1.5 km. Traverses were made west, south, east and north of Johannesburg.

Their data were consistent with one layer crustal model in which the depth to Moho is 35.1 $\pm$ 1.2 for Pwaves and 33.3$\pm$1.3 km for Swaves (fig.1.5c). Crustal and Moho velocities were obtained as 6.18 and 8.27 kms^{-1} for Pwaves and 3.66

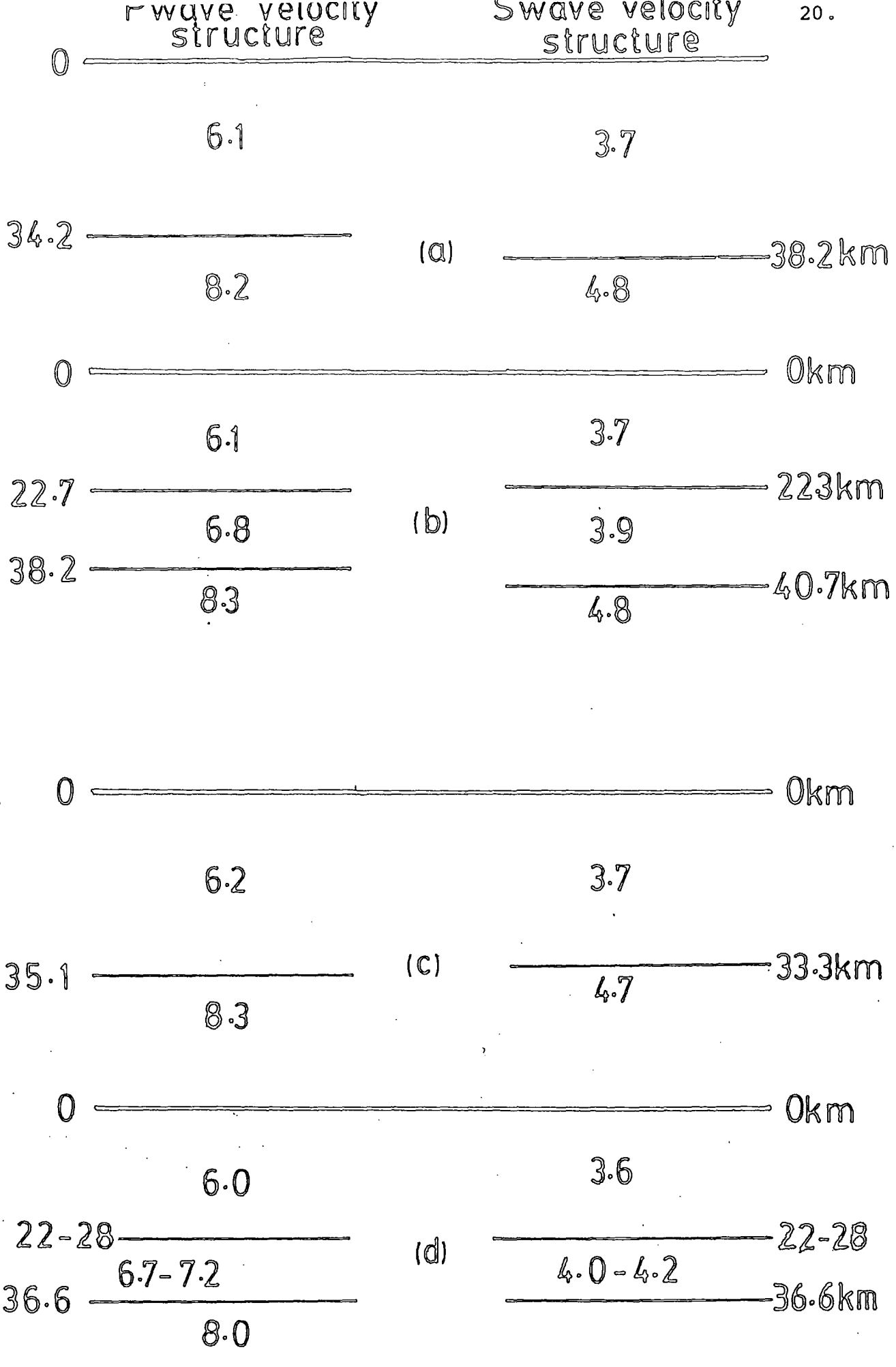

Fig 1·5 Seismic crustal models for southern Africa.
(a) and (b): Willmore et al.(1952); (c): Gane et al.(1956);
(d): Hales and Sacks(1959). Velocities in km/s.

and 4.73 kms^{-1} for S waves. No significant differences were observed in the results for different directions. The depth estimates include 1.3 km of superficial material of lower density.

These authors observed "rare occurrences of weak P and S phases" preceding the normal P and S_g beyond 180 km. Those phases could suggest the existence of an intermediate crustal layer as indicated above. The authors, however, interpreted them in terms of an increase in velocity with depth within a single layer crust. A relation of the form

$$\alpha = 6.00 + 0.011z$$

$$\beta = 3.60 + 0.007z$$

was suggested. α and β represent P and S velocities respectively and z represents depth below the surface. Because of insufficient data, this model was not advocated.

Tremors from the same source area as discussed above were recorded along a route in East Transvaal (Hales and Sacks, 1959). On the resulting seismograms, the authors found P and S phases which they interpreted as associated with an intermediate crustal layer. They therefore interpreted the travel time data in terms of a two-layer crustal model as shown in figure 1.5d. The layer thicknesses were derived from P-wave data.

Bott (1971) suggests that the P and S phases which these authors associated with an intermediate crustal layer may well be Moho reflections because of their high amplitude. It is evident, however, that reflection from the intermediate layer could have more energy than Moho reflections if the lower crust is thin compared with the upper crust (Clowes

and others , 1968, Berry and West, 1966). And that may well be case with the data under discussion. The model velocities and thicknesses (35-40 km) are typical of normal continental crust in shield areas.

From seismic data, therefore, it is evident that Africa away from the rift zone has a crust and an upper mantle structure typical of stable shield regions.

1.7.2 Evidence For Existence of Anomalous Upper Mantle Beneath the Rift Zone.

Evidence from geophysical data confirm the existence of anomalously low density and low velocity material in the upper mantle part of the East African plateau. Available data further show that this anomalous zone rises closest to the surface beneath the Gregory rift in Kenya. This implies extreme thinning of the lithosphere under the rift.

The first evidence for the upper mantle anomaly comes from gravity data. Bullard (1936) carried out large scale gravity survey in East Africa using data from pendulum measurements. He interpreted 56 of his own measurements and 33 measurements made by Kohlschutter in 1899 and 1900. From these, he observed broad negative anomalies over the East African plateau and established that the plateau as a whole is approximately isostatically compensated. This was interpreted (Bott, 1965) as requiring a low density body at the base of the crust or within the upper mantle. Later and more refined gravity data have shown that this anomaly is associated with low density upper

mantle.

Since the work of Bullard, the East African rift zone has been covered with more and better refined gravity surveys. Long Bouguer profiles across the East African plateau show that the uplifted region is characterized by broad negative anomaly values as low as -150 mgal with still more negative values over the rifts. Over the axial part of the Gregory rift, there is a small amplitude (40-50 mgls) shorter wavelength (40-80 km) positive anomaly superposed on the long wavelength anomaly (Searle, 1970). This axial positive ridge will be discussed in a later section.

All the different workers interpret the long wavelength negative Bouguer anomaly to indicate the presence of an anomalously low density material in the upper part of the upper mantle. But details of shape and thickness of models differ. Sowerbutts (1969) interprets it as due to the presence of a broad subcrustal lens of low density upper mantle or basal crust under the plateau. According to Girdler et al (1969), it is caused by a slightly lower density asthenosphere expanding to higher levels and engulfing part of the lithosphere. Darracott et al, (1972) interpret it as due to a low density asthenolith. The existence of low density upper mantle beneath the rift zone is also clearly supported by gravity data of Khan and Mansfield (1971) and Baker and Wohlenberg (1971). The various models describing this upper mantle low density material are shown in figure 1.6.

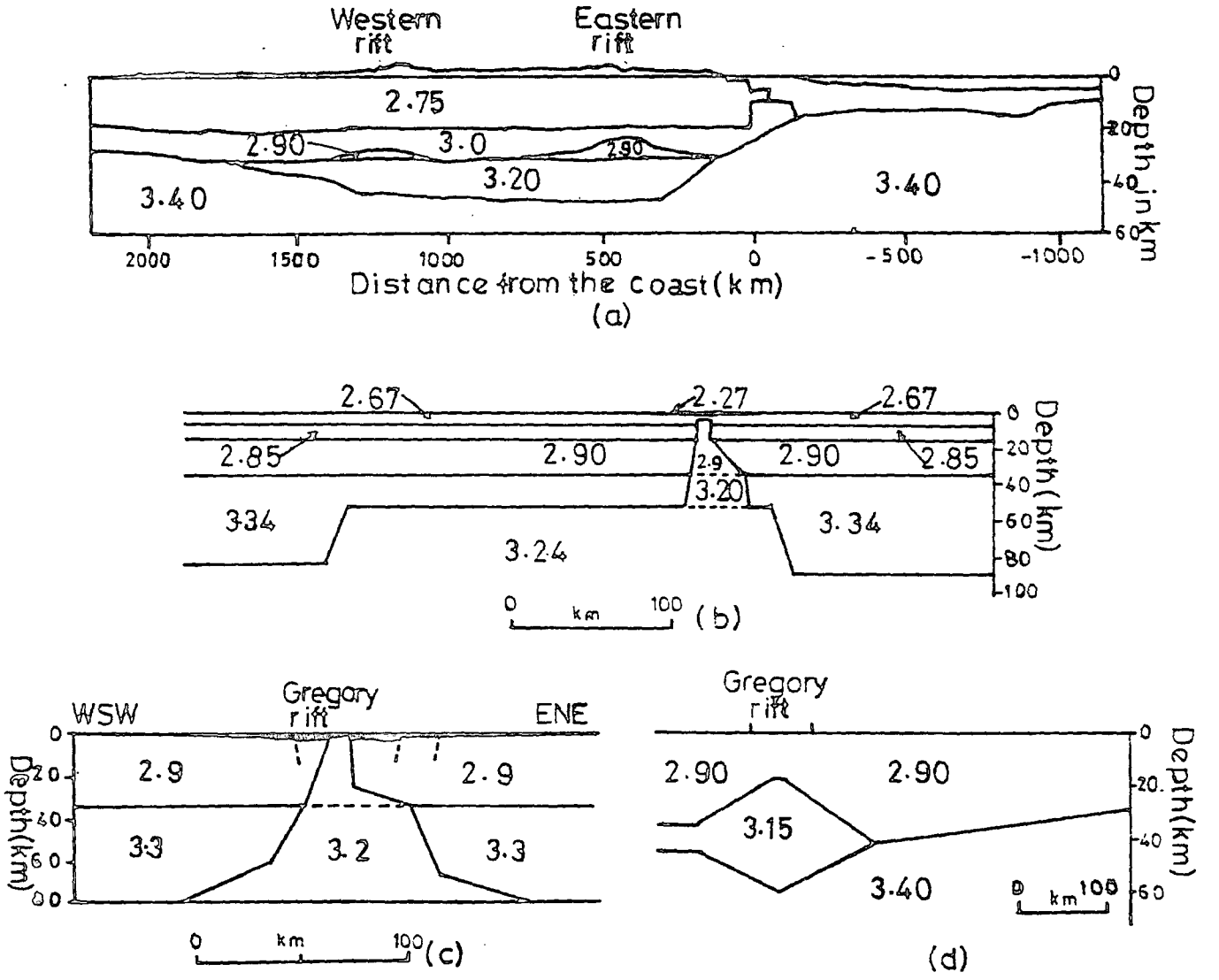

Fig 1.6: Gravity models for the Kenya dome and the Gregory rift. (a) Sowerbutts, 1969; (b) Darracott et al., 1972; (c) Baker and Wohlenberg, 1971; (d) Khan and Mansfield, 1971. Numbers are densities in g/cm^3.

The existence of anomalously low density material in the upper part of the upper mantle suggested by gravity data is supported by various other geophysical data. Surface wave dispersion data indicate the existence of anomalously low velocity upper mantle under the rift zone. The material of low density should exhibit low seismic velocity since reduction in density may arise from higher than normal temperatures.

Sundaralingham (1971) and Long et al. (1972) studied the dispersion of Rayleigh waves travelling between permanent stations of Addis Ababa (AAE), Nairobi (NAI), Lwiro (LWI) and Bulawayo (BUL). They measured inter-station phase velocities for events close to great circle paths through these stations. Their dispersion curves were then compared with the dispersion curve for AFRIC model of Gumper and Pomeroy (1970). The two curves tend to merge at shorter periods indicating some uniformity of the crust over Africa as a whole. Compared with the AFRIC model, there is a significant reduction in phase velocity at longer periods indicating anomalously low upper mantle velocities under the rift zone. They observed that this anomalous zone is well developed for the path AAE-NAI (which traverses the rift zone) and less extensive along other paths. The main anomaly, therefore, extends along the eastern branch of the rift system and is much less extensive beneath the western rift.

Knopoff and Schlue (1972) measured fundamental mode Rayleigh wave phase velocities from four teleseisms sufficiently close to the great circle path between the

recording stations AAE and NAI in the period range 20-125s. The observed Rayleigh wave phase velocities for the path AAE-NAI which samples the rift structure were comparable to those obtained for paths in the Basin and Range province of the U.S.A. In comparison, the Canadian shield profile of Brune and Dorman (1963) gives extraordinarily high velocities. The data of Knopoff and Schlue (1972) indicate that the upper mantle sampled along the path AAE-NAI has an extensive region of material with unusually low S-wave velocity. A region of perhaps 120 to 200 km in thickness has an S_n velocity between 4.25 and 4.45 kms^{-1} with little or no variation in gradient. Mueller and Bonjer (1973) have also used surface wave dispersion data to infer the existence of a well developed low velocity zone for S waves (asthenosphere) in the upper mantle in the depth range 80 to 210 km beneath the rift zone.

Studies of teleseismic P-wave delay times have shown that stations close to the rift indicate large positive delays compared with delays observed at stations sitting on normal shield structure. This suggests that arrivals at rift stations have passed through a low velocity zone on their path. Sundaralingham (1971) measured teleseismic delays at AAE, NAI and LWI relative to Bulawayo (BUL) using events in the distance range 25° to 90°. The relative delays are as shown below.

Locality	Delay (s)
AAE	2.7±0.3
NAI	2.3±0.3
LWI	1.1±0.3
Eastern rift station mean	2.5±0.3

These delays have been interpreted to indicate the existence of a substantial low velocity zone in the upper mantle beneath the eastern rift in comparison to the typical shield structure beneath Bulawayo.

Analysis of teleseismic events recorded along a 600 km long profile across the East African rift (Kenya) show delays greater than 1.5s centred on the rift which indicates a low velocity zone beneath the crust (Dahlheim et al., 1986). The delay pattern was explained as due to the upwarp of the asthenosphere/lithosphere boundary.

Savage (1979) and Savage and Long (1985) interpreted teleseismic P-wave delay times measured across the Gregory Rift near the equator and along a south eastern radius of the Kenya dome. The observed variation in delay time shows a broad zone over which there is substantial delay with a superimposed minimum along the ridge axis. This observation could only be explained by the presence of anomalously low velocity material within the upper mantle. The top surface of the anomalous zone comes to within 20 km of the surface along the rift axis. The data suggest the anomalous zone extends some 270 km south eastwards from the culmination of the dome. In general the zone thins rapidly to the south east away from the rift axis, mirroring the attenuation observed, from Kaptagat, for the same zone to the northwest by Long and Backhouse (1976). There is, however, a subsidiary thicknening under mount Kilimanjaro. A seismic

model of the axial intrusion is shown in figure 1.7.

Gumper and Pomeroy (1970) studied the propagation of S_n body waves and L_g along paths within Africa. They found that S_n is observed over all paths less than 3000 km in length that do not cross either the African rift zone or the Red Sea rift. S_n and L_g propagate across the southern part of the East African rift zone below about 10^oS, but their propagation across the northern part above the equator is inhibited. If S_n propagation is inefficient, then a high attenuation or low Q material exists (Oliver and Isaacks, 1967). The indication then is that at least the northern part of eastern rift zone is underlain by abnormally hot, less rigid upper mantle or that there is an upward protrustion of the asthenosphere into the more rigid lithosphere above (Molnar and Oliver, 1969). Upward protrustion of this high attenuation (low Q) mantle material has sproduced what Gumper and Pomeroy call a "gap" in the mantle portion of the lithosphere which closes towards the southern part of the rift zone. Nolet and Mueller (1982) do not agree with this interpretation of the observed S_n and L_g attenuation. These authors adduced some evidence to show that the only conclusion that may be drawn from L_g attenuation is that there is a gap in the crust. They also argued that S_n attenuation can be affected when not just the lithosphere (the upper 100 km or so), but a considerable portion of the upper mantle is disturbed.

Nolet and Mueller (1982) used simultaneous inversion of previously existing seismic data to obtain models for the western and eastern branches of the East African rift system in the latitude range 1^oS to 10^oN. These authors showed that the western branch is characterized by a 35 km crust and a thin high velocity lid over lying a channel possessing both low S and

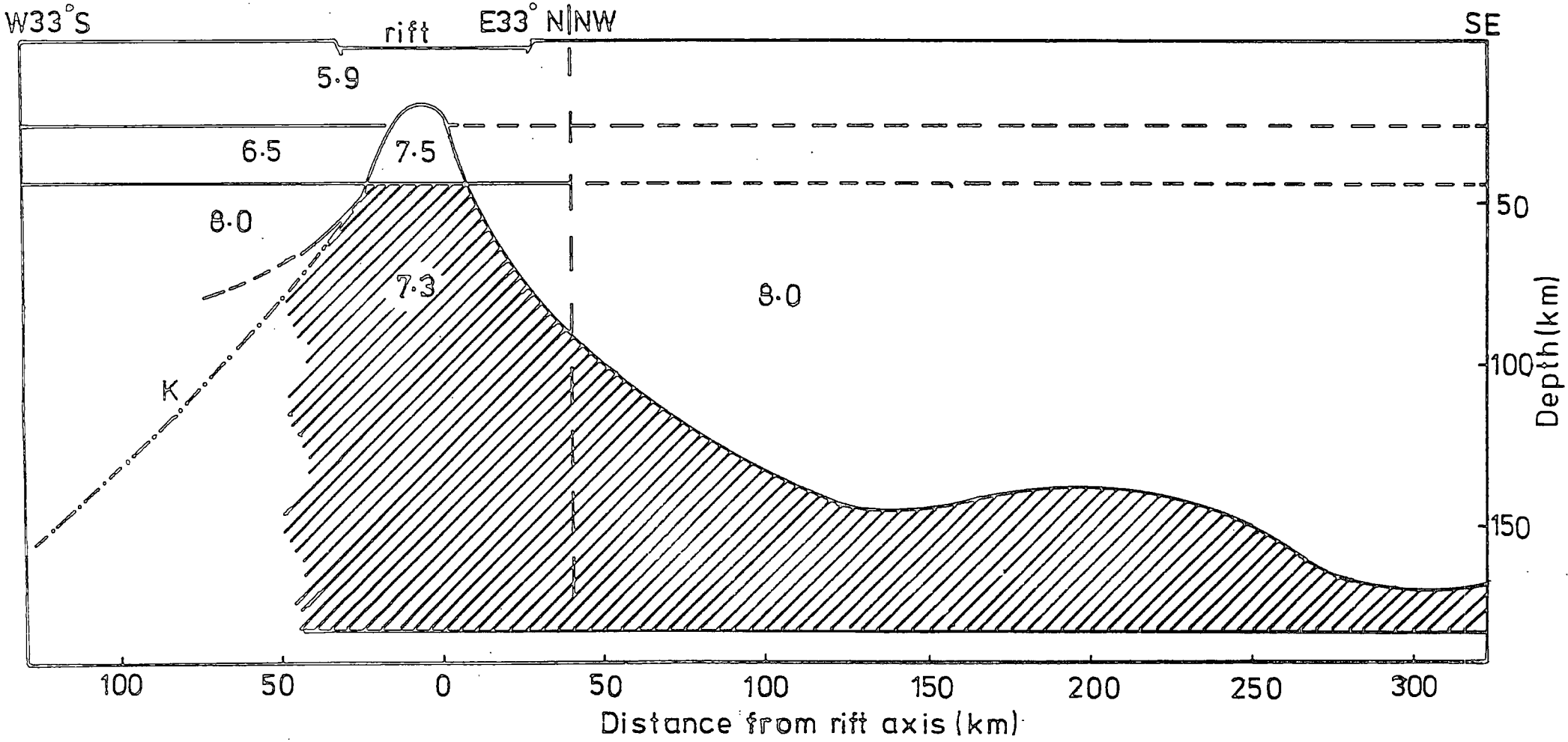

Fig 1.7 A seismic section of the Kenya dome. The shaded area denotes the anomalous zone. The numbers are velocities in km/s. (Savage and Long, 1985).

low P velocities (4.47 and 7.69 km/s respectively). A strong reflector at a depth of 140 km marks the lower boundary to the low velocity material. Their data suggest that the eastern branch has a crustal thickness of 40 km and is characterized by low S velocities, 4.43 km/s in the lid to a depth of 78 km, 4.09-4.21 km/s in a low velocity channel which extends to a depth of at least 161 km.

Geomagnetic deep sounding data provide evidence for anomalous upper mantle material under the Gregory rift. Banks and Ottey (1974) tried to define the anomalous material by its expected high conductivity. They investigated the response of short period variations in the earth's magnetic field using arrays of magnetometers. They found a region of high conductivity about 20 km beneath the rift floor and another at approximately 100 km to the east and at a depth of 100 km. Their model was however heavily dependent on previous gravity and seismic data and can hardly be said to offer independent evidence. But this interpretation has been confirmed by subsequent geomagnetic deep sounding data (Banks and Beamish, 1979). The deep body of high conductivity at a depth of about 100 km appears to correspond to the core of zone of melting in the upper mantle. This zone is responsible for the seismic and regional gravity anomalies and supports a part of the topographic elevation of the Kenya dome.

The magnetotelluric data of Rooney and Hutton (1977) provided the first independent evidence for the existence

of high conductivities at depths corresponding to the upper mantle below the Gregory rift. Their data required the presence of a conductive material at a depth of less than 8 km below the rift floor. To satisfy their long period data, a conductive material was also required at depths greater than 30 km, corresponding unambiguously to the upper mantle below the rift. The depth and thickness of this upper mantle conductor could not be resolved because of the obscuring effect of the crustal conductor.

The interpretation of slowness data provide another evidence for the presence of upper mantle low velocity zone beneath the Gregory rift. Array data recorded at the temporary station at Kaptagat have been used to study apparent slowness of teleseismic arrivals. Measured values of slowness differed significantly from the values expected from published epicentral determinations and travel time tables.

Backhouse (1972) interpreted the slowness anomalies in terms of a westerly thinning, plane sided wedge of anomalous low velocity (7.5 kms^{-1}) material embedded within normal 8·1 kms^{-1} material. Forth (1975) reached the same general conclusion but showed that the data could be better explained if a curved surface was introduced for the top of the anomalous zone while assuming a flat base.

Long and Backhouse (1976) interpreted slowness and delay-time data for teleseismic P-wave arrivals recorded at Kaptagat. They used apparent slowness vectors for 29 well recorded events in the distance

range 30^{o}-90^{o}. Measurements of P-wave delay times at Kaptagat relative to Bulawayo were made for 78 events in the distance range 25^{o}-99^{o}. Average positive delay of 2.4s was observed. This value was not significantly different from the values obtained for Nairobi and Addis Ababa relative to Bulawayo.

The authors explained the slowness anomalies in terms of lateral variation in velocity associated with a steeply dipping upper surface for the low velocity zone in the upper mantle. This upper surface of the zone was mapped (fig. 1.8) from the delay-time data to show a broad elliposoidal structure (lying at about 150 km depth) on which is superimposed a steep sided structure connecting it to the crustal intrusion along the rift axis. Fig. 1.9 represents a two dimensional model along a west-east profile assuming a uniform velocity of 7.3 km/s for the anomalous zone.

The authors showed that the zone thinned not only westwards away from the rift axis but also northwards to correspond to the dying out of the rift in northern Kenya. But they did not see any evidence to suggest that the zone is not continuous with the low velocity zone below Ethiopia indicated by large delay time at Addis Ababa. From the data, it is suggested that the centre of the structure corresponds to the centre of the uplift of the Kenya dome. This indicates that the uplift reflects the thickness of the low velocity zone in the upper mantle.

Thus geophysical data confirm the existence of anomalously low velocity and low density upper mantle

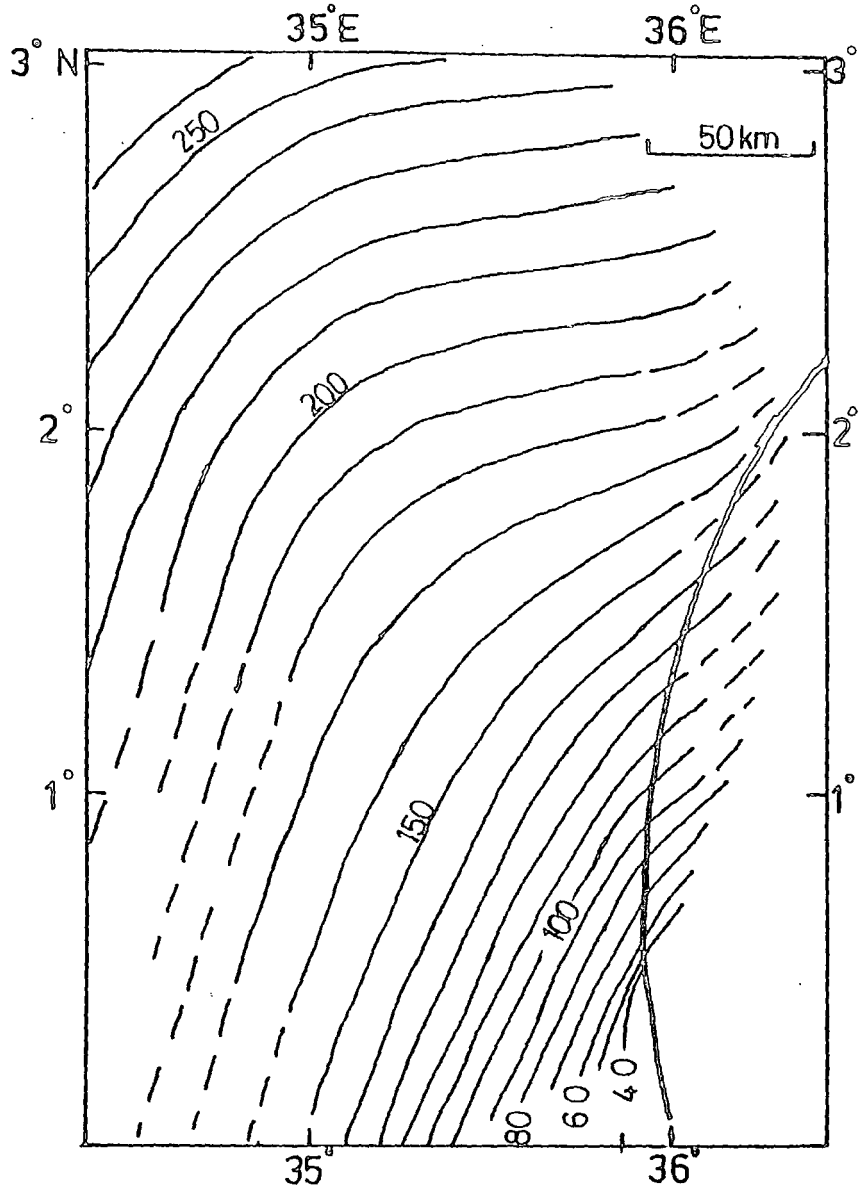

Fig 1·8 A contoured map of the upper surface of the upper mantle low velocity zone beneath the western flank of the Gregory rift · Contours are at 10 km intervals.
(Long and Backhouse, 1976).

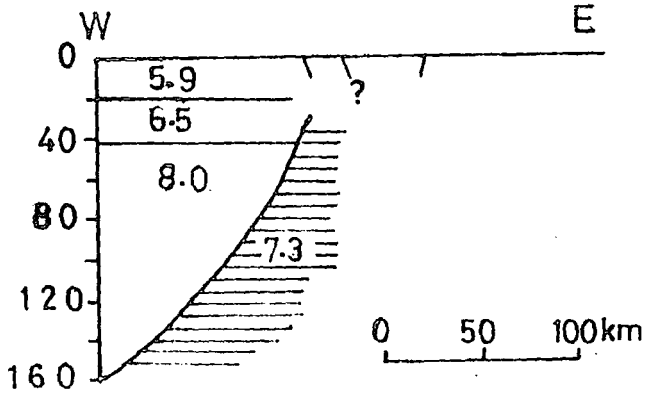

Fig 1·9 A cross section of the model for the western flank of the rift at about 0·5° N latitude· Depths are in km and velocities in km/s · (Long and Backhouse, 1976).

beneath the East African rift zone. This anomalous material could result from partial melting in the normal upper mantle. The expansion resulting from this would give rise to upward migration of the low density upper mantle material with the attendant increase in temperatures. Surface manifestations of this will be seen in the localised increase in heat flow (Crane and O'connel, 1983; Morgan, 1983) and magmatic and seismic activity in the rift zone. Extension of this anomalous mantle material up into the crust will obviously produce positive contrasts in both density and velocity. These are all evidenced in the structure of crust under the rift inferred from geophysical data.

1.7.3 Crustal structure close to but outside the Gregory Rift.

The structure of the crust in the central part of the Gregory rift has been found to be anomalous. It is manifested by high seismic velocities and significantly positive density contrast. But this anomalous crust has a limited lateral extent. Normal shield crust is found to exist in close proximity to the rift structure to the western and eastern flanks and also in the southern extremity of the Gregory rift. These conclusions are indicated by the following seismic data.

Bonjer et al (1970) analysed seismograms of two deep focus teleseismic Hindu Kush earthquakes recorded at Lwiro (LWI) on the western flank of the western rift, Nairobi (NAI) close to the eastern margin of the Gregory

Rift and Addis Ababa (AAE). From these seismograms they determined the spectral response ratios of long period body waves. From inversion of these data they produced thick two layer crustal models with horizontal interfaces; crustal thicknesses of 39, 43 and 35 km were obtained for AAE, NAI and LWI respectively (fig. 1.10). The observed average velocities and thicknesses are typical of shield areas. These crustal models for AAE, NAI and LWI are further confirmed by similar data obtained by Mueller and Bonjer (1973).

A further confirmation of the crustal thickness in this region is obtained from data on P to S conversion. Long period teleseismic P waves recorded at AAE and NAI show comparable P to S (P_S) conversions (Herbert and Langston, 1985). The timing of the P_S conversion relative to P suggests crustal thickness of 41 km for both stations.

Rykounov et al. (1972) showed that the crust in the southern part of the Gregory rift is near to typical for continents. They studied this part of the rift using P and S wave travel time data from local earthquakes in the magnitude range $1 \leq M \leq 3$. The region of study was from Lake Magadi in Kenya to mount Hanang in Tanzania. They showed that within the part of the Gregory rift contained in their survey area, the most probable focal depth was 10-20 km although their method of deriving focal depths was not, however, stated.

They derived a two layer crustal model (fig. 1.10) for their region of study. The P wave velocities for the upper crust, lower crust and Moho were 5.8, 6.5 and 8.0

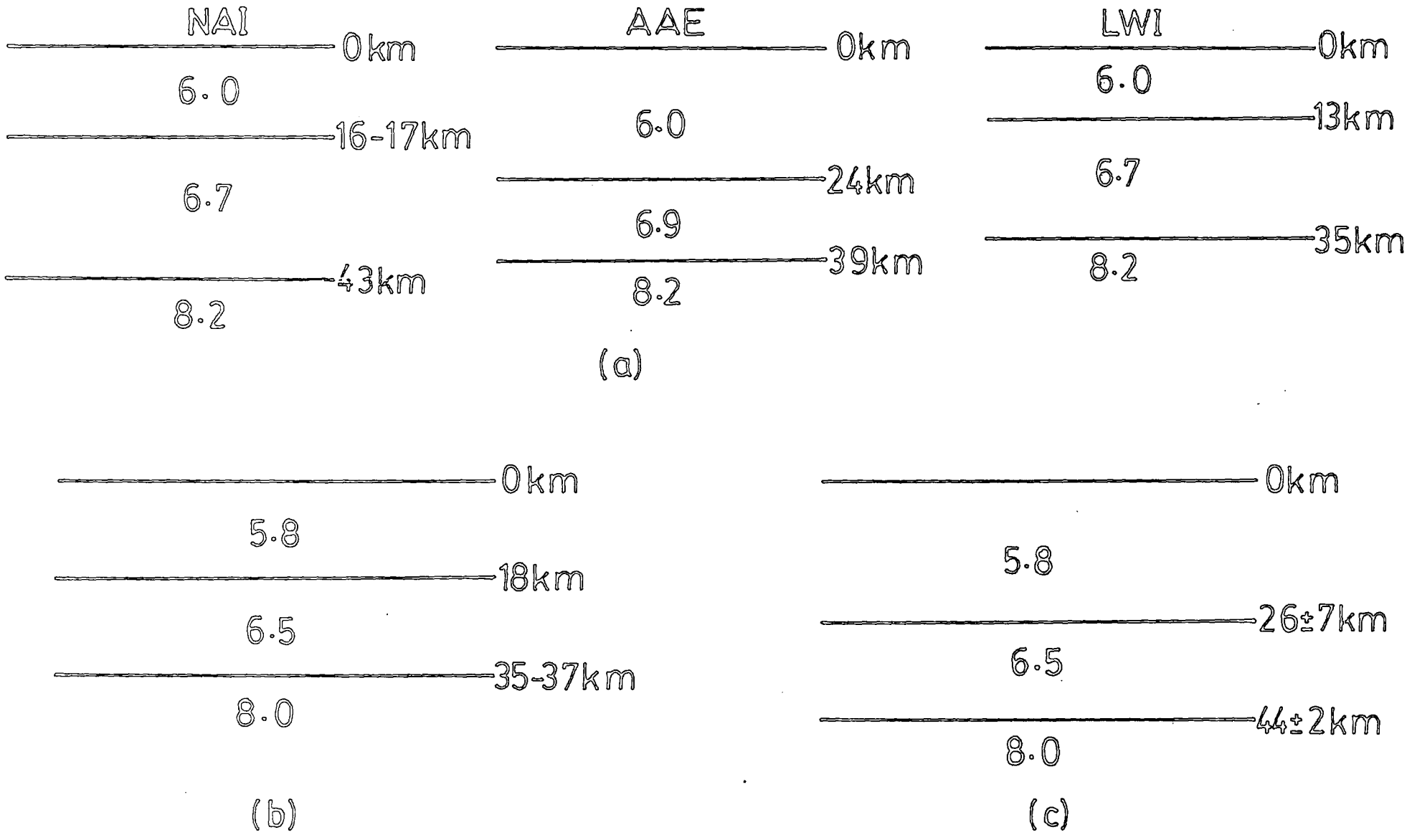

Fig 1.10 Pwave velocity models for the crust close to but not within the central part of the Gregory rift: (a) Bonjer et al. (1970), (b) Rykounov et al. (1972), (c) Maguire and Long (1976).

kms^{-1} respectively. The Moho depth was 35-37 km and the depth to the intermediate layer was about 18 km. These results compare well with the refraction data in southern Africa (Hales and Sacks, 1959).

Maguire and Long (1976) measured apparent velocities and azimuths of first arrivals from local and regional earthquakes recorded at Kaptagat array station located about 15 km west of Elgeyo escarpment. Data from arrivals coming from the west of the array (azimuth $160^{\circ}-360^{\circ}$) were consistent with a two-layer crustal model. An intermediate boundary in the crust at a depth of 26 ± 7 km was introduced to explain the 6.5 kms^{-1} peak in the histogram of first arrival apparent velocities. A crustal thickness of 44 ± 2 km was consistent with the data. Their preferred model shown in fig. 1.10 has upper crustal and sub-Mohovelocities of 5.8 and 8.0 kms^{-1} respectively.

This structure is similar to those obtained for southern part of the Gregory rift (Rykounov et al.,1972) and for Southern Africa (Gane et al., 1956; Willmore et al., 1952; Hales and Sachs, 1959). The conclusion to be drawn from this work is that normal shield type crust with normal sub-Moho material exists at least up to within 30 km of the rift axis on the immediate western flank of the Gregory rift. The implication, therefore, is that a steep structural boundary seperates normal shield crust and sub-Moho material beneath the western flank of the rift from a mantle derived crustal intrusion beneath the rift axis.

1.7.4 The structure of the lithosphere within the Gregory Rift.

Geophysical data discussed above confirm that the crust within the Gregory rift differs significantly from the normal shield crust outside the rift zone.

Over the axial part of the Gregory rift there is observed a positive ridge of short wavelength (40-80 km) Bouguer anomaly of low amplitude (30-60 mgal) superposed on the long wavelenth Bouguer negative anomaly (Searle, 1970). Quaternary volcanoes and segments of increased geothermal activity are confined to this axial anomaly. This positive anomaly is interpreted by several workers in terms of a dense mantle derived basaltic crustal intrusion probably continuous with the low density upper-mantle material associated with the long wavelength anomaly.

Estimates of the depth to the top surface of this crustal intrusion vary from 2 km (Searle, 1970) through 3.5 km (Fairhead 1976) to 20 km (Khan and Mansfield, 1971). The width within the crust is estimated at between 10 km (Baker and Wohlenberg, 1971; Fairhead, 1976; Darracott et al., 1972) and 20 km (Searle, 1970).

Griffiths et al. (1971) used explosion (refraction) data to determine the structure of the crust beneath the axial zone of the northern part of the Gregory rift. Disposition of the shot points and seismometer positions are shown in fig. 1.11a. Shots were let off in Lakes Turkana and Hannington and recorded at ten stations set up roughly along a line joining the shot points. Each station consisted of eight 2Hz vertical component seismometers laid

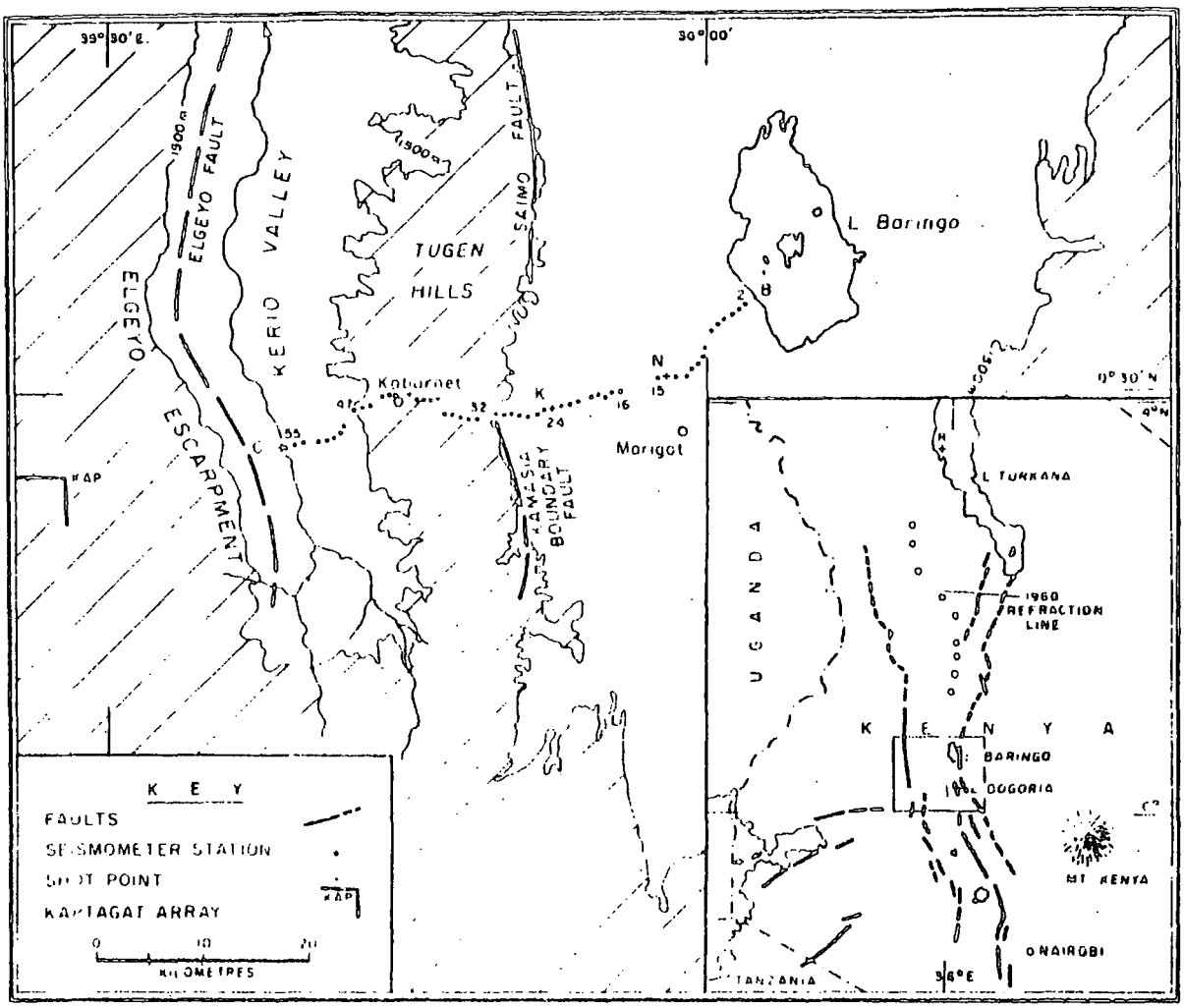

Fig·1·11a: Locations of the seismic lines used in the refraction studies of Griffiths et al·(1971) and Swain et al·(1981)· Ground above 1500m shown shaded· From Swain et al·(1981)·

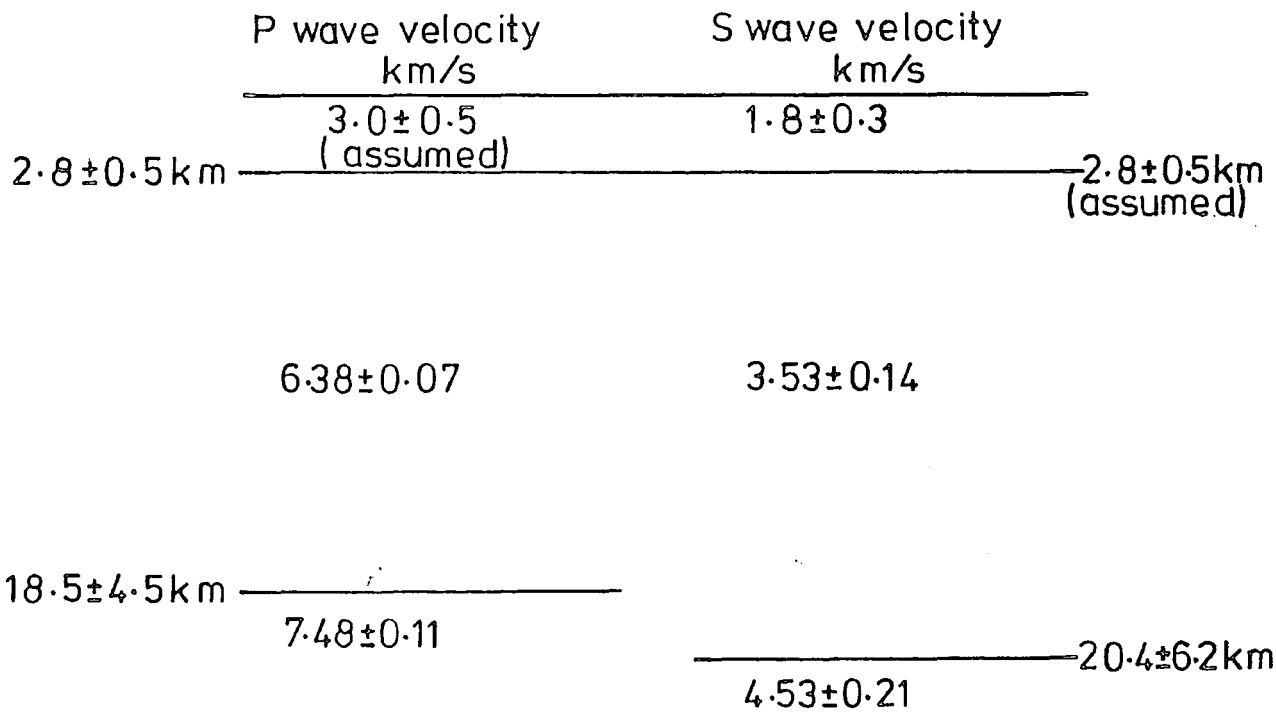

Fig·1·11b: Seismic model of the crust beneath northern part of the Gregory rift (Griffiths et al·,1971)·

out in a linear N-S array extending over 1 km and including a three component set near the centre point. The maximum range was about 367 km.

The profiles were, however, effectively unreversed because the Turkana shot was recorded clearly at all stations except station number 1. Interpretation was based on first P and the corresponding S arrivals. A head wave with a velocity of 6.4 km/s was recorded from shots in Lake Hannington, whereas 7.5 kms^{-1} velocity was recorded using shots in Lake Turkana in a similar distance range. This may suggest strong lateral heterogeneity but was inconsistent with large dips on the main refractor interface. The data was consequently interpreted in terms of a horizontal layer of material of velocity 6.4 kms^{-1} overlying a material of 7.5 kms^{-1} velocity at a depth of about 20 km (fig. 1.11b). These were unreversed velocity estimates.

The apparently high velocity of 6.4 km/s for crustal material at depths above 20 km suggests the presence of an axial crustal intrusion of higher velocity basaltic magma rising to shallow depths. Such intrusion model is consistent with gravity data discussed above.

Swain et al.(1981) analysed the data from a 50 km E-W reversed refraction (explosion) profile from Chebloch Gorge (C) to Lake Baringo (B) at the latitude of Kaptagat (fig. 1.11a). This experiment was designed to confirm the presence of the 6.4 km/s material and if possible establish its lateral extent and to provide control for the interpretation of the gravity data along the same profile.

The seismic data (first arrivals) were interpreted in terms of two/three layer model (fig. 1.12a). The top layer of P wave velocity 3.7 km/s is about 3 km thick and represents lavas and sediments.

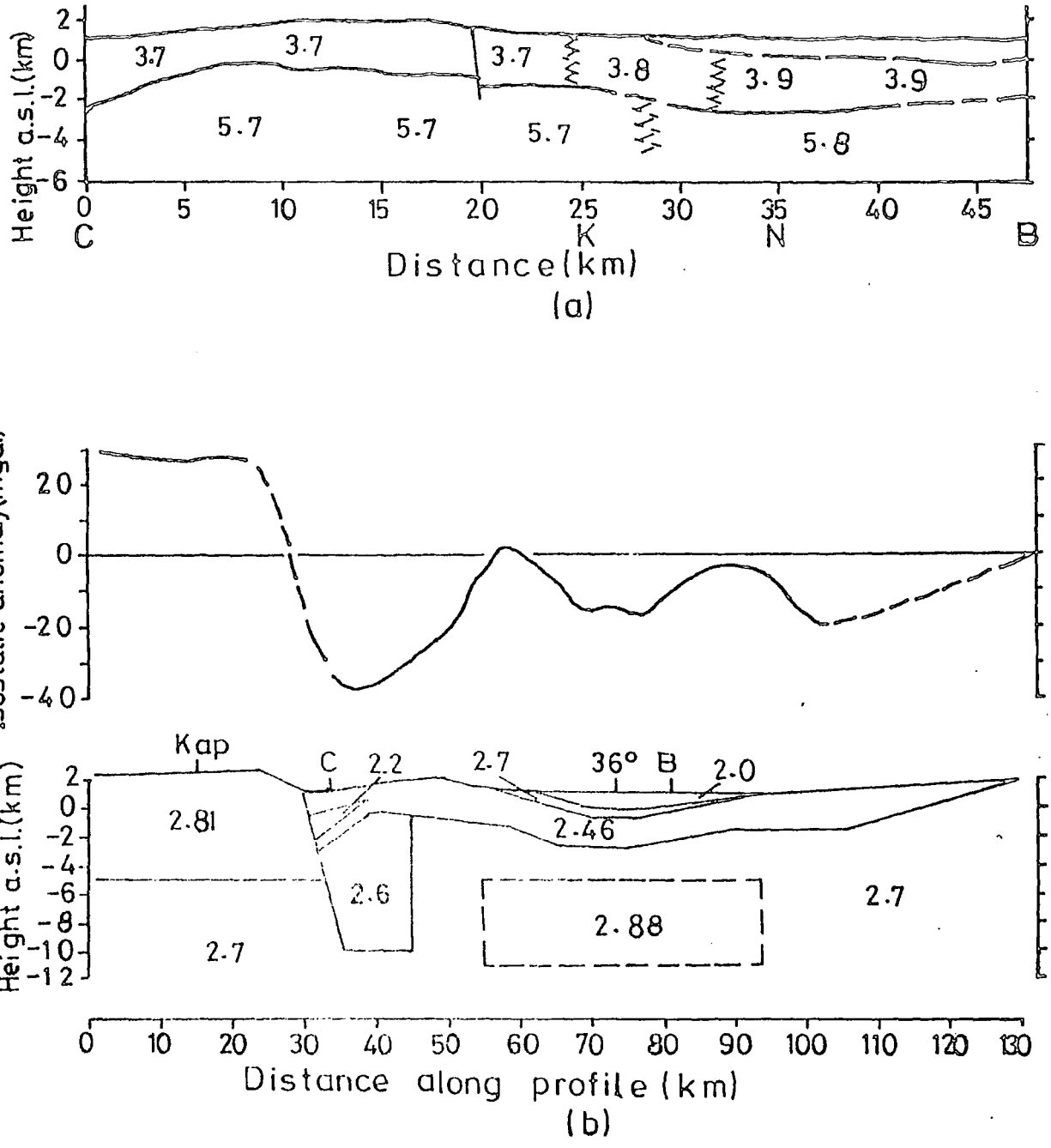

Fig.1.12 : (a) Velocity section derived from KRISP first arrival data. Mean velocities shown in km/s. The zig-zag lines do not represent actual structure. (b) Gravity profile at about 0.5°N. Isostatic anomalies and the corresponding two dimensional density model with densities shown in g/cm^3. (From Swain et al., 1981).

This layer overlies a layer of velocity about 5.8 km/s which represents the metamorphic basement and is observed throughout the profile. The seismic data, therefore, suggests that that metamorphic basement rocks exist below the full width of the rift floor at 0.5°N. This is in agreement with geological data (King, 1978; Chapman et al., 1978).

The 6.4 km/s refractor of Griffiths et al.(1971) was not, however, detected by the first arrival data, used by Swain et al. (1981). Such a body at a depth of more than about 6 km would not give rise to refracted first arrivals along this short line (about 50 km long). The 6.4 km/s refractor, if it exists, must therefore be deeper than about 6 km.

Although the 6.4 km/s refractor was not detected by their seismic experiment, their gravity profile at about 0.5°N suggests that such material may exist as an intrusion within the basement in the form of either a broad region of dykes or an elongated lopolith with the later being favoured (fig. 1.12b). The configuration of this dense rock responsible for the axial high gravity anomalies seem to form a broad (20-35 km) zone within the basement, with strike along the rift axis, and of limited vertical extent (4-6 km). It has its top surface at a depth of about 6 km for the profile at about 0.5°N. For the profile at 1°N the body shallows and the minimum depth to its surface is probably the base of the Caenozoic rocks at 3 km depth.

Khan et al.(1987) have derived a velocity model for the lithosphere beneath the axis of the southern part of the Gregory rift from KRISP 85 data. Their experiment consisted of two seismic refraction lines (fig. 1.12c). The 300 km long north-south line was located along the rift axis with end shot points at Lakes Baringo and Magadi. These and other inter-

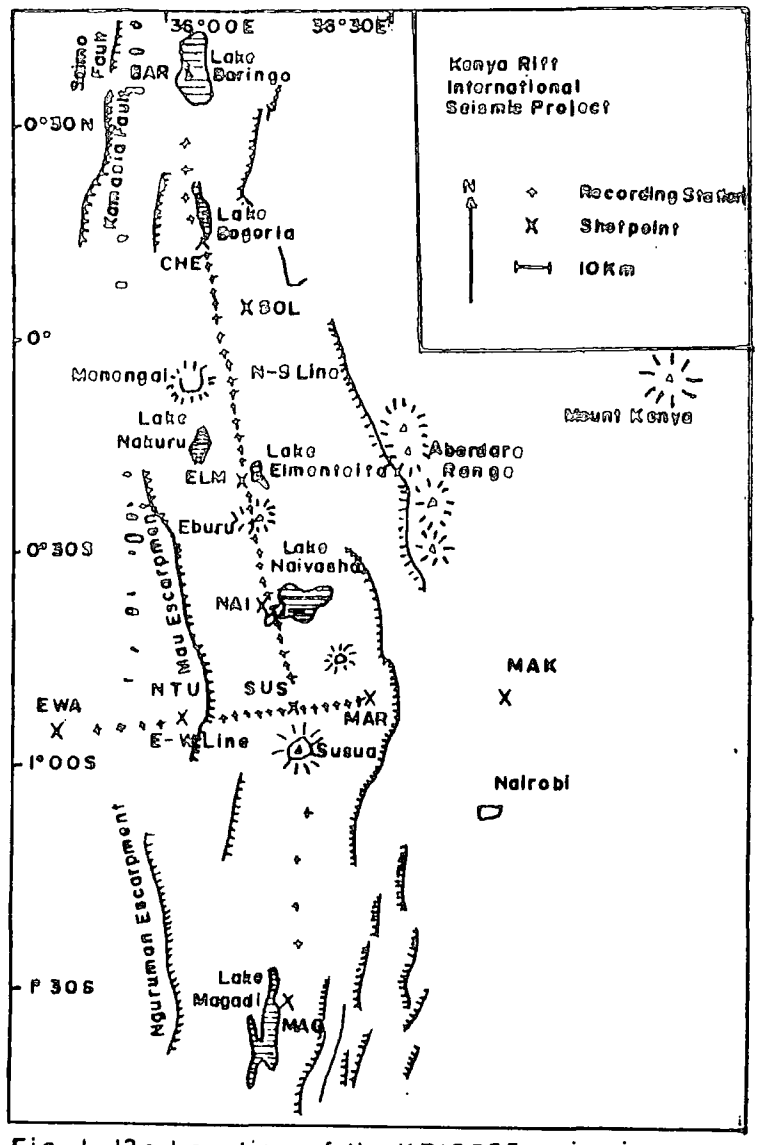

Fig. I. 12c Location of the KRISP85 seismic experiment showing the lines and shot points. Recording station locations for the east-west line are diagramatic, as the spacing is too small to be shown on this scale

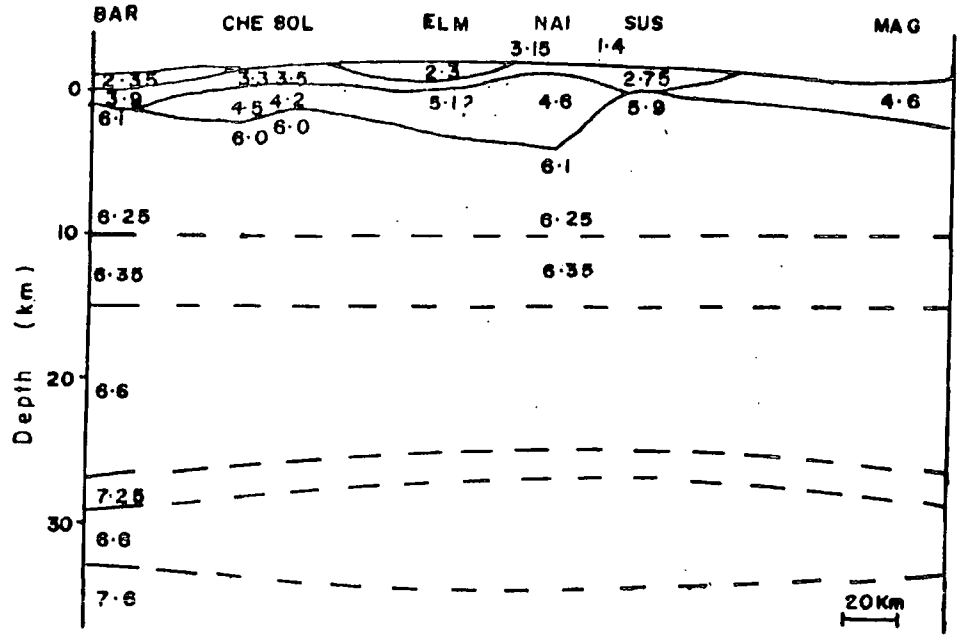

Fig. I.12d : Velocity-depth structure along the axis of the rift from Lake Baringo to Lake Magadi (velocities in Km/s).
(Khan et al., 1987)

mediate shots were recorded by 42 three component recording stations at 3.5 km intervals between Chepkererat and Susua. Across the rift an E-W line was completed with end shots at Ewaso Ngiro (EWA) and Makuyu (MAK) with recording stations at 1.25 km intervals. Interpretation was based only on the axial N-S line because the data from the E-W line were of poor record quality. The explosion program was also followed by three earthquake recording experiments.

Analysis of phases observed up to a few tens of kilometres from the shots on the N-S line and previous experiments show that the rift infill has velocities ranging from 1.4 to 4.6 km/s and thicknesses ranging from 2 km (beneath Lake Baringo and Susua) to 6 km (beneath Lake Naivasha). From phases identified as P_g, the authors established that the uppermost basement dips south from Lake Elmenteita to Lake Naivasha. Basement velocity increases from about 6.1 km/s at the top of the basement to about 6.25 km/s at 10 km depth.

The authors observed four correlatable phases three of which they identified as reflections. These phases were combined with others mentioned above to derive the model shown in fig. 1.12d. The model suggests crustal thinning away from the culmination of the Kenya dome where a 7.6 km/s layer at about 35 km depth is overlain by a 10 km thick lens including anomalous velocity (6.6 km/s) material regarded as the base of the crust.

The results suggest that the compensation of the Kenya topographic dome is due, at least in part, to crustal thickening. The basement velocities (about 6.1 km/s at the top) appear too low to be associated with the dense axial intrusion within the crust usually associated with the superposed axial positive Bouguer gravity anomaly. However, 6.1 km/s could represent

intrusive material, since lower basement velocities (about 5.8 km/s) have been measured off the rift axis (Swain et al., 1981; Maguire and Long, 1976) and velocity increases with depth, possibly indicative of multiple dyke injection from below. The results of this study also suggest significant variations in crustal structure both across and along the rift axis.

Maguire and Long (1976) analysed first arrival data from local and regional earthquakes recorded at Kaptagat. The eastern events (0^{o}-160^{o} azimuth) fell into two groups. The first group were those with P-S times greater than about 15s which originate from the rift at long distances (about 180 km) to the north and south. Apparent velocities for events in this group fall in the range 6.8 to 7.6 kms^{-1}. No attempt was made to interpret them as they may not have sampled the rift structure..

The other group includes events with P-S times less than 15 s which originate from the rift immediately to the east of Kaptagat. Events in this group were used to study the rift structure. These events could be divided into two satistically seperate groups with velocities of 7.9 $\pm$ 0.3 and 7.1 $\pm$ 0.3 kms^{-1} appearing at similar azimuths and P-S times. The authors offered no explanation for the 7.9 kms^{-1} group.

They explained the 7.1 kms^{-1} arrivals as headwaves from a shallow and nearly horizontal boundary. This interpretation immediately implies the foci must be near the surface for this group. They argued that the 7.5 kms^{-1} velocity observed by Griffiths and others could be due to a dip, towards the north, of the 7.1 kms^{-1} refractor whose true velocity must be less than 7.5 kms^{-1} and probably greater than 7.1 kms^{-1}. The 7.1 kms^{-1} material may exist beneath the 6.4 kms^{-1} material of Griffiths et al. (1971).

Savage (1979) and Savage and Long (1985) measured vertical delay times for teleseismic events recorded at stations on the Gregory rift close to the equator. Significantly smaller delay times were observed at the centre of the rift than at the edges. This dip in delay times runs along a line coincident with the rift axis and corresponding to the positive gravity anomaly. This was shown to indicate that the anomalously low velocity and low density zone within the upper mantle penetrates the crust to form an intrustion of relatively high velocity material along the rift axis.

The derivation of a structural model to fit their delay time data was based on certain reasonable assumptions. Their model assumes that a uniform crustal structure exists, both to the east and west of the rift as derived from Kaptagat data (Maguire and Long, 1976). A P-wave velocity for the anomalous zone at crustal depths was assumed as 7.5 km/s as recorded by Griffiths et al.(1971).

This data was then satisfactorily interpreted in terms of a model with a high velocity axial intrusion into the crust (fig. 1.13). The width of this intrusion at the normal base of the crust was estimated as about 30 km while the depth to its top surface was estimated to be about 20 km. The delay time data thus establishes, independently, the existence (suggested mainly by gravity data) of the low density, low velocity material in the upper mantle beneath the Kenya dome and the intrusion of this material to crustal levels.

The delay time minimum is associated with a localized region of topmost crust some 20 km deep and 20 km across, suggestive of a magma chamber (Long, 1986). Further evidence indicate that this chamber is probably being fed by a hot column of material arising from sub-lithospheric depths.

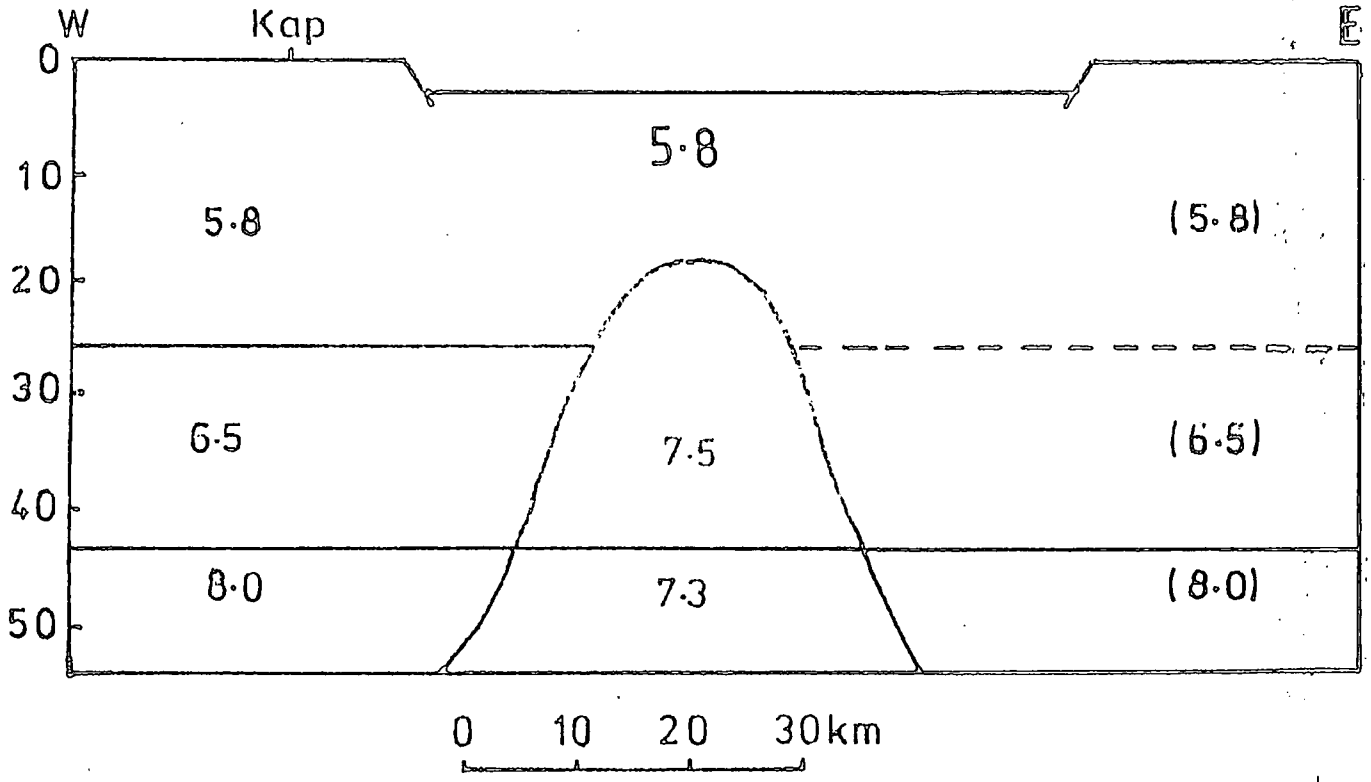

Fig 1·13: Seismic crustal model across the Gregory rift at about 0·5°N latitude. Depths are in km and velocities in km/s. (Griffiths et al. 1971; Maguire and Long, 1976; Savage and Long, 1985).

Teleseismic data are unlikely to give a unique and detailed geometry/size of the top surface of the intrusion at shallow crustal levels. Hence the depth to and the lateral extent of the top surface of this intrusion need to be determined more accurately by more suitable methods.

The existence of normal shiedl type crust in close proximity to anomalous rift structure implies the existence of a sharp boundary between the two structures. In this study attempts will be made to define the western limit of the rift crust/lithosphere. Velocity depth profile for the lithosphere beneath the Gregory rift at about 0.5^{o}N latitude will also be derived.

1.8 Theories of the rift formation.

The Cainozoic continental rift zones are associated with a number of common observed characteristic features. These features include higher than normal heat flow, large amplitude long wavelength negative Bouguer anomaly with a superposed positive low amplitude high along the rift axis, delayed teleseismic body wave travel times, seismic and volcanic activity with various depths of magma source. The crust/lithosphere in these rift zones is uplifted, thinned, domed and extended. These observations have been interpreted in terms of the existence of hot low density and low velocity material in the upper mantle. This material which is probably less dense than the mantle part of the lithosphere shallows beneath the rift zone resulting in thinning of the lithosphere. Isostatic equilibrium is maintained by crustal uplift and doming. Some of these geophysical data are discussed below.

Morgan (1983) analysed heatflow data from the Cainozoic continental rifts: Baikal, East Africa, Rhine and Rio Rande. Most of the data indicate higher than normal heat flow with means of

about 70-125 mW/m^{-2} restricted to the volcanic areas of the grabens in the rift systems. In the Gregory rift, a high mean heatflow of 105 mW/m^{-2} was observed in a zone (on the rift floor) dominated by volcanics while on the eastern and western rift shoulders, normal heat flow values of 39 and 57 mW/m^{-2} respectively were observed. This is consistent with data from geothermal mapping along the Gregory rift which indicate that an average of 11-30 MW/km of heat is advectively emitted along the rift (Crane and O'Connell, 1983). The bulk of the advected heat is lost through the central part of the Kenya dome on the rift floor. Local graben heat flow anomalies are thought to be primarily due to convection of heat through the lithosphere of the rift zones by ascending magmas.

Conductive zones have been detected in the lower crust and upper mantle beneath the Gregory rift by magnetotelluric and geomagnetic deep sounding data (Banks and Ottey, 1974; Rooney and Hutton, 1977; Banks and Beamish, 1979). Similar conductive zones have been observed in the Baikal, Rhine graben and Rio Grande rift zones (Jiracek et al., 1983). The intra crustal conductive zones are generally interpreted in terms of high temperatures and partial melt at crustal levels although Jiracek et al. (1983) argue that there can be alternative sources for a similar electrical anomaly observed in the Rio Grande rift. The upper mantle electrical anomally is associated with the low density low velocity material indicated, by gravity and seismic data, to exist in the upper part of the upper mantle beneath the Gregory rift.

Regional Bouguer anomalies of 100-200 mgal (Gregory rift), 160 mgal (Rio Grande rift), 20-30 mgal (Baikal rift) and $\pm$ 10

mgal (Rhine graben) have been reported (Neugebauer, 1983). These regional anomalies are associated with low density upper mantle. Superposed on the longwavelength regionals are shorter wavelength highs that may be related to magmatic intrusion in the crust (Baker and Wohlenberg, 1971; Searle, 1970; Banks and Swain, 1978).

Olsen (1983) has reviewed available seismic data from these rift zones; thinned crust and anomalously low compressional wave velocities in the upper mantle, generally interpreted as evidence of asthenospheric upwelling, are indicated by the seismic data in the rift zones studied.

The rift zones are also all associated with domal uplifts of the order of 1 to 2 km with diametres of a few hundred kilometers or more and with crustal extension. In the Gregory rift, geological evidence suggests that uplift began to grow in the Miocene before the development of the rift (Logatchev et al., 1983). This would suggest that here uplift may be cause of rifting. Crustal extension relative to the initial width of the graben zones have been estimated as about 25-35 km for the Kenya rift, 32 km for the Rio Grande rift, about 10 km for the Baikal rift and not more than 5 km for the Rhine graben (Neugebauer, 1983). The extension correlates with thinned crust and anomalous upper mantle indicated by the presence of low density and low velocity material beneath the rifts.

All these continental rifts exhibit pre rift and late rift volcanism. Crustal extension and total volume of volcanism appear to be proportional for example the total volume of volcanics is 20 times greater in Kenya rift zone than in the Baikal rift zone (Logatchev et al.,1983). In the Gregory rift, the maximum volumes of magma erupted during the pre-

and late rift periods.

These common features observed in the Cainozoic continental rifts suggest that one common mechanism of continental rifting may prevail. This common mechanism may be modified by the volcanic-tectonic activity in the plate induced by boundary conditions prevailing on the plate. Any acceptable mechanism for the rift formation must therefore be able to explain these observed features. The Gregory rift is the best example of a continental rift and a mechanism for its formation may be modified to apply to other continental rifts.

Current mechanisms proposed for continental rift formation generally fall into two classes: active and passive (Sengör and Burke, 1978). In active rifts extension and subsequent break up of the lithosphere result from convective upwelling of the asthenosphere due to gravitational instability. The asthenospheric upwellings thin the lithosphere causing isostatic uplift and lithospheric failure (Neugebauer, 1978). For active rifts, doming probably precedes/ causes rifting (Crough, 1983; Mareschal, 1983) although this view is not generally accepted (Baker et al. 1972). Kenya rift is generally held to be active (Girdler et al., 1969; Fairhead, 1976; Logatchev et al., 1983). Passive mechanism for continental rifting generally relate the tensional failure of the lithosphere to pre-existing tensional stresses, which are perhaps a consequence of large-scale plate interactions.

In this case the lithosphere is stretched and the asthenosphere plays a passive role (Keen, 1985). Hot less dense asthenospheric rocks rise passively through the colder and more dense mantle part of the lithosphere to the vicinity of the Moho and may displace crustal rocks. Uplift is caused by lateral spread of these diapiric rocks near the Moho (Turcotte and Emerman, 1983).

The sources of lithospheric stress have been reviewed by Bott and Kusznir (1984). Two main categories of lithospheric stress are suggested : the renewable and non-renewable. The renewable stresses are those that persist, as a result of continued presence or re-application of the causative boundary or body forces, even though the strain energy is being progressively dissipated. Important examples include plate boundary forces (Forsyth and Uyeda, 1975 ; Solomon et al., 1975) and isostatic effects associated with anomously uplifted areas such as deeply eroded mountain chains or high plateaus (Artyushkov, 1973; Turcotte and Oxburgh, 1976; Bott and Mithen, 1981). The non-renewable stresses are those that can be dissipated by release of strain energy initially present- these include bending stresses, thermal stresses and membrane stresses generated in a moving lithospheric plate in response to non-sphericity of the earth (Turcotte and Oxburgh, 1973; Freeth, 1980).

An important phenomenon that can generate large stresses at shallow depths is the stress amplification caused by lithospheric creep (Bott and Kusnir, 1984). This causes externally applied stress to be concentrated in the upper lithosphere as a consequence of creep and stress decay in the lower lithosphere. This stress amplification is applicable to renewable stresses and is most pronounced in regions of very high geothermal gradients; in these regions the stress can be amplified to levels sufficient to fracture the whole brittle-elastic part of the lithosphere. For the stress caused by isostatically compensated surface loads, the effect of stress amplification is most conspicous if the isostatic compensation is deep seated, that is, in the upper mantle (as in East Africa). Bott and Kusznir (1979) showed that the continental lithosphere of a plateau uplift region of 2 km elevation (as in East Africa) modelled in terms of an upper elastic layer 10 km thick above a visco-elastic lower crust and upper mantle, can give rise to stress differences of about 200 Mpa in the elastic layer at the top of the crust. This is sufficient to rupture the lithosphere.

In both active and passive models for rift formation, three basic mechanisms have been suggested for lithospheric thinning, and rifting. These are thermal thinning, mechanical thinning (or lithospheric stretching) and asthenospheric diapirism. In thermal

thinning the lithosphere is static, but material is removed from the base of the lithosphere by heating, conversion to asthenosphere and removal in an asthenosphere convection system. In mechanical thinning or lithospheric stretching, the lithosphere material moves laterally in response to a regional extensional stress field, and the asthenosphere rises passively to fill the void created by the thinning lithosphere. In asthenospheric diapirism, the asthenosphere penetrates the lithosphere driven by the gravitational instability of the less dense asthenosphere under a more dense mantle lithosphere, and then flow occurs in both the lithosphere and asthenosphere. All current theories of rift formation involve these mechanisms in varying degrees. Some of these proposed theories are now discussed.

McKenzie et al. (1970) applied the concept of sea floor spreading and plate tectonics to explain the formation of the Eastern rift. In this treatment, the Red Sea, the Gulf of Aden and the Eastern rifts are considered as three limbs meeting at a triple junction at Afar. These three axes seperate the Afro-Arabian region into the Nubian, Somalian and Arabian plates.

The relative motion between the plates on each side of the eastern rift can be obtained from the opening of the Red Sea and Gulf of Aden spreading axes. If the motions between the Arabian and Somalian and the Arabian and Nubian plates can be determined, the motion between Somalian and Nubian plates may be calculated from the postulates of plate tectonics.

Laughton (1966) used the strikes of transform faults in the Gulf of Aden to determine the motion between the Arabian and Somalian plates. He obtained a pole at 26.5°N and 21.5°E with a rotation angle of 7.6°. This result was consistent with geological

evidence, seismicity data, fault plane solution for earthquakes (Sykes and Landisman, 1964) and magnetic lineations in the Gulf of Aden.

From the fitting of the coastlines on both sides of the Red Sea, McKenzie et al. (1970) obtained a pole of rotation for the Arabian and Nubian plates at $36.5^{\circ}N$, $18^{\circ}E$. This is supported by the fault plane solution of earthquakes located in the Red Sea.

Combining the poles of opening and rotation angles for the Red Sea and Gulf of Aden, a pole and an angle of rotation between Nubian and Somalian plates were obtained. The resulting pole is at $8.5^{\circ}S$, $31.0^{\circ}E$ with the rotation angle of 1.9°. This implies that the opening that has taken place on the Eastern rift varies from 65 km in northern Ethiopia to 30 km in Kenya.

But geological data will allow only between 5 and 25 km of crustal extension in the central sector of the Gregory rift but not more than about 3 km at its extremeties (Baker and Wohlenberg, 1971). The rift formation is therefore difficult to explain in terms of the concept of plate tectonics in the simple form suggested above.

The concept of crustal (lithospheric) plate motion over mantle hot spots has been advanced by Wilson (1963) to explain the origin of the Hawaiian and other island arc chains. Morgan (1971) suggests that the mantle plumes or hot spots could also explain the formation of continental rifts and their transformation into ocean basins. He infers that there are about 20 deep mantle plumes bringing heat and relatively primordial material up to the asthenosphere. Horizontal currents in the asthenosphere flow radially away from each of these plumes. The currents produce

stresses on the bottoms of the lithospheric plates. These stresses combine with stresses generated by plate to plate interactions to provide the energy and direction for plate motion. It is argued that a line of hot spots could produce currents in the aesthenosphere in such a way as to cause continental breakup.

Burke and Wilson (1976) suggest that the Eastern rift may have formed as a result of the African continent coming to rest over a number of hot spots. The dome (e.g. the Kenya or the Ethiopian dome) that swells up over each hot spot is subsequently subject to fracturing which has characteristic three-arm pattern. Two successful arms on the Ethiopian dome (i.e. the Red Sea and the Gulf of Aden) opened up to form an ocean basin. The third arm (striking south into Ethiopia from Afar triangle) remains a dry fissure on the continental land mass.

Could this hypothesis be applied to the Kenya dome? The Gregory rift with its swing in direction at about the equator may represent the possible prospective successful two arms. The Kavirondo rift may then represent the third (failed) arm. Opinions on this view are divided. While some workers regard the Gregory rift as marking the initiation of an episode of crustal spreading, some geological data (King, 1978) suggest that the rift is at the closing stages of its evolution. Model calculations show that the continental lithosphere can be thinned to the base of the crust by mantle plumes in 50-75 million years. The long length of time required appears to rule out this lithospheric erosion mechanism as a viable mechanism for lithospheric thinning and rifting (Turcotte and Emerman, 1983; Oxburgh, 1978). Although the plume theory is not viable on its own, it may serve

as energy source for some models requiring heat input.

Membrane tectonics theory has been suggested as an explanation for the formation of the rift system in East Africa (Turcotte and Oxburgh, 1973, 1976; Turcotte, 1974; Oxburgh, 1978). According to this theory, the radii of curvature of a plate change as the plate changes latitude. This change of curvature enables the plate to accommodate its shape to the change in curvature of the geoid between the equator and the poles. It has been shown that a plate moving towards the equator should have its margins in compression and its central part in tension; for motions away from the equator the tensional and compressional zones are reversed.

Oxburgh and Turcotte (1974) applied this theory to explain the formation of the Eastern Rift. From palaeomagnetic evidence they infer that Africa started moving northwards since about 100 million years (my) ago at a constant rate of about 0.25°/my.

The African plate is of a size roughly 90° by 90°. The tensile stress in the centre of a circular plate of that size moving northwards towards the equator is of the same order as the strength of the plate and should be sufficient to rupture the plate. It is, therefore, argued that the East African Rift System was produced by membrane stresses in the lithosphere, developed in response to the rapid latitude change experienced by East Africa during the late Cretaceous and Tertiary.

This theory seemed capable of explaining most major features associated with the Gregory Rift. The East African Rift system seems to have developed in the central part of a plate moving towards the equator. According to the membrane theory, the central part is the region of tension. Accordingly, the crack (rifting) and accompanying volcanism will migrate southwards,

which is consistent with observation. The nature and finite extent of the extension are also explained. But the extension across the Red Sea and the Gulf of Aden is too much to be explained by the membrane tectonic theory. Perhaps membrane stresses may have started the initial fractures whose later developments were controlled by other processes.

Gass (1970, 1972) explains the formation of the Eastern Rift in terms of unusually high temperatures in the upper mantle. He argues that doming, rifting and magmatism are expressions of well localised thermal disturbance in the upper mantle. This disturbance is perhaps produced by Elder's (1966) lithothermal systems involving both heat and mass transfer.

Heat from rising lithothermal systems aided by the blanketing effect of radiogenic heat would cause partial melting in the upper mantle and therefore make magma available. Thermal gradient is increased necessitating the downward movement of the main phase boundaries in the mantle. The lowering of phase boundaries would result in an increase in volume because the low temperature, high pressure minerals would revert to their less dense high temperature equivalents. The increase in volume would then be relieved by vertical uplift of the overlying crust and upper mantle (e.g. Kenya dome) consistent with isostatic equilibrium (Bullard, 1936).

The continental crust (or better the lithosphere) is consequently fractured to relieve tensile stress. Lines of structural weakness thus created facilitate further faulting and magmatic activity. Gass shows that the zone of partial melting extends higher nearer the surface with time and crustal seperation results from injection of magma which later solidifies.

Using field petrochemical data, he shows that the chemistry of products of volcanic activity depends on the depth and temperature and pressure conditions in which the parent magma was formed. The deeper the magma source, the farther away the stage is from crustal seperation and formation of ocean floor.

The uplift stage is preceded and accompanied by eruption of alkali basalts. This is perhaps close to the present stage in the Gregory rift zone. In zones of crustal attenuation where the continent is extremely thin but still present, the volcanism is of intermediate type that leads on fractionation to peralkaline differentiates. Perhaps the Ethiopian rift typifies this stage. Where the seperation of the crust has taken place, new ocean floor of tholeiitic basalt is formed as in the Red Sea and Gulf of Aden although spreading in the Gulf is at a more advanced stage.

The lithospheric stretching mechanism first suggested for the formation of sedimentary basins (McKenzie, 1978) has been subsequently applied to graben formation. This involves uniform stretching of a section of the continental lithosphere resulting in the thinning of the lithosphere including the continental crust. Hot asthenospheric material wells up beneath the thinned lithosphere. The heating and thinning of the mantle part of the lithosphere causes isostatic uplift, but this is outweighed by the subsidence caused by thinning of the continental crust unless the lithosphere

is unrealistically thick. This mechanism, in its present form, is not considered as a viable mechanism because of lack of obvious evidence for intense crustal stretching and is also rejected on the basis of geothermal arguments (Bott and Mithen, 1983; Neugebauer, 1983).

Vening Meinesz (see Heiskanem and Vening Meinesz, 1958) has shown how tensional stress within the crust can lead to the formation of a graben. He assumed that the continental crust can be treated as an elastic layer floating on a denser fluid substratum formed by the underlying topmost mantle. The first stage is the formation of a planar normal fault (with hade in the range 50^{o}-70^{o}) in response to the crustal tension. The down-bending of the crust on the down-throw side produces a supplementary tension which initiates the formation of a second normal fault at the position of maximum bending, calculated to be at about 65 km distance from the first fault. If the second fault also dips inwards, then a downward narrowing wedge of crust subsides isostatically between the faults as adjacent parts of the crust bend upwards to form rim uplifts. The isostatic principle is not violated since the central block narrows downwards and has to sink farther before its weight is supported by hydrostatic upthrust (fig. 1.14a).

The Vening Meinesz hypothesis predicts a small crustal root beneath the graben, produced by the wedge subsidence. This is not borne out by observations, which suggest that the Moho certainly is not depressed and may even shallow beneath rift systems.

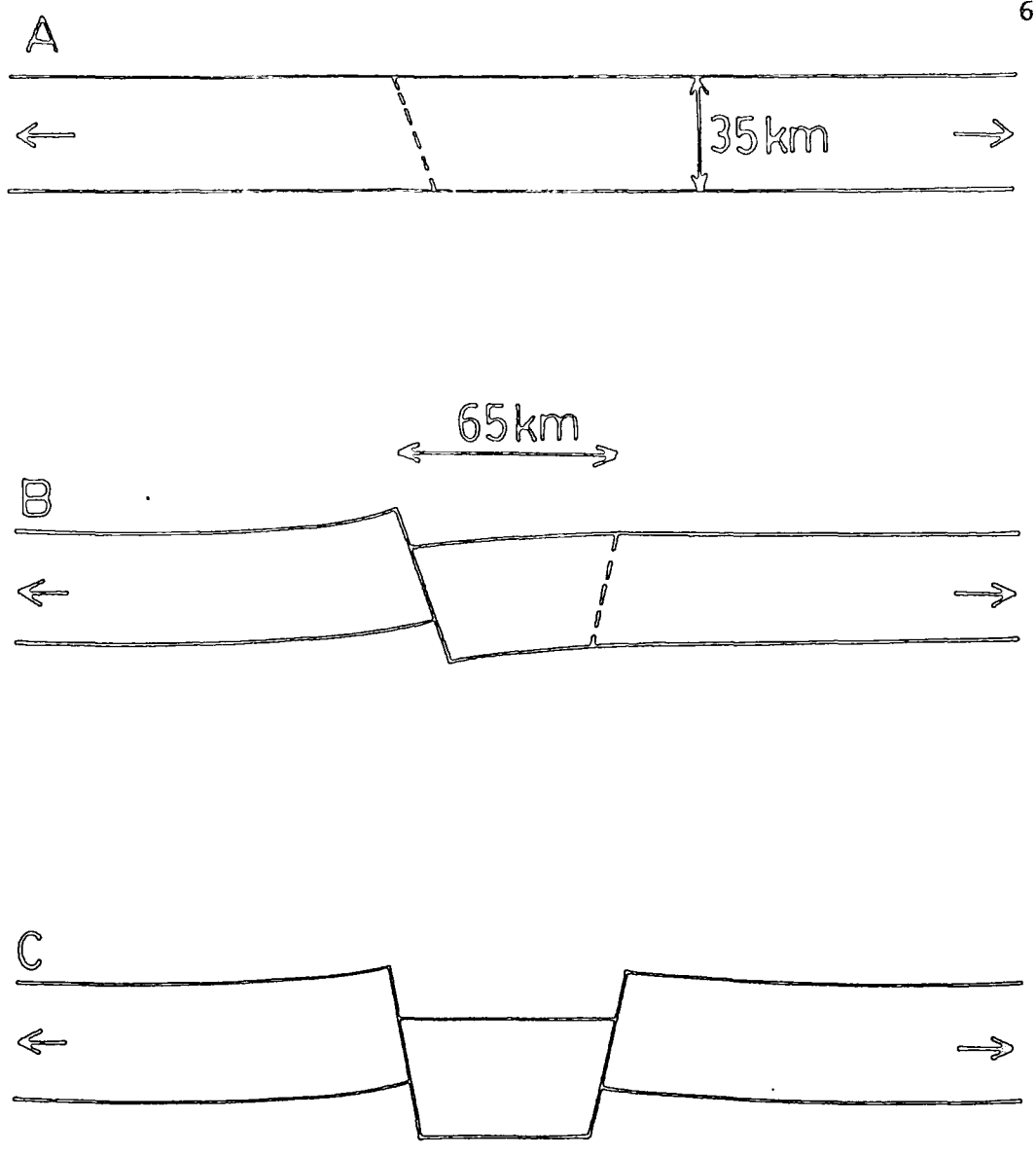

Fig 1.14a Crustal tension and the formation of grabens (Heiskanen and Vening Meinesz, 1958).

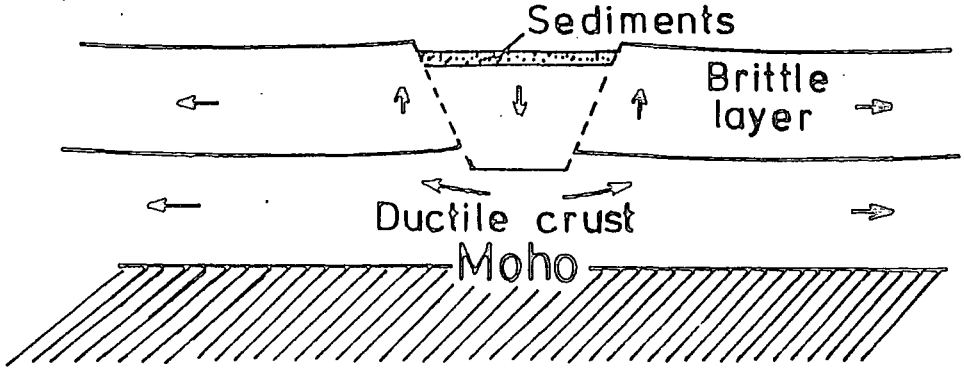

Fig 1.14b Graben formation by wedge subsidence (Bott, 1976).

The classical Vening Meinesz hypothesis has been extended to apply to subsidence of a wedge of brittle upper crust (rather than the crust as a whole), with outflow of ductile material occuring in the lower crust (Bott, 1976, 1981; Bott and Mithen, 1983). This modified wedge subsidence hypothesis is based on the loss of gravitational energy as the wedge of brittle upper crust subsides with bordering rim uplifts in response to deviatoric tension. Fig. 1.14b illustrates the process. The underlying part of the lithosphere can deform by creep so that outflow can occur in the lower crust in response to the wedge subsidence. The existence of a ductile zone within the crust of the rift zones is supported by heat flow and geomagnetic deep sounding data and by seismicity studies. The brittle-ductile transition is estimated at about 15-25 km depth within the crust. Bott and Mithen (1983) estimate that for continental rifts, a deviatoric stress of the order of 100-200 MPa (1-2 Kbar) is required if subsidence of the order of 5 km (with sediment loading) is to be explained for a graben about 40 km wide.

During rift development, therefore, this stress must be developed within the upper crust either as intraplate stress related to plate boundary forces, or as a result of lateral density contrast within the plate.

Plate boundary forces appear to be inapplicable to the present day situation in East Africa because ocean ridges developing ridge push force occur on both sides of the African plate. It has been shown that the required stress difference of the order of 100-200 MPa (1-2 Kbar) can develop

in the upper elastic part of the crust in regions such as East Africa in response to a 2 km plateau uplift isostatically supported by a low density region in the upper mantle caused by thinning and heating of the lithosphere (Bott and Kusznir, 1979; Bott, 1981; Neugebauer and Temme, 1981; Crough, 1983). The isostatic loading effect thus seems to be the most viable explanation of tension and rifting in the present day up arched rift regions such as East Africa. But as has been pointed by Bott (1981), it does not necessarily imply that doming must precede the main stages of rifting.

It is clear that the rift formation can not be fully explained by one of the mechanisms discussed above. The rift formation is probably a result of interplay between individual mechanisms, the contributions from a particular mechanism being a function of time.

In summary, doming and rifting processes in East Africa are probably caused by magma upwelling from the underlying mantle (hot spot) impinging at the base of the lithosphere (Bott, 1981). Possible stages in the rift development as suggested by Bott (1981) are shown in fig. 1.15.

In the first stage (a), hot spot forms below the continental lithosphere by upwelling from deeper parts of the mantle. In the second stage (b), the continental lithosphere becomes thinned, with consequent isostatic uplift and development of tensile stress system in the upper crust. In the third stage (c), graben formation starts when the tensile stresses become significantly large.

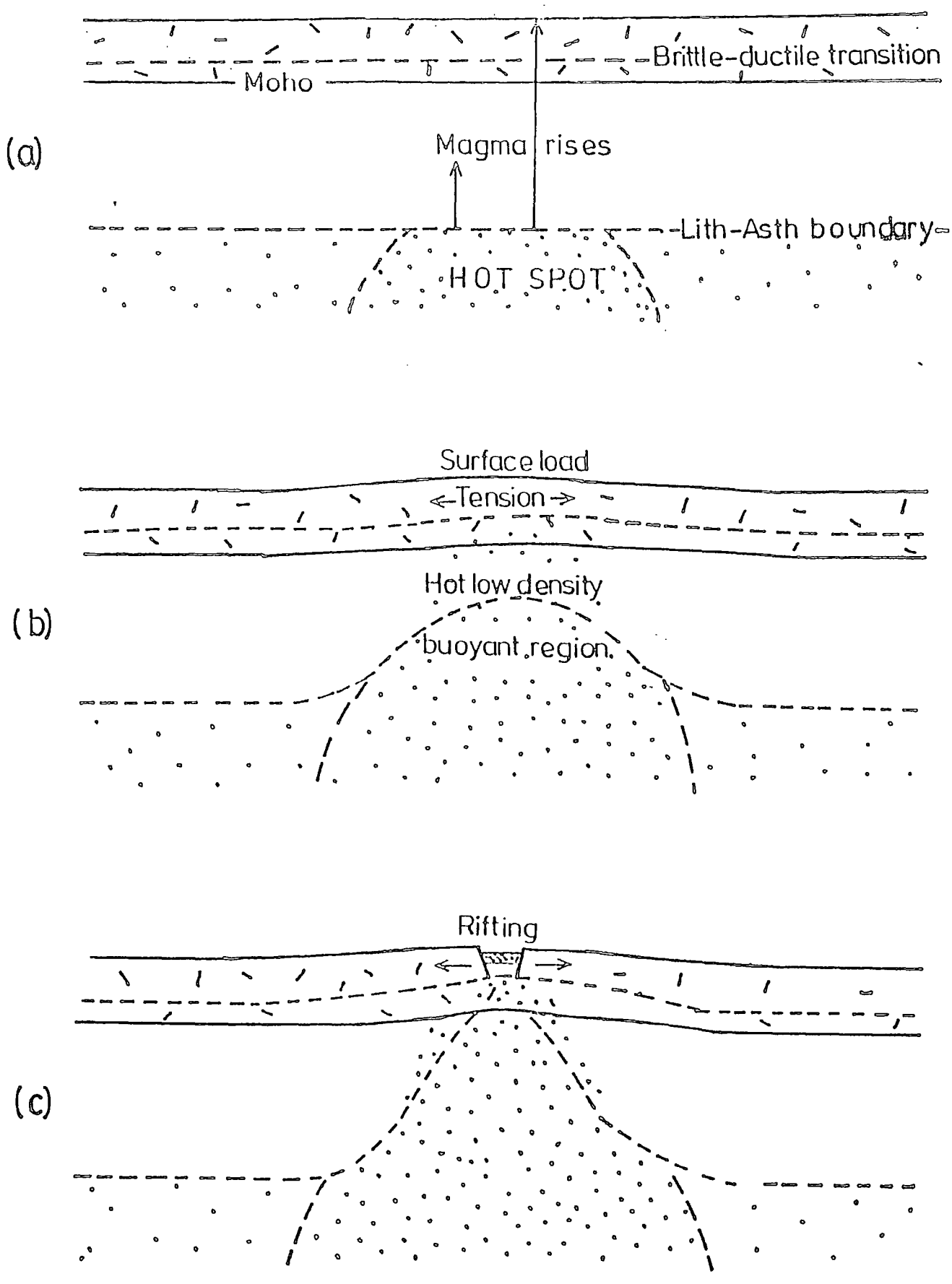

Fig-1-15: Stages in the development of a domed and rifted structure: (a) Hot spot forms below the continental lithosphere by upwelling from the deeper parts of the mantle. (b) The continental lithosphere becomes heated and thinned, with consequent isostatic uplift and development of tensile stress system in the upper crust. (c) Graben formation starts when the tensile stresses become sufficiently large. (From Bott, 1981).

Strong support for this active mechanism for the formation of the Eastern Rift comes from theoretical and experimental studies. From theoretical studies, Neugebauer (1983) explained continental rift formation in terms of mantle diapirs resulting initially from inverted density within the lithosphere/asthenosphere system. The resulting instability culminates in the thinning and doming of the lithosphere and the elastic deformation of the upper crustal layers. Wendlandt and Morgan (1982) studied dated igneous rocks within the Kenya dome from which they showed that the depth of origin of the source magma for rocks within the Gregory rift decreased from about 170 km (about 41 my ago) to crustal levels (about 5 my ago).

The mechanism suggested by Bott (1981) is broadly similar to the mechanisms suggested by Gass (1970, 1972) and Gass et al. (1978). Rifts form at the crest of domes. Eventually, the continent may split along a line of connecting rift arms of several domes.

CHAPTER 2

DATA COLLECTION

2.1 Introduction.

Data for the present study were recorded at the cross-linear array station which was installed at Kaptagat (in Northern Kenya) by the University of Durham. It was operated continuously from late 1968 to June 1972. The array was set up to supply data for the study of local seismicity and the structure of the crust and upper mantle in East Africa.

2.2 Geology of Kaptagat Area.

Kaptagat station (fig.1.2) at an elevation of about 2390 m was located on the Uasin Gishu plateau composed of tertiary phonolite lavas which dip gently to the west. Below the phonolites the geology is horizontally layered. The Uasin Gishu plateau is an upstanding block defined by the following major boundary faults. About 15 km to the east of Kapatagat is the Elgeyo escarpment which forms the western boundary of the Gregory rift. About 60 km west of the array station is the NNW-SSE trending Nandi fault. To the south is the Nyando fault which is the northern escarpment of the Kavirondo rift valley.

There are two major lava flows. The lower flow exposed to the west of Kaptagat is sparsely porphyritic. The upper flow contains abundant large nepheline and glassy feldspar phenocrysts. The greater part of the flat land of the plateau is formed by the lower flow. These phonolite flows were erupted after the early periods of major tertiary uplift and overflowed from the rift trough onto

the plateau. Age is estimated in the range 12-13.5 my. (King and Chapman, 1972). The lower flow lies directly on Precambrain basement system gneisses in the north (Jennings, 1964). The only borehole which pierced the phonolite showed a total thickness of 144 m. As this is only 15 km southwest of Kaptagat, it is inferred that the thickness of the phonolite beneath Kaptagat is between 150 and 200 m.

2.3 Array siting and instrumentation.

Birtill and Whiteway (1965) discuss the necessary conditions to be satisfied before a location can be chosen as suitable for siting an array of the type used in this study and the optimum spatial distribution of the array elements. The location should have low seismic noise level; this implies that the station must be far removed from coasts and major industrial centres. The geology of the site should be laterally homogeneous and horizontally layered. Well consolidated and unweathered rocks should be near enough to the surface so that the seismometers can be firmly coupled to them with minimum drilling costs. The elevation of the stations should be as constant as possible with a maximum tolerance of no more than $\pm$ 60 m. The sharpest velocity and azimuth response is obtained when the array aperture has dimensions comparable to the longest wavelength of the signal of interest. Spacing between adjacent seismometers should be small to ensure signal coherence but

large enough to decorrelate noise across the array.

Kaptagat satisfies most of these conditions. The array dimension (about 5 km) makes it suitable for the study of local and some regional events. In the present study, dominant frequency of selected events is about 4 to 5 hz; measured apparent surface velocity for the P wave is in the range 5.6 to 8.0 kms^{-1}. The longest apparent wavelengths are therefore about 2 km; the array dimension is, therefore, about 2½ times the longest apparent wavelength. Very sharp velocity and azimuth resolution should thus be achieved.

Kaptagat is about 600 km from the nearest coast (the East African coast); hence microseismic noise is low, about 7 mμ. To ensure efficient ground coupling, the seismometers were placed in solid phonolite outcrops which cover the entire area. Sites were surveyed to an accuracy of ± 30 m and differences in height were less than about 100 m. The site coordinates relative to the crossover point are shown on table 2.1.

Kaptagat was a small aperture cross-linear array. It consisted of ten Willmore Mark II short period seismometers set vertically to 2s period and arranged in an inverted 'L' shaped form (fig.2.1). The arms of the array run approximately east-west (yellow line) and north-south (red line). The inter seismometer spacing on each arm was about 1 km and the total length (dimension) of each arm was about 5 km.

Table 2.1

Seismometer site coordinates and altitudes

Pit	X(km)	Y(km)	Estimated error(km)	Altitude (m)
R_1	-0.098	-0.766	±0.010	+10
R_2	-0.114	-1.425	±0.020	+20
R_3	-0.365	-3.077	±0.010	+30
R_4	-0.663	-3.736	±0.030	+10
R_5	-0.925	-5.200	±0.010	+30
Y_1	-0.446	0.166	±0.001	0
Y_2	-1.888	0.003	±0.015	-30
Y_3	-2.645	0.025	±0.030	-50
Y_4	-3.720	-0.013	±0.010	-50
Y_5	-4.750	-0.250	±0.060	-70

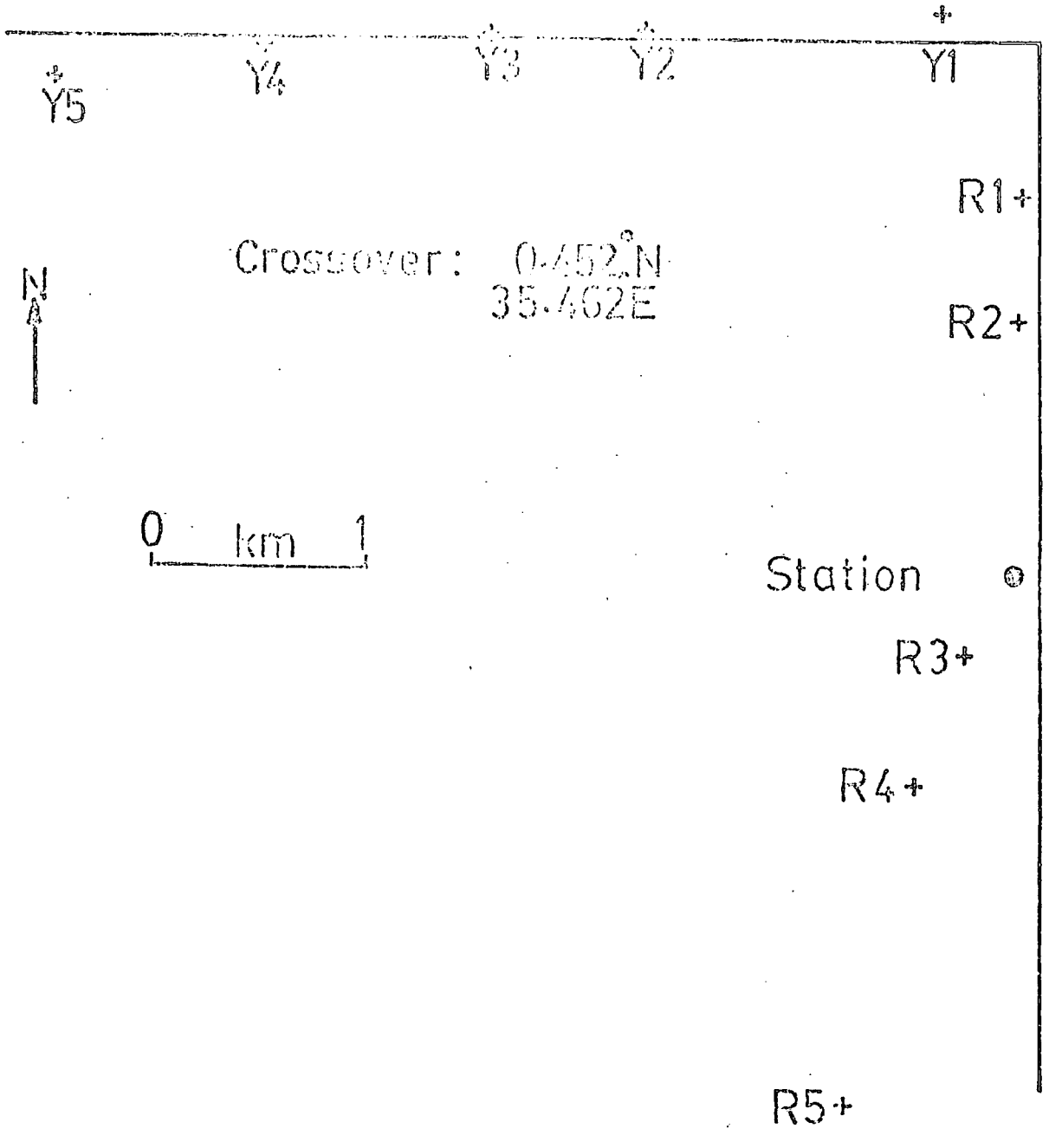

Fig 2·1: Plan of Kaptagat array with red(R) and yellow(Y) lines of seismometers.

The recording equipment used is similar to that described by Long (1968). Within each seismometer package the output from the seismometer was amplified and then frequency modulated. The frequency modulated signals from the ten seismometers were communicated to a central recording station by twin field telephone cables. These signals and a signal from a long period instrument were recorded onto one inch fourteen track analogue magnetic tape. The speed of the tape was $\frac{15}{160}$ inch per second.

A binary time code giving the day, hour, minute and second was generated by a quartz crystal clock and recorded on one track of the tape. Another track of the tape was used to record standard time signal from radio (Greenwich Mean Time). This was used to calibrate the local clock when radio reception was good enough.

To check that the seismometer lines were functioning and to give amplitude information, calibration pulses were generated in the seismometer package by a remote calibration unit that was triggered by a pulse sent down the line from the central recording station. Power for the whole array system was taken from a set of twelve 6 volt accumulators at the central recording station. Power (d.c.) was fed to the seismometer packages down the same twin telephone cables that also carried the frequency modulated seismic signals. Direct current was transmitted to simplify the seperation of signal and power. Each magnetic tape recorded for about eleven days.

Play back facilities were available at Kaptagat central recording station for preliminary picking and listing of events. But the main playback facilities and seismic data processing laboratory are housed in Durham.

CHAPTER 3.

VELOCITY FILTERING

3.1 Seismic Arrays.

A seismic array is considered here as a special deployment of seismometers at three or more sites on the earth's surface. The spacial extent (or aperture) may vary from one kilometre to hundreds of kilometres. The array is characterized by uniform instrumentation and a common time base. For small and medium aperture arrays, outputs from all seismometers are communicated through amplifiers and filters to a central control point and recorded on a multichannel analogue or digital magnetic tape as an ensemble. Beneath such arrays, it is assumed that the geology is uniform. Then provided that the distance to the source is large compared to the dimensions of the array, the signal of interest is assumed to be coherent across the sensors while noise is random or incoherent. The degree to which these assumptions are satisfied depends on inter-seismometer spacing, the nature of the noise prevailing in the locality and the degree of crustal homogeneity. Furthermore if the signal source is at a large enough distance from the array, the wave front can be assumed to be plane.

Data from seismic arrays are subsequently machine processed to achieve a number of objectives. By introducing time delays to compensate for the signal propagation time across the array and summing the coherent outputs from each seismometer, an improvement in signal-to noise ratio (SNR) of arriving signals is obtained. Time delays required to bring the signals into phase provide a direct estimate of the azimuth and apparent velocity (or slowness) of the signal. Signals, from different

events, which arrive at an instrument superimposed can be seperated in time if they cross the array with different apparent velocities and/or azimths. Seismic array data are also used for the study of seismic noise structure (Lacoss et al., 1969).

The earliest best known seismic arrays are the medium aperture crossed linear arrays which have been operated since early 1960s and which have since then been used for global seismology studies. The arrays sponsored by the United Kingdom Atomic Energy Authority (UKAEA) are operated in collaboration with the relevant scientific authorities of the countries in which they were established. They were installed in Eskdalemuir (EKA), Scotland; Yellowknife (YKA), Canada; Gauribidanur (GBA), India; Warramunga (WRA), Australia; and Brazilia, Brazil. These medium aperture linear cross arrays were designed primarily for the recording and analysis of teleseismic events (ranges > 25^{o}). These were 21 element arrays in which the elements were arranged in two orthogonal crossed lines (usually identified as the red and blue lines) each of ten short period vertical component seismometers and using apertures up to 25 km (Carpenter, 1965).

The interseismometer spacing of about 2.5 km was found, from empirical experience, to be small enough for teleseismic signal coherence but large enough to decorrelate noise across the array (Lacoss, 1975). With this condition, an achievement of $\sqrt{n}$ in SNR was aimed at from delay and sum processing (Birtill and Whiteway, 1965).

Results achieved by the use of medium aperture seismic arrays were sufficiently promising to suggest that substantial further improvements in SNR and identification might be expected from an even larger array having more than an order of magnitude greater number (n) of seismometers. Such a large aperture seismic array (LASA) was sponsored by the U.S. government and installed in Eastern Montana in 1965. The location chosen for this array was sparsely populated, relatively uniform geologically and remote from oceans.

A description of the geometry of LASA at about the time of its installation is given by Mack (1969) and Forbes et al. (1965). LASA consists of 21 subarrays or clusters in the configuration shown in fig. 3.1 and deployed over an aperture of about 200 km. The subarrays are considered to be located on 5 non circular rings labelled B, C, D, E and F with a central subarray labelled A_o. Each ring has four subarrays so that each subarray is identified by a letter and a number. A subarray consists of 25 short period (SP) vertical seismometers arranged in six radial arms and has an overall diameter of about 7 km. This aperture was chosen to allow suppression of surface wave modes of velocity lower than about 3.5 km/s and frequencies above 0.2 hz. The seismometers in each subarray were placed at the bottom of deep cased and cemented boreholes (about 152 m for the central hole and about 61 m for the other holes); this had the effect of further suppressing noise at higher frequencies.

At the centre of each of the 21 subarrays is a set of three component set of long period (LP) instruments. The LP instruments respond to frequencies in the range of about

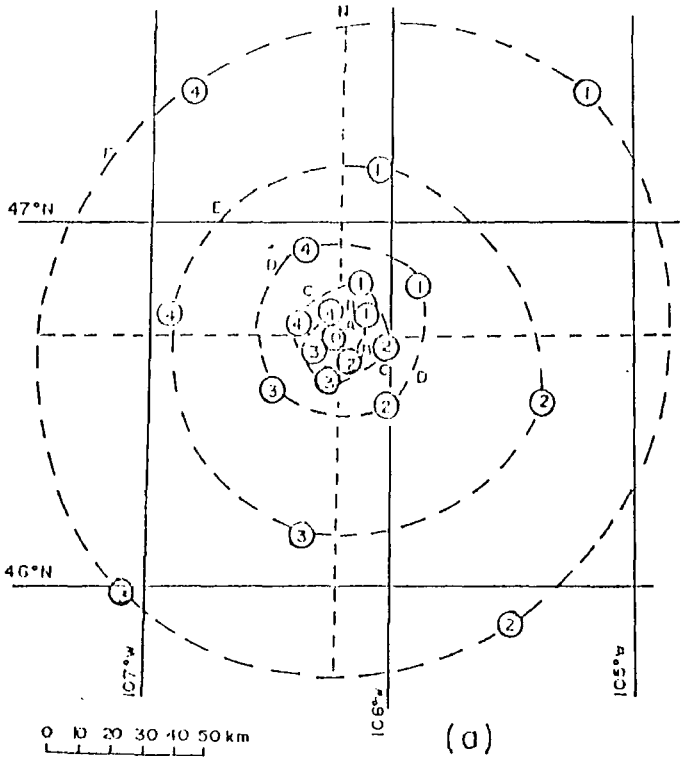

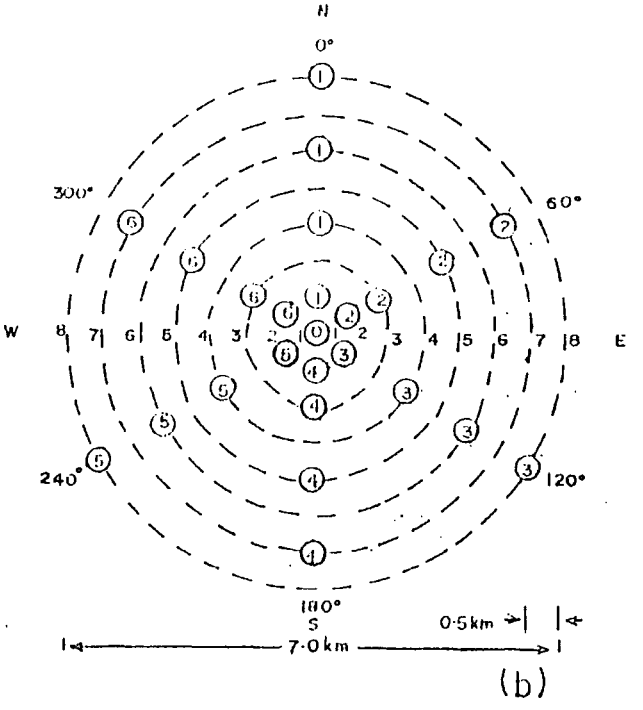

Fig. 3·1: (a) LASA plan and (b) the configuration of a typical subarray.

0.01 to 0.20 hz. On the whole, therefore, LASA consists of 525 SP instruments and 21 three component LP sets.

In a concrete vault near the centre of each subarray, a subarray electronics module multiplexes and digitizes the 25 seismometer outputs into a single bit stream which is then transmitted to the LASA data centre. At the data centre the bit streams from the 21 subarrays are combined, computer processed and the results displayed or transmitted to remote locations for further processing.

Most processing techniques for array data assume that the signal does not change within the area of the array or that it changes in a predictable manner. In the case of LASA this assumption is not valid for the array as a whole because of the large aperture involved.

The subarrays are of the right size to reject surface wave noise propagating at relatively low speeds. The short period data at each sub-array is processed as an ensemble to remove this surface wave noise leaving body wave noise coming across the array with much higher velocities. A second stage of processing would be to combine the processed outputs from the different sub-arrays to basically get rid of this body wave noise with the aim of maximising improvement in signal-to-noise ratio. In principle, applicable processing techniques include beam forming, filter and sum processing and frequency-wave number spectral analysis.

Lacoss (1975) observed that the desired goal of significant improvement in signal to noise ratio has not been achieved with the short period data because assumptions about noise

and signal characteristics are usually not fully satisfied. The inter seismometer spacing (about 0.5 km) within the subarray was, for example, not large enough to decorrelate noise. Furthermore, crustal heterogeneity results in some loss of signal coherence. On the other hand, more significant improvement in SNR has been recorded with the LP data.

Experience gained from the operation of LASA has been utilised in the installation of other large aperture arrays. The Norwegian seismic array (NORSAR) installed in 1970 is similar to LASA except that there are 22 long period sites and subarrays; the aperture is about 100 km. The Alaskan long period array (ALPA) has about the same aperture as NORSAR but contains 19 LP sets of instruments and no SP instruments.

3.2 Review of some array processing techniques

The output of each seismometer in an array is usually considered to be a composite waveform made up of the desired coherent signal perturbed by coherent and /or incoherent noise. For teleseismic events, the desired signal may be taken as the first P-wave arrival whose apparent surface velocity increases from about 8 km/s to 24 km/s as the distance increases from 2^{o} to 90^{o}; this signal is equally likely to come from any azimuth.

The noise obscuring the signal include noise generated locally by the signal from P-Rayleigh wave mode conversions at the surface near the array (Key, 1967). Also coherent and propagating mainly as Rayleigh waves are ocean microseisms and noise from local sources like factories and land

vehicular traffic. The surface wave noise mentioned above sweep through the array with apparent surface velocity of 2.5 to 4.0 km/s. There will also be high velocity coherent noise from multiple reflections, Rayleigh to P-wave mode conversions and other unwanted coherent phases. Incoherent noise arise from sources or scatterers within the array area including locally generated wind noise; the instrumental noise is also incoherent but the amplitude is usually small compared with the amplitude of other seismic noise. The signal and noise cover different frequency bands, about 2 hz to 20 hz for signal and about 0.1 hz to 10 hz for low velocity seismic noise. It is, therefore, sometimes useful to do wide band frequency filtering of individual seismometer outputs to improve signal/noise ratio prior to the array processing.

Usually the range of apparent horizontal surface velocity/azimuth covered by the coherent noise is different from that covered by the desired signal. Advantage is taken of this difference in array processing techniques designed to improve signal to noise ratio and confidently measure signal parameters.

The beam forming concept (Birtill and Whiteway, 1965) is fundamental to most techniques used for processing cross-linear array data. In its simplest form, beam-forming (array phasing, azimuth and velocity filtering) involves the summation of individual seismometer channels after steering delays have been inserted to align a group of arrivals with a particular velocity and azimuth and then taking the mean.

Consider an array of n seismometers deployed over a horizontal surface. The output recorded by seismometer, i, after the insertion of propagation delays, τ_i, corres-

ponding to the desired signal with apparent velocity v and azimuth θ is a time series with k sampled time points and can be expressed as

$$x_{ij} = s_j + n_{ij} + e_{ij};\ i=1 \ldots n, j=1 \ldots k \qquad \ldots \quad (3.1)$$

where

x_{ij} is the jth sample of the output of seismometer i

s_j is the jth sample of the desired signal, a coherent term identical on each trace.

n_{ij} is the jth sample of the coherent noise at seismometer i

e_{ij} is the jth sample of the incoherent noise at seismometer i

The delay, T_i, at seismometer i relative to the coossover point of the array (fig. 3.2) is computed from

$$T_i = \frac{d_i \cos (\theta - \alpha_i)}{V} \qquad \ldots \quad (3.2)$$

where d_i and α_i are the polar coordinates of the site of seismometer i relative to the origin at the crossover point. Because the traces have been time shifted by T_i, s_j which is identical on all traces, is in phase across the array.

The beam is then formed from the relation

$$b_j = \frac{1}{n} \sum_{i=1}^{n} x_{ij} = s_j + \sum_{i=1}^{n} n_{ij} + \sum_{i=1}^{n} e_{ij} \qquad \ldots \quad (3.3)$$

n^{ij} will be out of phase across the array since it is evident that the parameters of the desired signal (θ,v) are different from those of the coherent noise. e_{ij} is assumed random so that its summed output over all seismometers will have a mean close to zero. The resultant effect is the enhancement of the desired signal component with respect to noise.

In beam-forming, it is assumed that the desired signal is coherent across the array while noise is random. Where this

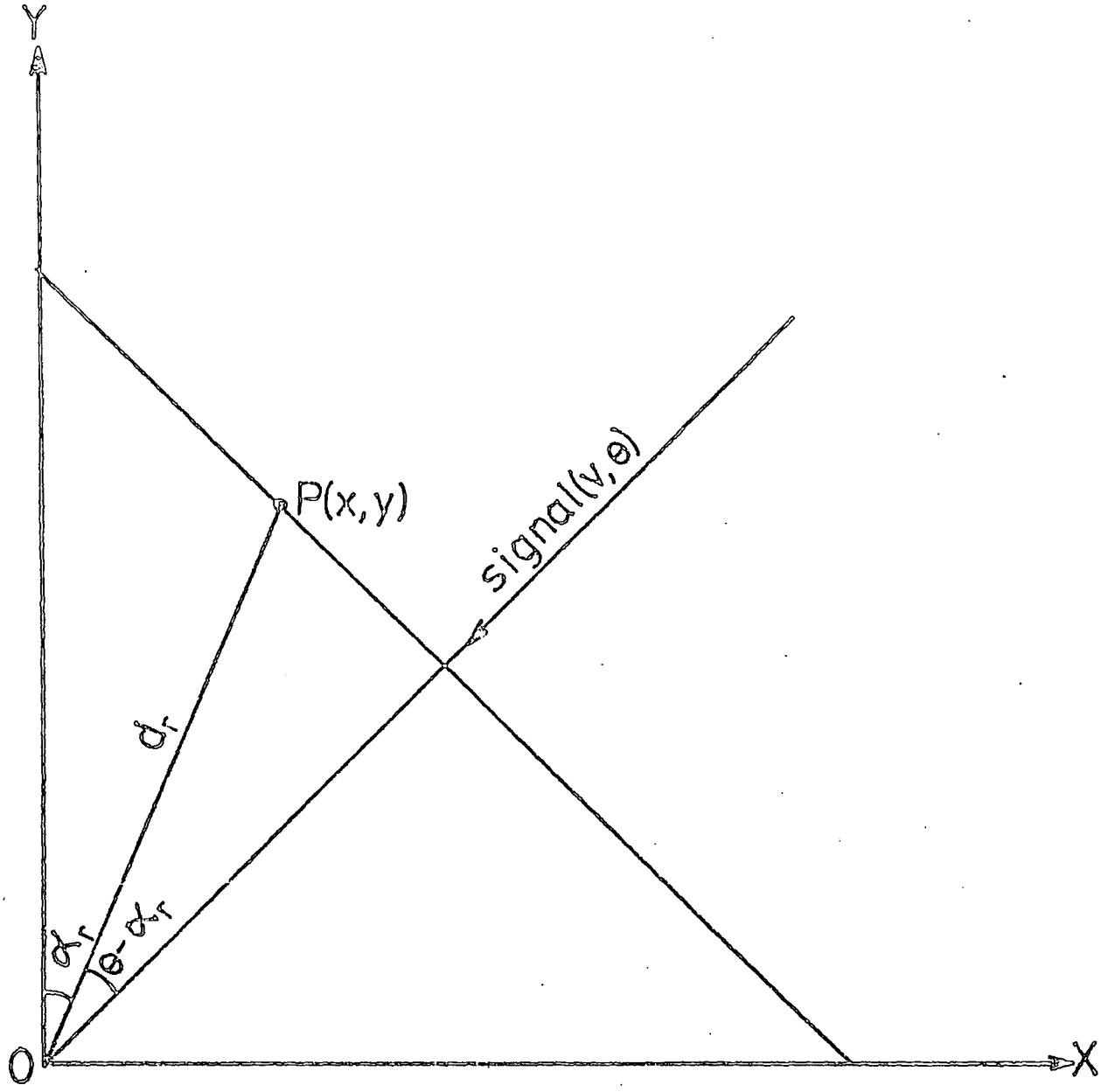

Fig 3.2: A plane wave front crossing a two dimensional array of seismometers.

assumption is not valid it becomes necessary to weight the channels prior to delaying and summing (Capon et al., 1967). It is also sometimes useful to frequency filter the channels before beam-forming.

Muirhead (1968) suggested the Nth root beam forming method as a means of suppressing the effect, on the beam, of large noise impulses recorded on one or more signal channels of the array. This is a non-linear filtering technique which involves delaying the various channels by time lag, T_i, as given in equation (3.2) to align a group of arrivals with a particular velocity and azimuth, taking the Nth root of the absolute value of each individual seismometer output with the original sign preserved, summing them and then raising the mean of the result to the Nth power; N is, in general, any positive integer (usually 2,4 or 8). If we denote the output of the ith seismometer after the insertion of delay T_i as x_{ij} then the beam r_j is given by

$$r_j = \{\frac{1}{n} \sum_{i=1}^{n} | x_{ij} |^{\frac{1}{N}} \text{signum } x_{ij} \}^N \quad \ldots \quad (3.4)$$

Kanasewich et al.(1973) conclude, on the basis of analysis of synthetic signals and real data, that the Nth root processing offers improvement in signal to noise ratio (SNR) and provided better resolution in velocity and azimuth than any linear processing method previously tried. The method is also much better than linear processing methods at handling non-Gaussian noise although at the expense of signal distortion (Ram and Mereu, 1975; Muirhead and Ram, 1976).

The delay-sum-correlate technique (Birtill and Whiteway, 1965; Whiteway, 1965) is the most commonly used method for processing the output of cross-linear arrays. In this method, the partial sums (beams), R and B, of the red and blue lines after phasing are cross multiplied and the product averaged over a moving square time window of fixed length containing M sample points. This product is the correlation coefficient the square root of which is designated the time averaged product (TAP). For a fixed length window containing M sample points and centred at the jth sample, the TAP, t_j, can be obtained from the relation :

$$t_j = \{\frac{1}{M} \sum_{m=r}^{k} (B_m \cdot R_m)\}^{\frac{1}{2}} \qquad \ldots \qquad (3.5a)$$

where R and B are the partial beams formed from the red and blue lines respectively; $r = j - M/2$, $k = j + M/2$ assuming M is even. If M is odd, the reference sample j may be taken at the start of the window and the TAP is then given by

$$t_j = \{\frac{1}{M} \sum_{m=j}^{k} (R_m \cdot B_m)\}^{\frac{1}{2}} \qquad \ldots \qquad (3.5b)$$

where $k = M + j - 1$.

Synthetic and real data studies show that the cross-correlation method gives better resolution in velocity and azimuth than simple beam forming (Birtill and Whiteway, 1965; Whiteway, 1965; Somers and Manchee, 1966). The cross correlation or TAP processing method is extremely useful in the identification of secondary phases, although it is incapable of resolving small differences in the values of

apparent velocity and azimuth of such phases (King et al., 1973).

Cleary et al.(1968) describe a manual technique for measuring relative onset times to 0.01s thus enabling precise determination of apparent velocity and azimuth. This 'eyeball' technique is not only tedious but also does not make full use of the shape of the signal waveform. It is prone to mistakes even with noise free records and can lead to erroneous results in the presence of interfering signal pulses.

In the adaptive processing method, precise determination of relative arrival times is done automatically. The method was originally developed by Gangi and Fairborn (1968) and subsequently described and evaluated by Farrel (1971), Bungum and Husebye (1971), King et al.(1973) and Ram and Mereu (1975). In this method, the arrival times of a wavefront at each seismometer is accurately determined by cross correlating the observed wavelet of interest with the corresponding wave on the beam trace. The position of the maximum value of this cross correlation function is used as the relative arrival time position of the wave. The new arrival times on the array sensors are then used to create a new and improved beam and the whole operation is repeated in an iterative manner until convergence takes place. The values of apparent velocity and azimuth which produce a maximum filtered signal are determined as the required signal parameters. This technique is now widely used for the processing of teleseismic array data.

Seismic signals recorded at a large seismic array can be analysed in terms of energy content of incoming signal as a function of azimuth and slowness. If the azimuth is known,

the TAP trace can be used to map power as a function simultaneously of slowness and time. This is the principle of the VESPA, velocity spectral analysis, process (Davies et al. (1971). These authors have used real data from LASA to show the effectiveness of this method in picking out teleseismic signals approaching the station from same azimuth but with different phase velocities. Since information on time of arrival and $dT/d\Delta$ is available, the method allows for confident estimation of the source of energy.

3.3 Array response

3.3.1 Introduction

Geophysically, crossed linear arrays have been primarily used to study the mantle and the core. Such studies have used teleseismic events and have concentrated on the source window in the range 30^{o} to 90^{o}. Refinements and innovations in processing techniques are aimed at improving accuracy in the measurement of signal parameters and consequently improving the ability to resolve overlapping phases in the presence of noise. Array response measures the ability of an array to emphasize the properties of a desired signal at the expense of those of random and/or coherent noise.

Theoretical responses of arrays of different configurations are given by Birtill and Whiteway (1965) and Whiteway (1965). They considered an array tuned to receive a signal from azimuth θ_1 and sweeping through the array with apparent horizontal surface velocity v_1 and then calculated the normalized response of the array to any other signal (θ,V).

The general conclusion from these studies is that the accuracy of determination of velocity or azimuth depends partly on the sharpness of the velocity or azimuth response; this in turn depends upon the dimensions of the array in relation to the wavelength of the signal, and to the array configuration concerned.

For cross linear arrays and for a single signal component with high signal to noise ratio, an error of up to about 3^{o} in azimuth and 5% in velocity is feasible when the length of each line is equal to the signal wavelength. Better accuracy can be achieved for larger dimensions of the array in relation to the signal wavelength although excessive dimensions should be avoided because the coherence of the signal across the array may then be degraded.

In general, for L shaped and symmetrical cross arrays, the correlator response is considerably better than the sum squared response and the L shaped array gives a better correlator response than the symmetrical cross. With the L shaped array, the best azimuth discrimination obtained from correlator response is at the azimuths (θ_1) of 45^{o} and 225^{o}. At these azimuths the width of the normalized azimuth correlator response at the half level point is 26^{o} if the dimensions of the array equal the signal wavelength. Birtill and Whiteway (1965) estimate that the error in azimuth at these azimuths can not be greater than $\frac{1}{20}$th of this half level response width; i.e. the error in azimuth in this case is 1.3^{o}. The corresponding error in azimuth at the azimuth of 90^{o} is then 1.8^{o}.

The best velocity discrimination for an L shaped array using correlator response is at the signal azimuth of 135°. At this azimuth, $\frac{1}{20}$th the widths of the correlator velocity response which estimates the error in velocity are 0.14, 0.16, 0.18 and 0.21 km/s for signal velocities of 6.0, 7.0, 8.0 and 9.0 km/s respectively. At 90° azimuth, the errors in velocity are 0.20, 0.23, 0.26 and 0.30 km/s for signal velocities of 6.0, 7.0, 8.0 and 9.0 km/s respectively.

King et al.(1973) argue that for medium aperture cross linear arrays, beam forming, TAP and VESPA are limited in their ability to resolve small differences in slowness and azimuth of partially overlapping phases. They showed that the adaptive processing technique has better resolution than these methods.

Experiments with synthetic data recorded at 20 samples per second and applied to a medium aperture array (Gauribidanur) showed that in the case where no interference and noise were present, values of velocity and azimuth of the signal computed from adaptive processing differed by no more than 0.5% from the correct values (Ram and Mereu, 1975). Better results could be produced by increasing the sampling rate.

To illustrate the ability of the array to resolve small differences in velocity and azimuth, the authors introduced two overlapping wavelets of equal amplitude and duration (3.0s) with an apparent azimuth of 200.0° and apparent velocities of 9.8 km/s and 10.2 km/s respectively across the array; the overlapping interval was 0.5s. Three sets of this array

record were produced. The first set was clean or noise free; the second and the third sets had medium and high seismic noise introduced. For the clean, medium and high noise records, adaptive processing gave computed azimuths correct to within 0.3°, 0.3° and 0.8° respectively of the given true azimuth (200.0°). Computed apparent velocities varied systematically from one value (9.8 km/s) to the next (10.2km/s). The noisier record produced the greater departure of measured values of velocity from the correct given values, e.g. for the clean record the measured adaptive processed velocities had values from 9.76 through 9.88 to 10.11 km/s.

The same synthetic data were also processed using Nth root beam forming method at a constant azimuth of 200.0°. Values of velocity between 9.5 and 9.6 km/s were obtained for the first wavelet (9.8 km/s), and for the second wavelet (10.2 km/s) the computed values of velocity were between 10.1 and 10.2 km/s.

Overall, the adaptive processing method was found more successful than the Nth root operation for precise and accurate determination of signal parameters. The adaptive processing method can resolve differences of 1 to 3° in apparent azimuth of interfering signals. The Nth operation, however, is better at enhancing signal to noise ratio at the cost of signal distortion.

Figures estimating array performance at resolution discussed above relate to theoretical models of signals and noise. Experience with medium aperture cross linear arrays show that beam forming and TAP processing do not give adequate resolution in slowness and azimuth for later phases.

King et al.(1973) showed that this occurred because the aperture (up to about 25 km) of such arrays is not large enough compared with apparent wavelength of the incident teleseismic signals. However for Kaptagat the array dimensions are about 2½ times the apparent wavelength of the recorded local events (see section 2.3). Simple beam forming and TAP processing are, therefore, considered adequate for apparent velocity and azimuth resolution. The present data are processed using cross correlation or TAP processing method.

Because of the short distances involved, a desired signal is often perturbed by onsets of other interfering coherent and/or random noise. A study of the array response in the presence of coherent and incoherent noise is, therefore, essential.

.3.2. Arry response in the presence of coherent noise.

Consider a plane wavefront crossing a two dimentional array of a seismometers on the x-y plane (fig. 3.2) with apparent velocity v, wavelength λ from an azimuth θ. Let the rth seismometer at point P(x,v) have polar coordinates (d_r, α_r) with respect to the origin at O. Between crossing P and O the wavefront travels a distance $d_r\cos(\theta-\alpha_r)$. The phase difference β_r between the outputs at P and O is therefore

$$\beta_r = 2\pi \frac{d_r}{\lambda} \cos(\theta-\alpha_r) \qquad \ldots \qquad (3.6)$$

The output of the rth seismometer may be represented by a vector of amplitude a_r and angle β_r. The sums X,Y of the orthogonal components of the seismometer outputs are

$$X = \sum_{r=1}^{n} a_r \cos \beta_r, \quad Y = \sum_{r=1}^{n} a_r \sin \beta_r$$

The amplitude, A_n, of the sum of the outputs of all n seismometers is given by

$$A_n^2 = \left(\sum_{r=1}^{n} a_r \cos \beta_r \right)^2 + \left(\sum_{r=1}^{n} a_r \sin \beta_r \right)^2 \quad \ldots \quad (3.7)$$

The phase angle γ_n of A_n with respect to the output at origin O is

$$\gamma_n = \tan^{-1} \left(\sum_{r=1}^{n} a_r \sin \beta_r \right) / \left(\sum_{r=1}^{n} a_r \cos \beta_r \right) \quad \ldots \quad (3.8)$$

If the outputs of all seismometers are equal ($a_r = a$, say), we have

$$A_n^2 = a^2 \left\{ \left(\sum_{r=1}^{n} \cos \beta_r \right)^2 + \left(\sum_{r=1}^{n} \sin \beta_r \right)^2 \right\} \quad \ldots \quad (3.9)$$

If, in addition, the seismometer outputs are all in phase, $\beta_r = 0$ and the resultant summed output has amplitude B_n given by

$$B_n^2 = n^2 a^2 .$$

This corresponds to infinite signal wavelength and vertical incidence. It also corresponds to a situation where the array has been correctly tuned to receive a required signal by insertion of appropriate steering delays to the various channels. The amplitude E_n (sum squared response) which is obtained by normalizing A_n to unity with respect to B_n is given by

$$E_n^2 = \frac{A_n^2}{B_n^2} = \left\{ \left(\sum_{r=1}^{n} \cos \beta_r \right)^2 + \left(\sum_{r=1}^{n} \sin \beta_r \right)^2 \right\} / n^2 \quad \ldots \quad (3.10)$$

If the array aperture is D, equation (3.6) can be written as

$$\beta_r = 2\pi \frac{d_r}{D} \cdot \frac{D}{\lambda} \cos(\theta - \alpha_r).$$

where D is introduced as a scaling factor to make the response dependent only on array configuration and not on array size. Hence from equation (3.10), contoured sumsquared response, E_n, can be obtained in polar form as a function of D/λ and azimuth θ.

For L shaped array, the correlator response gives better resolution than the sum squared response (Birtill and Whiteway, 1965). Kaptagat array has the shape of an inverted 'L' with the two arms called red(r) and yellow(y) arms. In the correlation method, the outputs of the red and yellow lines are summed (after the insertion of appropriate steering delays) seperately to produce partial beams. These two partial beams are then cross multiplied. If there are m seismometers on the red arm, the number on the yellow arm will be n-m.

Assuming the outputs of all seismometers are equal ($a_i = a$, say), then the amplitudes A_r, A_y of the partial sums are given by

$$A_r = a \left\{ \left(\sum_{r=1}^{m} \cos \beta_r \right)^2 + \left(\sum_{r=1}^{m} \sin \beta_r \right)^2 \right\}^{\frac{1}{2}} \qquad (3.11)$$

$$A_y = a \left\{ \left(\sum_{r=m+1}^{n} \cos \beta_r \right)^2 + \left(\sum_{r=m+1}^{n} \sin \beta_r \right)^2 \right\}^{\frac{1}{2}} \qquad (3.12)$$

Hence, the correlator output A is given by

$$A = A_r \cdot A_y$$

$$= a^2 \left\{ \left(\sum_{r=1}^{m} \cos \beta_r \right)^2 + \left(\sum_{r=1}^{m} \sin \beta_r \right)^2 \right\}^{\frac{1}{2}} \cdot \left\{ \left(\sum_{r=m+1}^{n} \cos \beta_r \right)^2 + \left(\sum_{r=m+1}^{n} \sin \beta_r \right)^2 \right\}^{\frac{1}{2}} \qquad \ldots (3.13)$$

If the outputs of all seismometers are in phase, the corresponding resultant output A is given by

$$A = m(n-m)a^2 \qquad \ldots \qquad (3.14)$$

If the seismometers are equally distributed between the two arms, we have $m = n/2$ and $A = n^2a^2/4$. Hence the correlator response, E_n, normalized to unity for the inphase condition becomes

$$E_n = \frac{4}{n^2}\left\{\left(\sum_{r=1}^{n/2}\cos\beta_r\right)^2 + \left(\sum_{r=1}^{n/2}\sin\beta_r\right)^2\right\}^{\frac{1}{2}} \cdot \left\{\left(\sum_{r=\frac{n}{2}+1}^{n}\cos\beta_r\right)^2 + \left(\sum_{r=\frac{n}{2}+1}^{n}\sin\beta_r\right)^2\right\}^{\frac{1}{2}} \qquad \ldots \qquad (3.15)$$

From equation (3.15), the correlator response as a function of $(D/\lambda,\theta)$ can be plotted as before in polar form. In applications of equations 3.10 and 3.15, delays are normally inserted so that the inphase condition corresponds to a desired signal of apparent velocity V_1 from an azimuth θ_1. The response to any other signal $(D/\lambda,\theta)$ is then required. For the signal $(D/\lambda,\theta)$ the resultant phase shift for the rth seismometer output at P relative to that at O for this condition is

$$\beta_r = 2\pi\,\frac{d_r}{D}\cdot\frac{D}{\lambda}\cos(\theta-\alpha_r) - 2\pi\,\frac{d_r}{D}\cdot\frac{D}{\lambda_1}\cos(\theta_1-\alpha_r)$$

$$= 2\pi\,\frac{d_r}{D}\cdot\left(\frac{D}{\lambda}\cos\theta - \frac{D}{\lambda_1}\cos\theta_1\right)\cos\alpha_r + \left(\frac{D}{\lambda}\sin\theta - \frac{D}{\lambda_1}\sin\theta_1\right)\sin\alpha_r$$

$$= 2\pi\,\frac{d_r}{D}\cdot\frac{D}{\lambda'}\cos(\theta'-\alpha_r) \qquad \ldots \qquad (3.16)$$

where $\frac{D}{\lambda'}\cos\theta' = \frac{D}{\lambda}\cos\theta - \frac{D}{\lambda_1}\cos\theta_1 \qquad \ldots \qquad (3.17)$

$$\frac{D}{\lambda'}\sin\theta' = \frac{D}{\lambda}\sin\theta - \frac{D}{\lambda_1}\sin\theta_1 \qquad \ldots \qquad (3.18)$$

Hence the resultant phase shift produced corresponds to that which would be produced by a signal of azimuth θ' and wavelength λ'. The vector representing this signal is equal to the difference in the two vectors $(\frac{D}{\lambda},\theta)$ and $(\frac{D}{\lambda_1},\theta_1)$. The response as a function of (V,θ) when the array is tuned to (V_1,θ_1) is thus determined by placing the origin at $(\frac{D}{\lambda_1},\theta_1+\pi)$. The array response does not change; it is the origin that shifts.

In the above equations, λ and λ_1 correspond to the same frequency. Array response is, in general, a function of frequency. However, for the local earthquakes recorded at Kaptagat, observed signal frequency variation is small. Variation of response with frequency is therefore ignored in this analysis.

The data in the present study was analysed using the cross correlation processing technique because, as has been discussed above, it gives better resolution than sum squared processing. The immediate eastern local rift events used in this study have azimuths and velocities centred around about 90° and 7.0 km/s respectively. The dominant frequency of the first arrivals is about 4 to 5 hz. The cross correlator response (with no scaling) for Kaptagat array and for a frequency of 5 hz is calculated and illustrated in fig. 3.3 for V_1 and θ_1 taking on the values of 7.0 km/s and 90° respectively. The illustration covers a range of velocities (3.2-10.0 km/s) and azimuths (50°-130°) centred at the point representing the signal (7.0 km/s, 90°) to which the array is tuned. Fig. 3.3 shows prominent side lobes at about (6.0 km/s, 55°) and (5.8 km/s, 123°) which could be mistaken for genuine second arrivals.

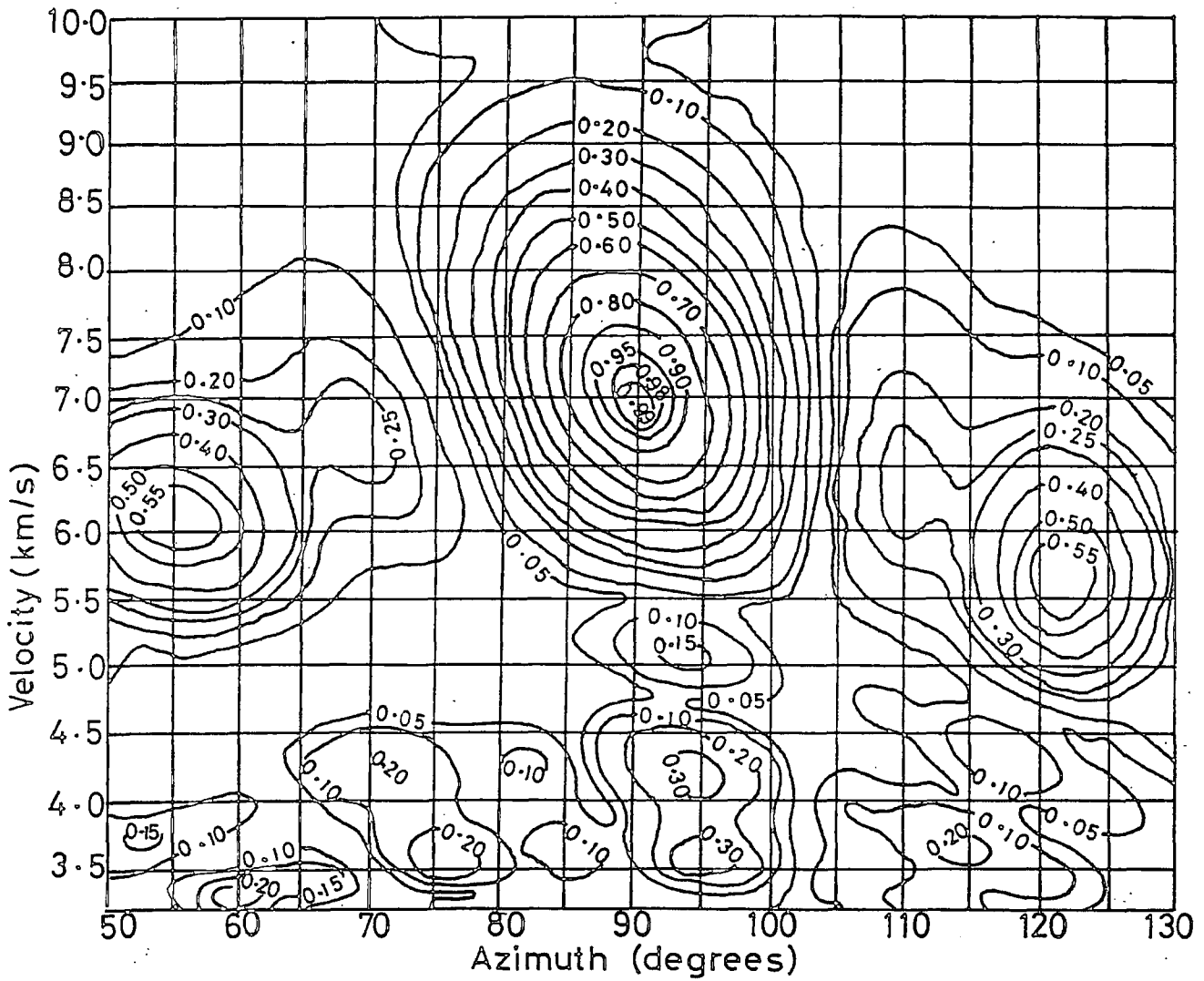

Fig. 3·3 : Contoured correlator response for Kaptagat array.

3.3.3 Array response in the presence of incoherent noise

It can be shown that when the array of n sensors is perturbed by random noise, beam forming improves signal to noise ratio by a factor of $\sqrt{n}$. If the noise is considered white, the amplitude, a, at each seismometer will be constant but the phase will be random. Let the phase angle at the ith seismometer be ϕ_i. If R_n is the resultant summed noise amplitude and γ its phase angle, then

$$R_n \cos \gamma = a \sum_{i=1}^{n} \cos \phi_i$$

$$R_n \sin \gamma = \sum_{i=1}^{n} \sin \phi_i$$

$$R_n^2 = a^2 \left(\left(\sum_{i=1}^{n} \cos \phi_i \right)^2 + \left(\sum_{i=1}^{n} \sin \phi_i \right)^2 \right)$$

$$= a^2 \left\{ \left(\sum_{i=1}^{n} \cos^2 \phi_i + 2 \sum_{\substack{i=1 \\ i \neq j}}^{n} \cos \phi_i \sum_{j=1}^{n} \cos \phi_j \right) + \right.$$

$$\left. \left(\sum_{i=1}^{n} \sin^2 \phi_i + 2 \sum_{\substack{i=1 \\ i \neq j}}^{n} \sin \phi_i \sum_{j=1}^{n} \sin \phi_j \right) \right. \quad \ldots \qquad (3.19)$$

In the typical terms $2\sin\phi_i \sin\phi_j$ and $2\cos\phi_i \cos\phi_j$ of the double summations, $\sin\phi_i$, $\sin\phi_j$, $\cos\phi_i$ and $\cos\phi_j$ have random values between $\pm$ 1 and the averaged sums of sets of these products is effectively zero since ϕ_i is random.

The average value of $\sin^2 \phi_i$ or $\cos^2 \phi_i$ is $\frac{1}{2}$.

Hence $R_n^2 = a^2 \left(\frac{n}{2} + \frac{n}{2}\right) = na^2$.

If the signal has amplitude, a, at each of the seismometers, then the summed signal output for the inphase condition is

$$R_s = na.$$

Thus without using the array the SNR is unity. But on using the array, beam forming increased the SNR by a factor of

$$\frac{R_s}{R_n} = \frac{na}{a\sqrt{n}} = \sqrt{n} \ .$$

3.4. Data Processing.

3.4.1. Processing facilities.

Local earthquake data recorded at Kaptagat array were used in the study of the lithosphere in and around the Gregory rift at the latitude of about 0.5N. These data were recorded on one inch analogue field magnetic tapes stored at the processing laboratory housed at Durham University's Department of Geological Sciences.

The processing laboratory consisted of one inch EMI tape deck with supporting electronics for demodulation and flutter compensation, a 16-channel jet pen recorder, a bank of three analogue band pass filters (Krohn Hite, and later Kemo) and a 12-channel oscilloscope. Digital processing was done on a CTL Modular One computer (Mod 1) with 16K core store and 8 bit word. Communication to this computer was via a teletype terminal. Output from the computer was routed through a matrix board to the jet pens, the oscilloscope, the teletype or the Hewlett Pakard X-Y plotter. Analogue signals on the field magnetic tapes were converted into digital form using an A/D converter. Backing storage for the computer was provided by attached tape and disk units.

A part of the core space is occupied by the executive, compiler and filters (programs). The remaining space is used

for the storage of the array data in time series channels. Each seismogram is allocated a time series channel. The process of velocity filtering involves application of positive and negative delays to these channels. It is therefore necessary to have sufficient samples in store at a given time to allow the necessary delays to be applied. The number of samples required to be stored is, consequently, in direct proportion to the digitization rate.

Each of the records used in this study was digitized at two sampling rates 50 and 100 samples per second. The normal disk file was 43 pages long and could contain about 13s of 8 channel array data recorded at a sampling interval of 0.01s. However, several disk files could be concatenated to produce a file of up to 250 pages corresponding to about 80s of 8 channel array data recorded at 100s/s. For higher/lower sampling rates, the length (in time) of the record that can be held is proportionately less/more.

Flexibility in processing on Modular one computer was enhanced when records digitized at 50s/s were used although the resolution in velocity and azimuth was then limited. On the other hand, flexibility in processing data recorded at 100s/s was severely limited because of the small storage space available in the machine. However, the velocity and azimuth resolution for such records was accurate enough without provision for interpolation between samples. For greater speed and flexibility the data recorded at 100s/s were all again processed on the NUMAC IBM 360/370 computer.

3.4.2. The Velocity filter program.

Velocity/azimuth filtering on Mod 1 computer was implemented using a program developed by Forth (1975) and written in a special language called SERAC (seismic record analysis compiler). This program is here modified (as listed in appendix A) and used for the present analysis to perform a search over ranges of velocity, v, and azimuth, θ. The operation of the program will be illustrated below for the case where the azimuth of a single arrival is known and it is required to determine its apparent surface velocity.

For the given azimuth, a value of starting velocity is selected. Steering delay, τ_i (with respect to the crossover point), for the seismometer, i, at the starting velocity and the given azimuth is calculated using equation 3.2. The output of the seismometer, i, is then dalayed in time by amount τ_i. At desired time points, the delayed seismometer outputs on the red and yellow arms are summed seperately to produce the red and yellow partial beams. The partial beams are weighted (if necessary) and then cross multiplied. The square root of the magnitude of this cross product is taken with the original sign of the cross product preserved. The resulting function is averaged or smoothed over a moving square time window of length not exceeding the uninterrupted duration of the signal. The operations described above simply implement equation (3.5). The resulting output (which may sometimes be band pass filtered) is the time averaged product (TAP) or correlation function for the starting velocity and the given azimuth. This TAP is plotted on the X-Y plotter as a function of time along the seismic record.

The velocity is then incremented and the corresponding TAP produced and plotted. In this way all the TAP traces for the required range of velocity are plotted for the given azimuth.

At the given azimuth, one TAP trace is plotted for each value of velocity in the velocity search range. Final plotter output then consists of any suitable single seismic channel shifted in time by amount corresponding to the pit coordinates of the corresponding seismometer and the measured first arrival velocity and azimuth, the TAP traces in increasing order of velocity and a time channel for relative time information. Each TAP trace has a DC base line from which the trace amplitude is normally measured, using a half millimeter scale attached to a magnifying lens. A graph of TAP trace amplitude against apparent velocity is obtained from measurements on the plotter output. The location of the maximum TAP amplitude can be obtained by fitting a parabola to the measured values of amplitude against velocity. The velocity at which the measured amplitude is maximum is taken as an estimate of the signal velocity at the given azimuth.

If the apparent velocity and azimuth of an arrival are both initially unknown, short TAP traces covering the full range of azimuth (0^{o}-360^{o}) and probable range of velocity are produced and the corresponding amplitudes measured. In this case initial velocity and azimuth increments are made large and only rough estimates of probable range within which the signal parameters lie can then be made. Subsequent filtering with finer increments in velocity and azimuth within this range can be used to give more precise estimates of the signal parameters.

On Mod 1 computer the program can also be used in a fully automatic mode (without plot option) to calculate TAP amplitudes for full ranges of azimuth and velocity. The calculated amplitudes are stored in a two dimensional array representing velocity-azimuth space. The position of the maximum amplitude in this space determines the required apparent velocity and azimuth of the signal. On this machine, the automatic version of the program for full ranges of azimuth and velocity takes too long (several hours) to run for one record. More over, because of the limited space available in the machine, data sampled at higher rates than 50s/s could be filtered for only severely limited ranges of velocity and azimuth. Use of lower sampling rates than this results in poor resolution in the determination of signal velocity and azimuth.

To overcome these problems and to obtain more precise data on first and later arrivals, a program was written in Fortran for implementation on the University of Durham's general purpose IBM 360/370 computer. This program (listed in appendix C), *VFIL*, performs the same functions of delaying, summing and cross correlating already described above. A brief description of the Fortran program is now given.

At any chosen point in time along the array record, defined search ranges of azimuth and velocity are swept through starting from initial values up to stipulated final values in specified increments. For any given time along the record, values of velocity v, and azimuth, θ, are selected within the given ranges. Arrival times, τ_r (relative to the crossover point) corresponding to the signal (v,θ) are calculated for the seismometer r assuming

plane wavefronts and using equation 3.2. The output of seismometer r is then delayed in time by amount τ_r. The delayed outputs or channels for the red and yellow arms are summed seperately. These partial sums are cross multiplied and the square root of the crossproduct taken with the original sign preserved. The output is then integrated over a time window of about one period of the uninterrupted signal.

For an azimuth θ_i and velocity v_i, a value of the correlator output, C_{ij}, is computed. If there are m values of velocity and n values of azimuth, then mn values of correlator output are calculated in the θ-v space. These mn values are smoothed out to reduce the effect of noise bursts. A test is then carried out to see which of the outputs, C_{ij}, is a maximum or peak in the θ-v space. All identified peaks in the field (with their corresponding values of θ and v) are then arranged in descending order of magnitude in a one dimensional array for each chosen time point.

The contents of this array can be printed and/or plotted as desired starting from the first element. Any desired number of peaks can thus be plotted/printed for a given point in time, By trial and error it was established that 1 or 2 peaks gave the best plots. The size of the character used in the plot is chosen proportional to the corresponding computed TAP amplitude. Four to five peaks were usually printed. The need to search for more than one peak in the field at a point in time arises from the fact that two or more seismic phases may overlap in time at the station.

3.4.3. Performance tests on the filtering program.

Local earthquakes recorded by Kaptagat array station and used for the study of the rift structure to the immediate east of the array station cover a frequency range of about 4 to 5 hz. After the first arrival which lasts uninterrupted for no more than about one period, there may be several partially overlapping phases resulting in signal interference. Tests on synthetic data were, therefore, carried out to estimate the accuracy with which velocity and azimuth of a single signal phase can be measured and also to determine the ability of the program and the array to resolve differences in velocity, azimuth and onset times of interfering signals.

To simulate a seismic wavelet, a decaying sinusoid of frequency f, amplitude A and duration T was generated as a time function from the relation

$$y = (A\sin 2\pi ft)\cot\left(\theta_1 + \left(\frac{\theta_2-\theta_1}{T}\right)t\right) \quad \ldots\ldots \quad (3.19).$$

θ_1 and θ_2 are chosen minimum and maximum values of the angle (in radians) whose cotangent modulates the sine function. By choosing the values 5 units, 0.40 rad., 1.45 rad., 4 hz and 0.50s for A, θ_1, θ_2, f and T respectively, about 2 cycles of this decaying 4 hz sinusoid lasting 0.50s was generated.

Using Mod 1 computer and the program listed in appendix B, this simulated wavelet was generated at sampling intervals of 0.02s and 0.01s. This wavelet formed each channel of a ten channel record (fig. 3.4a) stored on a disk file. These ten time series channels on the record were linked to the 10 co-ordinates of Kaptagat array seismometer pits. The channels could

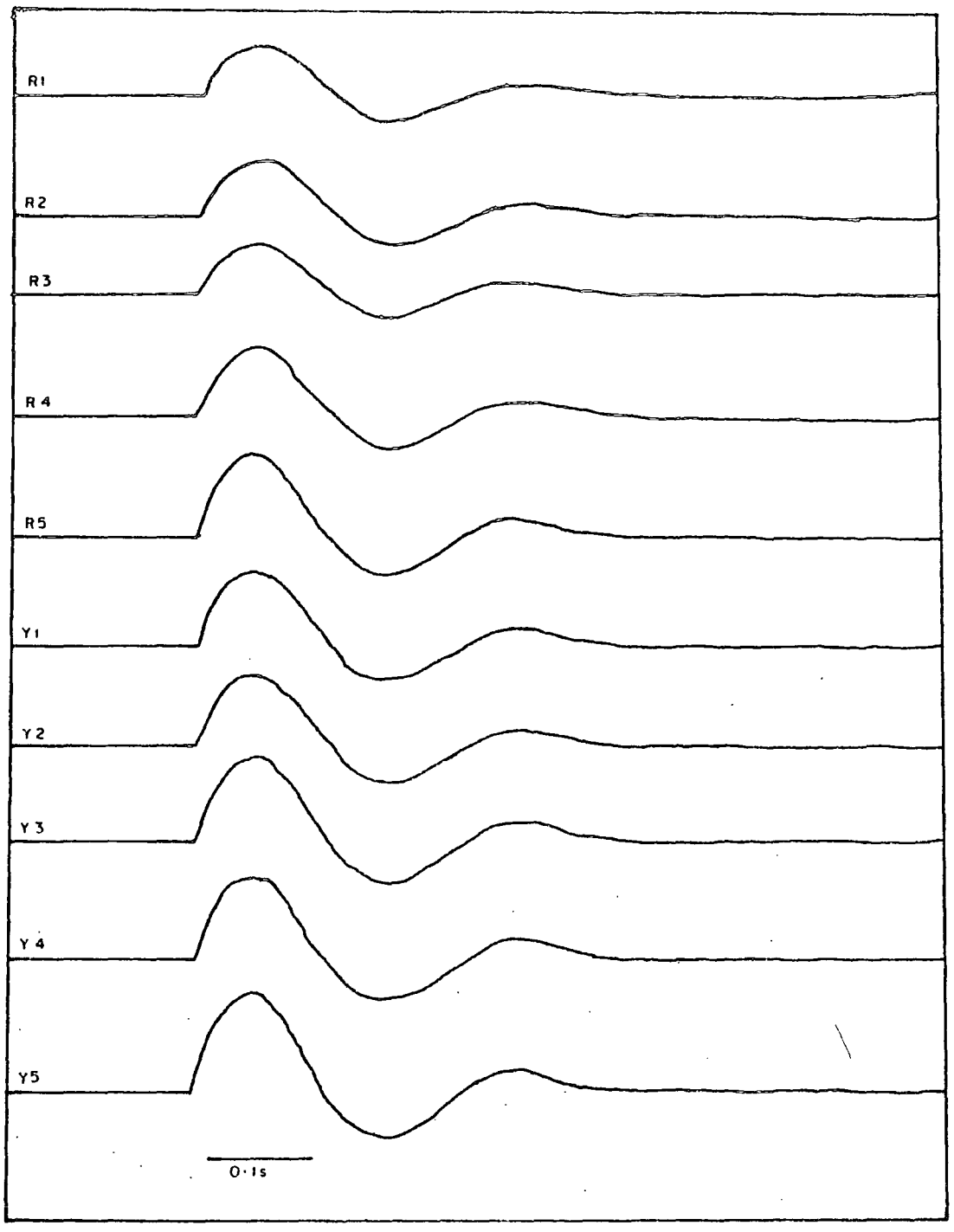

Fig. 3·4a : A decaying 5 hz sinusoid linked to each of the ten kaptagat pits.

then be given relative dalays corresponding to an arrival at the station with a given apparent velocity and from a given azimuth. The accuracy achieved by the array and the program in the measurement of velocity and azimuth for a single phase was studied using this delayed record. Delays corresponding to two or more arrivals with different apparent surface velocities and from same or different azimuths could also be introduced. In this way it was possible to test the ability of the array to seperate two interfering/overlapping arrivals in time and determine their signal parameters.

For use on Mod 1 computer, the synthetic data recorded at 50s/s were filtered in preference to records produced at 100s/s because the former allowed for coverage of wider ranges in velocity and azimuth. Finer resolution in the estimate of the signal parameters for the same event could then be obtained from data recorded at 100s/s within the narrower limits established by the previous data.

The delay τ_i, for the ith channel was calculated for a signal with velocity 6.0 km/s and from azimuth 225^{o} as before using equation 3.2 and the coordinates of Kaptagat pits. The number of samples involved in the delay, τ_i, is the nearest whole number to $50\tau_i$ since there was no provision in the program for interpolation between samples. After the application of the delays, the resulting record (fig. 3.4b) was stored on a disk file and subsequently filtered using the program listed in appendix A and discussed in section 3.4.2. An averaging time of 0.20s was used. This averaging time has been found by trial and error (as shown later in this section) to be the best value for use in filtering of records of the local events.

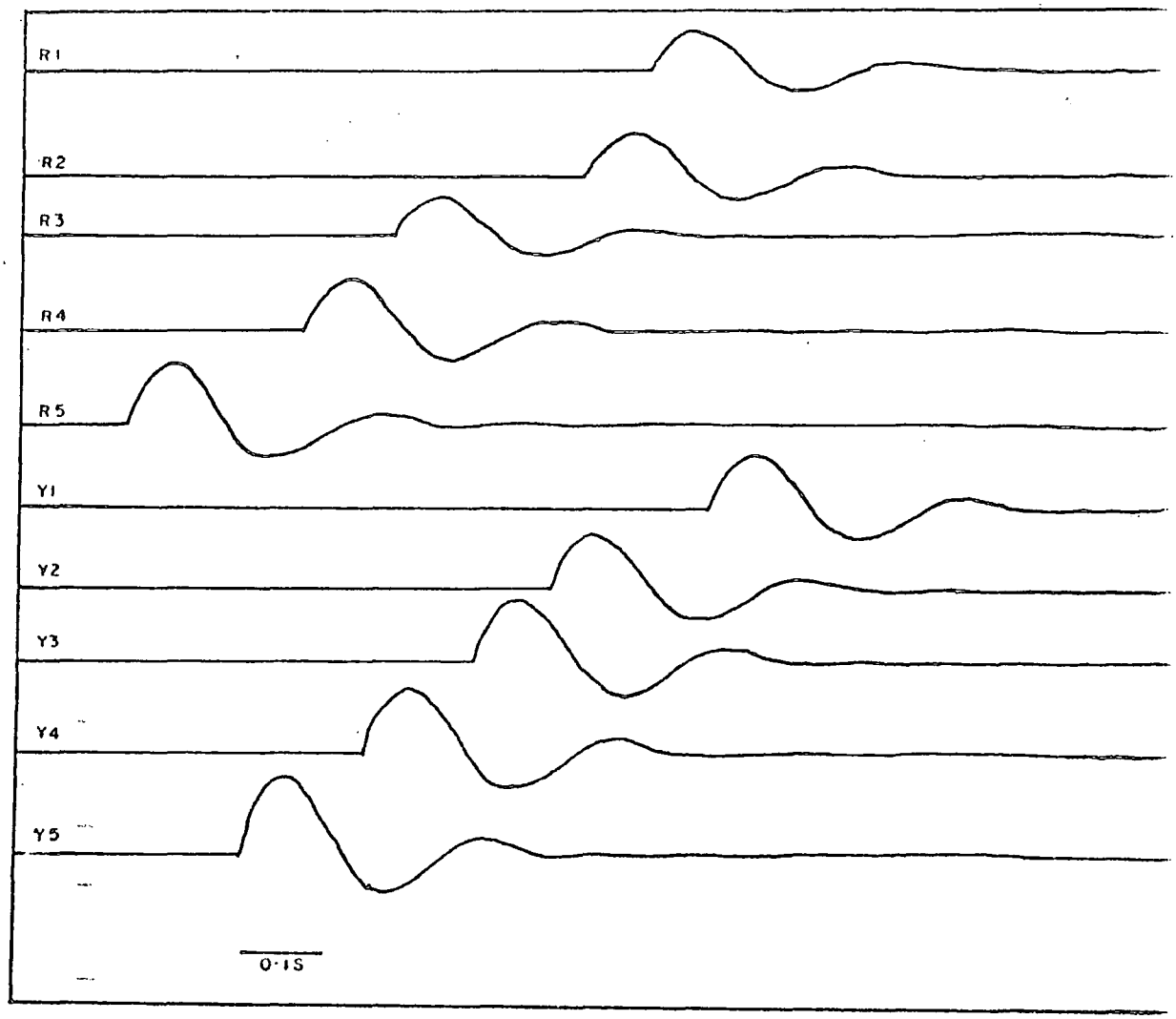

Fig.3·4b. The decaying sinusoids of Fig. 3·4a with delays inserted to correspond to a velocity 6·0 Km/s, azimuth 225°

Using a $\frac{1}{2}$ mm scale to which a magnifying glass was attached amplitudes of the correlator outputs were measured for signal velocities increasing from 5.0 km/s to 7.0 km/s in stepts of 0.2 km/s and for azimuths increasing from 221^{o} to 227^{o} in steps of 1^{o}. These amplitudes normalized to unity for maximum amplitude in the field is shown in table 3.1. The maximum normalized amplitude was located at the correct velocity of 6.0 km/s but at an azimuth of 224^{o} (instead of 225^{o}). However it is clear from table 3.1 that the measured azimuth lies between 224^{o} and 225^{o} suggesting a difference of less than 1^{o} between expected and measured azimuths. This small difference between expected and measured azimuths could possibly result from the coarse increments (0.2 km/s) in search velocity and from the quantization errors due to the sampling interval of 0.02s used.

Fig. 3.5 shows the correlator outputs for an azimuth of 224^{o}. At the top of the record is a single channel; this is followed by outputs for velocities increasing from 5.0 km/s to 7.9 km/s in steps of 0.1 km/s. Normalized correlator amplitudes measured from these outputs were then plotted against velocity (fig. 3.6). As expected, the curve peaks at 6.0 km/s which is the correct signal velocity. The corresponding peak for azimuth of 225^{o} is also at 6.0 km/s but the amplitude is then 95% the peak at 224^{o}. When steering delays corresponding to a signal with velocity 7.0 km/s and azimuth 225^{o} were inserted in the ten channel unphased record, maximum normalized correlator output was located at 224^{o} and 7.1 km/s.

Tests similar to those described above were also carried out for azimuths of $90^{o}(270^{o})$, $135^{o}(315^{o})$ and $180^{o}(0^{o})$ when

Apparent velocity (km/s) \ Azimuth (degrees)	221	222	223	224	225	226	227
5.0		0.43	0.45	0.61	0.69	0.71	0.59
5.2		0.56	0.49	0.72	0.80	0.80	0.67
5.4	0.39	0.63	0.57	0.81	0.89	0.86	0.75
5.6	0.46	0.72	0.67	0.90	0.95	0.89	0.74
5.8	0.50	0.83	0.85	0.98	0.93	0.86	0.72
6.0	0.59	0.93	0.88	1.00	0.95	0.80	0.70
6.2	0.75	0.99	0.98	0.96	0.89	0.80	0.54
6.4	0.81	0.96	0.97	0.92	0.82	0.71	0.52
6.6	0.86	0.93	0.94	0.86	0.76	0.67	0.53
6.8	0.85	0.89	0.89	0.80	0.70	0.63	0.51
7.0	0.85				0.67	0.63	0.49

Table 3.1 Normalized amplitudes in the neighbourhood of (6.0 km/s,225^{o}) when the array is tuned to the signal (6.0 km/s,225^{o}).

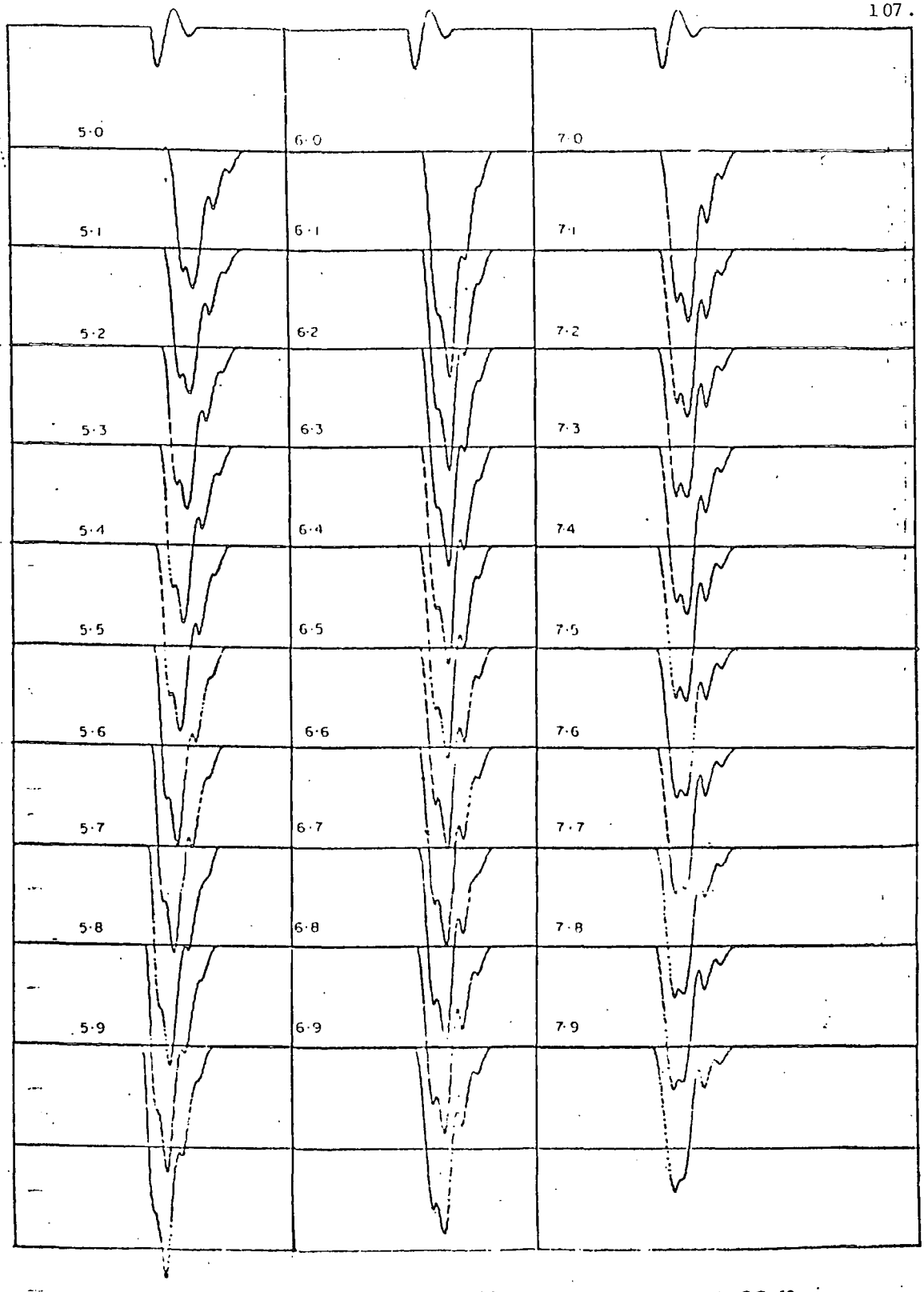

Fig·3·5 : TAP traces for data of Fig.3·4b at an azimuth of 224°.
Velocity increases from 5·0 Km/s to 7·9 Km/s in steps of 0·1 Km/s.

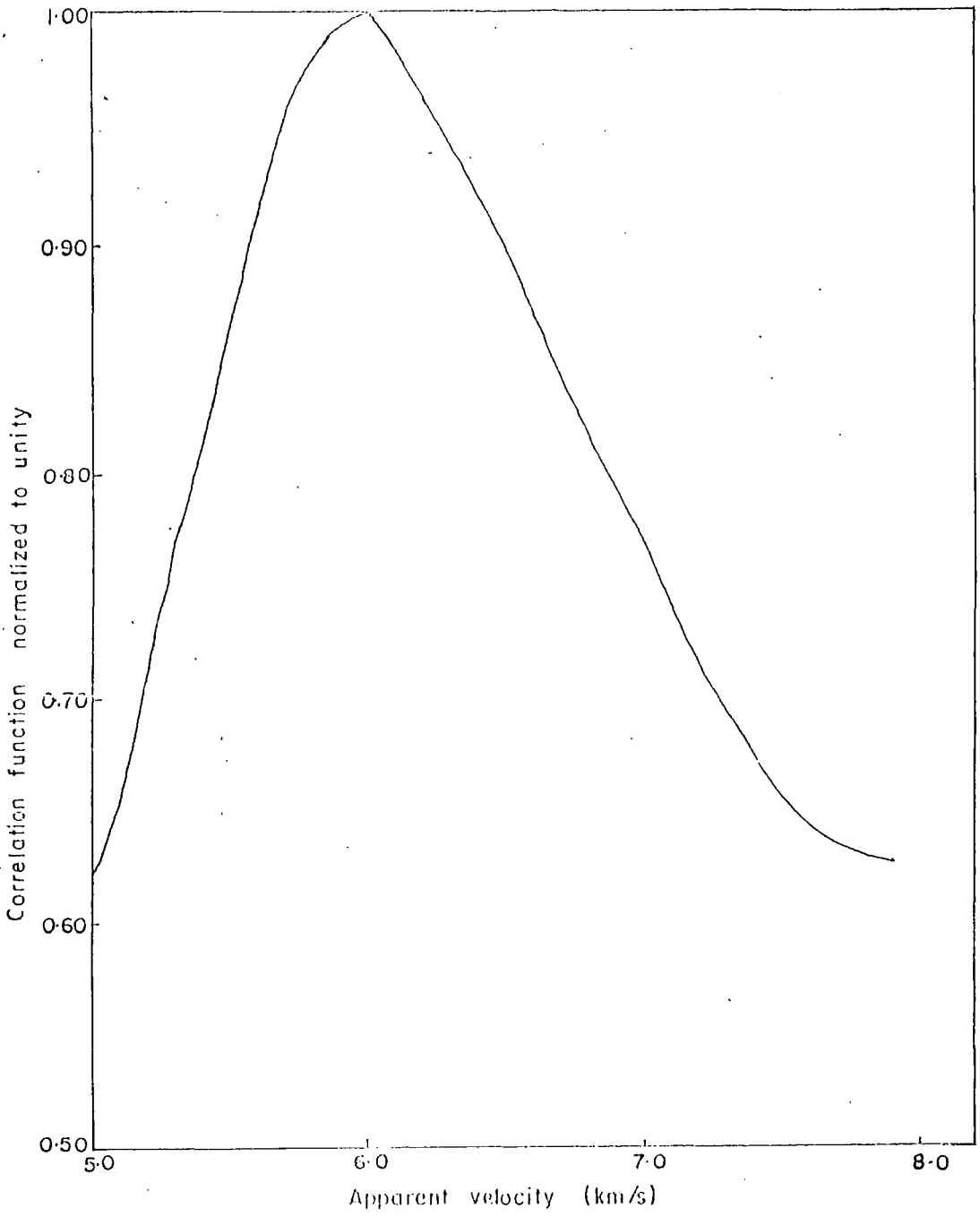

Fig. 3·6 : Plot of measured normalized correlator output against apparent velocity for an azimuth of 224°.

apparent velocity of signal was fixed at 7.0 km/s. The results for 270^{o} and 135^{o} are shown in tables 3.2 and 3.3 respectively. At 270^{o}, velocity and azimuth increments were 0.1 km/s and 1^{o} respectively and measured azimuth and velocity were 271^{o} and 7.1 km/s. At 135^{o} azimuth, increments of 0.2 km/s and 2^{o} in search velocity and azimuth were used and the resulting measured parameters were 6.9 km/s and 130^{o} (fig. 3.7). From table 3.3 and fig. 3.7 the peak at 135^{o} occurs at the correct velocity of 7.0 km/s although this peak is only 0.90 of the peak at 130^{o}. At all azimuths the measured velocity was within $\pm$ 0.1 km/s of the correct velocity. Except for the azimuth of 135^{o} each measured azimuth was within $\pm$ 1^{o} of the correct azimuth.

All the measurements discussed above are summarized in table 3.4. In all these discussions we have used synthetic data recorded at 50s/s to ensure flexibility while using Mod. 1 computer. Better resolution (than given above) in the measurement of signal parameters may be obtained with data sampled at 100s/s using a bigger machine.

Apparent velocity (km/s)

Azimuth (degrees)	6.4	6.5	6.6	6.7	6.8	6.9	7.0	7.1	7.2	7.3	7.4	7.5	7.6	7.7
266	0.90	0.93	0.91	0.91	0.91	0.78	0.75	0.71	0.62	0.68	0.58	0.58	0.58	0.41
267	0.86	0.94	0.94	0.92	0.94	0.89	0.90	0.86	0.84	0.76	0.68	0.58	0.58	0.59
268	0.89	0.89	0.97	0.96	0.96	0.94	0.91	0.92	0.90	0.83	0.73	0.73	0.74	0.55
269	0.81	0.88	0.97	0.97	0.97	0.98	0.97	0.89	0.83	0.73	0.81	0.81	0.71	0.63
270	0.68	0.81	9.81	0.94	0.95	0.98	0.99	1.00	0.99	0.98	0.95	0.89	0.89	0.85
271	0.63	0.74	0.86	0.91	0.95	0.99	0.99	1.00	0.99	0.90	0.91	0.91	0.82	0.71
272	0.59	0.59	0.76	0.82	0.86	0.92	0.96	0.00	0.00	0.96	0.91	0.91	0.87	0.78
273	0.37	0.37	0.59	0.59	0.64	0.73	0.81	0.86	0.94	0.96	0.96	0.96	0.94	0.88
274	0.36	0.45	0.60	0.64	0.70	0.81	0.81	0.94	0.80	0.97	0.97	0.93	0.92	0.88

Table 3.2 Normalized correlator amplitudes in the neighbourhood of the signal (7.0 km/s, 270°) to which the array is tuned.

Azimuth (degrees)

Apparent velocity (km/s)	122	124	126	128	130	131	132	133	134	135	136	137	138	139	140	142	144
6.0	0.58	0.56	0.43	0.45	0.41	0.42	0.43	0.39	0.40	0.43	0.42	0.41	0.34	0.30	0.32	0.28	0.28
6.2	0.65	0.62	0.64	0.58	0.55	0.55	0.51	0.47	0.43	0.44	0.48	0.43	0.43	0.42	0.35	0.35	0.33
6.4	0.69	0.76	0.82	0.81	0.65	0.65	0.68	0.55	0.55	0.55	0.55	0.51	0.48	0.49	0.43	0.42	0.41
6.6	0.77	0.77	0.92	0.89	0.85	0.85	0.83	0.78	0.70	0.70	0.81	0.62	0.64	0.64	0.55	0.54	0.45
6.8	0.66	0.78	0.90	0.95	1.00	0.99	0.97	0.88	0.93	0.90	0.92	0.87	0.78	0.79	0.74	0.68	0.56
7.0	0.67	0.72	0.83	0.85	0.91	0.92	0.94	0.96	0.95	0.95	0.94	0.92	0.86	0.83	0.80	0.74	0.64
7.2	0.50	0.58	0.66	0.78	0.81	0.81	0.87	0.91	0.89	0.89	0.88	0.83	0.83	0.80	0.80	0.73	0.67
7.4	0.39	0.47	0.51	0.48	0.55	0.55	0.52	0.69	0.82	0.77	0.67	0.72	0.67	0.65	0.71	0.61	0.62
7.6	0.28	0.31	0.35	0.30	0.40	0.40	0.52	0.52	0.57	0.57	0.46	0.47	0.55	0.55	0.52	0.60	0.56
7.8	0.23	0.23	0.17	0.26	0.28	0.28	0.33	0.38	0.45	0.42	0.41	0.41	0.36	0.41	0.46	0.45	0.48

Table 3.3. Normalised TAP amplitudes for signals in the neighbourhood of (7.0 km/s,135^{o}) when Kaptagat array is tuned to (7.00 km/s,135^{o}).

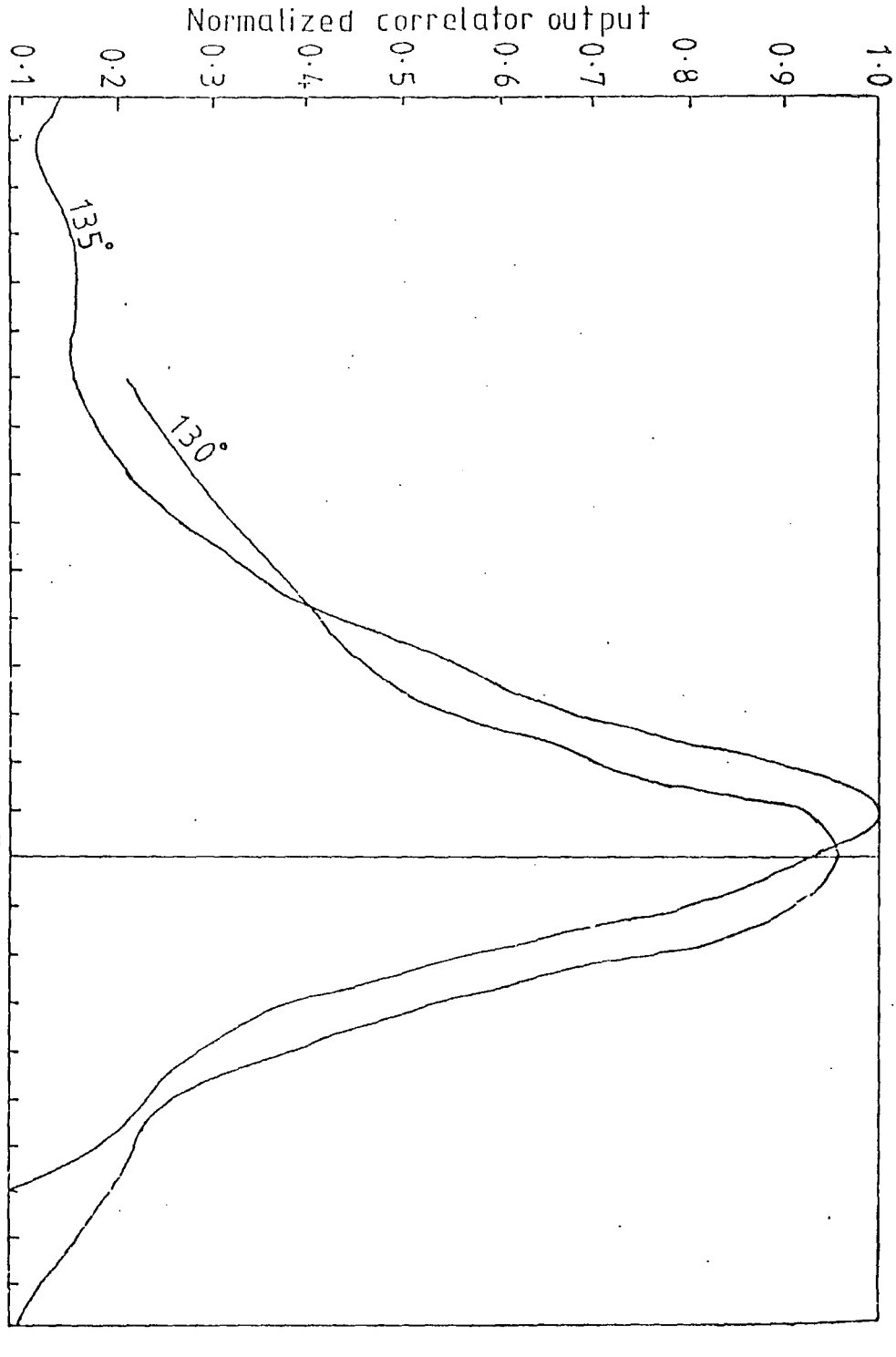

Fig.3.7: Velocity response at azimuths of 130° and 135°.

Correct azimuth (degrees)	Correct velocity (km/s)	Measured azimuth (degrees)	Measured velocity (km/s)
135	7.0	130	6.9
180	7.0	179	7.1
225	7.0	224	7.1
270	7.0	271	6.9

Table 3.4. Measured velocities and azimuths at different azimuths when the outputs of the array sensors are given delays corresponding to a signal crossing the array with velocity of 7.0 km/s at each of the given azimuths.

3.4.4. Interference problems.

Using a synthetic seismogram program, Maguire (1974) showed that for an event at a distance of about 55 km from Kaptagat sixty arrivals occurred within the first 9.63s of record if amplitudes within three orders of magnitude including P,S and mode conversions were considered. Calculated apparent surface velocities varied from 3.47 km/s to 13.57 km/s. Although the number of these theoretical arrivals will be drastically reduced when only measurable amplitudes are considered, signal interference between recorded phases certainly constitutes a problem for such small distances.

Distances covered by the immediate eastern local rift events used in this study range from about 50 km to about 80 km. Consequently, after the first arrival, superposition or interference of two or more recorded signal phases could result in measured velocities and azimuths which may differ significantly from those of the original single components.

To illustrate, we consider two simple harmonic waves of equal amplitude, a, propagating across the array with angular frequencies w_1 and w_2, wave vectors, $\underline{k}_1$ and $\underline{k}_2$ and with a phase difference ϕ between them. The displacements, y_1 and y_2, are then given by

$$y_1 = a \sin(w_1 t - \underline{k}_1 . \underline{r} + \phi)$$

$$y_2 = a \sin(w_2 t - \underline{k}_2 . \underline{r})$$

The displacement, y, resulting from interference between the two waves is given by

$$y = 2a\{\tfrac{1}{2}(w_1+w_2)t - \tfrac{1}{2}(\underline{k}_1+\underline{k}_2).\underline{r} + \frac{\phi}{2}\} X$$
$$\mathrm{Cos}\{\tfrac{1}{2}(w_1-w_2)t - \tfrac{1}{2}(\underline{k}_1-\underline{k}_2).\underline{r} + \frac{\phi}{2}\} \quad \ldots\ (3.20)$$

In the present data, frequency variation is small (section 3.4.3). On the other hand, measured apparent veolcities cover the range 5.6 to about 9.4 km/s. Interference effects in space are, therefore, more important than those in time. To further simplify the treatment, we can therefore assume that the two waves have the same frequency w, say, so that equation (3.20) reduces to

$$y = 2a\{wt-\tfrac{1}{2}(\underline{k}_1+\underline{k}_2).\underline{r}+\tfrac{\phi}{2}\}\cos\{-\tfrac{1}{2}(\underline{k}_1+\underline{k}_2).\underline{r}+\tfrac{\phi}{2}\} \quad .... \quad (3.21)$$

If the two waves have different velocities but come from the same azimuth, then the first term in equation (3.21) represents a wave travelling in the same direction (i.e. having the same azimuth) as the two interfering waves but with a wave vector $\underline{k}_3$ given by

$$|\underline{k}_3| = \tfrac{1}{2}(|\underline{k}_1|+|\underline{k}_2|)$$

Since $|\underline{k}_3|$ is not equal to $|\underline{k}_1|$ or $|\underline{k}_2|$, the apparent velocity of the resultant wave is different from that of either of the original waves. Interference in this case, therefore, results in correct measured azimuth but anomalous value for measured velocity.

If v_1 and v_2 represent the phase velocities of the interfering waves and v_3 the phase velocity of the resultant wave, it can be shown that for the same frequency,

$$V_3 = \frac{2v_1v_2}{v_1+v_2}$$

For normal East African shield crust and for surface focus, P_g and P_m phase velocities are about 5.8 km/s and 10.8 km/s at a distance of about 60 km. These two phases coming from the same azimuth can therefore interfer (if they have the right stepout time) to produce a new wave crossing the array with a phase velocity of about 7.6 km/s. A superposition of a surface wave (about 4.0 km/s) and a

Moho reflection (about 10.8 km/s) produces a wave of velocity 5.8 km/s.

The second term in equation (3.21) represents the interference envelope and is constant in time. The wavelength, λ_3, of this envelope at a frequency, f, is given by

$$\lambda_3 = \frac{2v_1v_2}{f(v_2-v_1)}$$

If λ_3 is large compared with the dimensions of the array, then its effect is negligible. For example at a frequency of 5 hz, the interference of waves of velocities 5.8 km/s and 6.5 km/s from the same azimuth results in interference envelope of wavelength 21.5 km. This is large compared with the array dimensions of about 5 km and does not introduce appreciable error in correlation measurements. On the other hand, for the same frequency and for velocities v_1 and v_2 of 5.0 km/s and 15.0 km/s, the interference wavelength is 3.0 km which is comparable to the dimensions of the array. The velocity filtering process may, therefore, correlate the interference envelope rather than the individual arrivals. This would produce a high correlation at an anomalous velocity but at the correct azimuth.

In equation (3.21), if two waves with different velocities and azimuths are considered, the resulting wave vector $\underline{k}_3$ is given by

$$\underline{k}_3 = \tfrac{1}{2}(\underline{k}_1+\underline{k}_2)$$

Since the magnitude and direction of $\tfrac{1}{2}(\underline{k}_1+\underline{k}_2)$ necessarily differ from those of $\underline{k}_1$ and $\underline{k}_2$, it follows that the velocity and azimuth of the resultant wave are different, in general, from those of the interfering waves. By similar argument it is seen that the interference pattern propagates with anomalous velocity and anomalous azimuth.

It is concluded from the discussions above that two waves from the same azimuth can interfer to produce correct azimuths but spurious velocities. Furthermore, interference of waves from different azimuths can lead to both anomalous velocities and anomalous azimuths. These observations suggest that caution should be exercised in the interpretation of velocity and azimuth data for later arrivals.

In reality the interference problem may not be as intractable as the simple discussions above would suggest. The phases that can usually be recorded may not have the right time relationships for interference to take place. Time distance graphs for important phases are plotted in fig. 3.8 for the normal East African shield crust and for surface focus. In the range of distance (about 50 to 90 km) covered by immediate eastern local rift events, the principal phases in increasing order of onset times are P_g, P_IP, P_m and surface waves.

As the distance increases from 50 km to 90 km the stepout times between P_g and P_IP decreases from 3.82 to 2.40s, and that between P_IP and P_m decreases from 4.62s to 2.79s. The surface waves, mainly Rayleigh waves with velocity of about 3.0 km/s trail P_g, P_IP and P_m by 8.05s, 4.20s and 0.00s respectively at 50 km distance and by 14.55s, 12.10s and 9.40s respectively at 90 km. The S phases equivalent to the P phases discussed above are expected to come in with very low amplitudes since they are best recorded by horizontal instruments; they will, therefore, produce minimal effects on correlation amplitudes. It should, therefore, be possible to seperate partially overlapping arrivals in terms of time, azimuth and phase velocity.

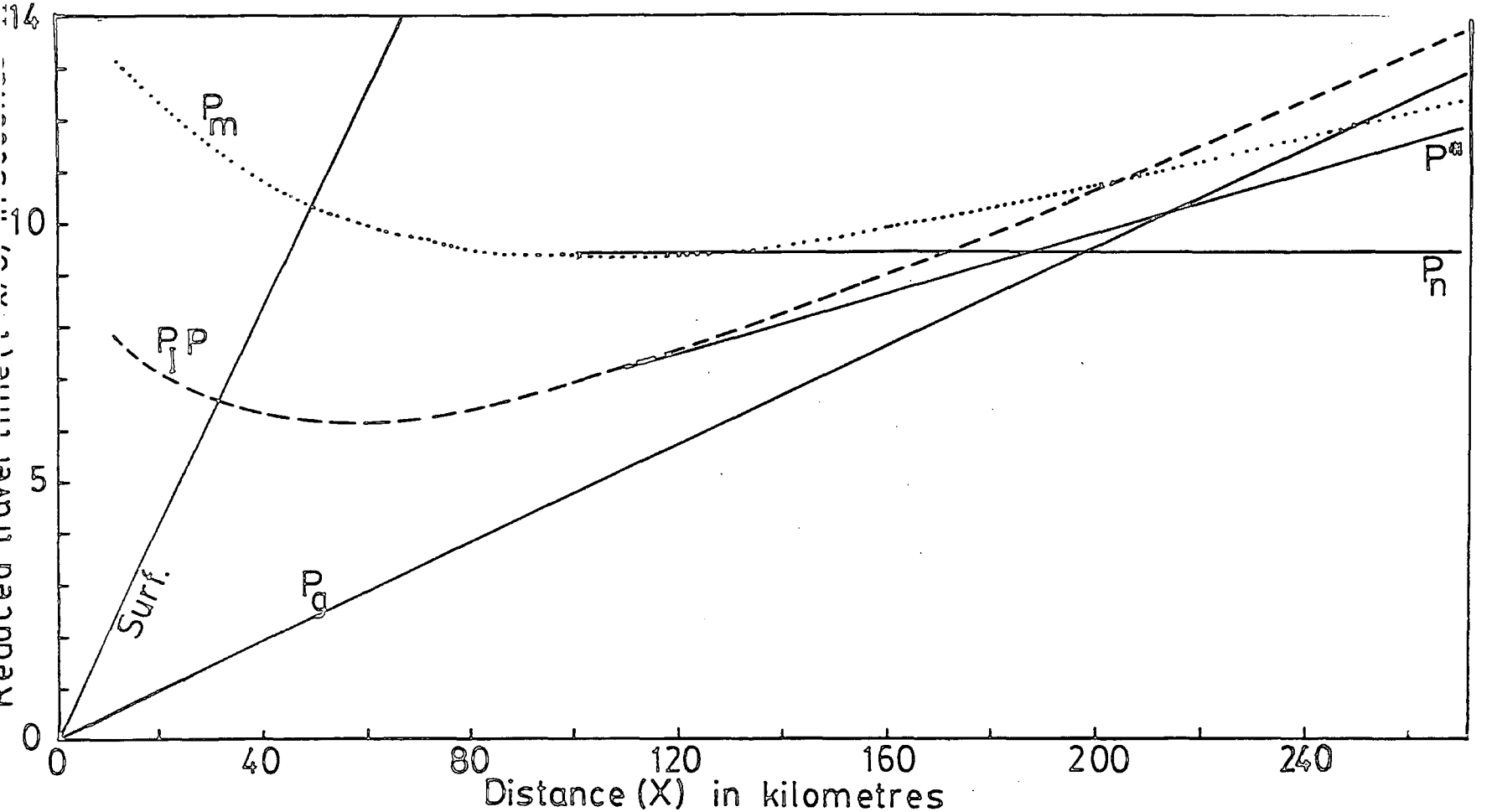

Fig-3-8: Reduced travel time graphs for some prominent phases from the crustal model of Maguire and Long(1976) and for a surface focus.

An investigation was carried out to test the ability of the array and the processing technique in seperating interfering arrivals (from the same azimuth) and in resolving their signal parameters. The test was carried out for an azimuth of 225° (which approximates the azimuth of local events from Kavirondo gulf) and for two signals with phase velocities of 6.0 km/s and 8.0 km/s which are typical crustal velocities.

The signal wavelet corresponding to each Kaptagat pit was delayed (relative to the crossover point) by lengths of time corresponding to two arrivals crossing the array with apparent surface velocities of 6.0 and 8.0 km/s respectively. The two delayed outputs for each pit were added to give a resultant composite signal. The calculated seperation in time between the onsets of the two arrivals at each of the ten pits (table 3.5) varies from 0.008s to 0.147s.

The resulting ten channel record was velocity filtered with the azimuth fixed at 225° and velocity swept from 5.0 to 10.0 km/s in steps of 0.5 km/s. Averaging times of 0.05, 0.10, 0.15, 0.20, 0.30 and 0.40s were used. Two distinct peaks were observed, one at about 5.5 km/s and the other at about 7.5 km/s independent of window length used. Fig. 3.9 shows the correlator output for window length of 0.20s and azimuth of 225° when velocity was incremented by 0.5 km/s.

The velocity filter program was then run with azimuth fixed at 224° and velocity incremented by 0.1 km/s. As shown in section 3.4.3 this is the azimuth at which maximum correlation occurs in azimuth-velocity space. A plot of normalized correlator amplitude against phase velocity was produced for each averaging time in the range 0.05s to 0.80s. For all values of window length, the interfering

Seismometer Pit	Time seperation (seconds)
R1	0.025
R2	0.045
R3	0.101
R4	0.130
R5	0.181
Y1	0.008
Y2	0.061
Y3	0.079
Y4	0.110
Y5	0.147

Table 3.5. Step out times of 6.0 km/s and 8.0 km/s arrivals at Kaptagat pits when the signals come in from an azimuth of 225^{o}.

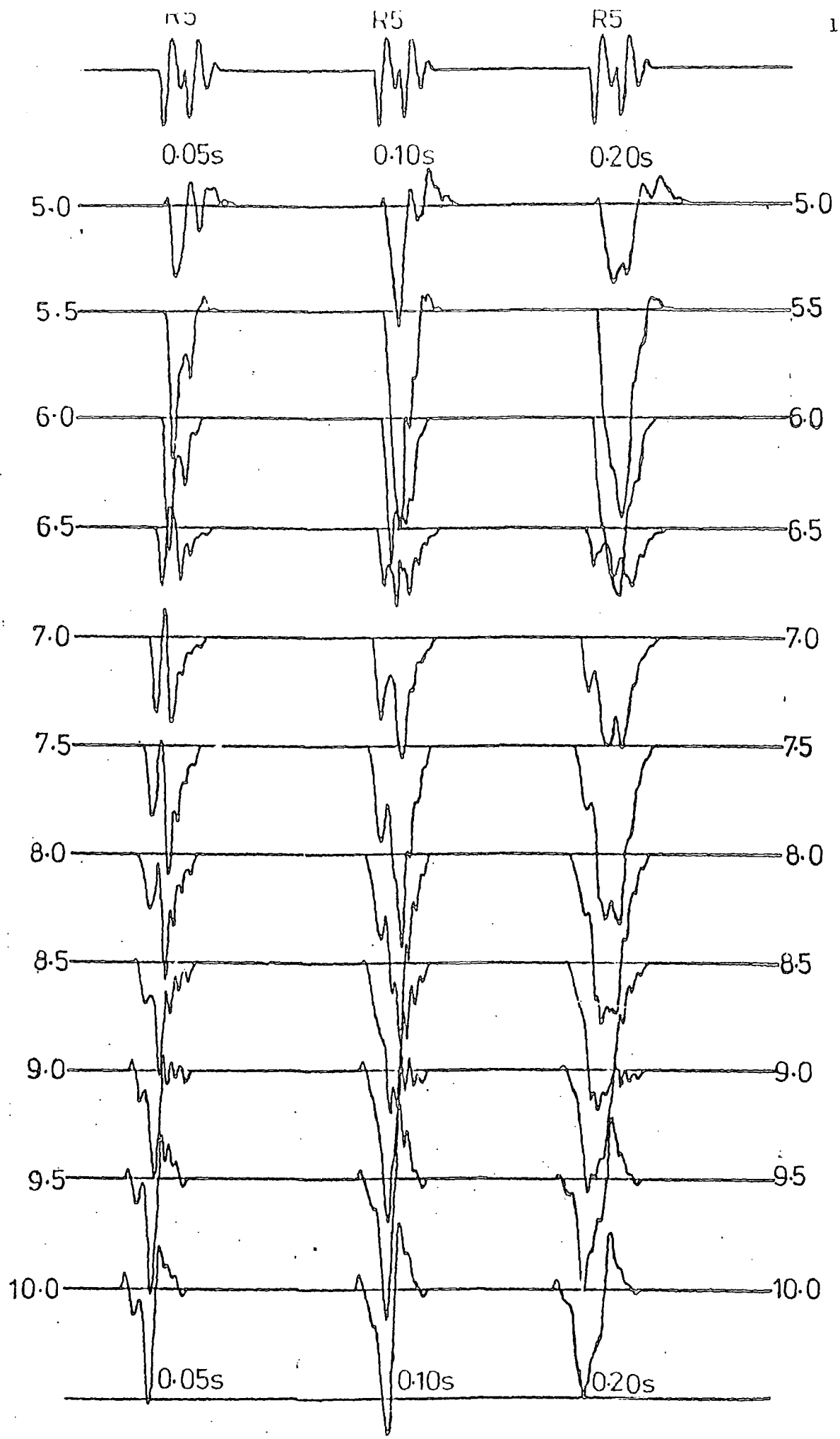

Fig 3·9: Correlator outputs for window lengths of 0·05s, 0·10s and 0·20s when two interferring signals cross the array with phase velocities of 6·0 and 8·0 km/s respectively. Numbers are are apparent velocities in km/s.

arrivals were seen to be seperated since all the curves show double peaking. Fig. 3.10 shows the velocities at which the peaks occurred for various averaging times.

Double peaking and hence signal seperation in time is most prominent for window length of 0.05s (fig. 3.11). But this size of averaging time was considered too small to give reliable results; for example the peaks occurred at velocities of 5.8 km/s and 8.8 km/s instead of 6.0 km/s and 8.0 km/s. It is evident from fig. 3.10 that window lengths between 0.15s and 0.30s gave both measured velocities to within 0.1 km/s of the correct velocities. Within this range, the averaging time of 0.20s gives correct values (6.0 km/s and 8.0 km/s) for both velocities but the double peaking (fig. 3.11) is not as prominent or as well defined as that for 0.05s. Window length of 0.20s was, therefore, considered the most appropriate value to use in filtering records from local events used in the present analysis where the dominant frequency is about 4 to 5 hz.

.5 Estimates of error in apparent velocity and azimuth measurements.

.1 Error due to assumption of plane wavefront.

In the plane wave front formulation used in the filtering program (section 3.4.2) the arrival time, t_p, of a plane wave front from an azimuth θ at a point $P(x_i, y_i)$ on the horizontal earth's surface with respect to zero time at the origin is

$$t_p = -(x_i \sin\theta + y_i \cos\theta)/v$$

This expression is correct for sufficiently large distances from the source. For small epicentral distances, the curvature of the wavefront must be considered to see if significant errors in

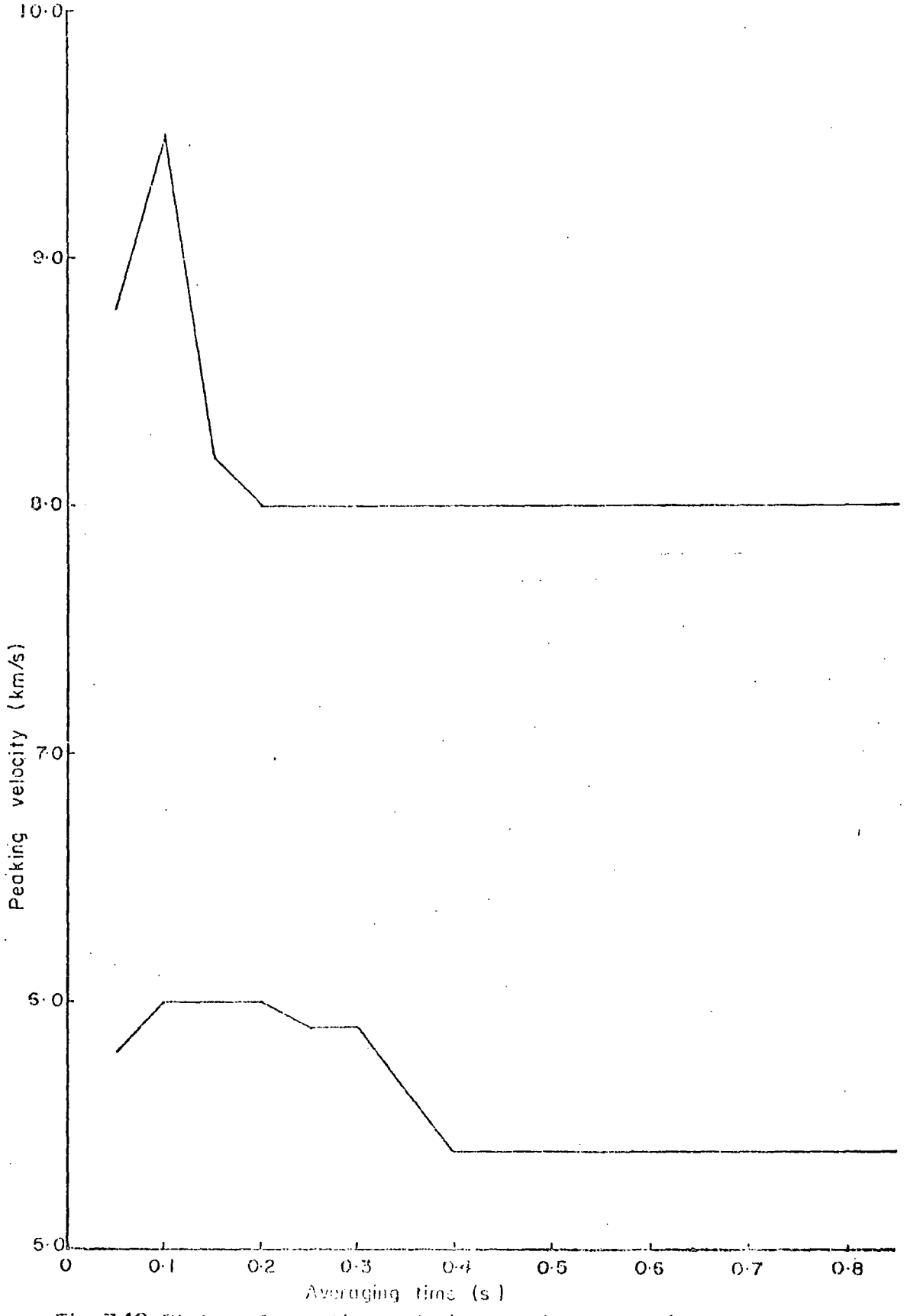

Fig. 3·10: Plot of peaking velocity against averging time.

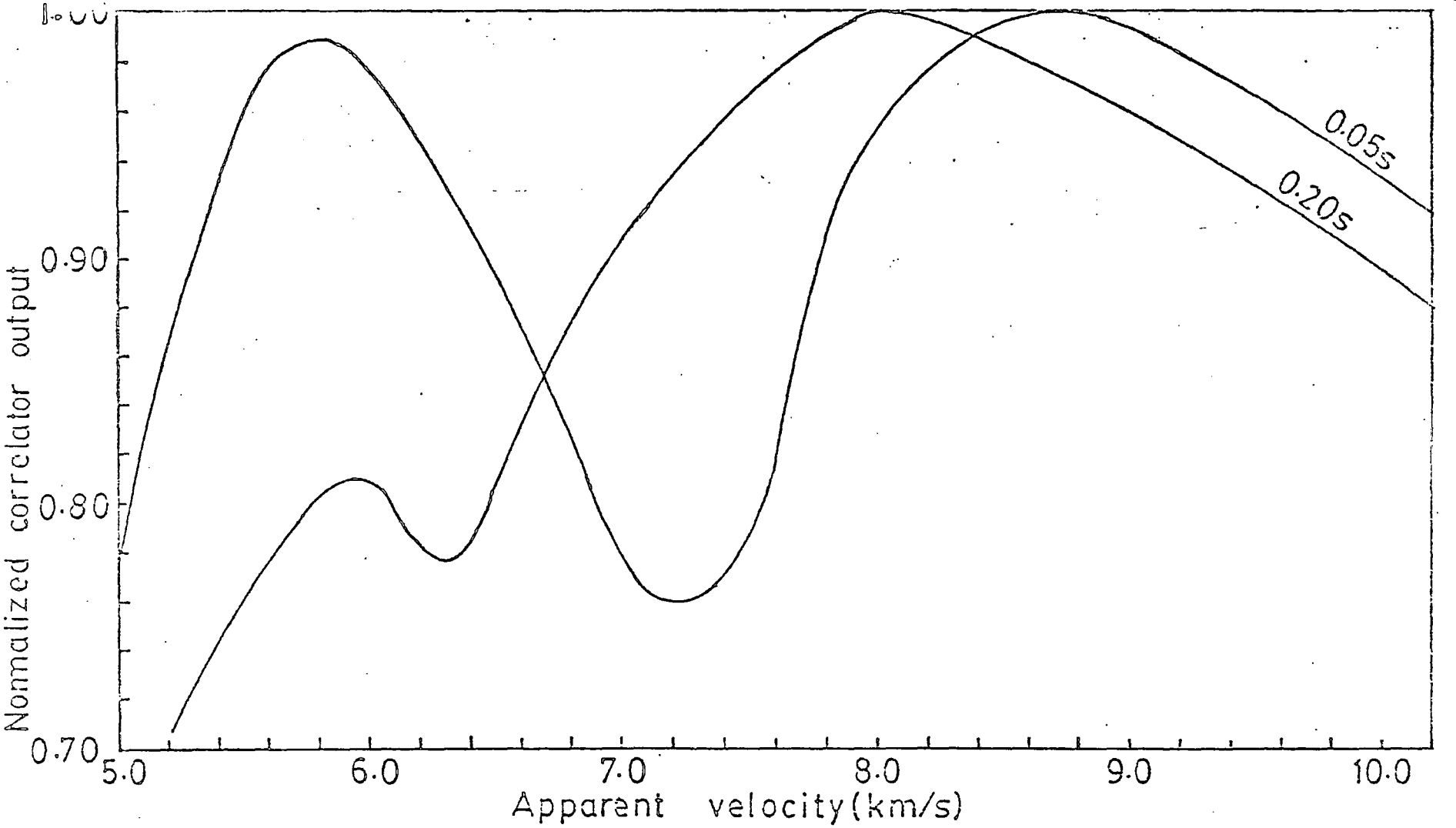

Fig 3.11 : Plots of normalized correlator output against apparent velocity at 224° azimuth and for averaging times of 0.05s and 0.20s.

measured velocity and azimuth result from the assumption of plane wavefronts.

Consider a point source, S(fig. 3.12) of spreading spherical wave fronts. The radial distance, D, from the source to $P(x_i, y_i)$ is given by

$$D = ((\Delta\cos\theta - y_i)^2 + (\Delta\sin\theta - x_i)^2)^{\frac{1}{2}}$$

where Δ is the radial distance from source to the origin or cross-over point. Assuming curvature in the wavefront, the arrival time, t_c, of the wave at P relative to zero at the origin is now

$$t_c = \frac{D-\Delta}{V}$$

This expression should give a better estimate of the times used for inserting delays into the various channels in the velocity filtering process. Because neither Δ nor D was known sufficiently accurately, this expression was not used. In its place the expression based on plane wavefront formulation was used.

Consider a point source S(fig. 3.13) generating spherical waves. At a radius r, the difference, x, in positions between plane (PR) and spherical (PQR) wavefronts is given by

$$X = r - \sqrt{r^2 - a^2}$$

where 2a is the aperture presented by the array at the given azimuth. The difference in arrival times of spherical and plane wavefronts is x/V where V is the apparent surface velocity.

Kaptagat array apertures at azimuths of 45^o and 90^o are about 7 km and 5 km respectively. The minimum estimated distance, r, for rift events to the immediate east of Kaptagat is about 60 km. At this distance the differences in calculated times (between

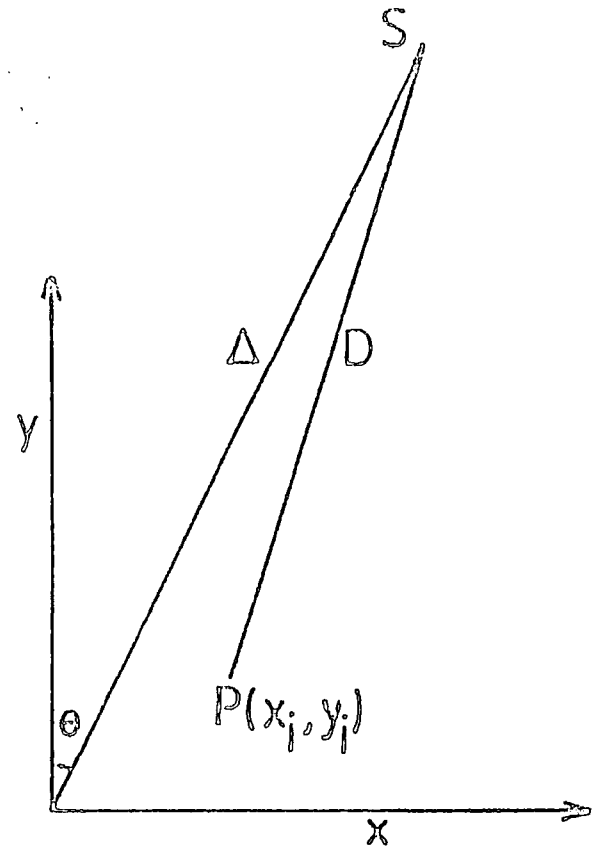

Fig. 3·12 : Schematic diagram for a curved wavefront crossing the array.

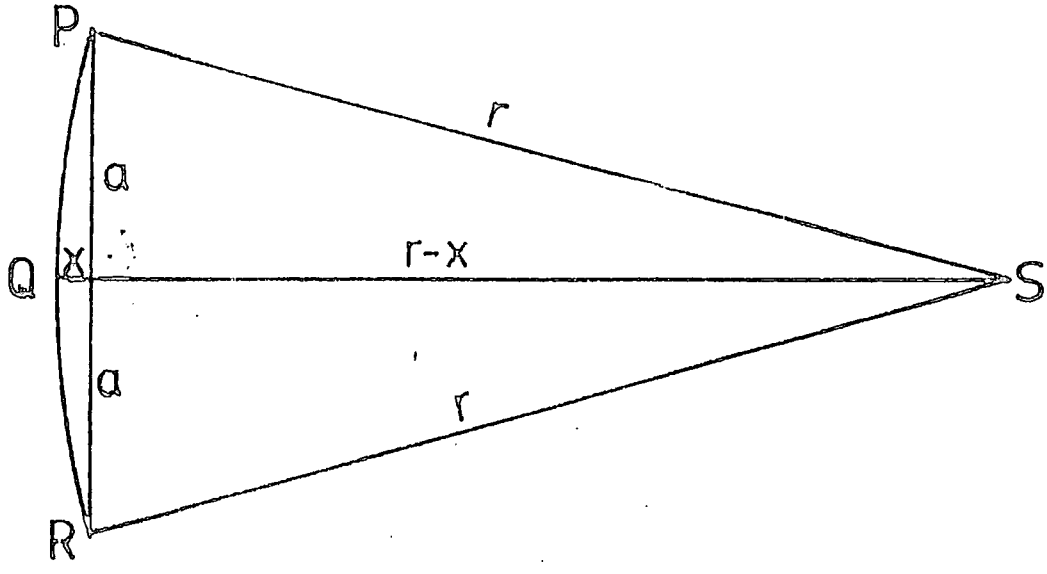

Fig. 3·13 : A diagram illustrating difference in positions of plane(PR) and spherical(PQR) wavefronts at a distance r from source.

plane and curved wavefront approaches) for a phase velocity of 7.0 km/s are 0.0145s and 0.00744s for azimuths of 45^{o} and 90^{o} respectively. These time differences are of the order 0.01s which is the sampling interval used to digitize the records. It is clear from this observation that a higher sampling rate than 100s/s will not necessarily improve the resolution of the data for this and smaller distances if the program assumes plane wavefronts.

3.5.2 Error due to finite sampling rate.

In the program used to calculate apparent velocity and azimuth, no provision was made for interpolation between samples because the data were sampled at 0.01s intervals and the required accuracy is achieved without need for interpolation. Delays were, therefore, applied to the nearest digit.

Consider a seismometer located at the point $P(x_r,y_r)$ in the x-y plane on a horizontal earth's surface and at an azimuth α_r (fig. 3.2). If a plane wave crosses the array with apparent velocity V from an azimuth θ , the arrival time, t, at P relative to zero time at the origin is

$$t = -(x_r \sin\theta + y_r \cos\theta)/v$$

If the seismogram is digitized at S samples per second, the wave will arrive P at sample N where

$$N' = -\frac{(x_r \sin\theta + y_r \cos\theta)S}{v}$$

and N is the digit nearest to N'. For reliable estimation of velocity/azimuth, it is necessary that for each seismometer these digits, N, change for a change in velocity/azimuth.

The rates of change of N' per unit change in azimuth and velocity are given by

$$\frac{\partial N'}{\partial \theta} = \frac{(-x_r \text{Cos}\theta + y_r \text{Sin}\theta)S}{V} \quad \text{and}$$

$$\frac{\partial N'}{\partial V} = \frac{(x_r \text{Sin}\theta + y_r \text{Cos}\theta)}{V^2} \quad \text{respectively.}$$

Tables 3.6a,b,c also give the number of seismometers, m, changing whole number of samples, N, at a particular azimuth when the apparent velocity at that azimuth changes by 1 km/s, 0.5 km/s, 0.2 km/s and 0.1 km/s respectively. Table 3.6b computed for a phase velocity of 7.0 km/s shows that when the phase velocity changes by 0.5 km/s, an average of 6 seismometers change samples at an azimuth of about 90°. Two of these seismometers are on the red arm and four on the yellow arm of the array. For a change of 0.2 km/s in velocity at about 90° azimuth, an average of 4 seismometers (all on the yellow arm) change samples. For a change of 0.1 km/s at 7.0 km/s velocity and same azimuth only three seismometer, (y_3, y_4, y_5), all on the yellow arm, (though not all on a straightline), change integral number of samples.

It is evident, therefore, that in this direction, even when all seismometers are functioning, phase velocity measurements can not be made to a precision better than $\pm$ 0.1 km/s if the sampling interval is 0.01s. The resolution improves/worsens as the apparent velocity decreases/increases at the same azimuth.

Table 3.6d shows $\frac{\partial N'}{\partial \theta}$ values computed at a phase velocity of 7.0 km/s for different azimuths. The last row on this table gives the number, m, of seismometers changing samples by whole numbers when azimuth changes by 1° and 2° respectively at various azimuths. For a change of 1°, only three seismometers are effective while four seismometers change samples by whole numbers for a change of 2°. In both cases all the seismometers are on the red arm although they do not lie on a straightline.

Pits	$\frac{\partial N'}{\partial V}$ at 6.0 kms^{-1} for azimuths of								
	75°	60°	85°	90°	95°	100°	105°	110°	115°
R1	0.8	0.6	0.5	0.3	0.1	0.1	0.3	0.5	0.7
R2	1.3	1.0	0.7	0.3	0	0.4	0.7	1.1	1.4
R3	3.2	2.5	1.8	1.0	0.3	0.5	1.2	2.0	2.7
R4	4.5	3.6	2.7	1.8	0.9	0	0.9	1.8	2.7
R5	6.2	5.0	3.8	2.6	1.3	0	1.3	2.5	3.8
Y1	1.1	1.1	1.2	1.2	1.3	1.3	1.3	1.3	1.3
Y2	5.1	5.2	5.2	5.2	5.2	5.2	5.1	4.9	4.8
Y3	7.1	7.2	7.3	7.3	7.3	7.2	7.1	6.9	6.7
Y4	10.0	10.2	10.3	10.3	10.3	10.2	10.0	9.7	9.3
Y5	12.9	13.1	13.2	13.2	13.1	12.9	12.6	12.2	11.7
m for 1 km/s change	10	10	10	8	7	6	9	10	10
m for 0.5 km/s change	9	9	8	8	6	5	7	9	9
m for 0.2 km/s change	7	7	6	5	4	4	4	5	7
m for 0.1 km/s change	5	5	4	4	4	4	4	4	4

Table 3.6a. Values of $\frac{\partial N'}{\partial V}$ computed for Kaptagat pits at signal azimuths in the range 75° to 115° for an apparent velocity of 6.0 kms^{-1}. m is the number of seismometers changing samples by whole numbers for the given velocity change.

	$\frac{\partial N'}{\partial V}$ at 7.0 km/s for azimuths of								
Pits	75^{o}	80^{o}	85^{o}	90^{o}	95^{o}	100^{o}	105^{o}	110^{o}	115^{o}
R1	0.6	0.5	0.3	0.2	0.1	0.1	0.2	0.3	0.5
R2	1.0	0.7	0.5	0.2	0	0.3	0.5	0.8	1.0
R3	2.3	1.8	1.3	0.7	0.2	0.4	0.9	1.4	2.0
R4	3.3	2.7	2.0	1.4	0.7	0	0.7	1.3	2.0
R5	4.6	3.7	2.8	1.9	1.0	0	0.9	1.9	2.8
Y1	0.8	0.8	0.9	0.9	0.9	1.0	1.0	1.0	1.0
Y2	3.7	3.8	3.8	3.9	3.8	3.8	3.7	3.6	3.5
Y3	5.2	5.3	5.4	5.4	5.4	5.3	5.2	5.1	4.9
Y4	7.3	7.5	7.6	7.6	7.6	7.5	7.3	7.1	6.9
Y5	9.5	9.6	9.7	9.7	9.6	9.5	9.2	8.9	8.6
m for 1 km/s change	10	10	9	8	7	5	9	9	10
m for 0.5 km/s change	8	7	7	6	5	5	5	8	9
m for 0.2 km/s change	6	6	5	4	4	4	4	4	5
m for 0.1 km/s change	3	3	3	3	3	3	3	3	2

Table 3.6b. Values of $\frac{\partial N'}{\partial V}$ computed for Kaptagat pits at signal azimuths in the range 75^{o} to 115^{o} for an apparent velocity of 7.0 km^{-1}.

	$\frac{\partial N'}{\partial V}$ at 7.5 km/s for azimuths of								
Pits	75°	80°	85°	90°	95°	100°	105°	110°	115°
R1	0.5	0.4	0.3	0.2	0.1	0.1	0.2	0.3	0.4
R2	0.9	0.6	0.4	0.2	0.0	0.2	0.5	0.7	0.9
R3	2.0	1.6	1.1	0.6	0.2	0.3	0.8	1.3	1.7
R4	2.9	2.3	1.8	1.2	0.6	0.0	0.6	1.2	1.7
R5	4.0	3.2	2.4	1.6	0.8	0.0	0.8	1.6	2.4
Y1	0.7	0.7	0.8	0.8	0.8	0.8	0.8	0.8	0.8
Y2	3.2	3.3	3.3	3.4	3.3	3.3	3.2	3.2	3.0
Y3	4.5	4.6	4.7	4.7	4.7	4.6	4.6	4.4	4.3
Y4	6.4	6.5	6.6	6.6	6.6	6.5	6.4	6.2	6.0
Y5	8.3	8.4	8.5	8.4	8.4	8.2	8.0	7.8	7.5
m for 1 km/s change	10	9	8	8	7	5	9	9	9
m for 0.5 km/s change	7	7	7	6	4	4	4	7	7
m for 0.2 km/s change	6	5	4	4	4	4	4	4	4
m for 0.1 km/s change	2	2	2	2	2	2	2	2	2

Table 3.6c. Values of $\frac{\partial N'}{\partial V}$ computed for Kaptagat pits at signal azimuths in the range 75° to 115° for an apparent velocity of 7.5 km^{-1}.

$\frac{\partial N'}{\partial \Theta}$ at 7.0 km/s for the azimuths of

	75°		85°		90°		95°		105°		115°	
Pits	1°change	2°change	1°change	2°change	1°change	2°change	1°change	2°change	1°change	2°change	1°change	2°change
R1	0.2	0.4	0.2	0.4	0.2	0.4	0.2	0.4	0.2	0.4	0.2	0.4
R2	0.3	0.6	0.4	0.8	0.4	0.8	0.4	0.8	0.4	0.8	0.3	0.6
R3	0.7	1.4	0.8	1.6	0.8	1.6	0.8	1.6	0.8	1.6	0.7	1.4
R4	0.9	1.8	0.9	1.8	0.9	1.8	0.9	1.8	0.9	1.8	0.9	1.8
R5	1.2	2.4	1.3	2.6	1.3	2.6	1.3	2.6	1.3	2.6	1.3	2.6
Y1	0.1	0.2	0.1	0.2	0.0	0.1	0.0	0.0	0.0	0.0	0.0	0.0
Y2	0.1	0.2	0	0	0.0	0.0	0.0	0.0	0.1	0.2	0.2	0.4
Y3	0.2	0.4	0.1	0.2	0.0	0.0	0.1	0.2	0.2	0.4	0.3	0.6
Y4	0.2	0.4	0.1	0.2	0.0	0.0	0.1	0.2	0.2	0.4	0.4	0.8
Y5	0.2	0.4	0	0	0.1	0.2	0.2	0.4	0.4	0.8	0.6	1.2
	3	4	3	4	3	4	3	4	3	5	4	7

Table 3.6d Values of $\frac{\partial N'}{\partial \Theta}$ computed for Kaptagat pits at signal azimuths in the range 75° to 115° for phase velocity of 7.0 km/s.

The minimum number of instruments that can measure velocity/azimuth uniquely is three spread in two dimensions. From the discussions above, it is therefore concluded that for a sampling rate of 100s/s the theoretical resolution that can be achieved by Kaptagat array in the indicated directions is about 1° in azimuth and 0.1 km/s in velocity when all the ten seismometers are functioning. The resolution possible from the record of any event depends on the particular seismometers that produce usable records of that event.

3.5.3. Determination of centre of the correlator peak.

The accuracy to which azimuth or velocity can be determined depends partly upon the accuracy to which the centre of the correlator peak can be estimated (Birtill and Whiteway, 1965), that is on the sharpness of the velocity or azimuth response which in turn depends on the dimensions of the array in relation to the wavelength of the signal and the configuration of the array concerned.

From theoretical studies of responses of arrays of different configurations, it is concluded that for ideal response curves, the error in azimuth/velocity should not exceed $\frac{1}{20}$th of the response beam width at the half level points (Birtill and Whiteway, 1965). Velocity and azimuth responses for Kaptagat array for azimuth of 90° shown in fig. 3.14 and fig. 3.15 are calculated (for a frequency of 5 hz) from equation 3.15 when the array is tuned to receive a signal with phase velocity of 7.0 km/s. The widths w_v (for velocity) and w_θ (for azimuth) of the response curves at half level points are

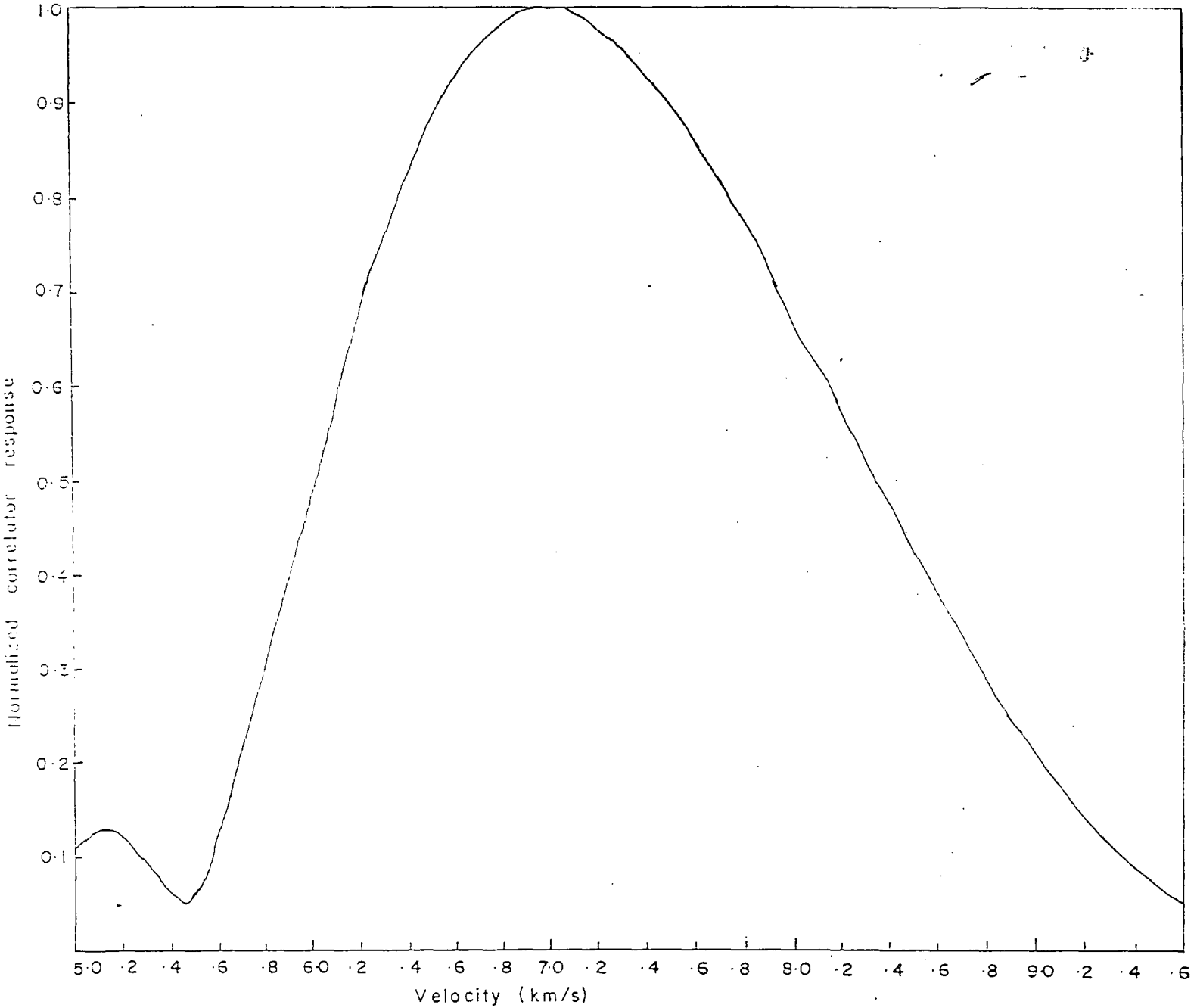

Fig. 3·14: Velocity correlator response at an azimuth of 90° when the array is tuned to receive a signal with velocity 7·0 km/s and azimuth 90°.

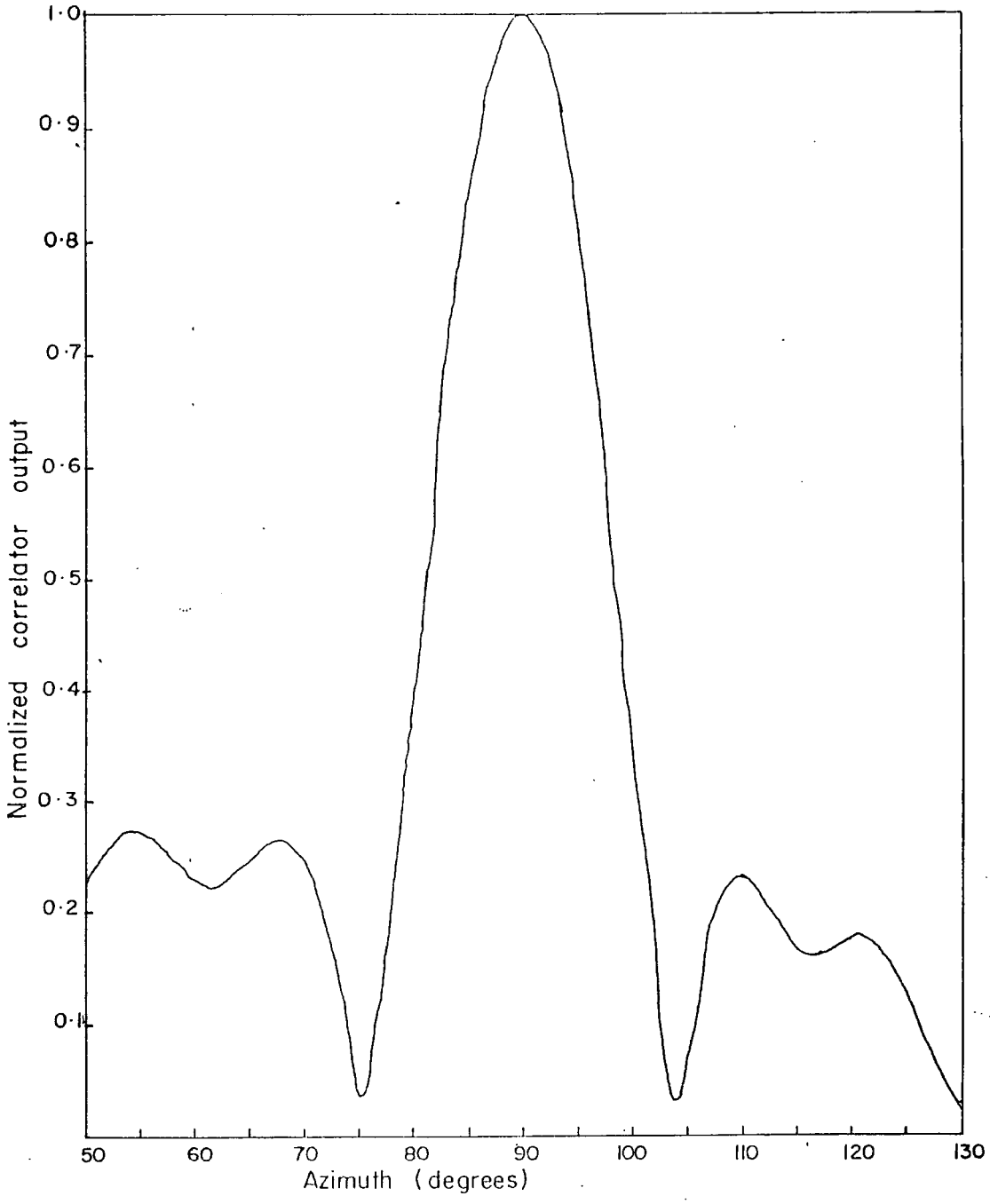

Fig. 3·15. Azimuth correlator response at the velocity of 7·0 km/s for kaptagat array when the array is tuned to receive a signal with velocity of 7·0 km/s from an azimuth of 90°.

2.3 km/s and 17° respectively. These figures show that for an ideal noisefree record, an error of not more than ± 0.1 km/s in velocity and ± 1° in azimuth is expected from Kaptagat array data at this azimuth. This corresponds to the width of velocity and azimuth responses at the 0.995 and 0.95 levels respectively.

3.5.4. Errors due to incorrect assumed velocity/azimuth.

Fig. 3.3 gives the correlator response as a function of signal azimuth and velocity when the array is tuned to receive a signal crossing Kaptagat array with velocity 7.0 km/s from an azimuth of 90°. Side lobes of amplitudes about half the maximum in the field are centred around (6.1 km/s, 55°) and (5.6 km/s, 122°); this can introduce erroneous results from velocity/azimuth filtering if search azimuth/velocity differ widely from the correct values.

From fig. 3.3, azimuth responses at a discrete number of velocities can be obtained. From such curves, the magnitude of the correlator response peak as a function of velocity (fig. 3.16) is determined; the numbers indicate the azimuths at which the peaks occur. It is assumed that the azimuth of the event is initially unknown. Search for event azimuth is then made at a number of assumed velocities. If the assumed velocity is the correct velocity, the measured azimuth will also be correct.

From fig. 3.16 it is observed that if the velocity used in the search for azimuth differs from the correct velocity by as much as ± 0.2 km/s, the correct azimuth is always measured.

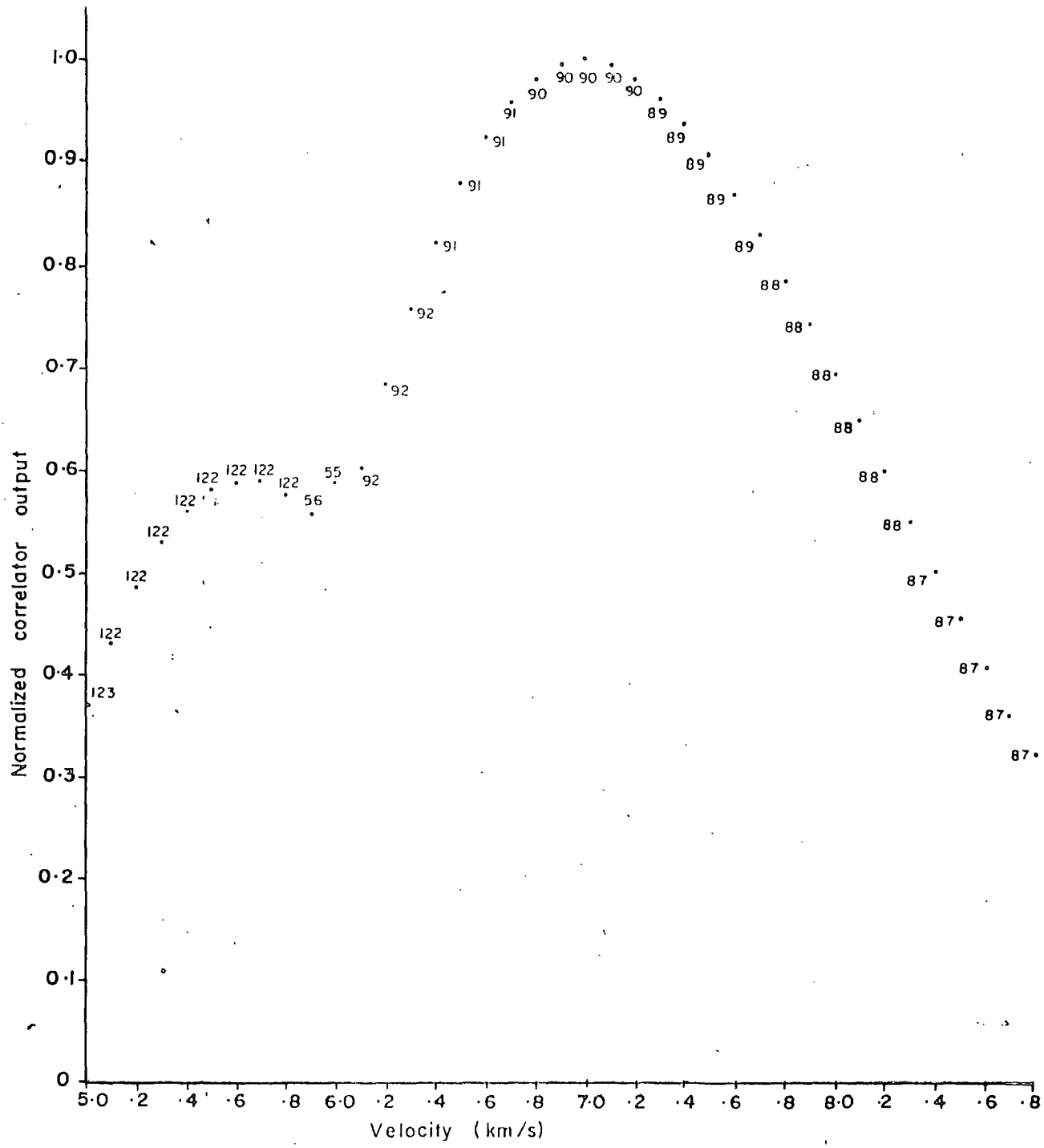

Fig. 3·16 : Plot of correlator peak azimuth response against search velocity. Numbers indicate azimuth (in degrees) of peak for the corresponding velocity

If the search velocity differs from the correct velocity by up to $\pm$ 0.5 km/s, the measured azimuth is within $\pm$ 1^{o} of the correct azimuth. And for an error of $\pm$ 0.9 km/s in velocity, the measured azimuth is in error by no more than $\pm$ 2^{o}. It is evident, therefore, that accurate knowledge of velocity is not critical to the determination of the azimuth to within 2^{o} of the correct azimuth at azimuths around 90^{o}.

Similar treatment applied to velocity response is illustrated in fig. 3.17. If the search azimuth is within $\pm$ 1^{o} of the correct azimuth, the measured velocity does not differ significantly from the correct velocity. But departures of $\pm$ 2^{o}, $\pm$ 3^{o}, $\pm$ 5^{o}, $\pm$ 7^{o} and $\pm$ 8^{o} from the correct azimuth result in errors of $\pm$ 0.1, $\pm$ 0.2, $\pm$ 0.3 and $\pm$ 0.4 km/s respectively in measured velocities. Hence for an ideal noise free record at this azimuth an accuracy of $\pm$ 2^{o} in azimuth is required if velocity is to be measured to within $\pm$ 0.1 km/s of the correct velocity.

3.6 Processing of Kaptagat data.

.6.1 Analogue to digital conversion of the array data.

Events used in the present study were selected from those used by Arnold (personal communication) in seismicity study of the region. The analogue field tapes were played back (unfiltered) with demodulation and flutter compensation at a speed of 15/16 inch per second which is ten times the recording speed. The analogue seismic channels and the time channel were displayed on the 16 channel jet pen recorder and/or on the oscilloscope for visual inspection. Some of the events played out were then selected for digitization and subsequent velocity filtering.

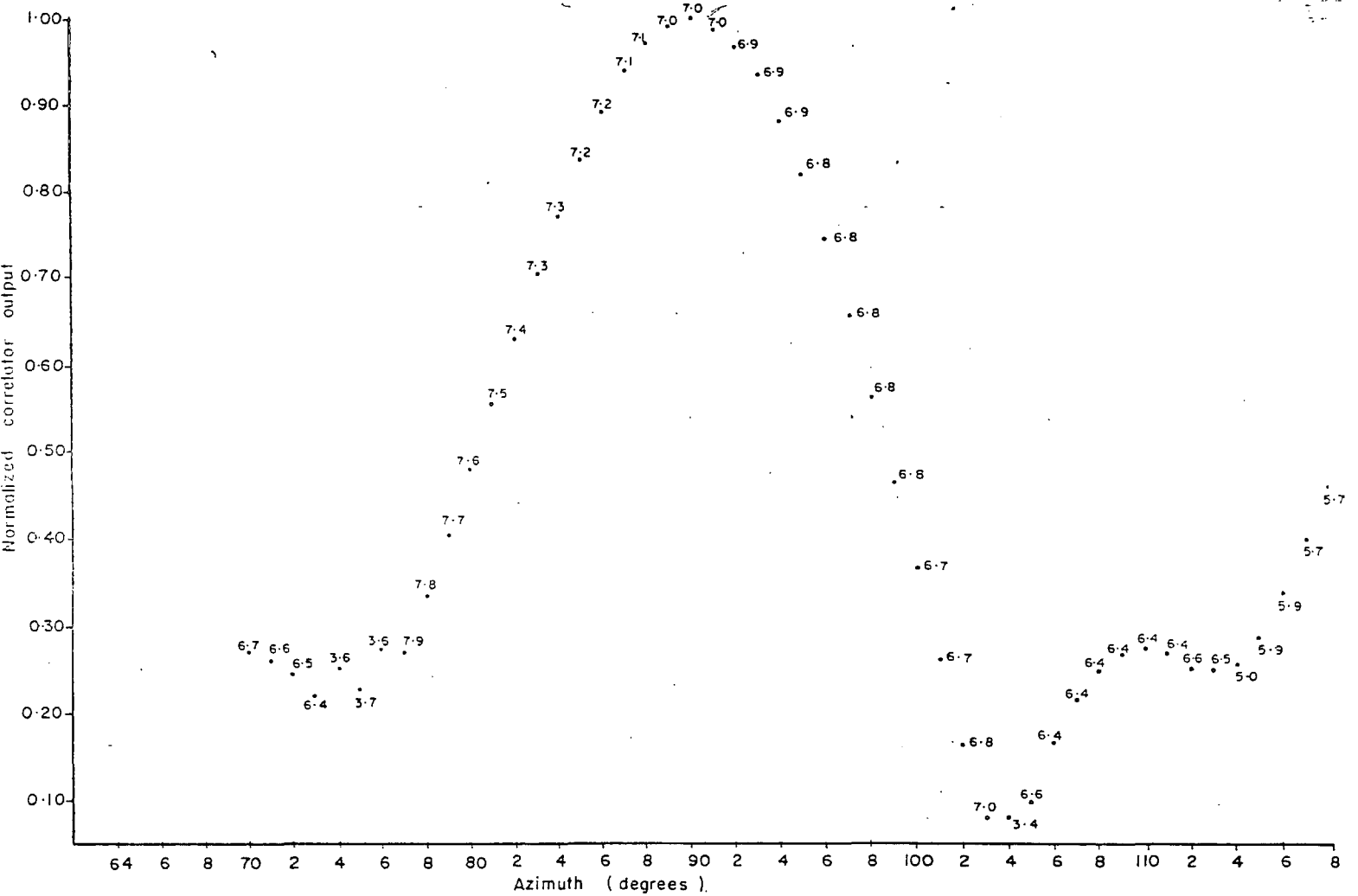

Fig. 3·17: Plot of correlator peak velocity response against search azimuth. Numbers indicate velocity (in km/s) of peak for the corresponding azimuth.

An event was selected if its seismograms had a high signal to noise ratio, showed little or no saturation and had a good number of operative seismometers evenly distributed between the two arms of the array. In the selection, preference was given to records with sharp first arrival P-wave onsets. Only events with P-surface (or X?) wave times of less than about 30s were selected.

Each selected analogue record was digitized on Mod 1 computer using the ADC. The resulting digital file was copied onto a disk file from which it was then transferred to a magnetic tape file for permanent storage. A record to be digitized was first played out onto the jet pens at paper speeds of 2.5 mm or 5.0 mm per recorded second for observation of first motion on each seismic trace. For some records it was found that the first motions of the outputs of the seismometers were not all in the same sense. The differences in the direction of the first motion could have arisen from the polarities of the connections from the seismometers to the recording system. Where necessary, the inverters were used to get the first motions the same way up in all the seismic traces. The direction of first motion is easier to see on records with sharp onsets. For records with emergent onsets, the direction of first motion could not be determined with certainty and the waveform of any well recorded and correlatable later arrival was used.

It was observed that the maximum number of traces that can be conveniently and confidently digitized on Modular one computer at 100s/s was eight if the length of each seismogram was about 30s. At 50s/s, comparable lengths of all ten seismograms and time channel could be conveniently digitized without difficulty or

error. Hence from the analogue record of each event, two digital files were created, one at 50s/s and the other at 100s/s. Experience during subsequent processing showed that a record digitized at 50s/s allowed greater flexibility (in the ranges of azimuth and velocity covered) than the same record sampled at 100s/s. On the other hand, the higher sampling rate provided better resolution in velocity/azimuth especially for velocities higher than about 6.5 km/s. The two digital files of the same event, therefore, complemented each other and were used in a way to reduce the problems created by limited space within the computer.

If the number of acceptable seismograms on an analogue array record was less than 8, a digital file of 8 channels was created. This digital file included all the unfiltered seismic traces and the time channel. Band pass filtered (0-10 hz) seismic channels (usually R1 and/or Y1) were recorded on any of the remaining unused channels.

If an event recorded exactly eight acceptable seismograms, four digital files were produced from it. Two 9 channel digital files of the 8 seismic traces (excluding the time channel) were made at sampling rates of 50s/s and 100s/s respectively. For the same analogue record, two digital files, each including three band pass filtered (0-10 hz) seismic traces (usually R1, R2 and Y1), these same three traces unfiltered, one other unfiltered seismic trace and the time channel, were created at sampling intervals of 0.02s and 0.01s respectively. The time channel was later used to provide time scales for the set of records with eight seismic traces. Onsets of later arrivals were identified more easily on the filtered traces.

The eight channel record digitized at 50s/s was found extremely useful in velocity filtering for low velocities (e.g. 3 to 4 km/s) because there would be sufficient storage space for the relatively smaller number of samples corresponding to the large system delay required for such low velocities. In the system, the space occupied by an eight channel data is half that occupied by a 16 channel data recorded at the same sampling interval. If the number of channels in an analogue record is more than 8 but less than 16, the corresponding digital record occupied the same space as a 16 channel record during velocity filter processing. Hence, in order to leave more space in the computer store for programs and time delays, 8 channel data were used even at a sampling rate of 50s/s unless the number of seismic channels exceeded 8.

If an event recorded more than eight acceptable seismic traces, the best eight were selected and four digital files made of them as described in the preceding paragraphs. Then, in addition, all the acceptable seismic channels together with a time channel were digitized at 50s/s.

In all cases, the digital file was copied from disk onto paper using the jet pen recorder. After inspection to ensure a satisfactory analogue to digital conversion, the record was copied onto tape. At the time of digitization, a note was made of the pit coordinates corresponding to each seismic channel.

3.6.2 Velocity filtering on Mod 1 computer.

Because of the stringent requirements which data for reliable velocity filtering must satisfy, only eleven sets of array data from local rift events to the immediate east of Kaptagat were

selected as adequate for such processing. Some more distant rift events to the north and south of Kaptagat and a few local events originating from the west in the Kavirondo gulf were also processed.

The procedure adopted for the velocity filtering of the present array data recorded for each event will be described with reference to a record shown in fig. 3.18a. At the time of recording, six seismometers were operating, four on the red arm and two on the yellow arm. Using onset time analysis, Arnold (personal communication) had determined the first arrival azimuth for this event as 99^{o}. This azimuth was taken as the provisional starting point. The record of this event digitized at 50s/s was first filtered (using an averaging time of 0.20s) to determine the first arrival azimuth and apparent velocity. For this purpose only a very short section of the record including the first arrival was processed as described below.

For the first stage in velocity filtering of the data from this event, nine values of azimuth starting from 80^{o} and increasing in steps of 5^{o} up to 120^{o} were used. At each value of azimuth, velocity was swept from 3.0 km/s to about 10.0 km/s in steps of 0.5 km/s. At the starting azimuth the TAP amplitudes for the first arrival were measured for all values of velocity. This procedure was repeated for all azimuths in the given range. In this way all the first arrival correlator amplitudes in the given velocity-azimuth space were measured. The velocity and azimuth corresponding to the measured maximum amplitude in velocity-azimuth plane estimated roughly the region within which the event first arrival velocity and azimuth are located. The search was then concentrated in smaller ranges of azimuth and velocity centred around the

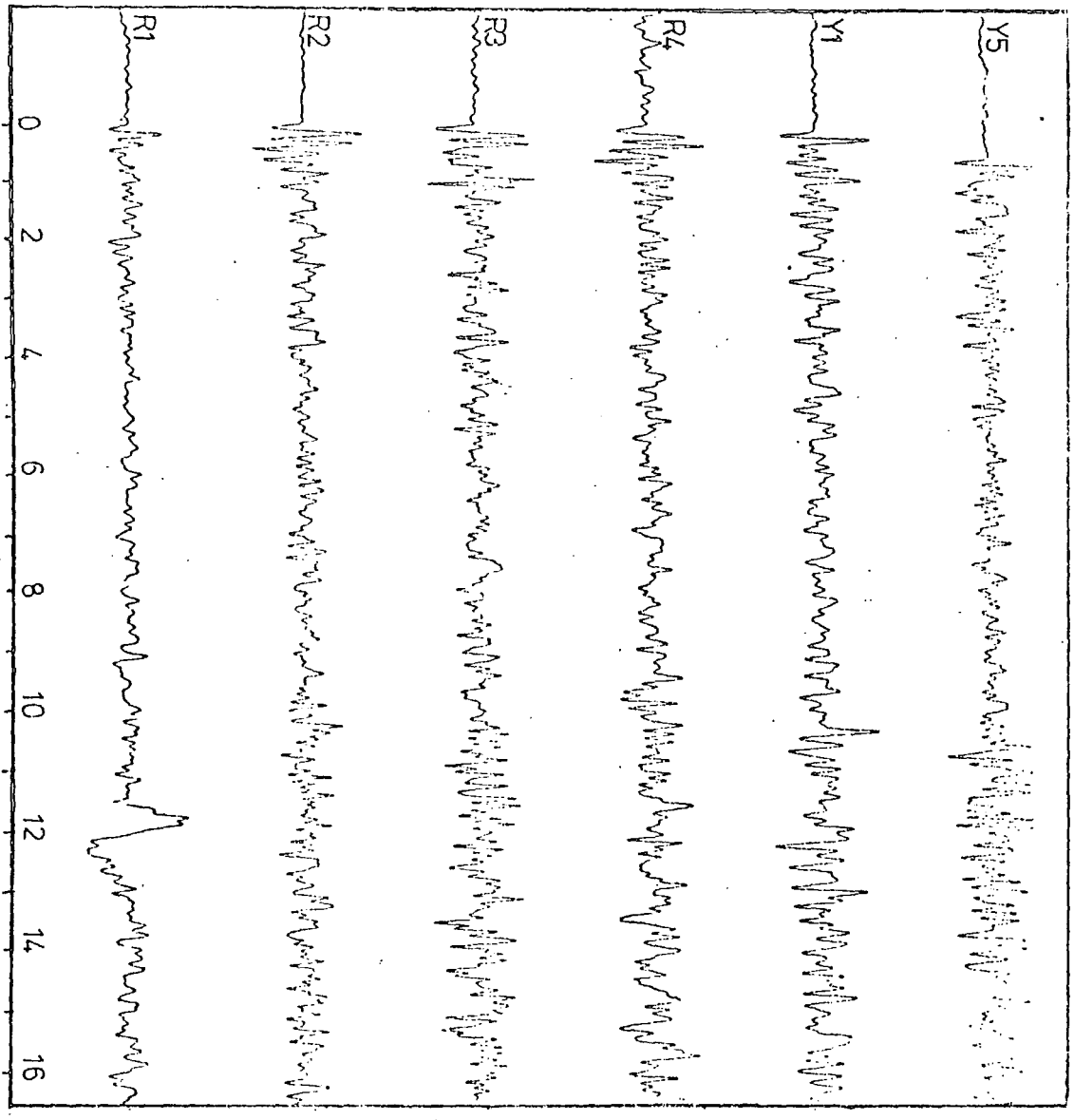

Fig. 3·18a A record of event number 7 including six seismic channels.

correlator amplitude maximum. A more refined maximum was obtained with increments of 0.2 km/s in velocity and 02^{o} in azimuth leading to better definition of the region where the first arrival velocity and azimuth should lie.

The region in and around the new resulting TAP maximum was further investigated with data recorded at 100s/s using increments of 0.1 km/s in velocity and 1^{o} in azimuth. This last stage ensured improved velocity and azimuth resolution. The final refined first arrival velocity and azimuth for this event were finally estimated as 7.6 km/s and 105^{o} respectively. Fig 3.18b is the correlator plot output for azimuth of 105^{o} and for velocity increasing from 5.2 km/s to 10.2 km/s in steps of 0.5 km/s. Other arrivals are indicated on this output and it is necessary to measure the parameters of all significant arrivals.

Close to the rift where lateral variations in structure may be expected, azimuths of first and later arrivals from the same event may not, in general, be expected to be the same. However, for the processing on Mod 1, because of the limitations already discussed, flexibility is severely limited and azimuths of all arrivals from the same event are assumed to be the same as the azimuth determined for the first arrival.

With the azimuth fixed at the value measured for the first arrival (105^{o} for this event), and using data recorded at 100s/s velocity was swept from 5.0 km/s to 12.0 km/s in steps of 0.1 km/s. For each arrival the measured amplitude at each velocity was normalized to unity with respect to the maximum amplitude measured for the first arrival and plotted against the corresponding velocity. Such velocity response curve for the first arrival is shown in fig. 3.19. The least squares parabola fitting the data of fig. 3.19 from 6.2 km/s to 8.5 km/s is

$$Y = -16.612 + (4.594 \pm 0.597)V - (0.301 \pm 0.041)V^{2}$$

where Y is the normalized correlator response and V is the measured apparent velocity. Estimates are standard error. The maximum response occurs when the gradient of this curve is zero, that when V=7.63 km/s which confirms earlier estimate. Inspection of this curve indicates that a smaller amplitude arrival with a velocity of about 5.8 km/s appears to be recorded at about the same time as the 7.6 km/s arrival. This subsidiary peak is more clearly indicated in the filter output from subsequent processing discussed in section 3.6.3.

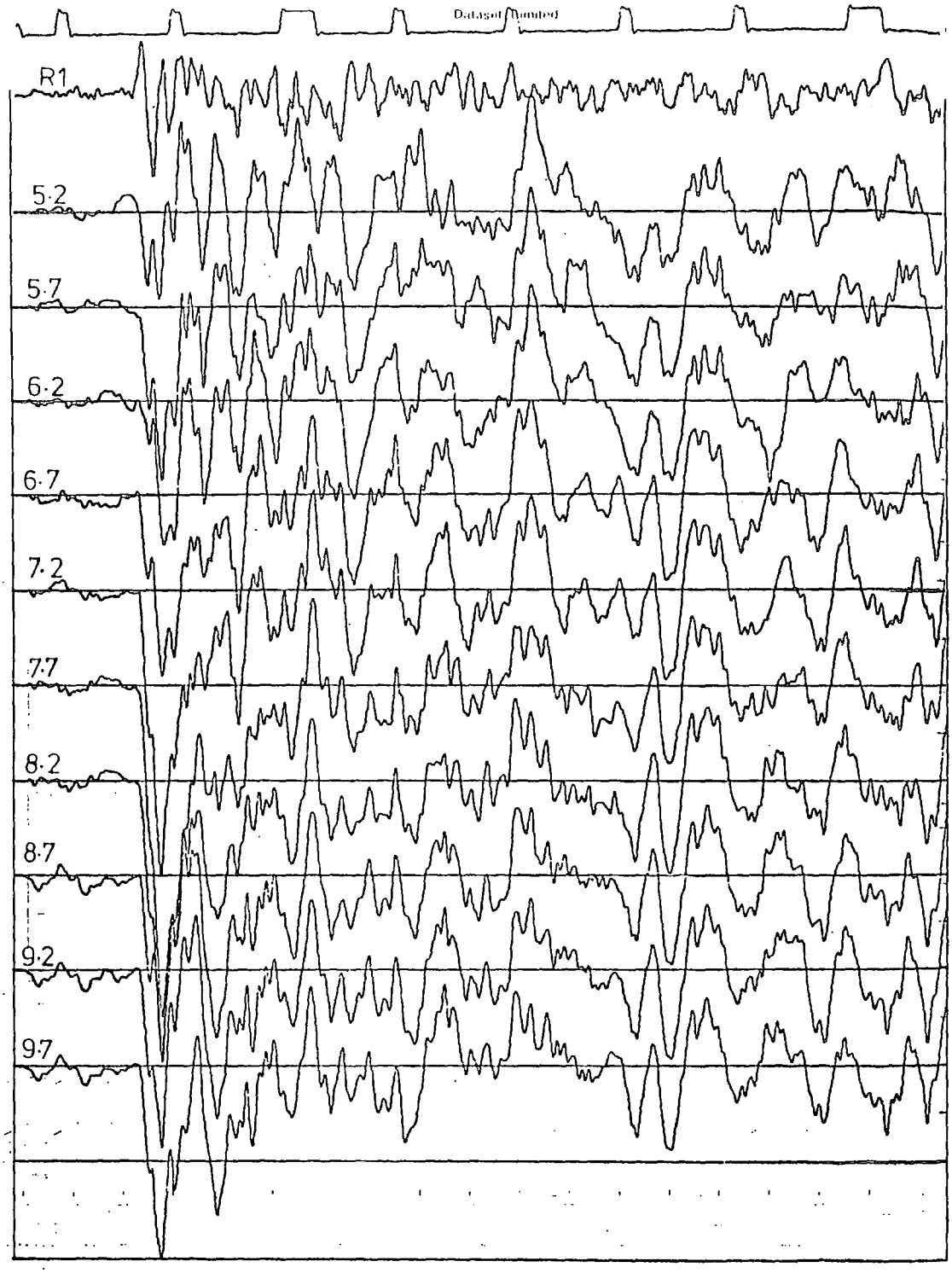

Fig 3·18b Correlator output from unfiltered record of event number 7 for an azimuth of 105° and a range of phase velocities. Numbers in the figure represent phase velocities in km/s.

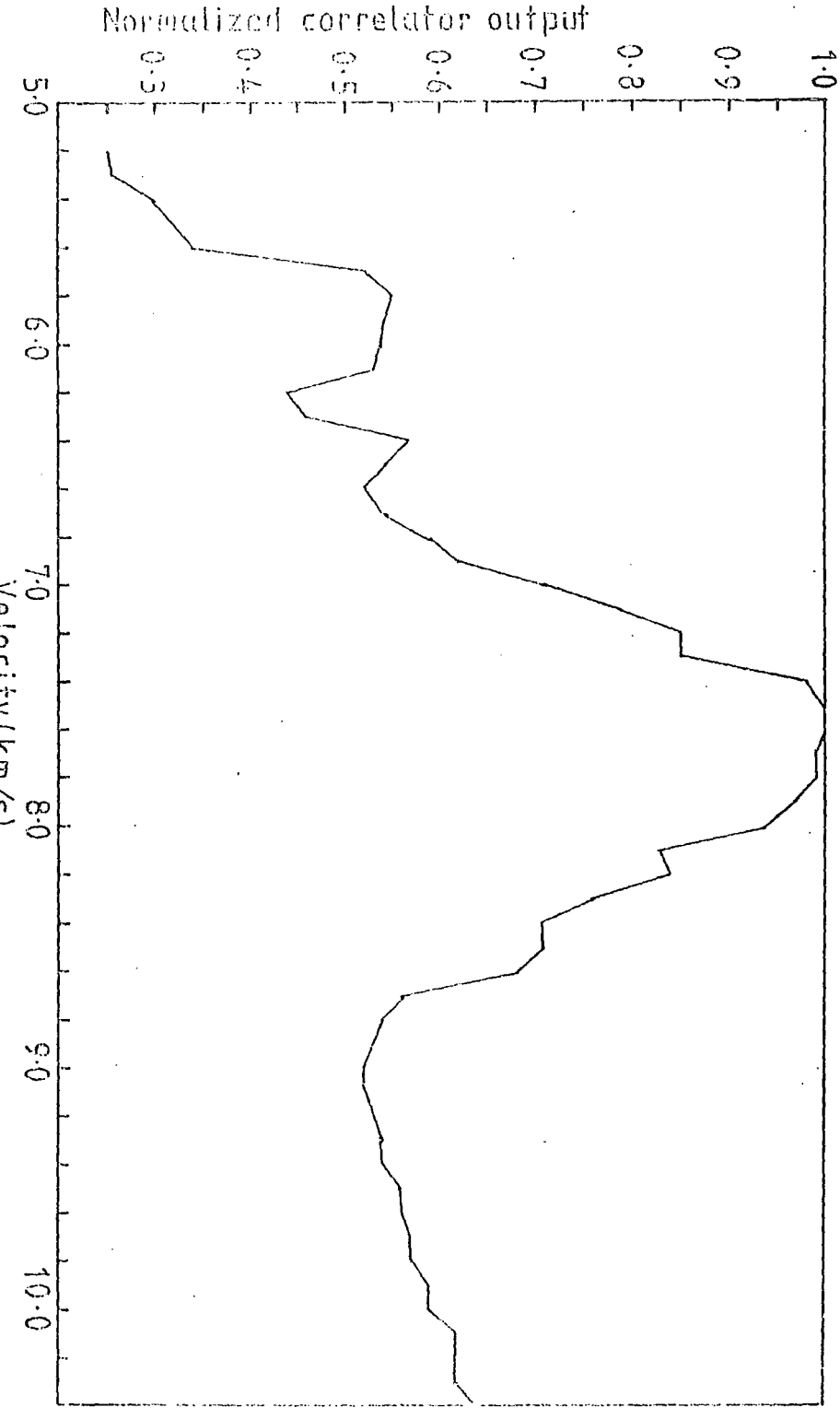

Fig 3.19: Velocity response for event number 7 at 105° azimuth.

The velocity of each later arrival was determined by plotting its normalized correlator amplitude against velocity. The value of velocity corresponding to the maximum of this curve was taken as the best estimate for the apparent velocity of that arrival. In this way the apparent velocities of all prominent later arrivals from the given event were measured. To objectively determine each peak and the corresponding velocity, it was necessary, in some cases, to fit a parabola to the measured values of correlation against phase velocity.

For velocities less than about 5.0 km/s, difficulty was encountered in filtering data digitized at 100s/s for reasons already discussed. The severity of this problem depended on the signal azimuth and the coordinates of the pits of the operating seismometers. To get over this problem, data of the same event digitized at 50s/s was filtered with the azimuth fixed at the value already determined above for the first arrival. A velocity sweep from about 3.0 km/s to about 6.0 km/s in steps of 0.1 km/s was then easily implemented. This range of velocity was expected to provide information on onset times of S and mode converted phases. Although 3.0 km/s may be high for some S phases, it was not possible on Mod 1 to go below that velocity even for data recorded at 50s/s. However, subsequent processing on a bigger machine (section 3.6.3) handled velocities well below 3.0 km/s without difficulty.

The procedure described for the event mentioned above was applied in filtering the digital records of all the other events used in this study. Rift events to the north and south of Kaptagat have longer periods than the local events to the immediate

east and west. The period of the first arrivals of these north and south rift events was about 0.30s. Smoothing time window of 0.30s was, therefore, used for processing data from these events.

The resulting data are shown in fig. 3.20. The correlator amplitude of each later arrival at the velocity determined for it was normalized to unity with respect to the corresponding amplitude of the first arrival at the measured first arrival velocity. The normalized correlator amplitude was plotted as a vertical line at the corresponding arrival time (relative to the first arrival). The number below each line is the estimated apparent velocity of the arrival at that time.

6.3 Filtering on IBM 360/370 computer.

The assumption that later arrivals come in from the same azimuth as first arrival of the same event may not be justified for all events because of possible lateral variations in the structure within the rift zone. Such variations will result in the event rays being deflected in the horizontal as well as in the vertical directions. Signal components from the same event may, therefore, arrive Kaptagat from azimuths different from one another and from the first arrival azimuth. There was, therefore, the need to determine not just the velocity but also the azimuth of each later arrival. Secondly, more than one arrival may be recorded at the station at about the same time. In effect, more than one peak may exist in the velocity-azimuth space at any given time point along the seismic record. For example, unwanted large amplitude low velocity signal generated Rayleigh waves can partially

Fig. 3.20a : The data (velocity and azimuth) for closein immediate eastern rift events assuming first and later arrival azimuths are the same. Number below each vertical line is apparent velocity in km/s. Relative onset times are marked in seconds.

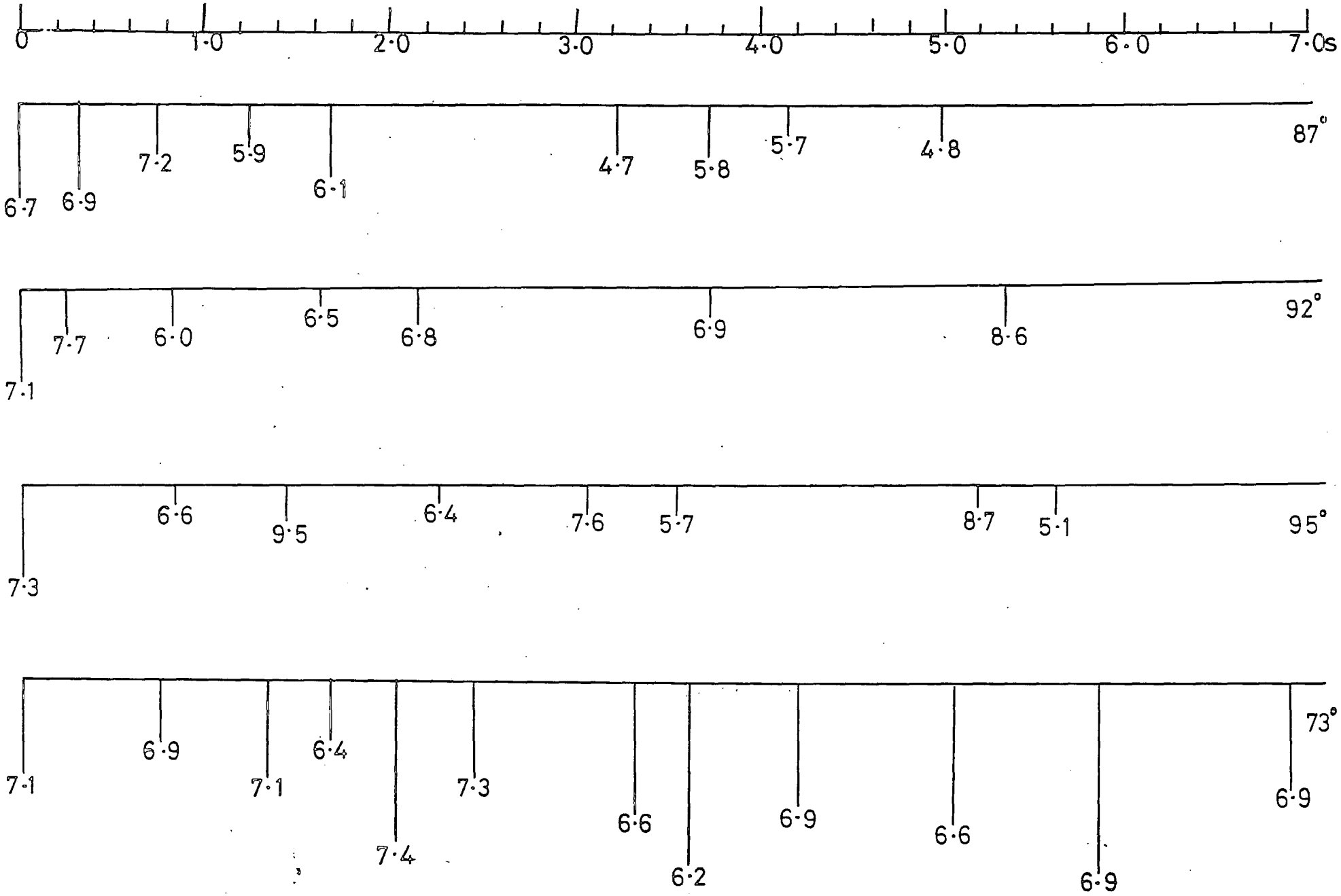
0
1·0
2·0
3·0
4·0
5·0
6·0
7·0s
6·7
6·9
7·2
5·9
6·1
4·7
5·8
5·7
4·8
87°
7·1
7·7
6·0
6·5
6·8
6·9
8·6
92°
7·3
6·6
9·5
6·4
7·6
5·7
8·7
5·1
95°
7·1
6·9
7·1
6·4
7·4
7·3
6·6
6·2
6·9
6·6
6·9
6·9
73°

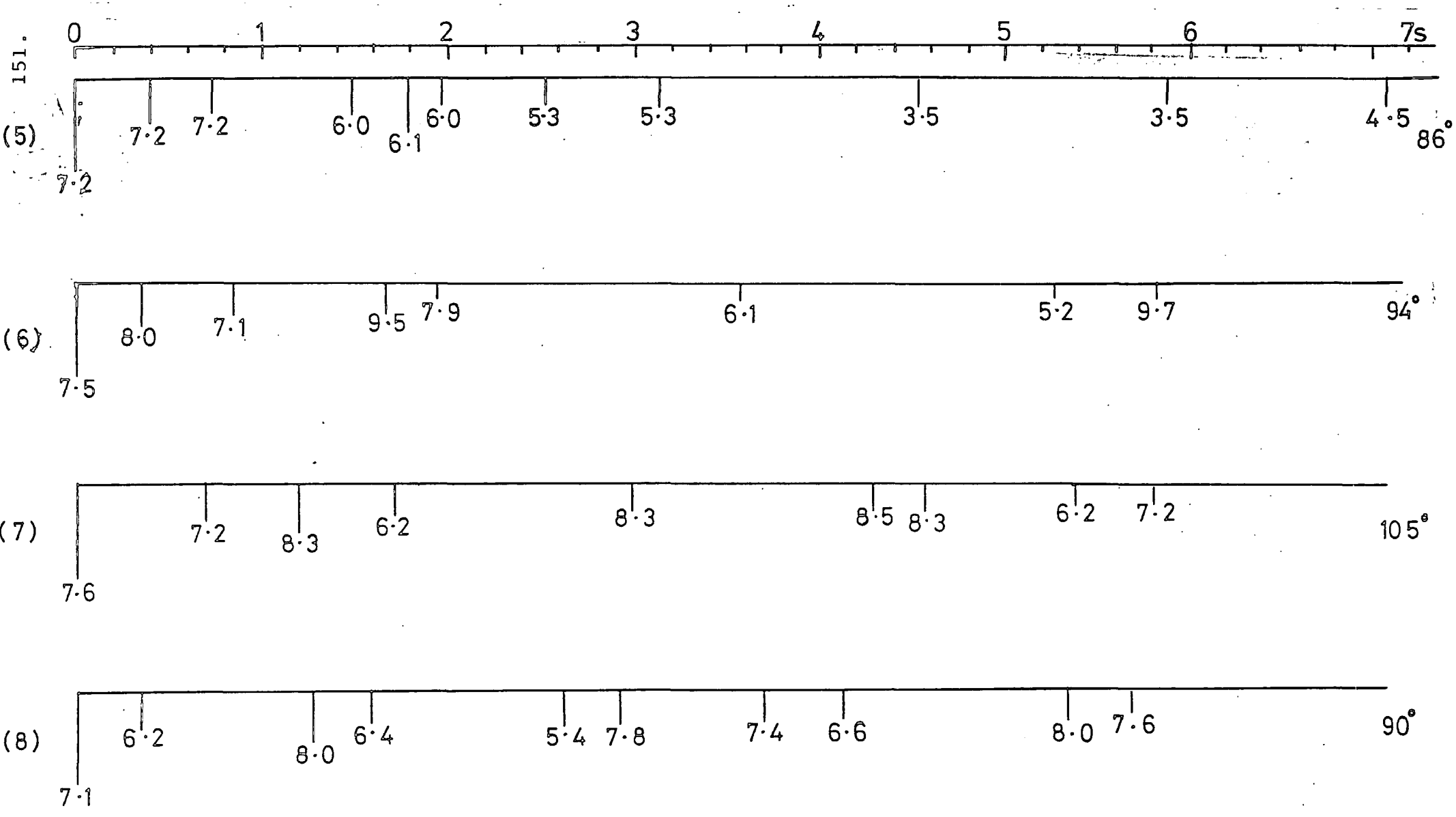
0
1
2
3
4
5
6
7s
(5)
7·2
7·2
7·2
6·0
6·1
6·0
5·3
5·3
3·5
3·5
4·5
86°
(6)
7·5
8·0
7·1
9·5
7·9
6·1
5·2
9·7
94°
(7)
7·6
7·2
8·3
6·2
8·3
8·5
8·3
6·2
7·2
105°
(8)
7·1
6·2
8·0
6·4
5·4
7·8
7·4
6·6
8·0
7·6
90°

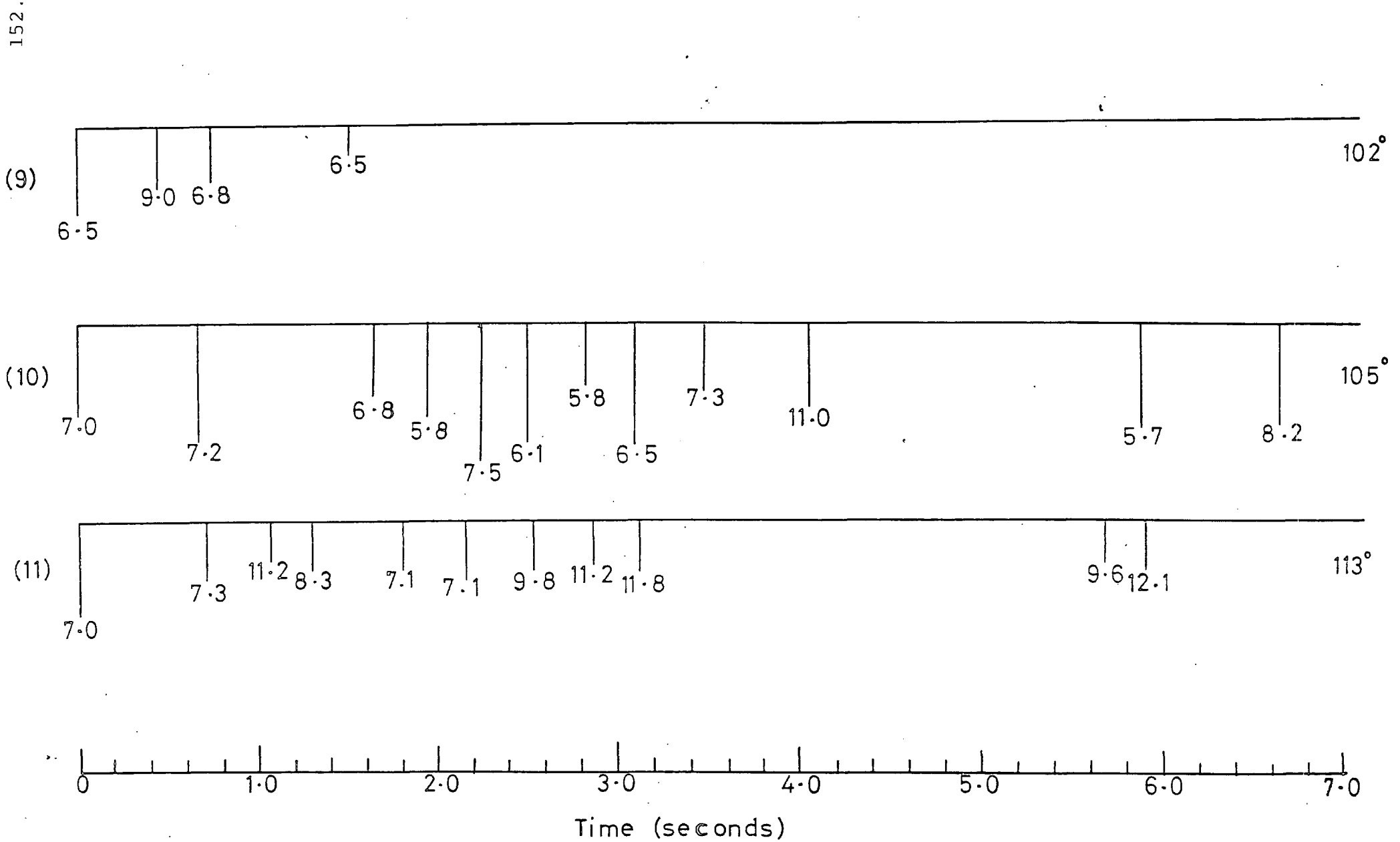

Fig·3·20a: The data for closein immediate eastern rift events assuming first and later arrival azimuths are the same. Numbers below each vertical line are apparent velocities in km/s·

Fig. 3.20b: The velocity and azimuth data for distant rift events to the north and south of Kaptagat. For a given event, the azimuths of the first and later arrivals are assumed to be the same. The number below each vertical line is the corresponding phase velocity in km/s.

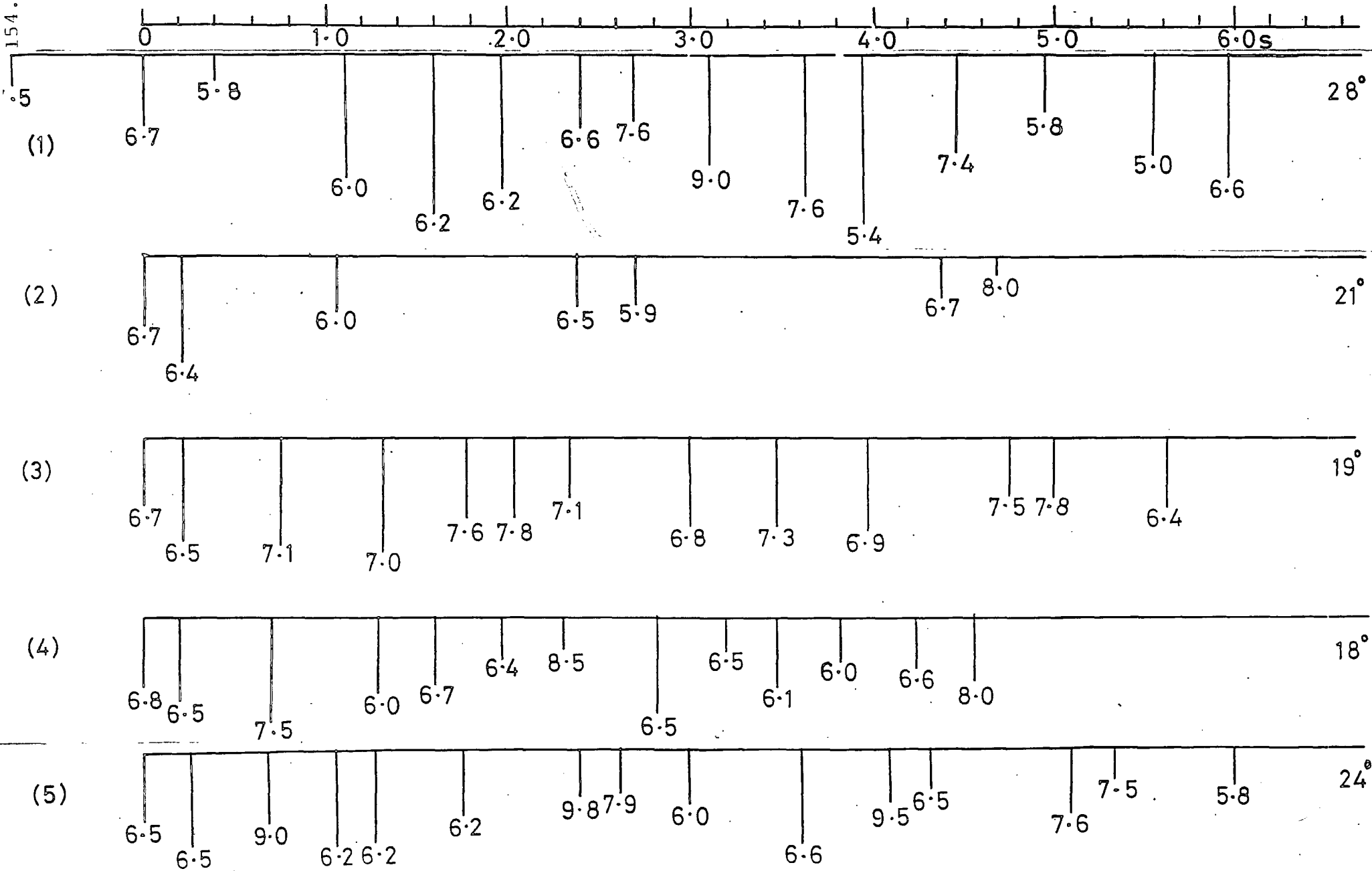
0
1·0
2·0
3·0
4·0
5·0
6·0s
(1)
·5
5·8
6·7
6·0
6·2
6·2
6·6
7·6
9·0
7·6
5·4
7·4
5·8
5·0
6·6
28°
(2)
6·7
6·4
6·0
6·5
5·9
6·7
8·0
21°
(3)
6·7
6·5
7·1
7·0
7·6
7·8
7·1
6·8
7·3
6·9
7·5
7·8
6·4
19°
(4)
6·8
6·5
7·5
6·0
6·7
6·4
8·5
6·5
6·1
6·0
6·6
8·0
18°
(5)
6·5
6·5
9·0
6·2
6·2
6·2
9·8
7·9
6·0
6·6
9·5
6·5
7·6
7·5
5·8
24°

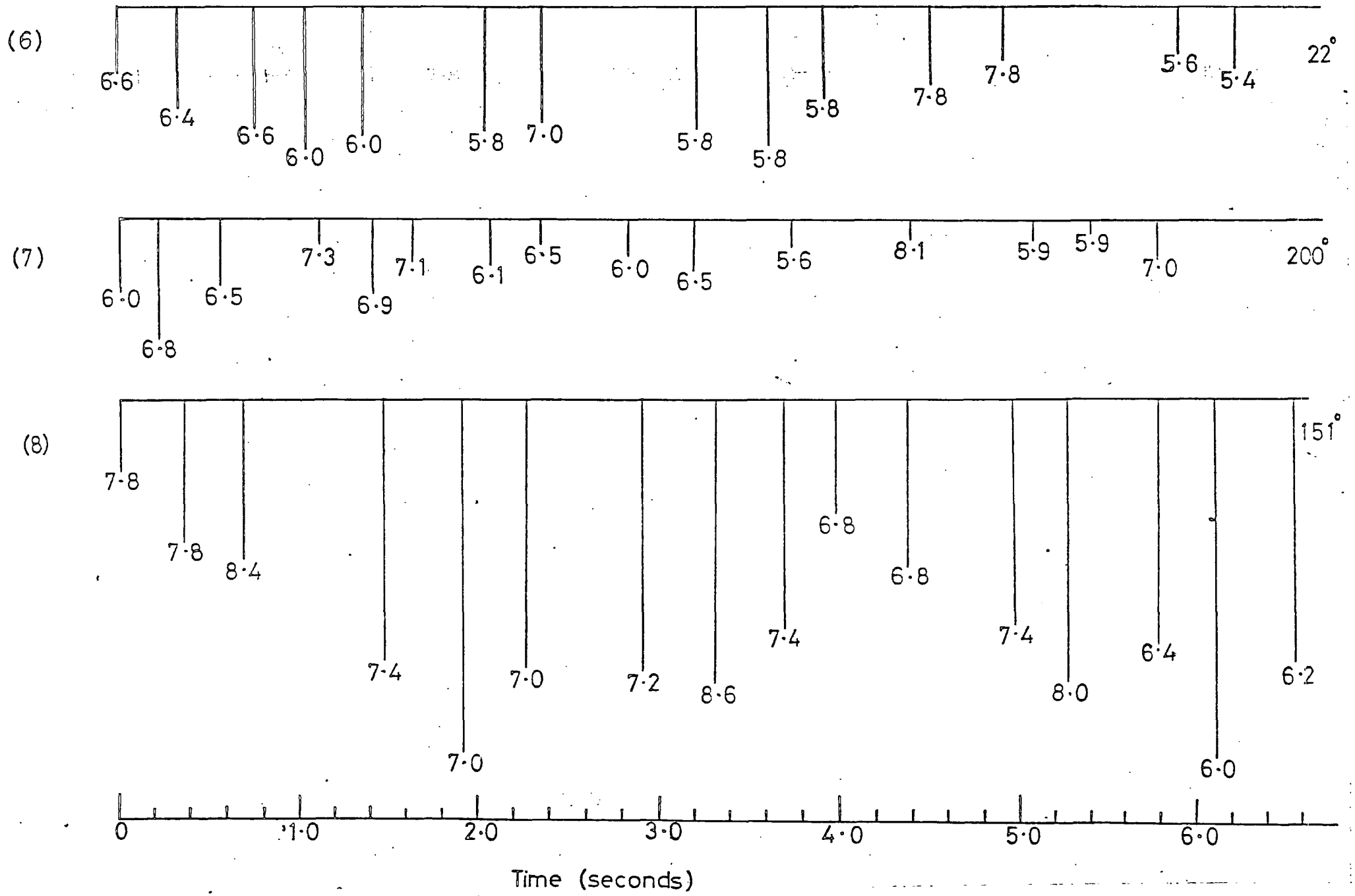
(6)
6·6
6·4
6·6
6·0
6·0
5·8
7·0
5·8
5·8
5·8
7·8
7·8
5·6
5·4
22°
(7)
6·0
6·8
6·5
7·3
6·9
7·1
6·1
6·5
6·0
6·5
5·6
8·1
5·9
5·9
7·0
200°
(8)
7·8
7·8
8·4
7·4
7·0
7·0
7·2
8·6
7·4
6·8
6·8
7·4
8·0
6·4
6·0
6·2
151°
0
1·0
2·0
3·0
4·0
5·0
6·0
Time (seconds)

overlap and mask the desired but low amplitude crustal arrivals. In a situation such as this, it becomes necessary to determine all the significant correlator peaks in the field and then select those relevant to the physical problem in hand.

The principles of operation of the program VFIL (appendix C) written to perform this task on Durham University's IBM 360/370 computer has been described in section 3.4.2. The data guided through this program were all digitized at 100s/s, and were exactly the same as those processed on Mod 1 computer using the earlier program. For reasons discussed in section 3.6.2, time window of 0.20s was used for local events to the immediate east and immediate west of the station while window length of 0.30s was used for filtering rift events to the north and south of Kaptagat. This program was designed to confirm and complement the results obtained from Mod 1.

The implementation of the program will be illustrated with the processing of data from event 11 digitized at 100 samples per second (fig. 3.21). From velocity filtering on Mod 1 computer, the first arrival velocity and azimuth of this same data were determined as 7.0 km/s and 113^{o} respectively.

The new program was now used to repeat the measurement of the first arrival parameters. Initially filtering covered ranges of 3.0 km/s to 12.0 km/s in velocity and 60^{o} to 160^{o} in azimuth and started at the 50th sample on the original digital file on tape. Increments in velocity, azimuth and time were 0.5 km/s, 5^{o} and 0.05s respectively. With this coarse processing the maximum correlator output in the velocity-azimuth space was located at

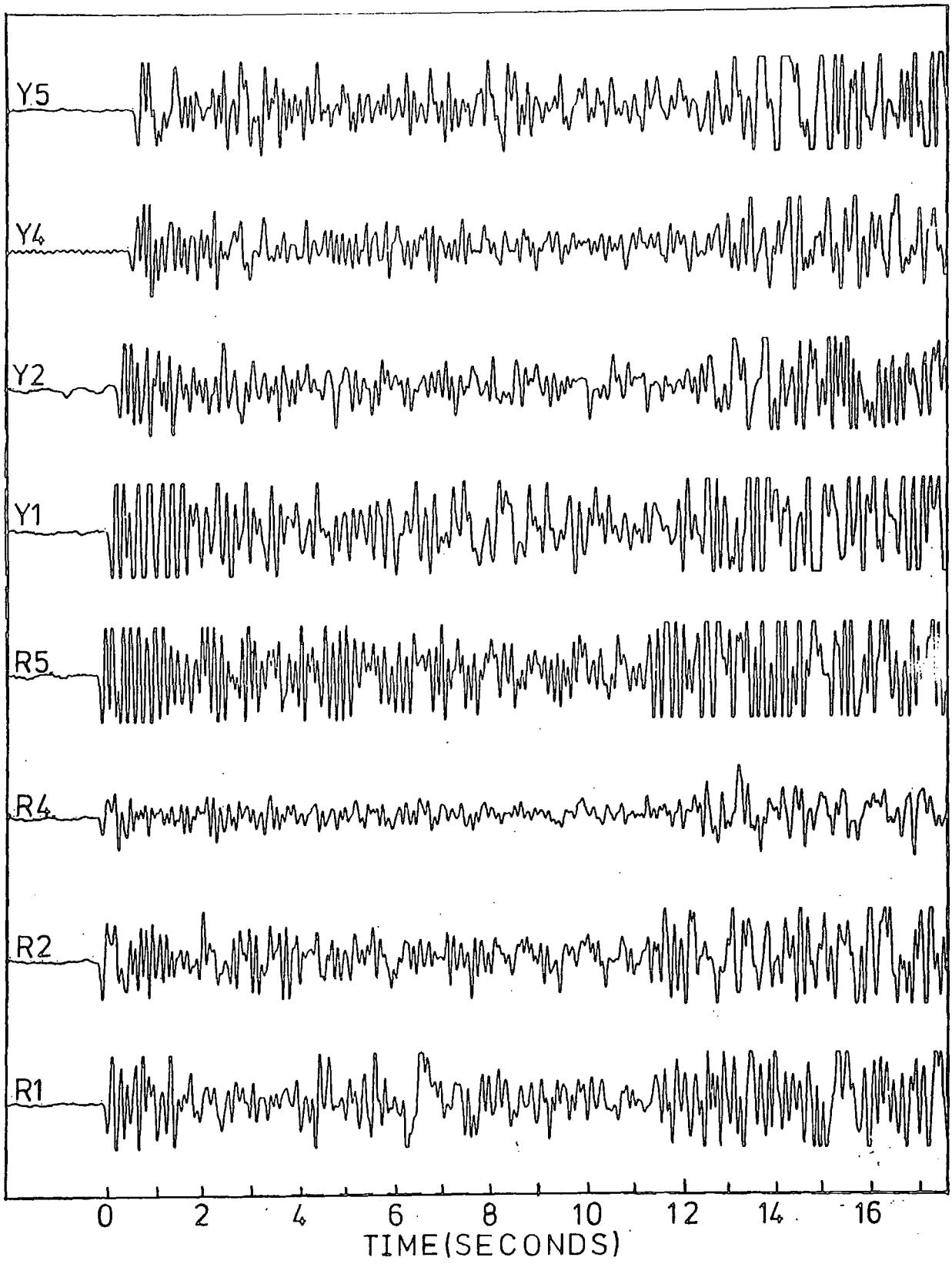

Fig. 3.21 : A record of a closein local rift event from the immediate east of Kaptagat.

7.0 km/s, 115^{o} and at 2.05s from the beginning of the original file.

To determine the parameters of this first arrival more precisely, velocity was increased from 4.0 km/s to 10.0 km/s in steps of 0.1km/s while azimuth was increased from 85^{o} to 145^{o} in steps of 1^{o}. Correlator outputs were computed at intervals of 0.01s in the time range from 1.90s to 2.40s from start of the original digital file. The major peak of the first arrival occurred at 2.06s as shown in table 3.7 which includes two other peaks. The parameters of the three peaks in decreasing order of peak magnitude are (6.8 km/s, 113^{o}), (6.6 km/s, 125^{o}) and (8.3 km/s, 137^{o}).

With the time pointer at 2.06s (the time for the first arrival peak), correlator outputs in the velocity-azimuth space were calculated for azimuths increasing from 85^{o} to 145^{o} in steps of 1^{o} and velocity increasing from 4.0 to 10.0 km/s in steps of 0.1 km/s. These outputs were then normalized to unity with respect to the maximum output in the field. The main part of this normalized correlator output values are contoured as shown in fig. 3.22 in which three peaks designated A, B and C have normalized outputs of 1.00, 0.73 and 0.66, respectively at their centres. To the nearest 0.1 km/s in velocity and 1^{o} in azimuth, the measured parameters of the centres of A, B and C are (6.9 km/s, 114^{o}), (6.6 km/s, 125^{o}) and (8.2 km/s, 136^{o}) respectively. These values should be compared with the printout values of (6.8 km/s, 113^{o}), (6.6 km/s, 125^{o}) and (8.3 km/s, 137^{o}) on table 3.7. The difference of 0.1 km/s in velocity and 1^{o} in azimuth between the parameters of the centres of A and C and the printout on table 3.7 may have arisen from the element of subjective judgement involved in smoothing by hand in the course of producing fig. 3.22. Values of the parameters for the three peaks are, therefore, in agreement with the contents of table 3.7.

Table 3.7 : Correlator print output from program VFIL showing first arrival parameters for event 11. Velocity was incremented from 4.0 to 10.0 km/s in steps of 0.1 km/s while azimuth was incremented from 85^{o} to 145^{o} in steps of 1^{o}. Three peaks were printed every 0.01s.

$RUN VFIL.C**GHOST 1=A6152 2=ST 3=PLOT
Execution begins 19:15:00

EVENTN= 6152
TAPEN=136
FILEN= 60

IP= 190SAMPS
IST=P= 1 SAMPS
INT. WINDOW = .20 SECONDS
NPEAK = 5

	START	TERMINAL	INCREMENT
VELOCITY (KM/S)	4.00	10.00	0.10
AZIMUTH (DEGS)	85.00	145.00	1.00

SP	VELOCITY	AZIMUTH	CORREL

PDS: PLOT DESCRIPTION GENERATION BEGINS.

190

	6.60	125.00	22138.51
	6.30	127.00	22005.34
	6.80	119.00	17573.36
-16.09	6.60	125.00	22138.51

191

	6.60	125.00	23454.81
	6.80	126.00	23131.29
	6.80	118.00	18093.16
-17.09	6.60	125.00	23454.81

192

	6.70	124.00	24525.27
	6.60	117.00	19196.04
	7.10	134.00	14679.61
-14.09	6.70	124.00	24525.27

193

	6.70	123.00	25711.69
	7.10	134.00	14883.41
	7.40	126.00	14305.88
-19.09	6.70	123.00	25711.69

194

	6.70	123.00	26384.07
	6.90	116.00	19129.86
	7.10	134.00	15167.61
-17.09	6.70	123.00	26384.07

195

	6.90	122.00	26827.02
	6.90	114.00	19769.10
	7.10	134.00	15286.28
-18.09	6.90	122.00	26827.02

196

	6.90	122.00	27316.05
	7.10	134.00	15260.52
	7.40	125.00	14922.25
-18.09	6.90	122.00	27316.05

197

	6.70	121.00	27859.97
	7.10	134.00	15008.28
	7.40	125.00	14882.67
-15.09	6.80	121.00	27859.97

198

	6.90	119.00	28938.23
	7.50	123.00	23534.10
	7.40	125.00	14456.13
-12.09	6.80	119.00	28938.23

199

	6.90	119.00	30272.25
	7.40	125.00	13566.75
	7.10	134.00	13036.40
-8.09	6.90	119.00	30272.25

200				
		6.90	113.00	31798.45
		8.20	137.00	14609.70
		8.20	140.00	13515.41
	-1.09	6.90	113.00	31798.45
201				
		6.90	117.00	33366.27
		6.70	127.00	17405.23
		8.20	137.00	16855.69
	6.91	6.90	117.00	33366.27
202				
		6.90	116.00	35318.94
		6.70	127.00	20504.62
		8.20	137.00	19126.99
	12.91	6.90	116.00	35318.94
203				
		6.90	116.00	36810.47
		6.60	126.00	23060.88
		8.20	137.00	21213.95
	16.91	6.90	116.00	36810.47
204				
		6.90	116.00	37187.11
		6.80	114.00	36558.24
		6.60	125.00	25295.89
	21.91	6.90	116.00	37187.11
205				
		6.80	114.00	37234.32
		6.60	125.00	26910.49
		8.20	137.00	24139.12
	19.91	6.80	114.00	37234.32
206				
		6.80	113.00	37356.55
		6.60	125.00	27171.03
		8.30	137.00	25159.52
	6.91	6.80	113.00	37356.55
207				
		6.90	113.00	36989.73
		6.70	125.00	26864.40
		8.30	137.00	25570.04
	-7.09	6.90	113.00	36989.73
208				
		6.80	112.00	35613.12
		6.70	125.00	25545.23
		8.30	137.00	23492.05
	-34.09	6.80	112.00	35613.12
209				
		6.90	114.00	33723.34
		8.30	137.00	25326.88
		6.60	123.00	23130.35
	-70.09	6.90	114.00	33723.34
210				
		6.90	114.00	32568.92
		6.60	110.00	22743.68
		8.30	108.00	25664.90
	-122.09	6.90	114.00	32568.92
211				
		6.90	113.00	31054.04
		8.30	136.00	25005.50
		6.30	110.00	24194.09
	-134.09	6.90	113.00	31054.04
212				
		6.90	113.00	29312.30
		8.30	136.00	24162.49
		6.30	110.00	22459.67
	-254.09	6.90	113.00	29312.30

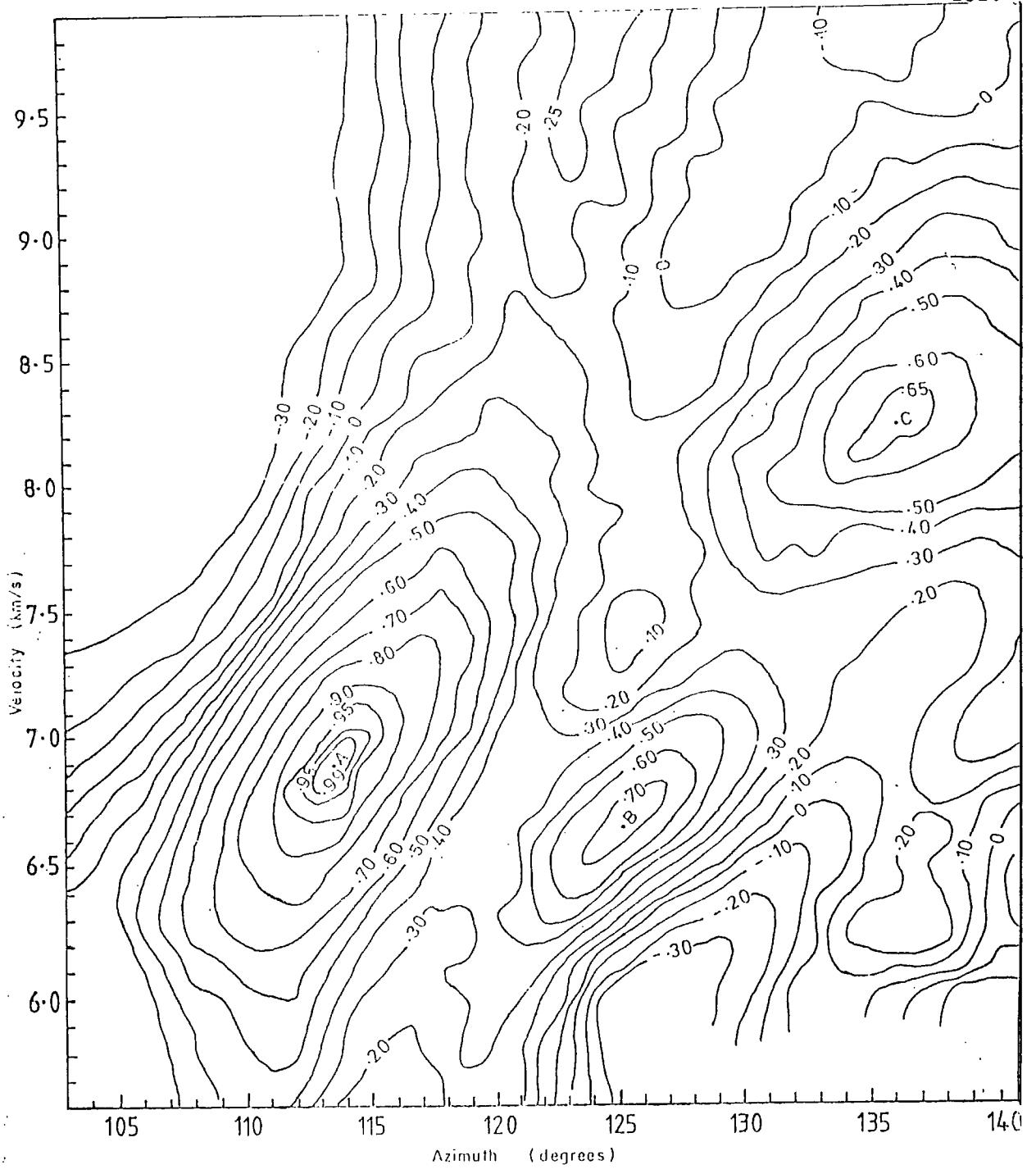

Fig. 3·22: Contours showing the three peaks indicated in table 3·7

It is evident, from this observation, that the peaks shown on plot and print outputs of the program are not spurious peaks. Furthermore, results obtained here (6.9, 114^{o}) compare very well with the values (7.0, 113^{o}) obtained from processing on Mod 1.

The accuracy achieved in the determination of velocity and azimuth depends on the accuracy with which the centre of the correlator peak can be measured. For ideal curves, the error in the determination of the centre of the correlator peak should not exceed one-twentieth of the beam width at the half level points of the response curves (Birtill and Whiteway, 1965). The width of the half level contour for peak A in fig. 3.22 for velocity and azimuth corresponding to its centre is 10.5^{o} in azimuth and 1.45 km/s in velocity. This indicates that the centre of the peak A, and hence, the corresponding signal parameters can be measured to a precision of about 0.07 km/s in velocity and 0.50^{o} in azimuth. These errors should be suitably combined with errors from other sources discussed in section 3.5 in estimating the overall errors in velocity and azimuth measurements.

The normalized peak outputs and the corresponding peaking velocities and azimuths close to and including the centre of peak A is shown in table 3.8. It is evident from this table that an error of 1^{o} in azimuth may introduce an error of 0.1 km/s in measured velocity. An error of 2^{o} in azimuth introduces an error of 0.2 km/s in measured velocity. These observations are illustrated in fig. 3.23.

Plot output in the vicinity of the first arrival is given in fig. 3.24a for velocity and azimuth ranges of 5.0 to 10.0 km/s and 100^{o} to 130^{o} respectively. Azimuth and velocity increments

Table 3.8 Normalized peak correlator outputs and the corresponding first arrival velocities measured at azimuths close to the azimuth of the first arrival for event 11.

Azimuth (degrees)	Normalized correlator peak output	Velocity of peak (km/s)
110	0.829	6.6
111	0.893	6.6
112	0.973	6.8
113	1.000	6.8
114	0.999	6.9
115	0.977	7.0
116	0.926	7.1
117	0.883	7.2
118	0.799	7.3

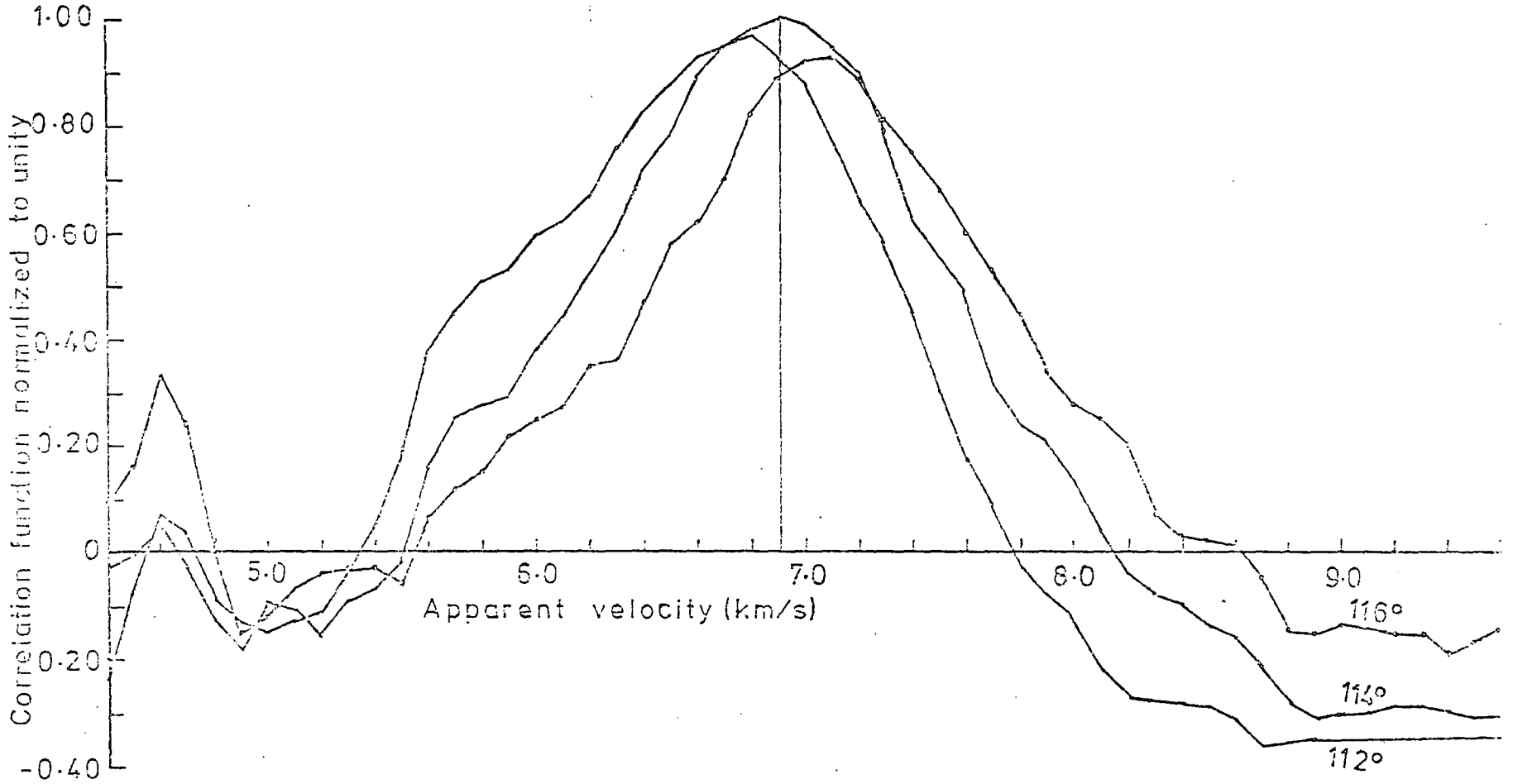

Fig 3·23 First arrival velocity responses for event 7 at azimuths of 112°, 114° and 116°.

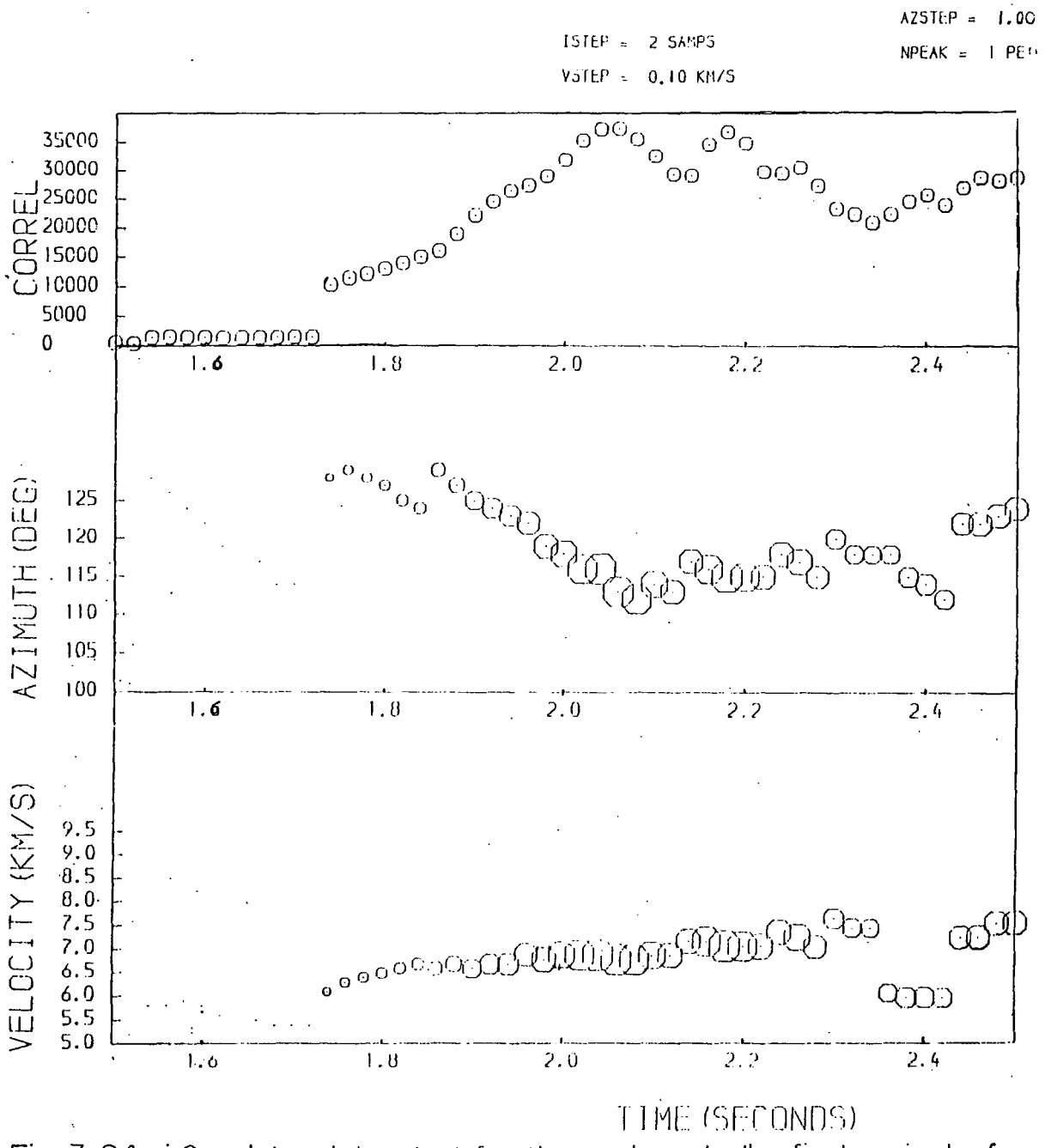

Fig. 3.24a : Correlator plot output for times close to the first arrival of event II. Velocity and azimuth increments are 0·1 km/s and 1° respectively. One peak plotted every 0·02s. Size of character used in the plot is chosen proportional to the corresponding computed correlation amplitude.

were 1^{o} and 0.1 km/s. One peak was plotted at 0.02s intervals. Output for about the same length of time is shown in fig. 3.24b where two peaks were plotted at intervals of 0.01s but with azimuth increasing from 80^{o} to 140^{o} in steps of 2^{o} and velocity from 5.0 km/s to 10.0 km/s in steps of 0.2 km/s.

Velocity filtering was used to estimate the onset of the S waves corresponding to and having the same propagation path as the first arrival. Such a phase will have an azimuth not significantly different from the first arrival azimuth. For this search, velocities in the range 2.0 km/s to 10.0 km/s with increments of 0.2 km/s and azimuths in the range 110^{o} to 120^{o} with increments of 2^{o} were used. One peak was plotted at time intervals of 0.05s from 0.50s to 16.00s (fig. 3.25). Measured velocities (about 2.8 km/s) and azimuths (about 114^{o}) for arrivals between about 13.50s and 14.00s suggest that these arrivals may be S or surface waves.

For a closer examination of these arrivals, the filter was applied to part of the record between 12.50s and 16.50s. Ranges in velocity and azimuth were 2.0 km/s to 10.0 km/s and 108^{o} to 118^{o} respectively. Azimuth and velocity increments were 2^{o} and 0.2 km/s and only one peak was plotted at intervals of two samples (fig. 3.26). A single seismic channel was plotted at the top of this figure. A section of the corresponding printout is shown in table 3.9.

From fig. 3.26 and table 3.9 it is clear that these low velocity arrivals are recorded continously between 13.78s and 13.98s along the record. The peak correlator output is located at 13.90s or 11.85s from the peak of the first arrival; the final measured velocity and azimuth were 2.6 km/s and 112^{o} respectively. The correlator output of this arrival relative to the first arrival is

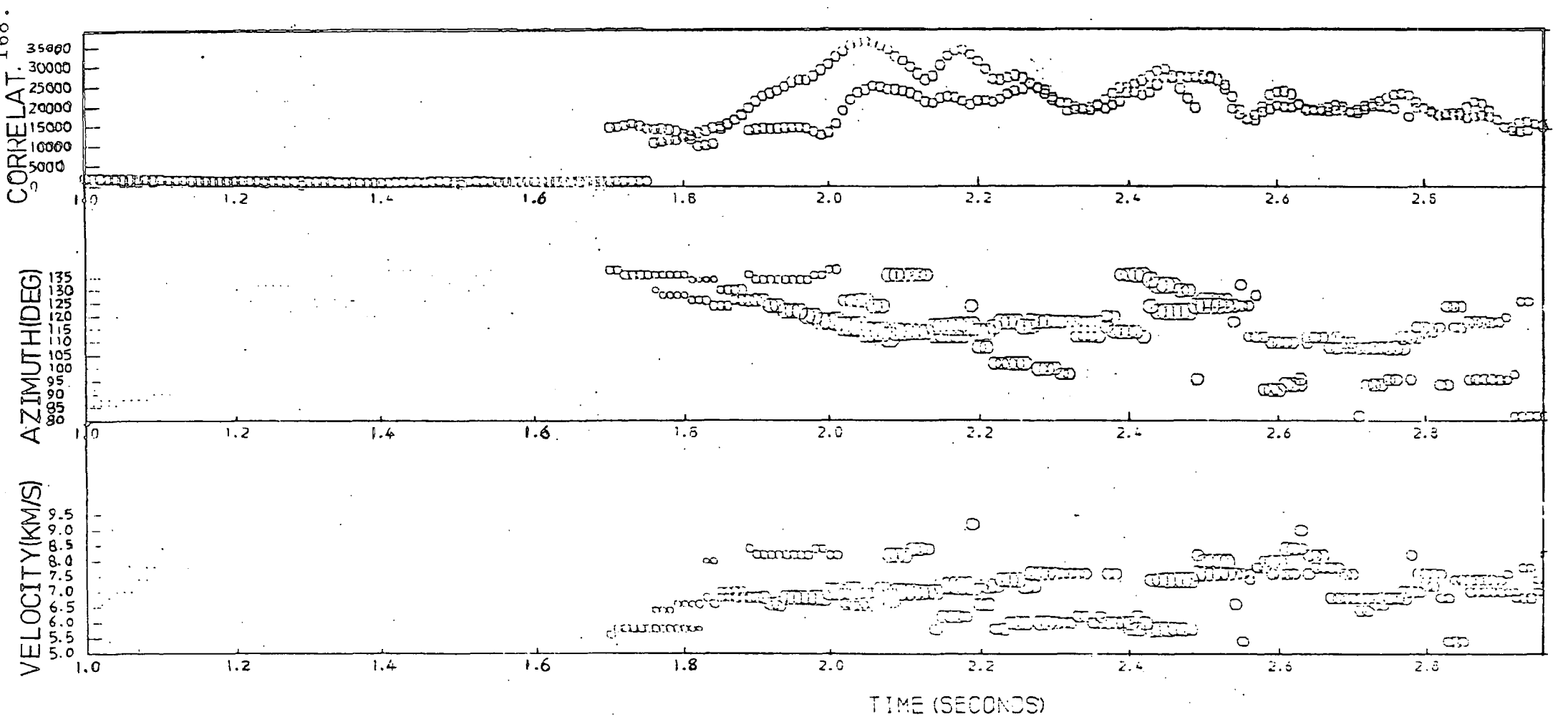

Fig. 3.24b: Correlator plot output for times close to the first arrival of event II. Two peaks are plotted every 0·01s. Azimuth coverage is from 80° to 140° in steps of 2°. Velocity range is from 5.0km/s to 10·0km/s in steps of 0·2 km/s. Size of plotting symbols chosen proportional to the corresponding computed correlation function.

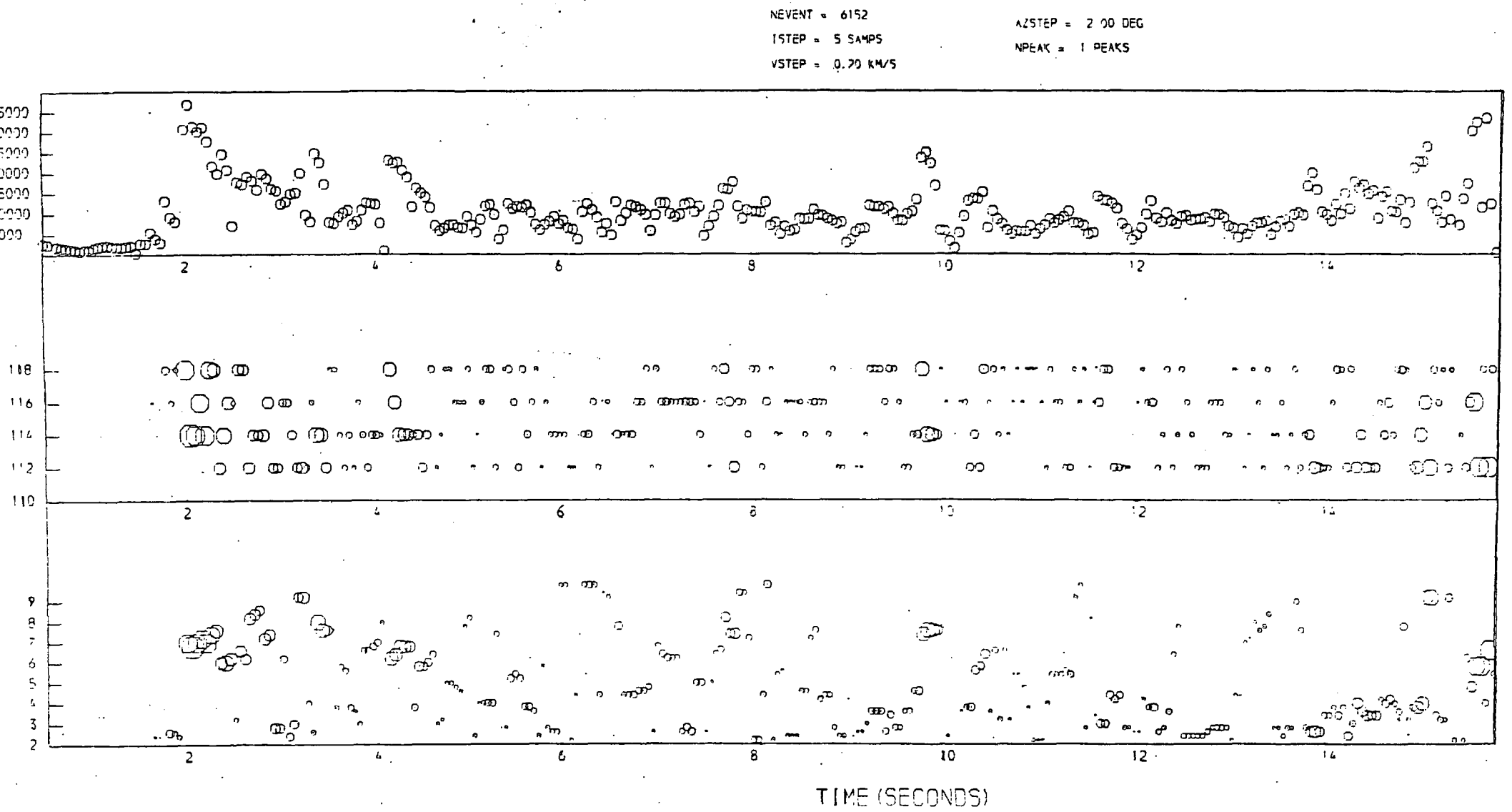

Fig. 3.25: Correlator plot output for event II. Outputs at intervals of 0·05s. Azimuth search range is 110° to 120° in steps of 2° and velocity varied from 2·0km/s to 10·0 km/s in steps of 0·2 km/s. Size of plotting symbols chosen proportional to the output TAP amplitude.

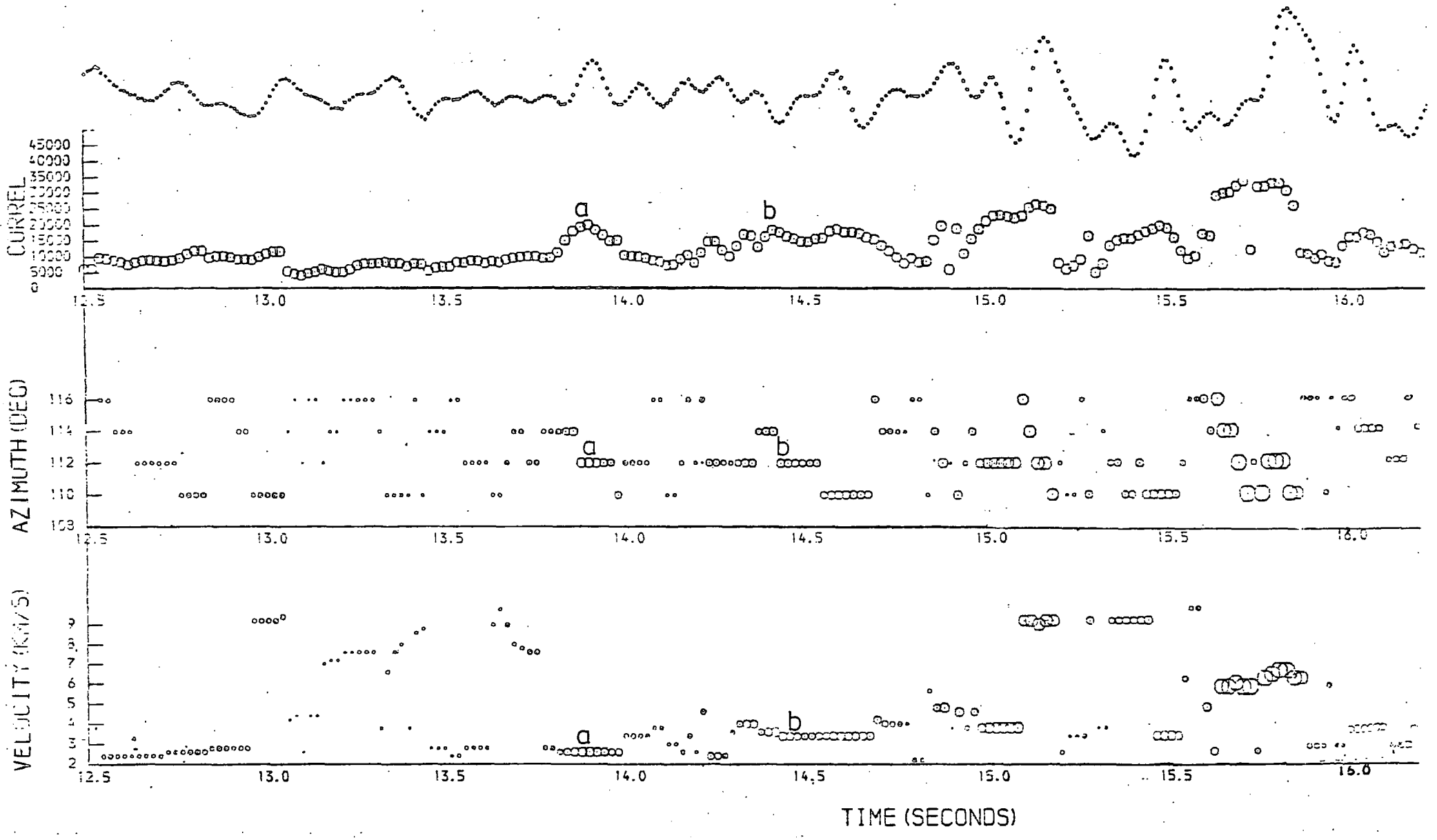

Fig.3.26. Correlator plot output for event II beyond 12·50s. Outputs at intervals of 0·02s. Search ranges in velocity and azimuth are 2·0 to 10·0 km/s and 108° to 118° respectively. Increments in velocity and azimuth are 0·2 km/s and 2° respectively.

Table 3.9 : Correlator print output for event 11 in the time range containing the X arrivals. Two peaks printed at 0.02s intervals. Velocity incremented from 2.0 to 10.0 km/s in steps of 0.2 km/s. Azimuth incremented from 108^{o} to 118^{o} in steps of 2^{o}.

```
$RUN VFIL.C+*GHOST 1=A5152 5=28P 9=-PLOT
Execution begins   21:47:55

          EVENTN= 5152
          TAPEN=136
          FILEN= 60

            IP= 1250SAMPS
            ISTEP=    2 SAMPS
            INT. WINDOW = .20  SECONDS
            NPEAK =   2

                                        START    TERMINAL   INCREMENT

            VELOCITY (KM/S)              2.00       10.00       0.20
            AZIMUTH (DEGS)             108.00      118.00       2.00

              SP     VELOCITY  AZIMUTH      CORREL

PDS: PLOT DESCRIPTION GENERATION BEGINS.

1372
                       7.80    114.00      9941.01
                       8.40    114.00      9493.22
          -144.09       7.80    114.00      9941.01
1374
                       7.60    112.00     10140.67
                       2.80    114.00      7444.54
          -131.09       2.00    108.00     10741.46
1376
                       7.60    112.00     10139.55
                       2.80    114.00      8530.76
           -93.09       2.00    108.00     14397.67
1378
                       2.80    114.00      9513.94
                       7.60    112.00      9343.37
           -45.09       2.00    108.00     13863.18
1380
                       2.80    114.00      9654.92
                       7.60    112.00      7564.79
            40.91       2.00    108.00     13631.91
1382
                       2.60    114.00     11303.69
                       7.60    112.00      6263.12
           188.91       2.00    108.00     15356.98
1384
                       2.60    114.00     15146.07
                       4.60    114.00      4823.50
           365.91       2.60    114.00     15146.07
1386
                       2.60    114.00     17971.13
                       3.80    114.00      4250.68
           501.91       2.60    114.00     17971.13
1388
                       2.60    112.00     19276.00
                       4.20    110.00      6932.08
           517.91       2.60    112.00     19276.00
1390
                       2.60    112.00     19946.10
                       4.20    110.00      5399.68
           438.91       2.60    112.00     19946.10
1392
                       2.60    112.00     18402.49
                       3.30    112.00      4797.95
           339.91       2.60    112.00     18402.49
```

1394				
		2.60	112.00	16793.03
		3.80	112.00	2887.94
	213.91	2.60	112.00	16798.03
1396				
		2.60	112.00	14921.82
		5.60	110.00	172.39
	-26.09	2.00	112.00	14921.82
1398				
		2.60	110.00	15185.52
		3.40	112.00	9141.21
	-326.09	2.60	110.00	15185.52
1400				
		3.40	112.00	10460.72
		3.00	110.00	6091.61
	-504.09	2.60	108.00	16811.44
1402				
		3.40	112.00	10167.52
		3.00	110.00	6785.37
	-282.09	2.60	108.00	19723.52
1404				
		3.40	112.00	9960.33
		3.00	110.00	7175.75
	239.91	2.60	108.00	20915.10
1406				
		3.40	112.00	9461.07
		3.00	110.00	7242.60
	634.91	2.60	108.00	19419.95
1408				
		3.80	116.00	8724.21
		3.40	112.00	8526.07
	536.91	2.60	108.00	17166.76
1410				
		3.80	116.00	8358.63
		3.40	112.00	7987.86
	38.91	2.60	108.00	14607.50
1412				
		3.00	110.00	7164.53
		3.40	112.00	6952.95
	-249.09	2.60	108.00	13020.29
1414				
		3.00	110.00	7424.14
		3.60	112.00	6086.47
	-229.09	3.80	118.00	14550.81
1416				
		2.60	112.00	9250.25
		6.80	114.00	6915.65
	-67.09	3.80	118.00	16778.13
1418				
		3.40	116.00	10492.02
		2.60	112.00	9283.42
	-170.09	3.80	118.00	14559.93
1420				
		2.60	112.00	7961.34
		6.80	114.00	7447.34
	-580.09	3.20	118.00	10870.06
1422				
		4.60	116.00	11293.97
		2.40	112.00	11260.26
	-934.09	3.20	118.00	14401.09

1424				
		2.40	112.00	14713.59
		6.80	114.00	9929.32
	-855.09	2.40	112.00	14713.59
1426				
		2.40	112.00	14743.62
		6.80	114.00	10865.64
	-294.09	2.40	112.00	14743.62
1428				
		2.40	112.00	11910.73
		6.80	114.00	9672.72
	344.91	8.60	118.00	15065.47
1430				
		3.60	112.00	9942.04
		4.00	112.00	9335.75
	771.91	8.60	118.00	16752.31
1432				
		4.00	112.00	13369.34
		3.60	112.00	12926.55
	837.91	9.00	118.00	17706.96
1434				
		4.00	112.00	16978.51
		4.20	116.00	15218.23
	636.91	9.00	118.00	17435.16
1436				
		4.00	112.00	16603.50
		4.20	116.00	14033.11
	316.91	4.00	112.00	16608.50
1438				
		3.60	114.00	13066.05
		4.00	112.00	12644.27
	-13.09	9.20	118.00	13441.21
1440				
		3.60	114.00	16264.23
		2.60	110.00	12434.01
	-236.09	3.60	114.00	16264.23
1442				
		3.60	114.00	13317.19
		2.60	110.00	14139.24
	-243.09	3.60	114.00	13317.18
1444				
		3.40	112.00	17627.27
		5.40	116.00	12855.34
	-20.09	3.40	112.00	17627.27
1446				
		3.40	112.00	16444.54
		5.60	116.00	14177.35
	313.91	3.40	112.00	16444.54
1448				
		3.40	112.00	15686.29
		5.60	116.00	15032.94
	546.91	3.40	112.00	15686.29
1450				
		3.40	112.00	14830.89
		5.60	116.00	14573.41
	539.91	3.40	112.00	14830.89
1452				
		3.40	112.00	14577.23
		5.60	116.00	13976.76
	303.91	9.80	106.00	15414.67

0.54. From about 14.32s to 14.74s, arrivals with velocities in the range 3.4-3.6 km/s and azimuths of 110^{o} to 114^{o} are recorded with peak correlator output occuring at azimuth of 114^{o}, velocity of 3.6 km/s and at time 14.42s (i.e. 12.36s from the peak of the first arrival). For this arrival the output peak was 0.49 that of the first arrival.

The 2.6 km/s arrival may be direct S waves in the volcanics while the 3.6 km/s arrival may represent S waves refracted from the top of the basement. The onset of the 2.6 km/s and 3.6 km/s arrivals are also clearly seen on both the single seismogram and on the correlator output function as 'a' and 'b' in fig. 3.26.

From the plot and print outputs of the program, the velocities and azimuths for arrivals along the record of this event number 11 were extracted and plotted. Such a plot is shown in fig. 3.27 where the single seismogram, the normalized correlator output, velocity and azimuth are plotted at discrete time points along the record. Wide ranges in search velocity and azimuth were used in measuring parameters of arrivals along the record.

The procedure described above in the processing of the data from event 11 was applied in filtering the records of all the other selected events, but with varying details. Fig. 3.28 is the plotter output from the data of fig. 3.18a. Here the ranges in velocity and azimuth were 3.0 km/s to 12.0 km/s and 50^{o} to 150^{o}; increments in velocity and azimuth were 0.4 km/s and 4^{o}. Two peaks were plotted at intervals of 0.04s.

In figs. 3.29a/b which are the outputs from the same record (fig. 3.18a), the azimuth and velocity increments were reduced to $2^{o}/1^{o}$ and 0.2/0.1 km/s for narrower ranges in search

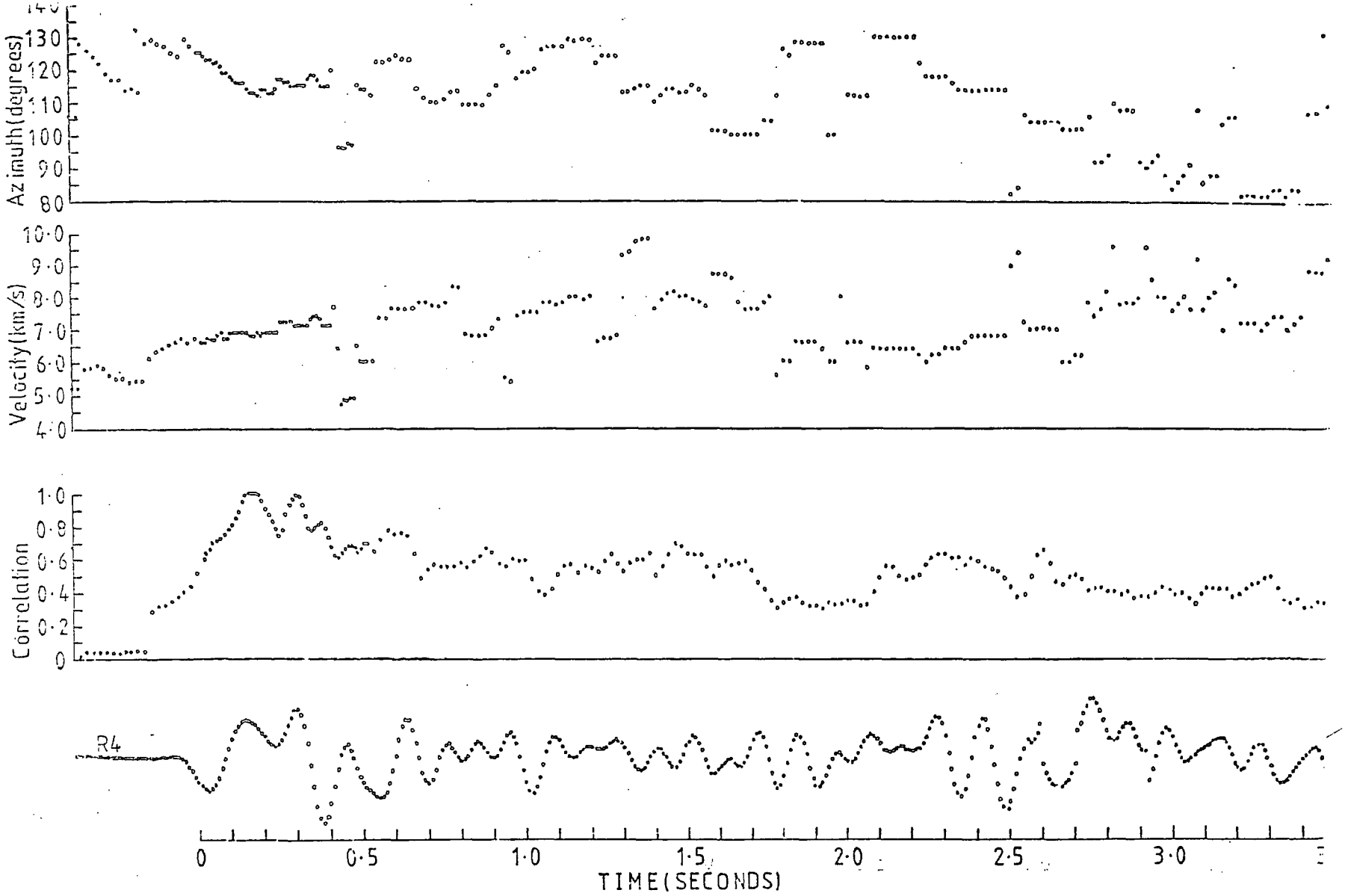

Fig·3·27: Plot of correlation, apparent velocity and azimuth as functions of time along the seismic trace

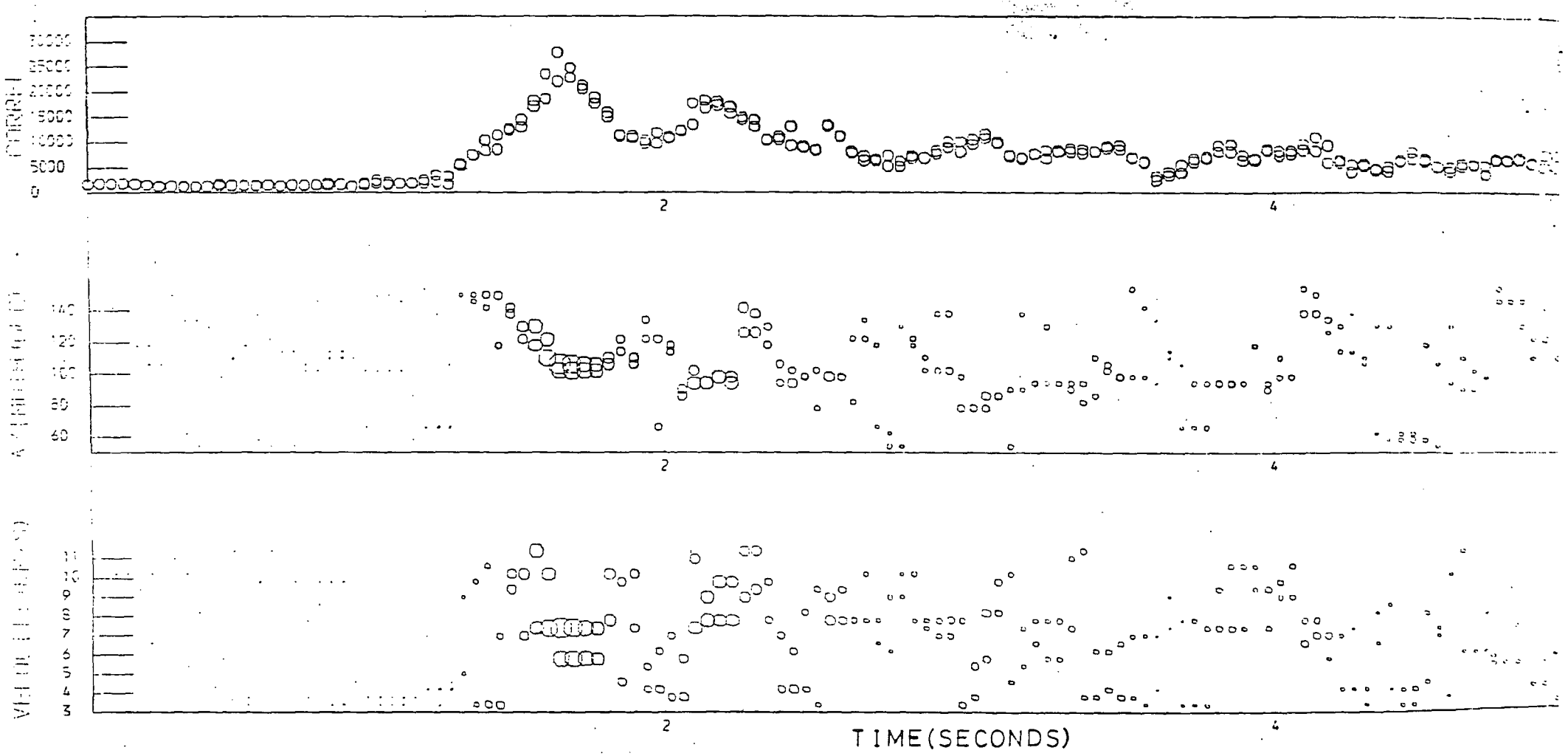

Fig-3-28: Plotter output from program VFIL for event number 7 with 2 peaks plotted at intervals of 0.04s-Velocity and azimuth increments are 0.4 km/s and 4° respectively.

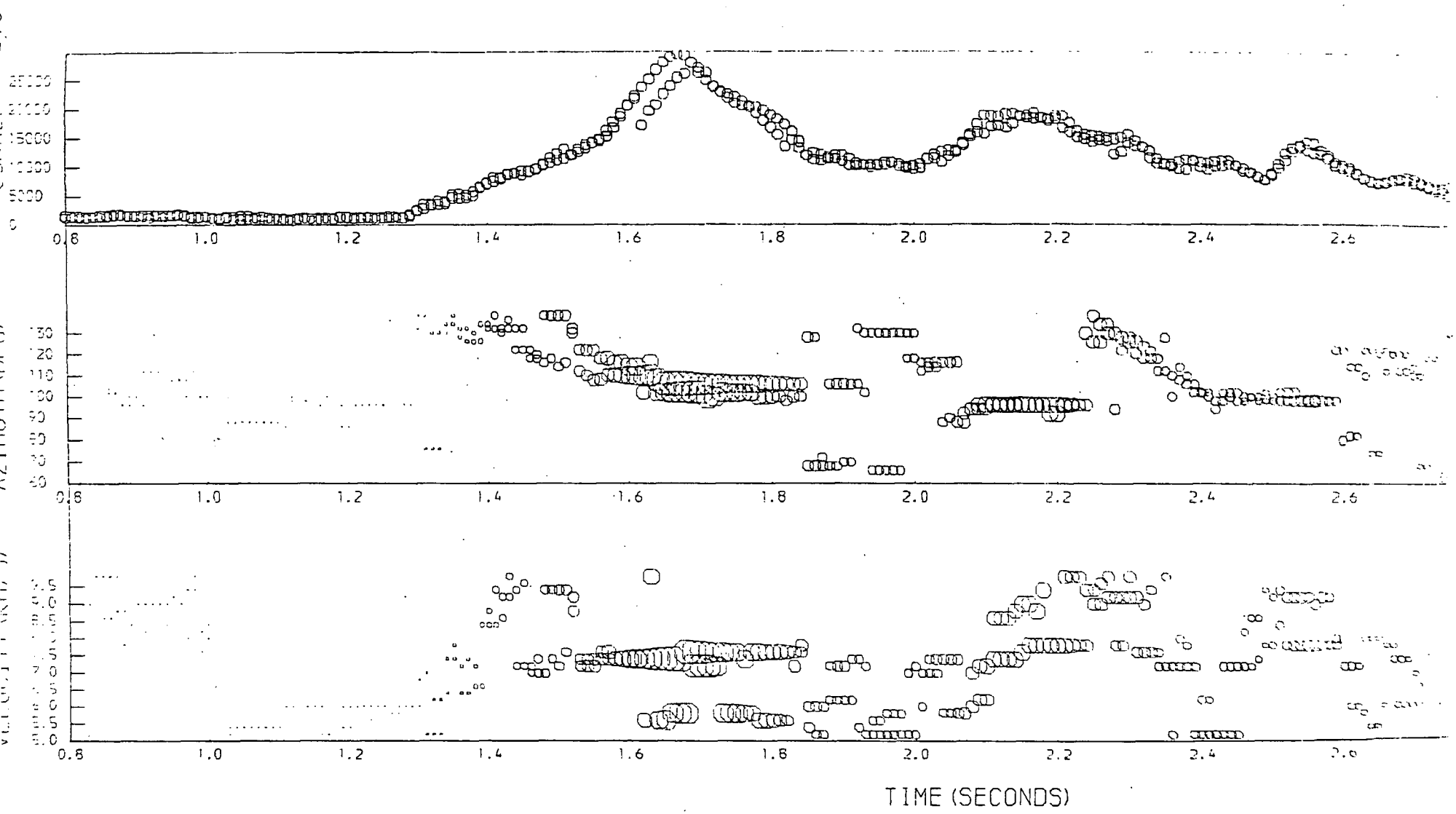

Fig-3-29a: Plotter output for event number 7 with 2 peaks plotted at intervals of 0.01s. Velocity and azimuth increments are 0.2 km/s and 2° respectively.

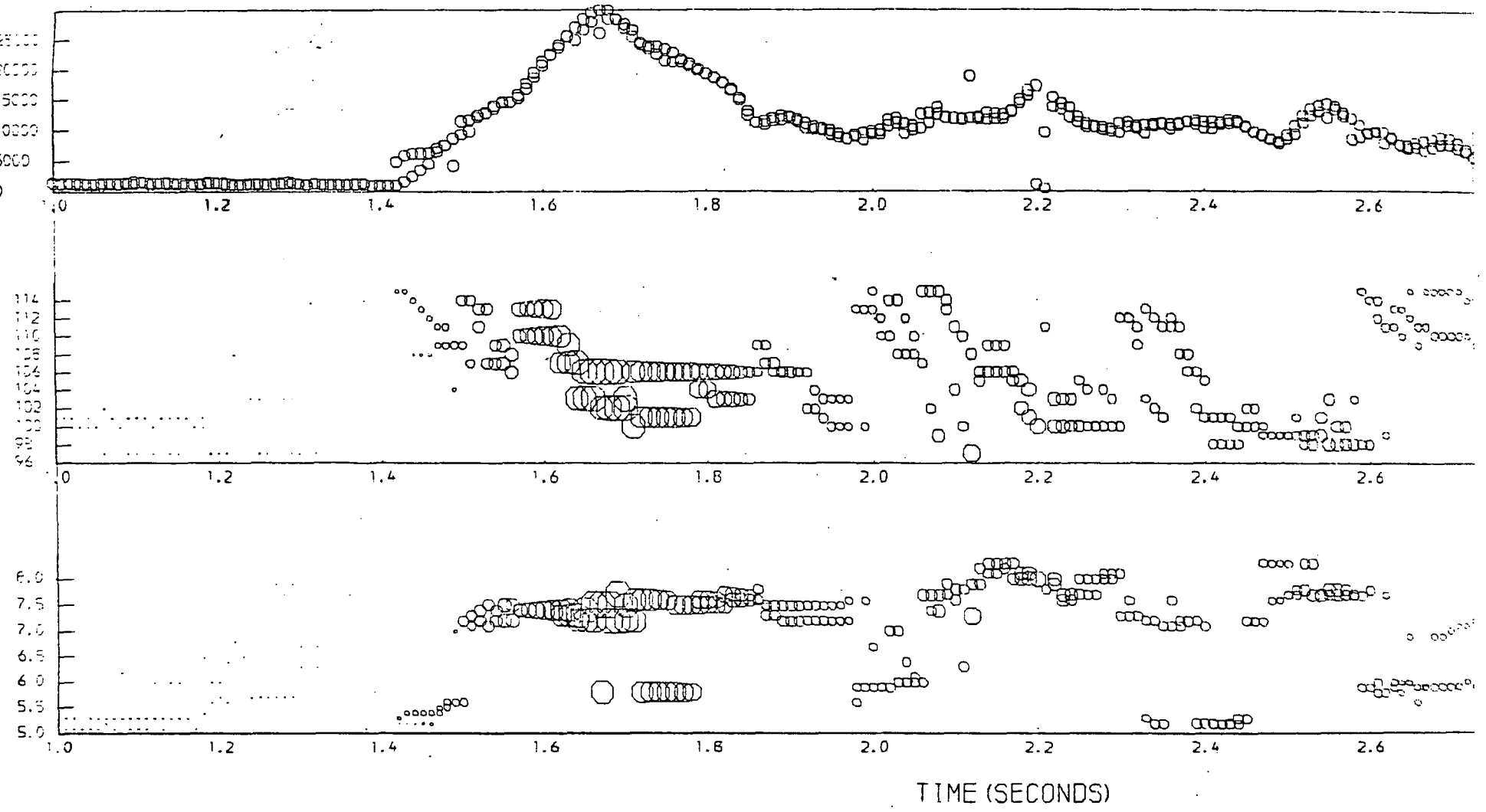

Fig.3.29.b: Plotter output for event number 7 with two peaks plotted at 0.01s intervals. Velocity and azimuth incremented by 0.1 km/s and 1° respectively.

parameters. In each case, two peaks were plotted at intervals of 0.01s. A portion of the printout corresponding to fig. 3.29b is shown in table 3.10. A subsidiary peak occuring at about the same time as the main peak of the first arrival was previously indicated from Mod 1 processing of this record. This subsidiary peak is here seen more clearly in figs. 3.28 and 3.29 and also in table 3.10. Fig. 3.30 for event 7 is similar in function to fig. 3.27 for event 11 with only the maximum peak plotted.

3.7 The data

The errors in the measurement of first arrival velocities and azimuths of the records of all events processed were estimated from the contributions of the sources of error discussed in section 3.5. The first arrival velocities and azimuths of the rift events to the immediate east of Kaptagat with their estimated measurement errors are shown in table 3.11. Similar first arrival data for more distant rift events to the north and south of Kaptagat are shown in table 3.12. The first arrival data for local events from the west are shown in table 3.13.

In the plotter output for the record of each event, the significant arrivals were identified by an increase in the correlator amplitude. It was useful, where possible, to check that the arrivals seen on the correlator outputs could also be identified on a single seismic trace. The correlator amplitudes of all arrivals for the record of a given event were normalized to unity with respect to the event's first arrival correlator amplitude. The normalized output for each arrival was then plotted as a vertical line at the corresponding arrival time. The numbers below each line represent the velocity and azimuth of the corresponding arrival.

Table 3.10 : Correlator print output for event 7 with two peaks plotted every 0.01s. Velocity and azimuth increments are 0.1 km/s and 1^{o} respectively. Velocity and azimuth search ranges were 5.0 to 10.0 km/s and 60^{o} to 140^{o} respectively.

```
 EVENTN= 6945
TAPEN=136
FILEN= 56

  IP=    80SAMPS
  ISTEP=     1 SAMPS
  INT. WINDOW = .20   SECONDS
  NPEAK =    5

                              START     TERMINAL    INCREMENT
  VELOCITY (KM/S)              5.00       10.00        0.20
  AZIMUTH (DEGS)              60.00      140.00        2.00

        SP      VELOCITY   AZIMUTH      CORREL

PDS: PLOT DESCRIPTION GENERATION BEGINS.

159
                             7.40      116.00      19217.61
                             7.40      110.00      18670.61
                             9.80      124.00      17645.88
                             5.60      102.00      13185.97
                             5.80      112.00       9278.24
            -47.64           7.40      116.00      19217.61

160
                             7.40      114.00      20706.92
                             7.40      110.00      20617.09
                             5.60      102.00      14780.75
                             9.40      138.00       8236.31
                             8.80      100.00       7208.81
            -107.64          7.40      114.00      20706.92

161
                             7.40      110.00      22355.27
                             7.40      114.00      21925.25
                             5.60      102.00      15929.29
                             9.40      138.00       8211.87
                             6.80      130.00       6282.64

            -134.64          7.40      110.00      22355.27

162
                             7.40      110.00      23917.41
                             5.60      102.00      17161.47
                             7.00       96.00      13077.09
                             8.60      138.00       8666.61
                             9.40      138.00       8302.57
            -141.64          7.40      110.00      23917.41
```

163				
		7.40	110.00	25257.62
		9.80	116.00	19722.89
		5.60	102.00	18870.30
		7.00	96.00	14594.66
		8.60	138.00	8805.07
	-271.64	7.40	110.00	25257.62
164				
		7.40	108.00	26888.58
		5.60	102.00	20822.79
		7.00	96.00	16607.10
		8.60	138.00	8721.83
		7.00	128.00	7809.63
	-397.64	7.40	108.00	26888.58
165				
		7.40	106.00	28123.57
		5.60	102.00	22677.88
		8.60	138.00	8920.92
		9.20	132.00	8690.91
		5.80	122.00	3486.12
	-459.64	7.40	106.00	28123.57
166				
		7.40	106.00	29041.28
		5.80	102.00	24069.10
		9.40	112.00	18464.67
		9.20	132.00	9262.96
		8.60	136.00	9200.39
	-420.64	7.40	106.00	29041.28
167				
		7.40	106.00	29453.00
		5.80	102.00	25583.54
		9.40	112.00	18281.38
		7.20	122.00	10552.07
		9.20	130.00	9531.57
	-366.64	7.40	106.00	29453.00
168				
		7.60	106.00	29410.19
		5.80	102.00	26186.42
		9.40	112.00	16933.25
		7.20	122.00	10990.92
		9.40	128.00	9962.68
	-329.64	7.60	106.00	29410.19
169				
		7.20	102.00	28112.00
		7.60	106.00	28084.97
		5.80	102.00	25756.43
		7.00	118.00	11079.37
		9.00	126.00	9994.23
	-210.64	7.20	102.00	28112.00
170				
		7.20	102.00	27214.86
		7.60	106.00	26448.73
		5.80	100.00	25594.39
		7.00	118.00	11767.75
		9.00	126.00	10122.14
	43.36	7.20	102.00	27214.86
171				
		7.20	100.00	26462.95
		7.60	106.00	25129.65
		5.80	100.00	24124.67
		9.00	122.00	10224.28
		6.40	114.00	10043.69
	276.36	7.20	100.00	26462.95

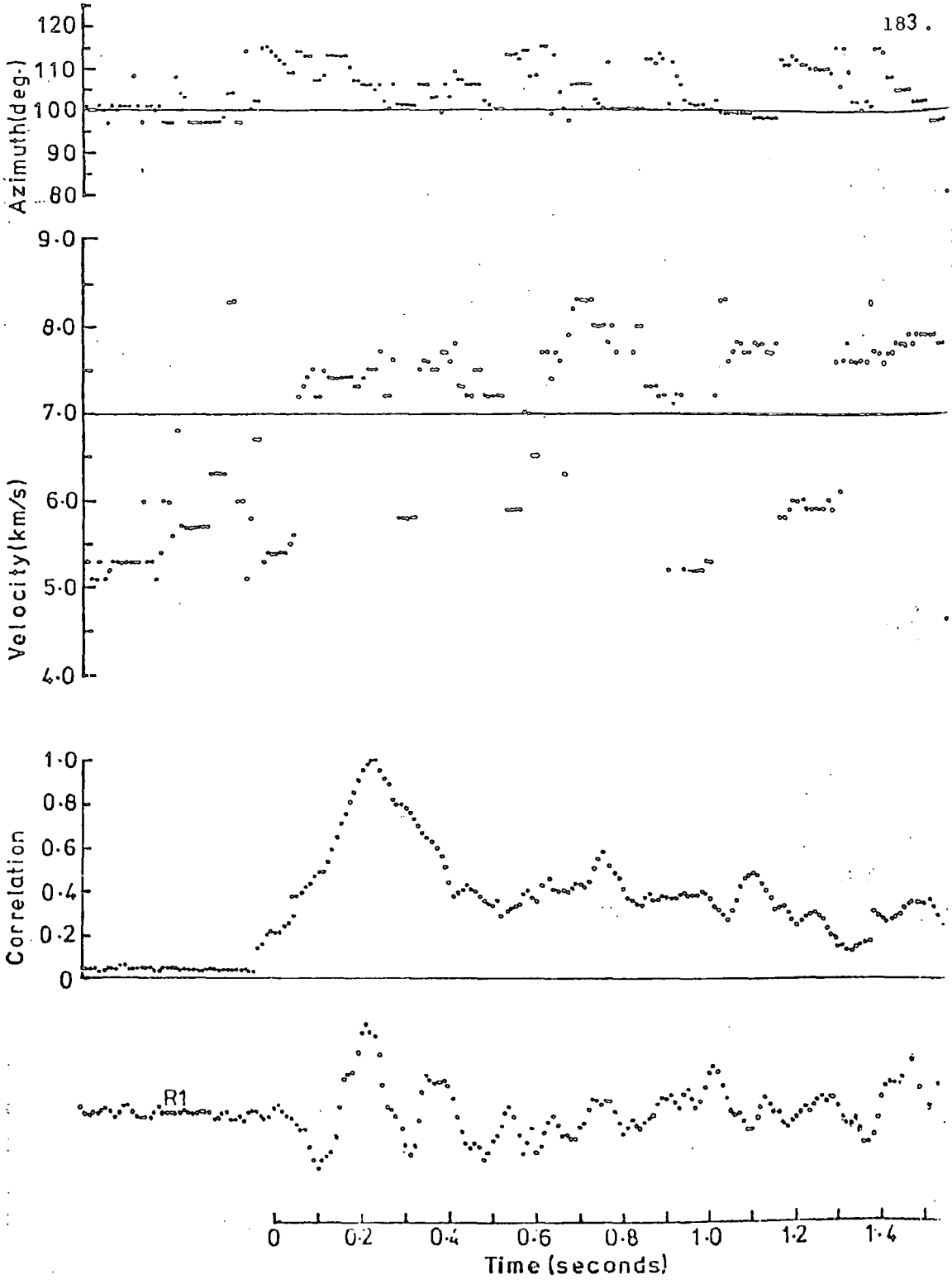

Fig·3·30: Plot of correlation, apparent velocity and azimuth as functions of time along the seismic trace for event number 7

Event number	Apparent azimuth (degrees)	Apparent Velocity (km/s)	P to X time (seconds)
1	102±4	7.1±0.5	8.1
2	94±4	7.2±0.3	8.2
3	95±4	7.3±0.2	8.2
4	74±2	7.0±0.2	8.3
5	87±2	7.3±0.2	9.0
6	94±2	7.5±0.2	9.1
7	106±2	7.5±0.4	9.7
8	88±2	7.0±0.2	9.8
9	107±2	6.9±0.5	10.3
10	106±2	7.0±0.2	10.8
11	114±2	6.9±0.2	11.7

Table 3.11: Measured P-X times and the corresponding first arrival measured apparent velocities and azimuths of the local rift events to the immediate east of Kaptagat.

Event number	Apparent azimuth (degrees)	Apparent velocity (km/s)	P to X time (seconds)
1	29±2	7.7±0.2	24.7
2	21±3	6.7±0.2	26.1
3	19±4	6.7±0.2	26.4
4	18±4	6.8±0.2	26.7
5	23±3	6.7±0.2	27.0
6	22±4	7.0±0.2	28.1
7	148±2	7.8±0.2	29.7

Table 3.12: Measured P-X times and the corresponding measured first arrival apparent velocities and azimuths of rift events to the north and south of Kaptagat.

Event number	Apparent azimuth (degrees)	Apparent velocity (km/s)	P to X time (seconds)
1	224±2	6.0±0.2	7.7
2	224±3	5.6±0.2	7.7
3	196±3	6.0±0.2	8.3
4	222±4	6.4±0.2	10.6
5	240±2	6.2±0.2	12.1
6	234±2	6.4±0.1	17.4
7	236±2	6.4±0.1	19.8
8	200±3	6.5±0.2	28.6
9	200±3	6.4±0.2	29.3

Table 3.13: Measured P-X times and the corresponding measured first arrival apparent velocities and azimuths of events originating mainly from the south west of Kaptagat.

The resulting data for closein eastern rift events are shown in fig. 3.31. Fig. 3.32 gives the corresponding data for distant rift events to the north and south of Kaptagat. Data for local events coming mainly from the south west are shown in fig. 3.33.

The letters used in fig. 3.31 are for phase identification. Arrivals from different events and labelled by the same letters are thought to be the same phases. For example, arrivals marked 'a' are identified in this study as first arrival headwaves. The significance of other letters are explained in section 6.3 on the interpretation of second arrival data from local rift events originating from the immediate east of Kaptagat.

Fig. 3.31: Apparent surface velocity (km/s), azimuth (degrees) and relative onset time data for closein local rift events from the immediate east of Kaptagat. Estimated epicentral distances are shown in km.

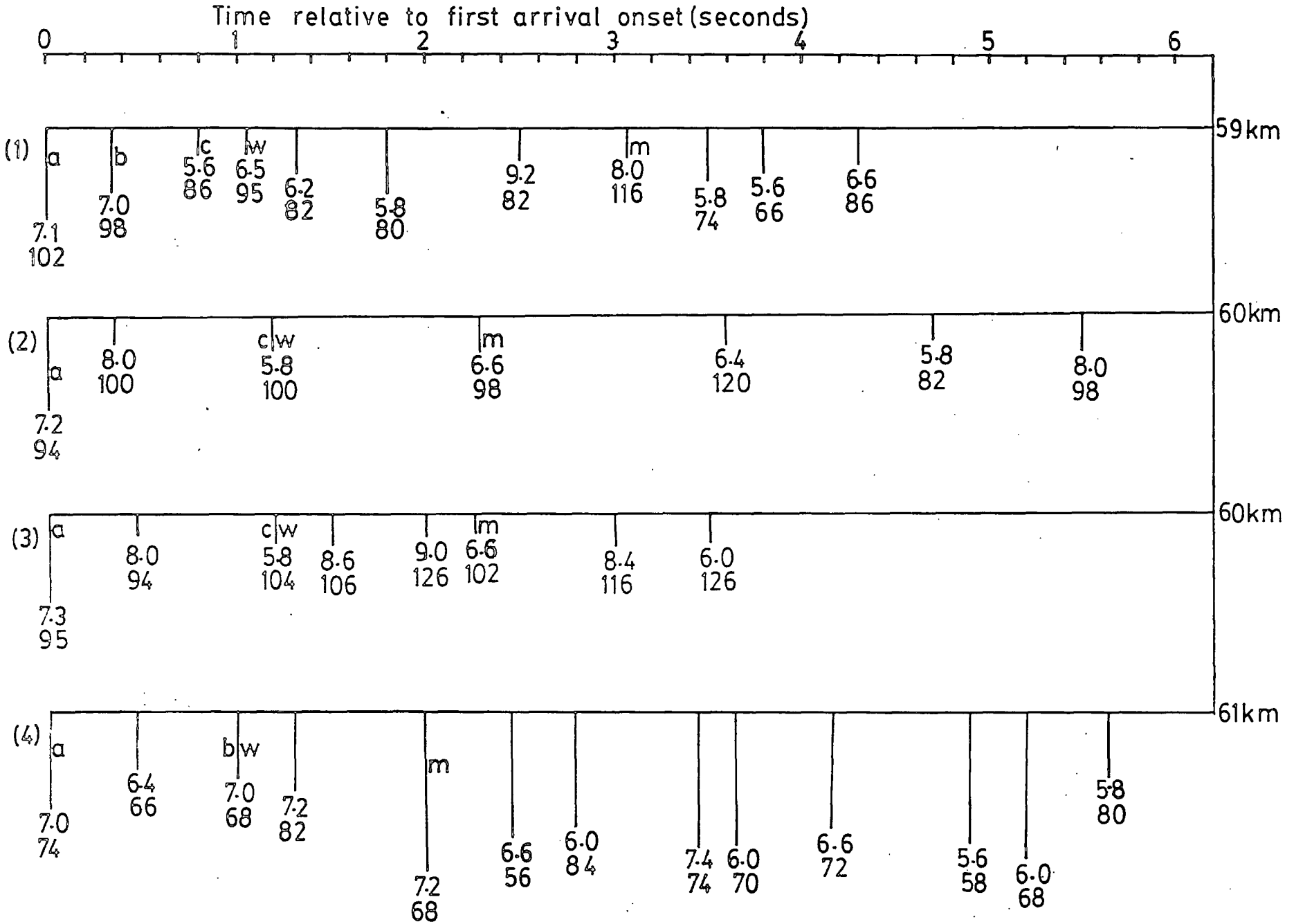
Time relative to first arrival onset (seconds)
0
1
2
3
4
5
6
(1)
a 7.1 102
b 7.0 98
c 5.6 86
w 6.5 95
6.2 82
5.8 80
9.2 82
m 8.0 116
5.8 74
5.6 66
6.6 86
59km
(2)
a 7.2 94
8.0 100
c w 5.8 100
m 6.6 98
6.4 120
5.8 82
8.0 98
60km
(3)
a 7.3 95
8.0 94
c w 5.8 104
8.6 106
9.0 126
m 6.6 102
8.4 116
6.0 126
60km
(4)
a 7.0 74
6.4 66
b w 7.0 68
7.2 82
m 7.2 68
6.6 56
6.0 84
7.4 74
6.0 70
6.6 72
5.6 58
6.0 68
5.8 80
61km

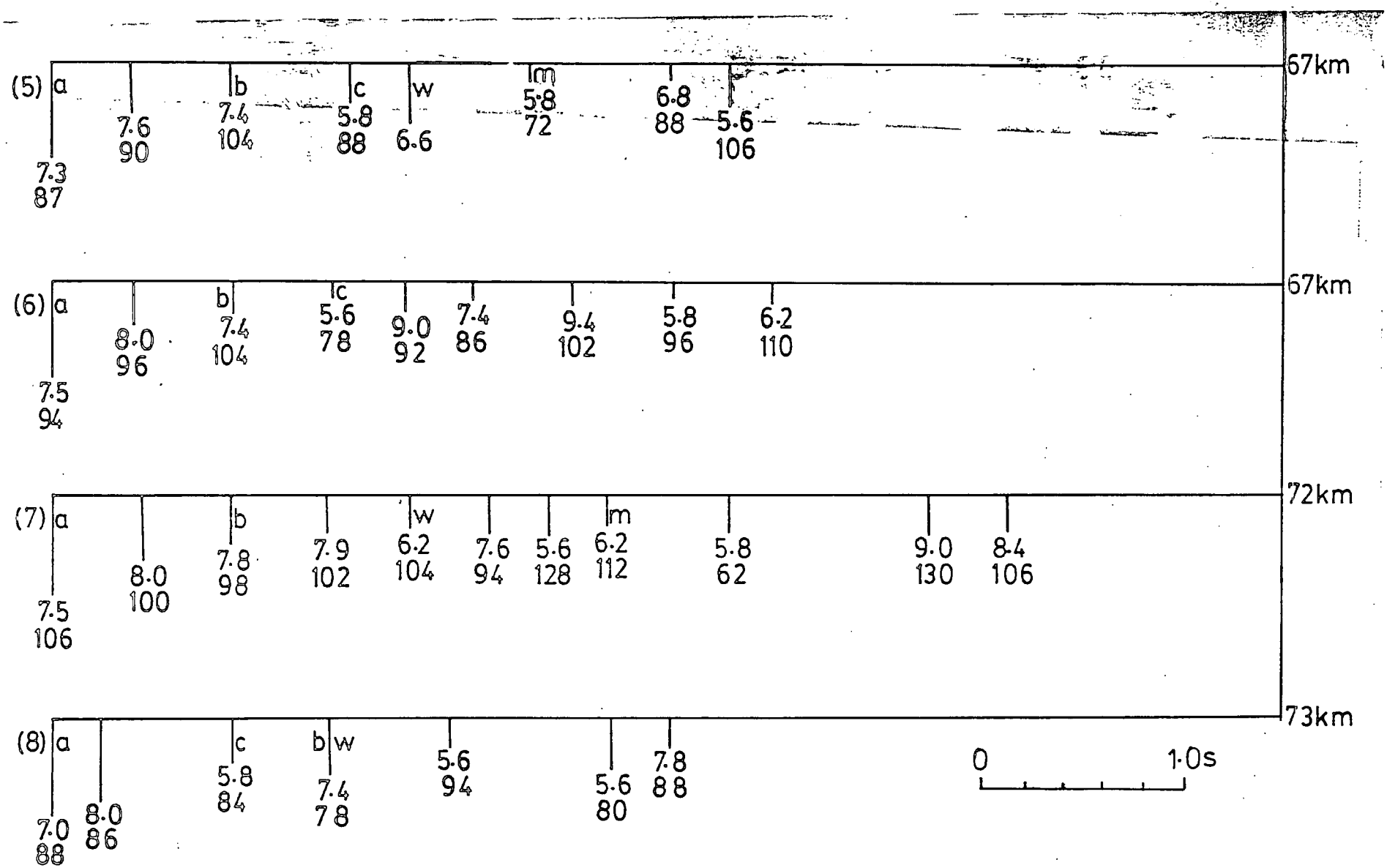
(5)
a
7.3
87
7.6
90
b
7.4
104
c
5.8
88
w
6.6
m
5.8
72
6.8
88
5.6
106
67km
(6)
a
7.5
94
8.0
96
b
7.4
104
c
5.6
78
9.0
92
7.4
86
9.4
102
5.8
96
6.2
110
67km
(7)
a
7.5
106
8.0
100
b
7.8
98
7.9
102
w
6.2
104
7.6
94
5.6
128
m
6.2
112
5.8
62
9.0
130
8.4
106
72km
(8)
a
7.0
88
8.0
86
c
5.8
84
b
w
7.4
78
5.6
94
5.6
80
7.8
88
73km
0
1·0s

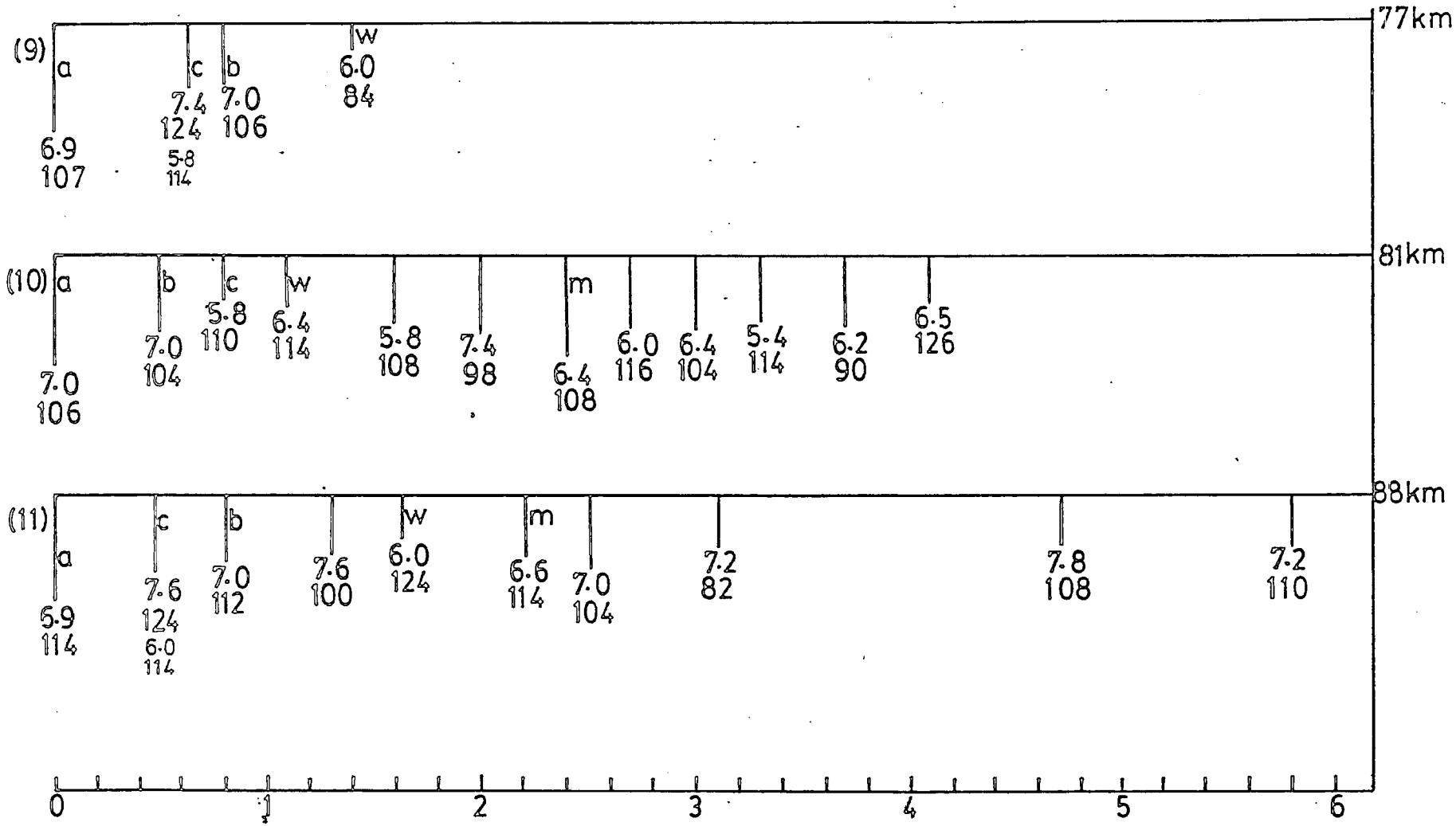

Fig 3·31: Apparent surface velocity (km/s), azimuth (degrees) and relative onset time data for closein local rift events from the immediate east of Kaptagat. Estimated epicentral distances are shown in km.

Fig. 3.32: The data (velocity and azimuth) for rift events to the north and south of Kaptagat. Numbers below each vertical line represent apparent velocity in km/s and azimuth in degrees.

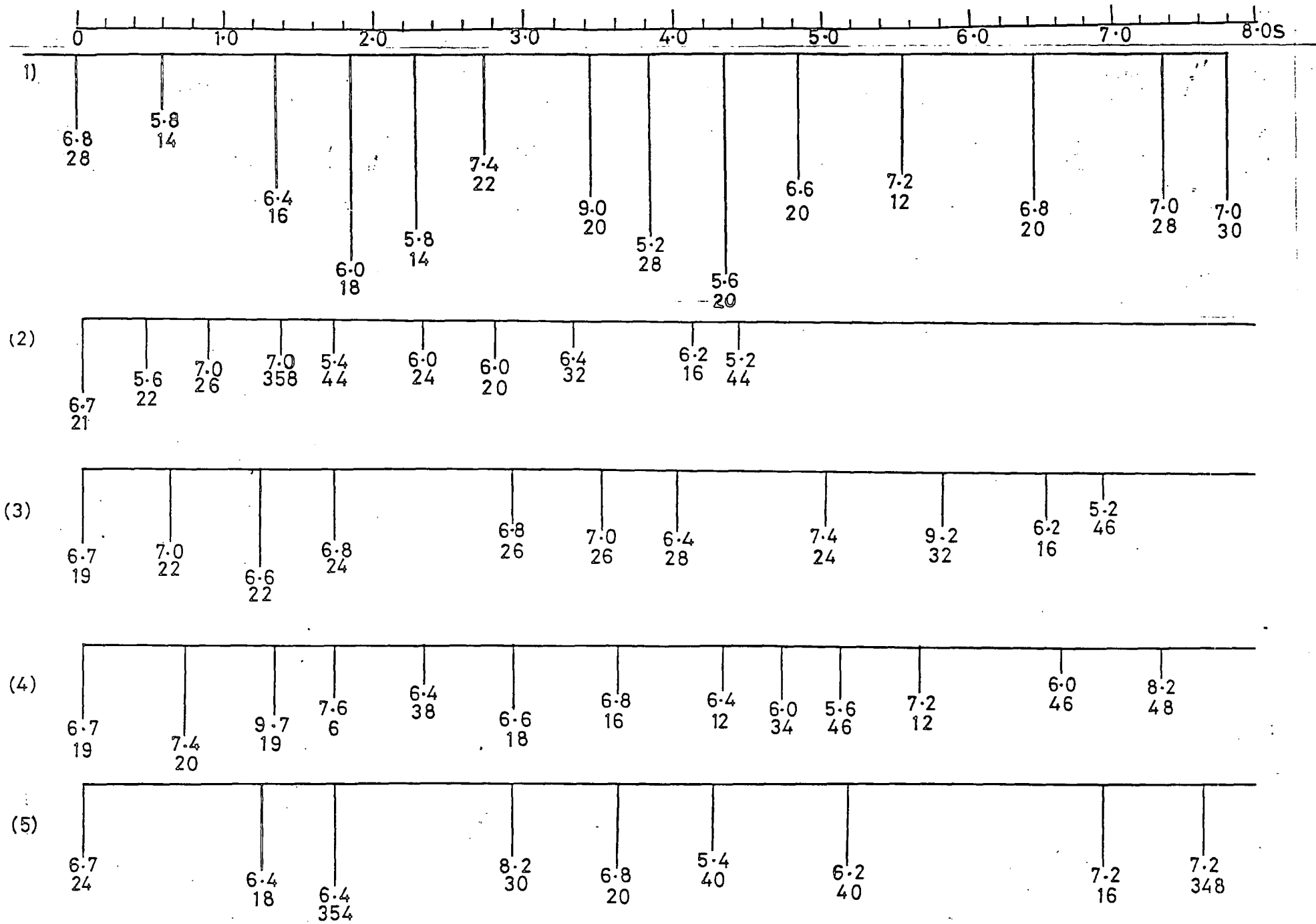
0
1·0
2·0
3·0
4·0
5·0
6·0
7·0
8·0s
1)
6·8 28
5·8 14
6·4 16
6·0 18
5·8 14
7·4 22
9·0 20
5·2 28
5·6 20
6·6 20
7·2 12
6·8 20
7·0 28
7·0 30
(2)
6·7 21
5·6 22
7·0 26
7·0 358
5·4 44
6·0 24
6·0 20
6·4 32
6·2 16
5·2 44
(3)
6·7 19
7·0 22
6·6 22
6·8 24
6·8 26
7·0 26
6·4 28
7·4 24
9·2 32
6·2 16
5·2 46
(4)
6·7 19
7·4 20
9·7 19
7·6 6
6·4 38
6·6 18
6·8 16
6·4 12
6·0 34
5·6 46
7·2 12
6·0 46
8·2 48
(5)
6·7 24
6·4 18
6·4 354
8·2 30
6·8 20
5·4 40
6·2 40
7·2 16
7·2 348

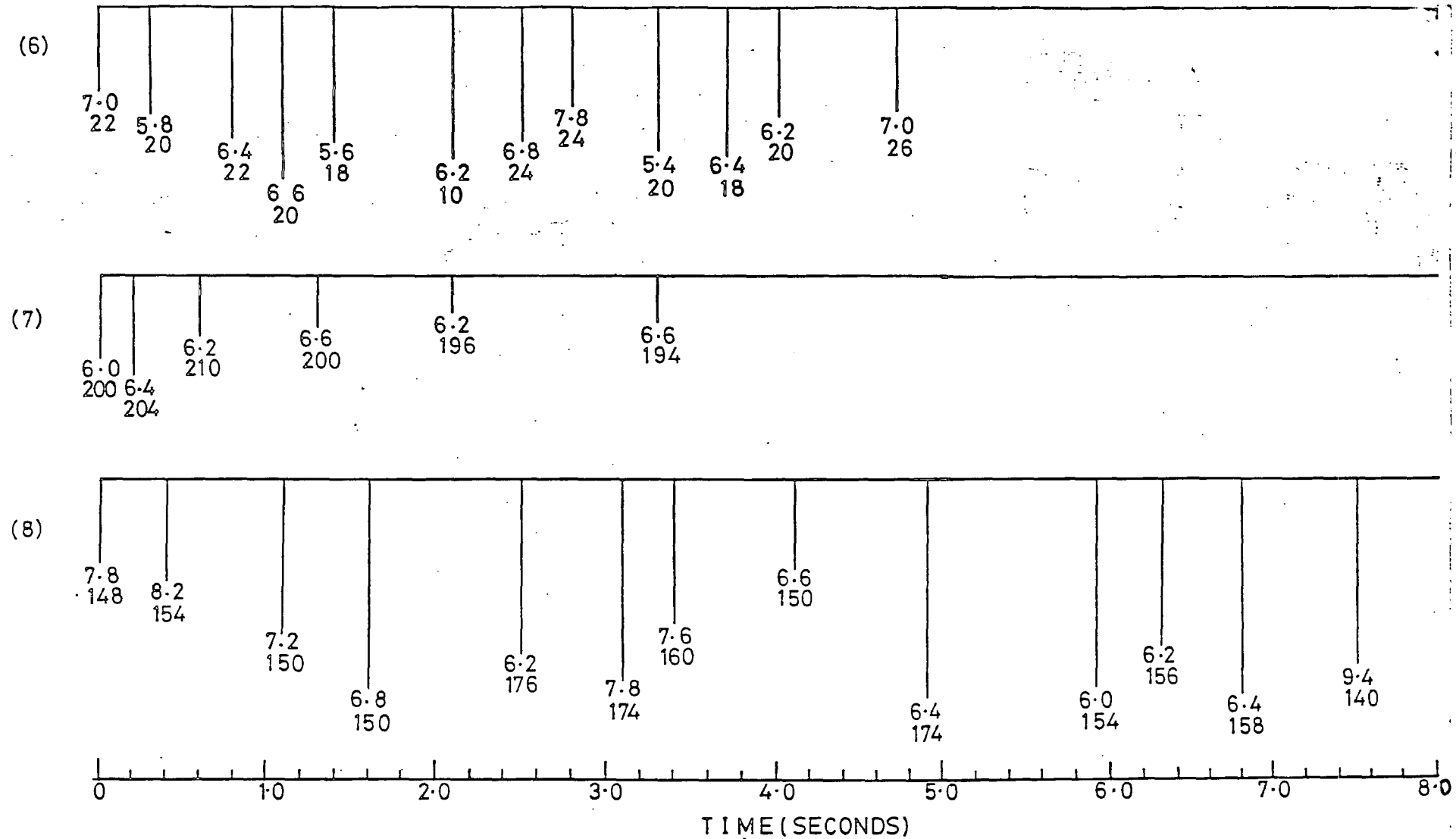

Fig. 3-32 : The data for rift events to the north and south of Kaptagat . Numbers below each vertical line are apparent velocity in km/s and azimuth in degrees.

Fig. 3·33: Local events originating from the west of Kaptagat. Numbers below each vertical line are apparent velocity in km/s and azimuth in degrees. For each event, the lengths of the vertical lines indicate the relative values of the TAP for the corresponding phases.

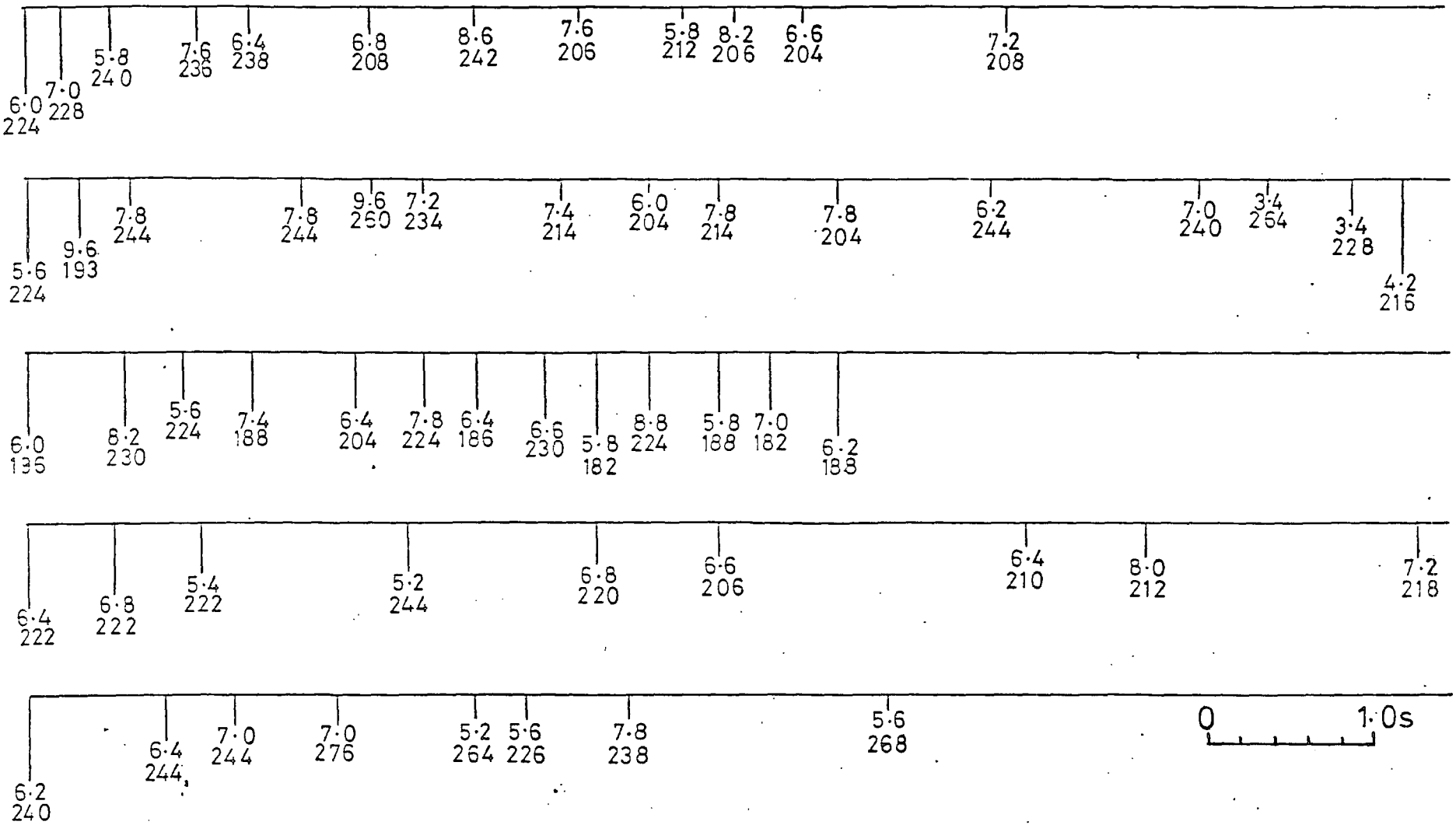

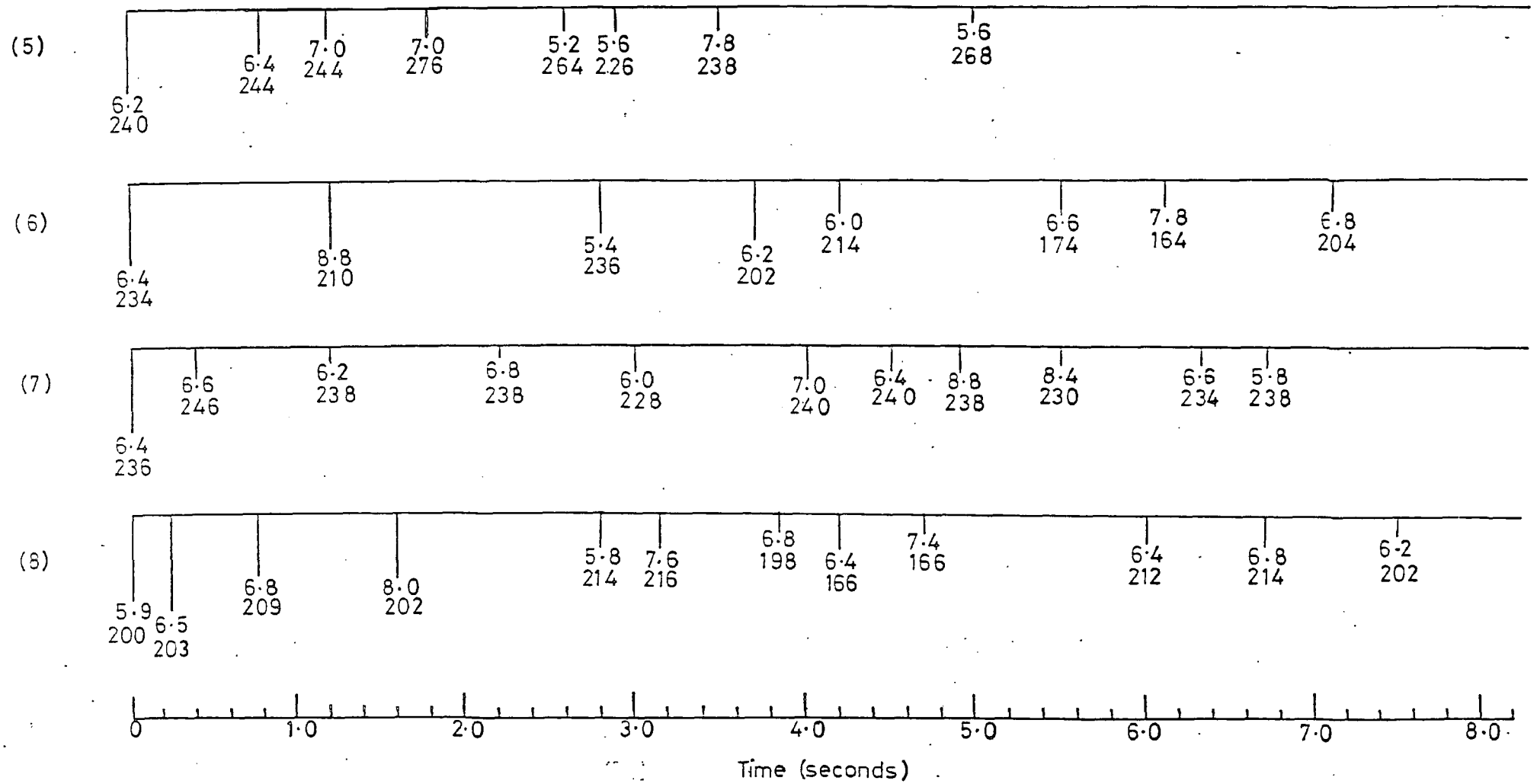
(5)
6·2 240
6·4 244
7·0 244
7·0 276
5·2 264
5·6 226
7·8 238
5·6 268
(6)
6·4 234
8·8 210
5·4 236
6·2 202
6·0 214
6·6 174
7·8 164
6·8 204
(7)
6·4 236
6·6 246
6·2 238
6·8 238
6·0 228
7·0 240
6·4 240
8·8 238
8·4 230
6·6 234
5·8 238
(8)
5·9 200
6·5 203
6·8 209
8·0 202
5·8 214
7·6 216
6·8 198
6·4 166
7·4 166
6·4 212
6·8 214
6·2 202
0
1·0
2·0
3·0
4·0
5·0
6·0
7·0
8·0
Time (seconds)

CHAPTER 4

LOCATION OF EPICENTRES

4.1 Introduction

In the previous chapter, the apparent veolcities and apparent azimuths of first and later arrivals in the records of selected earthquakes were determined. In the present chapter, the epicentres of these events are located in relation to the rift structure. Ideally focal depth and structural model are required for locating epicentres; these quantities are initially unknown. Epicentres are, therefore, here located without assuming any particular structural model or any definite focal depth.

4.2 Normal multistation location procedure

The techniques normally applied to locate earthquakes are based on the method of least squares. The basic principles underlying these techniques are discussed in Richter (1958) and Jeffreys (1970) and are outlined in this section for local earthquakes. The coordinates and origin time of an earthquake are determined from records of a multistation network by iteratively changing a preliminary hypocentre and origin time to minimize the sum of the squares of the differences between observed and calculated arrival times of first arrival P and possibly other phases.

To be located with high precision, the epicentre for local earthquakes should be well surrounded by recording stations at distances (large compared with probable focal depth) preferably in the range 60 km to 100 km and well distributed in azimuth. On the other hand, high accuracy in depth determination demands

that at least one station in the network of local stations must be close to the epicentre.

For local earthquakes, epicentral distance may be measured with direct waves P_g and S_g since P_g is the first arrival for most crustal models in the distance range 60 to 100 km. Here the data are the onset times T_p and T_s of the directwaves. If the Poisson's ratio, σ , is assumed constant, it can be shown that for P_g and S_g propagating along the path with velocities α and β respectively, then

$$T_s - T_p = R(T_p - T_o);$$

$$\text{and that } D = \frac{\alpha}{\sqrt{3}}(T_p - T_o)$$

$$\text{where } R = \left(\frac{\alpha}{\beta} - 1\right).$$

D is the linear distance from focus to station and T_o is the origin time of the event.

For the network, measured values of $T_s - T_p$ are plotted as ordinates against measured P_g onset times, T_p as abscissae. The graph should be a straight line crossing T_p axis at time T_o which estimates the origin time. The time interval $T_p - T_o$ for each station is multiplied by the best estimate of α to give D.

The normal network location procedure was not used in locating events analysed in this study because the Kaptagat array had a relatively small aperture in comparison with the epicentral distance. The array aperture is so small that the array can be regarded effectively as one station. Since data on first arrival apparent velocity and azimuth have been obtained, a location procedure involving these measured quantities was adopted.

4.3 Location procedure from a single array station

To locate the epicentre of an event from a single array station, the azimuth and the epicentral distance are used. The azimuth is usually obtained from velocity filtering. The distance, Δ, may be measured by the time difference between any pair of arrivals, normally P and S. The P-S time may be converted to distance using the following data :

(a) the ratio, R, of P-wave velocity, α , to S-wave velocity, β .

(b) the seismic velocity model of the structure through which the waves pass, and

(c) the focal depth, h, of the event if no direct arrivals can be identified.

The ratio, R, for the propagation path is related to Poisson's ratio, σ, by

$$R = \frac{\alpha}{\beta} = \left(\frac{1.0 - \sigma}{0.5 - \sigma}\right)^{\frac{1}{2}}.$$

For most rocks σ is about 0.25. In the present study an average value of 1.74 is adopted for R (Anderson, 1965) corresponding to a value of 0.254 for σ .

However, at the latitude range covered by the present data, it has been established that there is a lateral variation of structure in and around the Gregory rift zone (Maguire and Long, 1976; Griffiths et al 1971; Savage and Long, 1985). It is, therefore, to be expected that there will also be a lateral variation in σ, and hence R. In practice, then, R will be expected to vary from path to path and also along a given path. To simplify the discussion, however, an average value will here be assumed for R.

In general the P and S phases need not have the same propagation paths. All that is required is that the P and S phases be correctly identified. The main source of error in measuring P-S time in this study arose from the uncertainty in the identification and in determining the onset time of the S waves which come in as later arrivals and were recorded with vertical instruments. S waves are better recorded with horizontal instruments. But as discussed in the next section, S wave onset can be more confidently identified from the measured apparent velocities of the arrivals suspected to be S.

4.4 Structure of the seismograms and the identity of a prominent arrival.

On the seismograms used in the present study, S wave onsets were not identified with confidence for reasons given above. S phases may be expected to come in as a low energy later arrivals obscured in the coda of higher amplitude P wave arrivals. Fig. 3.21 reproduced here as fig. 4.1 shows a typical set of seismograms from a local earthquake recorded by Kaptagat array.

The first arrival which is a P wave is impulsive and clear. In the next few seconds following this first arrival, each seismogram shows other high amplitude P wave arrivals. The record then tends to get quieter with time until at about 12s from the first arrival when a high energy burst (whose estimated onset time is indicated by the arrow) appears and persists for several seconds. This energy burst is seen clearly in the seismograms of all events studied and will here be labelled arrival X. If the identity (i.e. the phase) of X is known, its onset time relative to the first arrival onset can be

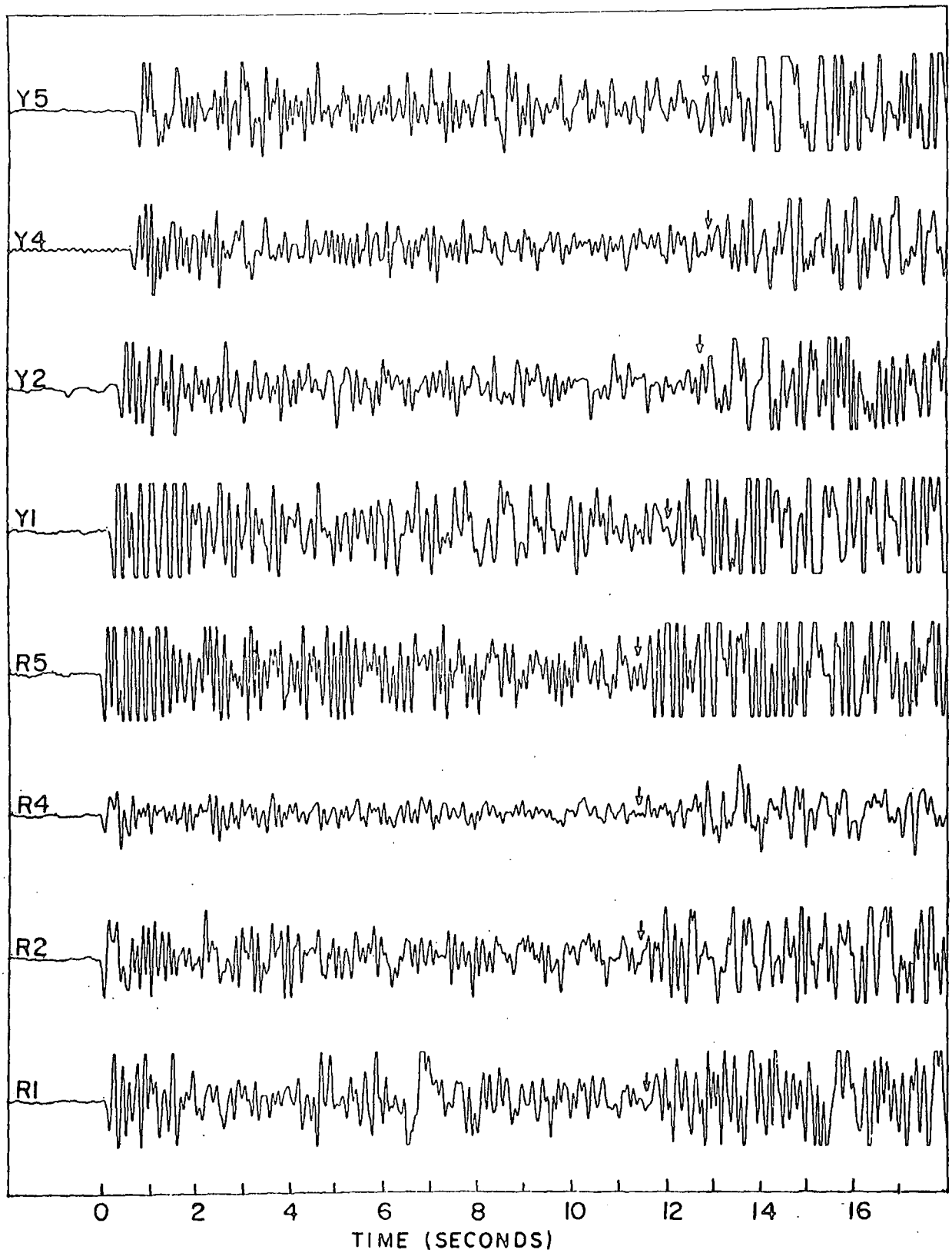

Fig. 4·1 : A record of a closein local rift event coming from the immediate east of Kaptagat.

used to estimate the epicentral distance of the corresponding event for a given structural model. X may be direct waves, head waves or reflections of the P, S or the mode converted type. It may also be a surface wave.

The later part of the array data of fig. 4.1 containing the arrival X was velocity filtered (using VFIL) to estimate the velocities of arrivals in the time range containing X. The plot output shown in fig. 4.2 (reproduced from fig. 3.26) includes a single seismic channel at the top. Times marked on this diagram are times measured from the beginning of the original digital tape file on which the array seismograms for this event were stored. Times measured from the peak of the first arrival are obtained by subtracting 2.06s from the times in fig. 4.2. The search ranges used to produce the output shown in this figure are 2.0 to 10.0 km/s in steps of 0.2 km/s in velocity, 108° to 118° in steps of 2° in azimuth and 12.50s to 16.50s in steps of 0.02s in time.

In fig. 4.2 both the single seismic trace and the correlator output indicate a sudden rise in amplitude starting at about 13.82s. From this time and persisting for a duration of about 0.20s is an arrival with velocity 2.6 km/s and azimuth 112°. The onset of this arrival is 11.76s from first arrival peak; this time is close to the P-X time of 11.7s measured from the seismogram of pit R1 for this same event. An arrival with velocity of 3.4 km/s and azimuth of 110° to 112° persists for about 0.24s starting from 14.44s. The onset of this arrival is 12.38s from the peak of the first arrival, which again is close to the measured P-X time. For a duration of 0.22s from 14.90s to 15.12s an arrival with velocity 3.8 km/s and azimuth 112° is observed. The velocities of all these arrivals (in

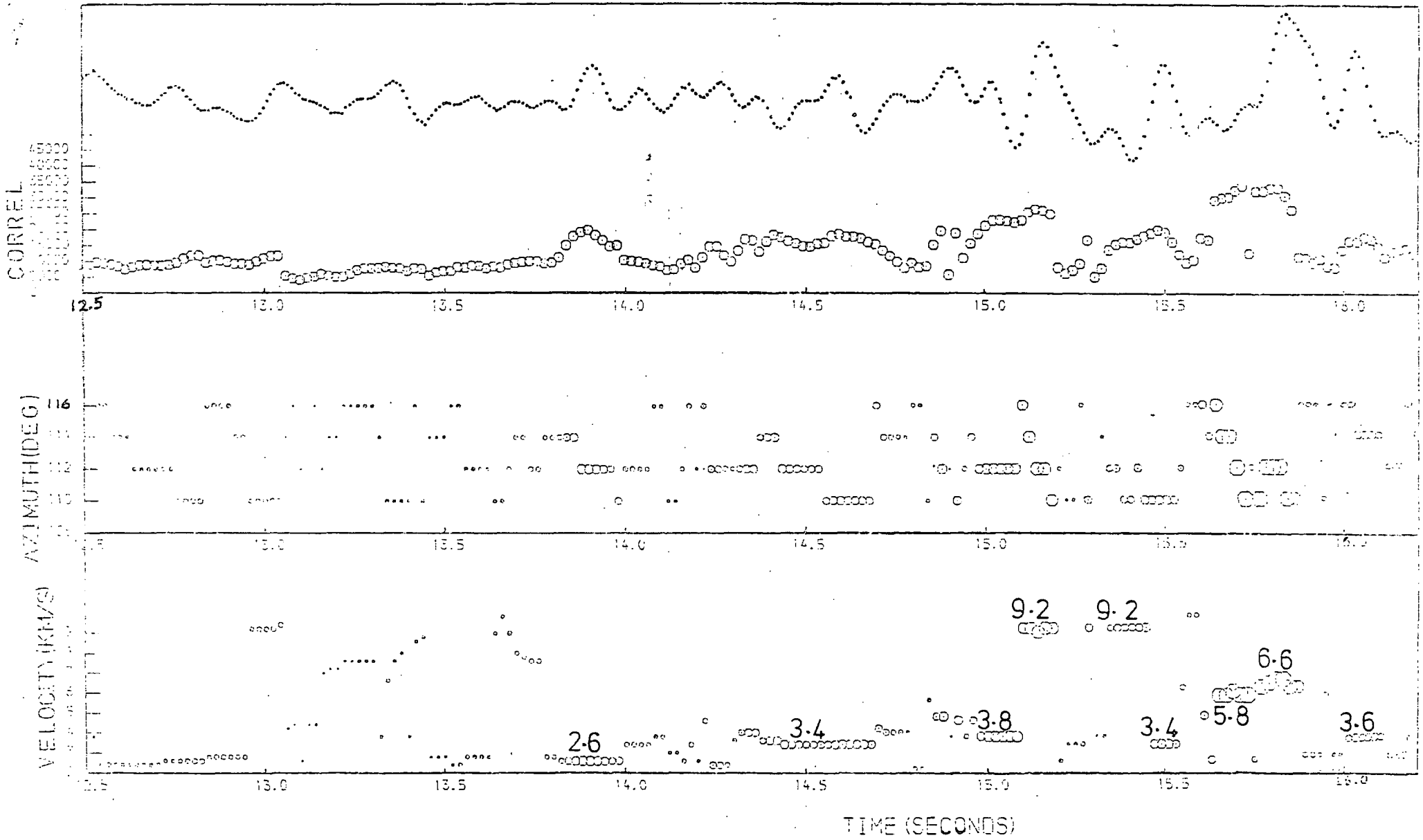

Fig. 4.2: Correlator plot output for event 11 in the time range containing the onset of 'X' arrivals. Velocity sweep from 2·0 to 10·0 km/s in steps of 0·2 km/s and azimuth sweep from 108° to 118° in steps of 2°. One peak plotted at intervals of 0·02 s.

km/s) are marked in the diagram.

In the 1.20s time interval from about 13.82s to about 15.02s only six out of the sixty measured velocities are above 4.0 km/s. The rest are below 4.0 km/s and above about 2.5 km/s. These arrivals may, therefore, be considered as surface waves or S waves. The amplitudes of the arrivals are too small for them to be considered as surface waves unless the focus is unusually deep. These low energy and low velocity arrivals precede and are very close to the high amplitude arrivals whose estimated onset is associated with X. The low energy arrivals may, therefore, be considered as S waves.

The 2.6 km/s arrival may be identified as S waves in the volcanics, the 3.4 km/s arrival as S_g propagating in the basement. This interpretation is supported by the P-wave velocity of about 4.6 km/s obtained for the main basement volcanic cover (Khan et al., 1987) and the basement velocity of about 5.8 km/s (Swain et al., 1981). The 3.8 km/s arrival may be identified as an S phase having the same propagation path as the first arrivals.

Values of other measured velocities beyond about 15.00s are shown in fig. 4.2. A 9.0 km/s arrival from azimuth of 112° has correlator amplitude peak at 15.14s; this time corresponds to the time of the first peak of the large amplitude signal seen on the single seismogram. This high amplitude arrival could be explained as a wide angle multiple reflection. As an illustration, consider a horizontal layer of thickness H and average velocity V. Then the apparent surface velocity V_a of a wave that has been reflected two times from each of the upper and lower boundaries of the layer is given by

$$V_a = \frac{V}{\Delta} \left(\Delta^2 + (4H-h)^2 \right)^{\frac{1}{2}}$$

where h is focal depth and Δ the epicentral distance. For a layer of thickness 26 km, velocity 5.8 km/s, the calculated apparent surface velocity is 8.95 km/s at a distance of about 80 km and a focal depth of 10 km. Although this velocity agrees with the observed value of 9.0 km/s, it is difficult to explain the theoretical difference in time (about 5.6s) between such multiple reflection and the first arrival when the observed difference is about 12.0s.

Because of their high amplitudes, these arrivals could also be considered as near critical point reflections probably from the Moho. Consider a normal continental crust. For a distance region just beyond the geometrical ray theory critical distance, the reflected waves and the head waves (from the Moho, say) interfere, resulting in large amplitude arrivals (Cerveny, 1966). This distance region, of the order of 10-50 km, depends on the frequency of the reflected wave and increases with a decrease in frequency. The amplitude of the resulting waves is further enhanced if there is a positive velocity gradient immediately beneath the Moho or the relevant first order discontinuity (Braile and Smith, 1975; Cerveny and Ravindra, 1971). These near critical point diving waves have apparent velocities higher than crustal velocities. The observed velocity of about 9.0 km/s would seem to suggest that these high energy arrivals may be diving waves. But the step-out time of about 13s from the first arrival is difficult to explain.

On the output of the program showing more than one peak, the 9.0 km/s arrival is observed simultaneously with the low velocity arrivals with velocity mostly in range 2.5 km/s to

4.0 km/s. It is thus suggested that what is probably S and/or surface wave precedes and continues into the high energy portion of the record. Although the identity of X is not known for certain, it is probable that its onset time is close to but later than the onset of S waves. The onset time of X may, therefore, be an overestimate of the onset time of S. Location of epicentres will, however, be carried out without assuming an identity for X. For placing epicentres, information about focal depths is required. An attempt is now made to place some limits on the probable values of focal depth.

4.5 Focal depth estimates.

For events outside a network of stations, focal depths can normally be determined if the structure containing the propagation paths is known. In this study, the structure is not known initially and subsequent discussions will treat focal depth and structure collectively. Attention is focussed on the 11 selected closein eastern events having azimuths in the range 74° to 114° and P-X times in the range 8.1s to 11.7s and probably originating from within the confines of the rift.

For the interpretation of the velocity data, knowledge of focal depths of the events is essential. But focal depths can not be uniquely determined from the present data. However, on geological and geophysical evidence, limits can be put on realistic values of focal depth estimate. An average value may then be estimated and used for all events.

The events under study are probably located within the confines of the Gregory Rift (section 4.6). This part of the Gregory rift, is associated with microseismic, geothermal and recent volcanic activity. This suggests that rocks at shallow

depths are probably in a partially molten state. For example, near the steam jets south of Lake Naivasha, a temperature of 177°C was reached suddenly in a drill hole at 936m depth (Thompson and Dodson, 1963). Extrapolated to a few kilometers depth, melting temperatures for the rocks will be attained.

From a study of focal depths of intraplate earthquakes, Chen and Molnar (1983) established that the temperature at the source region is an important factor determining whether deformation occurs seismically or not. From estimates of the temperatures at depths of deepest events, they conclude that these limiting temperatures are 250°-450°C and 600°-800°C for crustal and mantle materials respectively. They deduce that in zones of continental extension focal depths are mostly shallower than 12-15 km. Most activity in the Basin and Range province, for example, occurs at depths of less than about 15 km where calculated temperatures are $350^{\circ} \pm 100^{\circ}C$.

Data from geothermal mapping along the Gregory rift using ground and aerial infrared techniques indicate that some 8835 to 21,915 MW are released in the form of geothermal cooling by both advection and conduction (Crane and O'Connel, 1983). It is estimated that from each kilometre of the rift a range of 14-35 MW is released. From a study of the compilations of heat flow data in Cainozoic rift systems a high mean heat flow, 105 mWm^{-2}, has been determined within the Kenya rift (Morgan, 1983). However, low to normal mean heat flow values, 57 and 39 mWm^{-2}, were determined for the volcanic flow covered shoulders of the rift to the west and east respectively. These low to normal mean heat flows compare well with the mean heat flow of 45 mWm^{-2} for cratons in Africa (Gass et al., 1978). Regions of abnormally

high heat flow within the Gregory rift are also associated with grid faulting, active volcanism and numerous hot springs.

The implication of the heat flow data within the confines of the Gregory rift is that partial melting accompanying high temperatures will occur at shallow crustal depths. Large focal depths are, therefore, improbable since rocks in partially molten state can not store enough strain energy for the generation of the observed tectonic earthquakes.

The axial zone of the Gregory rift is, in parts, associated with dense crustal intrusion indicated by a positive axial Bouguer anomaly (Searle, 1970; Baker and Wohlenberg, 1971) and confirmed by a depression in teleseismic delay time profile (Savage and Long, 1985) and a higher than normal crustal velocity (Griffiths et al., 1971). This instrusion which may be continuous with the upper mantle anomalous material is associated with higher than normal temperatures indicated by presence of steam jets, active volcanoes and high electrical conductivities (Banks and Ottey, 1974; Rooney and Hutton, 1977; Banks and Beamish, 1979; Morgan, 1983). It is probable, therefore, that earthquake foci may be located above this intrusion or within its relatively cool upper part.

Gravity interpretations suggest that the top surface of this crustal intrusion is in the depth range of about 0 to 20 km (Searle, 1970; Khanand Mansfield, 1971; Baker and Wohlenberg, 1971; Baker et al., 1972). Explosion data suggest that the top surface must be deeper than about 6 km (Swain et al., 1981) while teleseismic delay time studies put the depth at less than about 20 km (Savage and Long, 1985).

Molnar and Aggarwal (1971) studied microearthquakes in Kenya and showed that seismic activity was not restricted to

a central zone within the rift but was scattered through out the rift. In Lake Magadi area (about $2^{o}S$), approximate locations showed that depths of focus appeared shallow, less than about 15 km with a most probable value at about 5 km. In the Homa Bay area of the Kavirondo rift where about 300 microearthquakes were recorded per day, the focal depths were estimated at between 3 and 5 km. Foci in the central part of the rift covered in this analysis are, therefore, likely to be shallower than those in the regions discussed above. Further evidence in support of this expectation come from the interpretation of seismicity and geomagnetic deep sounding data.

Hamilton et al. (1973) investigated seismicity in the Gregory rift in the area of geothermal prospects near Lakes Naivasha and Hannington. In the region near Lake Naivasha focal depths were estimated at 3 to 4 km. In the Lake Hannington area focal depths as large as 6 to 10 km were observed although depths of 2 to 5 km were estimated for the southern end of the Lake. Data from a small aperture seismic network sited over an area covering Lake Bogoria and its surroundings show that local events within the lake occur at depths up to 14 km (Maguire et al., 1986).

Rykounov et al (1972) studied local earthquakes in the southern part of the Gregory Rift from Lake Magadi in Kenya to Mount Hanang in Tanzania. The magnitudes of earthquakes studied were in the range 0.5-3.5; this range is similar to the magnitude range of 1.8-3.1 (Arnold, personal communication) covered by earthquakes used in the present analysis. Their survey covered a latitude range from about $2^{o}S$ to $4.5^{o}S$. Histograms for focal depth distributions (fig. 4.3) show that for rift earthquakes, the most probable focal depth is 10-20 km (nearer 10 than 20 km).

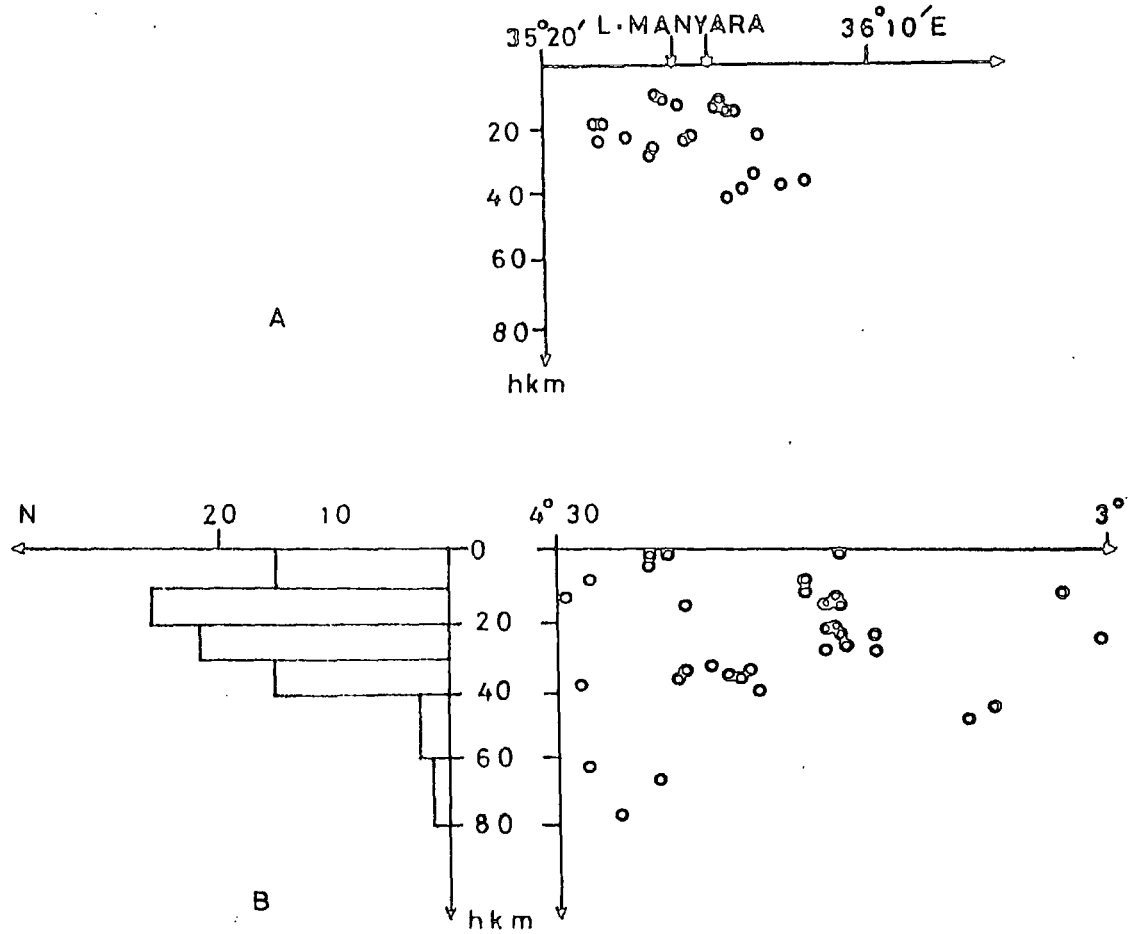

Fig.4.3: Vertical distribution of earthquake foci.
A. From east to west through Lake Manyara.
B. Along the southern part of Gregory Rift.
(Rykounov et al., 1972)

However this region has near normal shield type structure and foci may therefore be expected to be deeper there than in the region of the present study where extreme thinning of the lithosphere has been established.

Geomagnetic deep sounding experiments in and around the Gregory rift have shown that currents are concentrated by three regions with high electrical conductivity (Banks and Beamish 1979; Beamish, 1977; Banks and Ottey, 1974). Two of the anomalies are related to the rift structure, and other geophysical evidence strongly suggests that the high conductivity is due to the presence of molten material in the rocks of the lower crust and the upper mantle. The shallower crustal zone of partial melt is located directly beneath the rift floor. Its upper surface is no deeper than 20 km; it probably may be as shallow as 5 km.

From magnetotelluric data, the shallow conducting zone is interpreted in terms of high temperatures and water saturation in the crust (Rooney and Hutton, 1977). The top surface of this crustal zone is estimated at a depth of less than 8 km. This zone underlies the part of the rift studied here.

Thus on the strength of available geological and geophysical evidence, focal depths of more than about 20 km are unlikely in the part of the Gregory rift zone covered in the present analysis (i.e. the rift within about 0.5°N). An average focal depth of about 5 to 10 km would seem realistic.

4.6 Estimating epicentral distances from P-X times.

P-X times, t, for the 11 selected local eastern events were measured from the outputs of seismometer Y1 (or R1 if Y1 was not functioning) and are shown in table 4.1. These measurements were

Event number	P-X time (seconds)	Apparent azimuth (degrees)
1	8.1	102
2	8.2	94
3	8.2	95
4	8.3	74
5	9.0	87
6	9.1	94
7	9.7	106
8	9.8	88
9	10.3	107
10	10.8	106
11	11.7	114

Table 4.1 : Measured P-X times and azimuths for the 11 local rift events to the immediate east of Kaptagat.

made on records obtained from fast paper playouts to improve precision in the determination of t. The uncertainty in the measurement of t was better than about $\pm$0.5s in most of the records. The main source of error was the uncertainty in the determination of onset of X; the first arrival P-wave onset was impulsive and easy to read. In this section the epicentral distances are derived from the measured values of t.

In section 4.4, it was suggested that X could be surface waves, direct waves, reflections or headwaves of S or P phases. From measured values of apparent velocity, it was shown, however, that the onset of X is preceded by and is close to the onsets of phases suspected (on the bases of their measured velocities) to be S and/or surface waves. X onset time may, therefore, be an overestimate of onset time for S waves. Derivation of distance from t does not here assume that the identity of the phase X is known.

To derive distances from P-X times, knowledge of the structural model and of focal depth is required along with the identity of X. None of these is known initially. However, two structural models for the Gregory rift zone have been established, one for the western flanks at the latitude of Kaptagat and the other for the axial part of the rift (Maguire and Long, 1976; Griffiths et al, 1971). The details of these models are discussed in section 1.5. These models were used in the way described below to estimate epicentral distances from P-X times.

For each of the two models, differences in travel times between the first arrival P wave and each of the prominent later arrival phases were calculated as a function of epicentral distance, Δ. The arrivals considered were direct waves, head

waves and reflections of P and S modes as well as surface waves. In estimating S velocity from known P velocity, the ratio R of P wave velocity to S wave velocity was assumed as 1.74 as discussed in section 4.3. Recorded surface waves would be expected to be predominantly Rayleigh waves because the seismograms were written by vertical component instruments which normally have poor response for horizontal earth motion characteristic of Love waves. A Rayleigh wave rock velocity was deduced from the S wave velocity in the top layer. The range of distance covered was from 0 to about 250 km in steps of 10 km. For each phase, focal depths of 0,5 and 15 km were used in calculating differences in travel times for the corresponding propagation path. The plots of distance against time difference are shown in fig. 4.4 and the labels on this diagram are explained in table 4.2.

A mean line PQ, put centrally through the set of curves in fig. 4.4 gives the desired mean relationship between P-X times, t, and epicentral distance, Δ. Although it has been supposed that X could be any of the phases plotted, it should be emphasized that the velocity data is more in favour of X being S or surface waves than other phases.

To arrive at the average line PQ, it was necessary first to eliminate some curves that are obviously not consistent with the observed P-X times. For example curves labelled 8,12, 22 and 26 are not relevant to the present data because they suggest distances which could lead to apparent velocities significantly higher than measured apparent velocities. Furthermore, curves 8, 12 and 22 suggest that time difference decreases with increase in distance contrary to observations. Curves, like

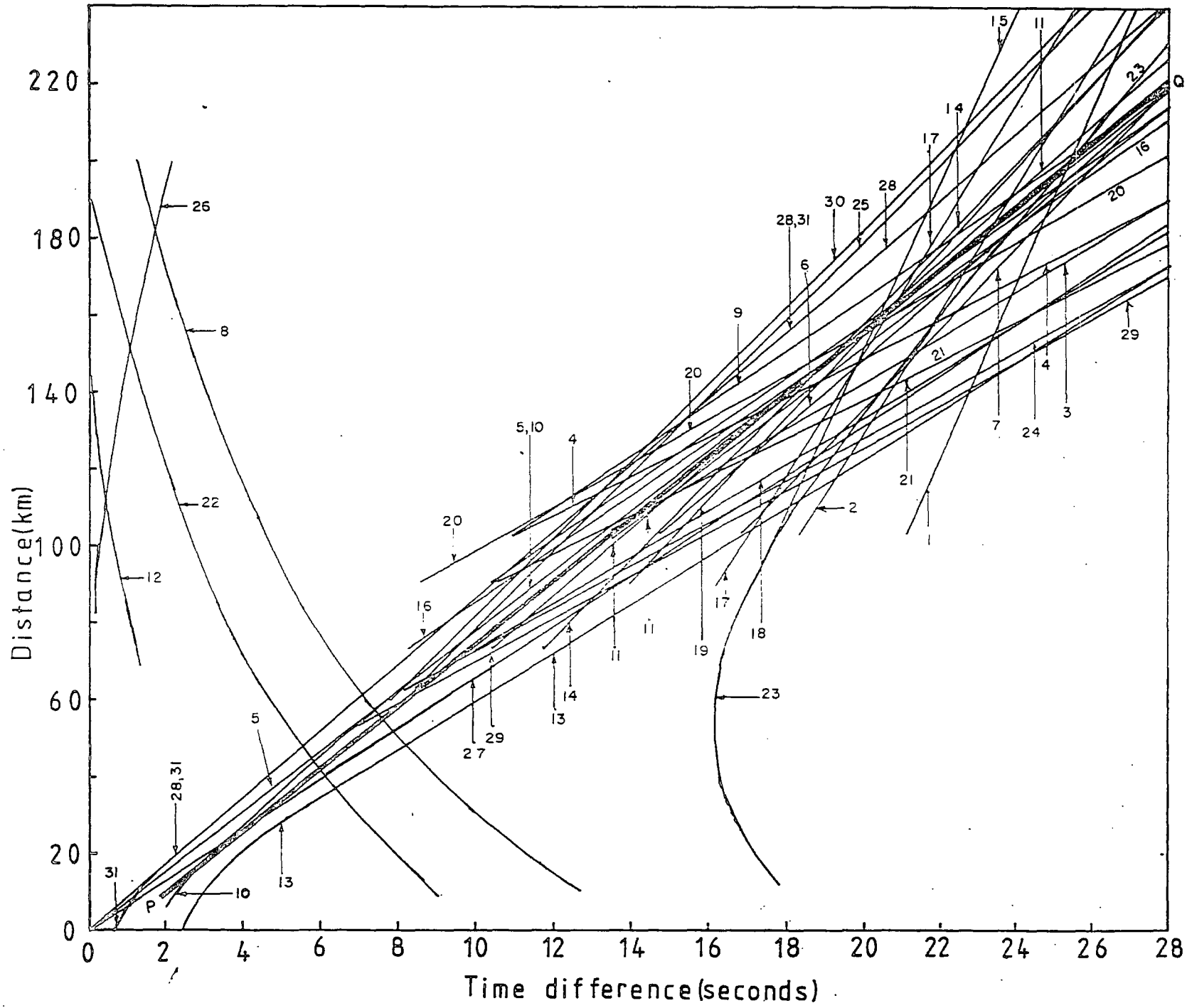

Fig.4.4: Plot of epicentral distance against time difference between selected pairs of phases.

Table 4.2 Explanation of labels on the curves of distance against time difference shown in fig. 4.4.

Label	Model	Time difference (seconds)	Focal depth (km)
1	Maguire and Long (1976)	Sn-Pg	0
2	"	Sn-P*	0
3	"	Surf.-P*	0
4	"	Surf.-Pn	0
5	"	Sg-Pg	0
6	"	S*-P*	0
7	"	S*-Pg	0
8	"	Pm-Pg	0
9	"	Sg-P*	0
10	"	Sg-Pg	15
11	"	S*P*	15
12	"	S*-Pg	15
13	"	Surf.-Pg	15
14	"	S*-Pg	15
15	"	Sn-Pg	15
16	"	Sg-P*	15
17	"	Sn-P*	15
18	"	Surf.-P*	15
19	"	S*-Pn	15
20	"	Sg-Pn	15
21	"	Surf.-Pn	15
22	"	Pm-Pg	15
23	"	Sm-Pg	15
24	Griffiths et al (1971)	Surf.-P*	0
25	"	S*-P*	0
26	"	PIP-P*	0
27	"	Surf.-Pg	0
28	"	Sg-Pg	0
29	"	Surf.-P*	5
30	"	S*-P*	5
31	"	Sg-Pg	5

that labelled 23, which are outside the observed range of P-X times were not considered in obtaining the mean line PQ.

The thick line PQ is estimated as the best line through the set of lines and represents the required average relationship between P-X times, t, and distance, Δ. Measured values of t were converted to Δ using this line whose equation is of the form

$$\Delta = a + bt$$

where a and b have the values -6.3 km and 8.1 kms^{-1} respectively for focal depths in the range 0 to 15 km. The expression is, of course, valid for the range of t covered by the data.

The range of t covered by the present data is from about 8.0s to about 12.0s. From line PQ, this range of t corresponds to a range of distance from about 59 km to about 91 km. Fig. 4.4 gives a range of distance for a given time difference, t. At time difference of 8.1s, line PQ in fig. 4.4 gives a mean value of 59 km for Δ with an uncertainty of $\pm$ 16 km. But P-X time is typically about 9.0s and the estimated uncertainty at this value of t is $\pm$ 13 km. This estimate of uncertainty applies to small distances and include closein events from the east and the local western events from the Kavirondo gulf whose P-X times are within the stated limit. For the more distant rift events to the north and to the south, measured values of P-X times range up to about 25s and the uncertainty in the estimate of distance is certainly greater.

It is probable that the estimates of distance and its uncertainty given above may be exagerrated. A close look at fig. 4.4 in the time difference range from 8.0s to 12.0s shows that the plotted lines are enveloped at the top by lines 28 and

31 and at the bottom by line 13. Lines 28 and 31 represent S_g-P times while line 13 represents Surface - P_g time. It is unlikely that S_g will have the high amplitude observed in the X arrivals. If lines 28 and 31 are ignored, the estimated average line would move down towards lines 13 and 27 which represent Surface - P_g times for focal depths and models indicated in table 4.2.

It is reasonable, therefore, to consider also the use of surface wave times as one possible alternative for converting P-X times to distances. The relevant surface wave lines are 13, 27 and 29. The average line through these three lines gives a relation of the form

$$\Delta = a + bt$$

where a and b have values 0.7 km and 6.5 km/s respectively. This relation shows that if t is increased from 8.0s to 12.0s, Δ increases from 53 km to 79 km; this suggests smaller values of distance than estimates based on the average line PQ.

The derived distances (table 4.3) were combined with the corresponding measured azimuths to locate the epicentre in relation to the rift structure (fig. 4.5) and the gravity map of the area (fig. 4.6). The open circles in fig. 4.5 and fig. 4.6 represent epicentres based on the use of surface waves. The blackened circles represent epicentres derived from the average line PQ in fig. 4.4. If X were actually surface or S waves, it is clear that location based on line PQ would tend to push epicentres further to the east than they really should be. However, from fig. 4.5 and fig. 4.6 the epicentres are all located within the confines of the rift and in a part of the rift where the Bouguer anomaly is flat.

Event number	P-X times (seconds)	Apparent azimuth (degrees)	Apparent velocity (km/s)	Distance in kilometres	
				Based on average line PQ	Based on regarding X as surface waves
1	8.1	102 ± 4	7.1 ± 0.5	59	53
2	8.2	94 ± 5	7.2 ± 0.3	60	54
3	8.2	95 ± 4	7.3 ± 0.2	60	54
4	8.3	74 ± 2	7.0 ± 0.2	61	55
5	9.0	87 ± 2	7.3 ± 0.2	67	59
6	9.1	94 ± 2	7.5 ± 0.2	67	60
7	9.7	106 ± 2	7.5 ± 0.4	72	64
8	9.8	88 ± 2	7.0 ± 0.2	73	64
9	10.3	107 ± 2	6.9 + 0.5	77	68
10	10.8	106 ± 2	7.0 ± 0.2	81	71
11	11.7	114 ± 2	6.9 ± 0.2	88	77

Table 4.3. Estimated epicentral distances for close in local rift events to the immediate east of Kaptagat. The corresponding P-X times and first arrival apparent velocities and azimuths are also shown.

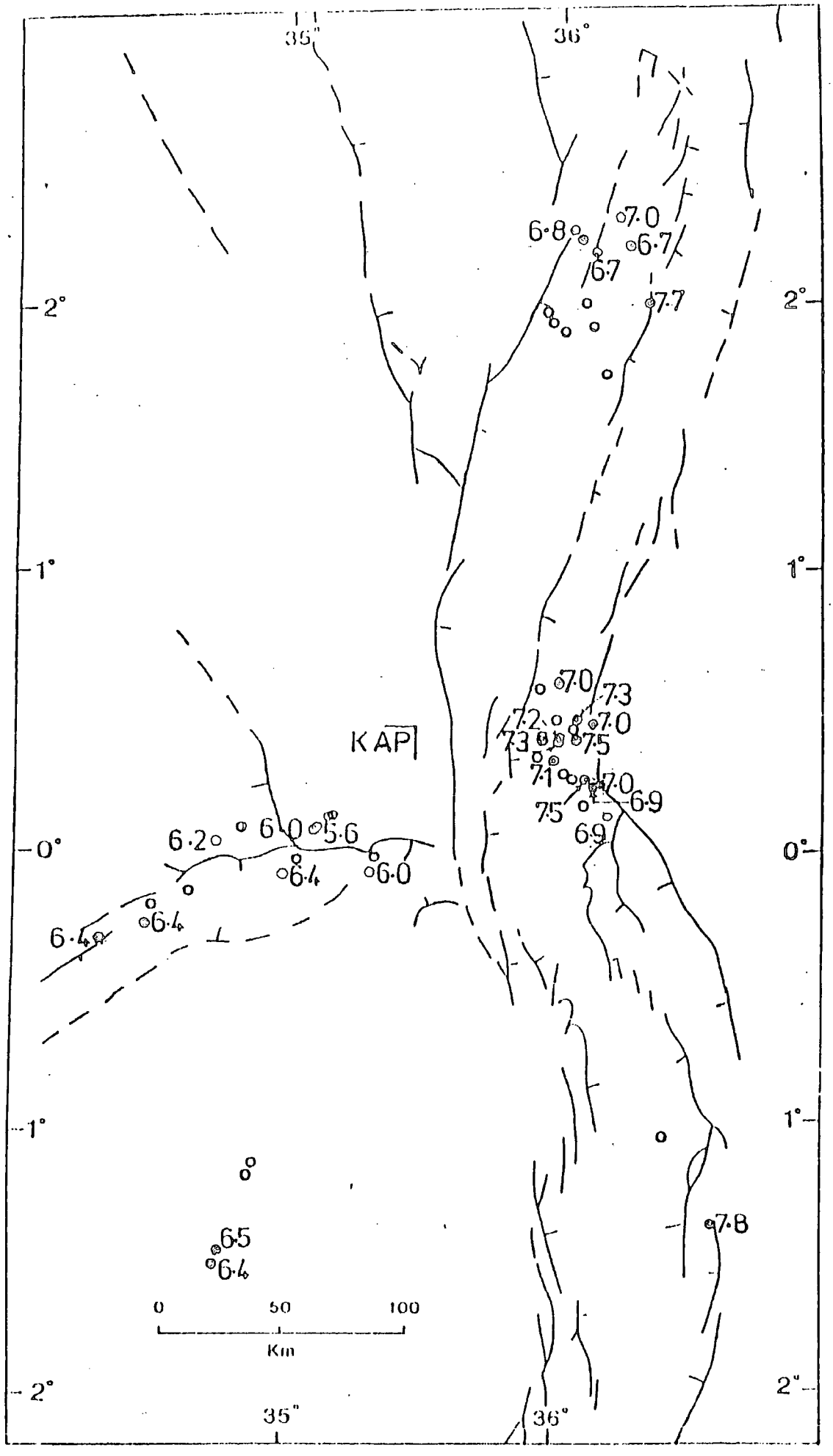

Fig 4·5a: Location of epicentres (black circles) in relation to the rift structure. Figures indicate first arrival velocities in km/s.

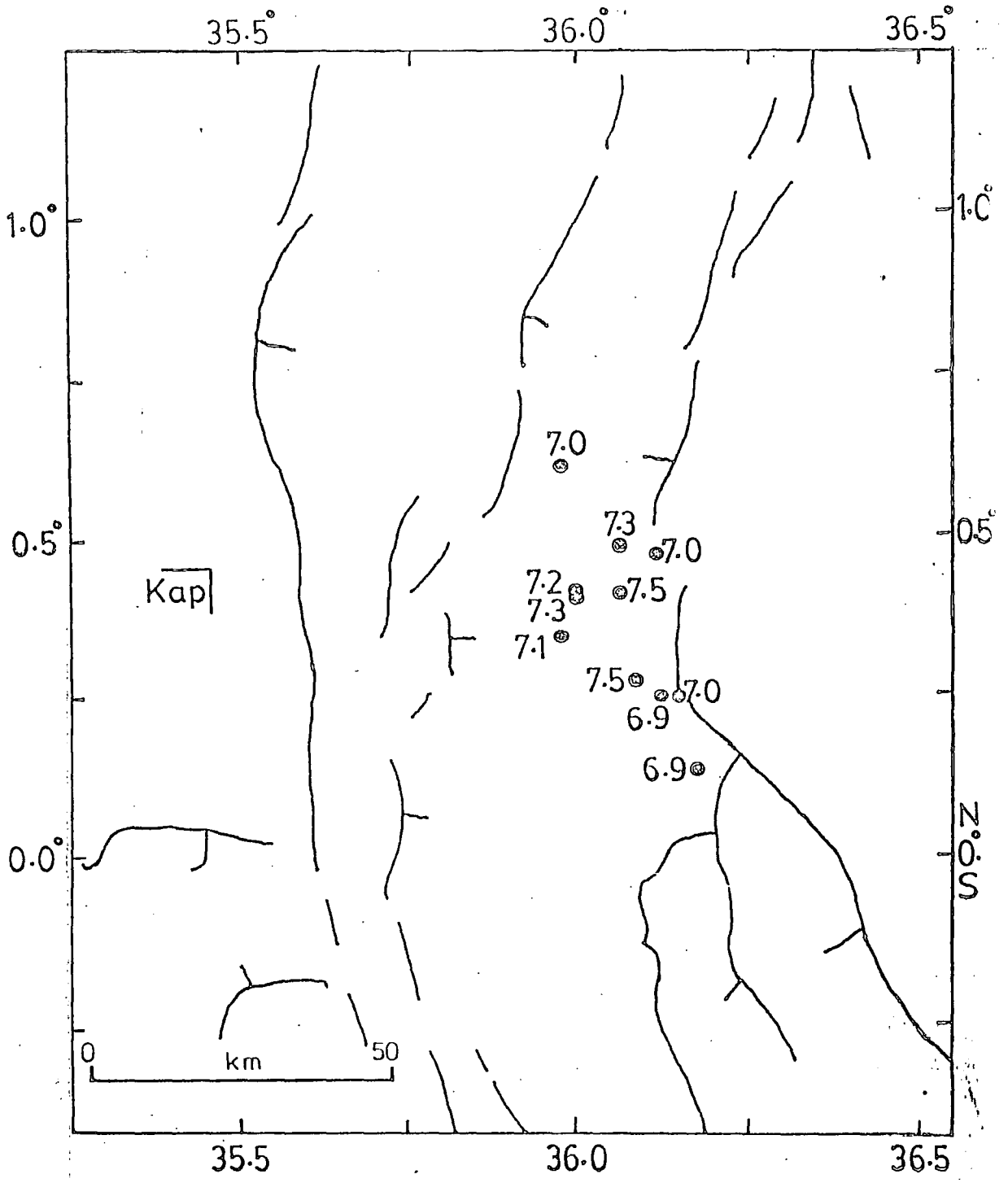

Fig 4·5b: Location of epicentres of local events to the immediate east of Kaptagat in relation to the rift structure·Figures indicate first arrival apparent velocities in km/s·

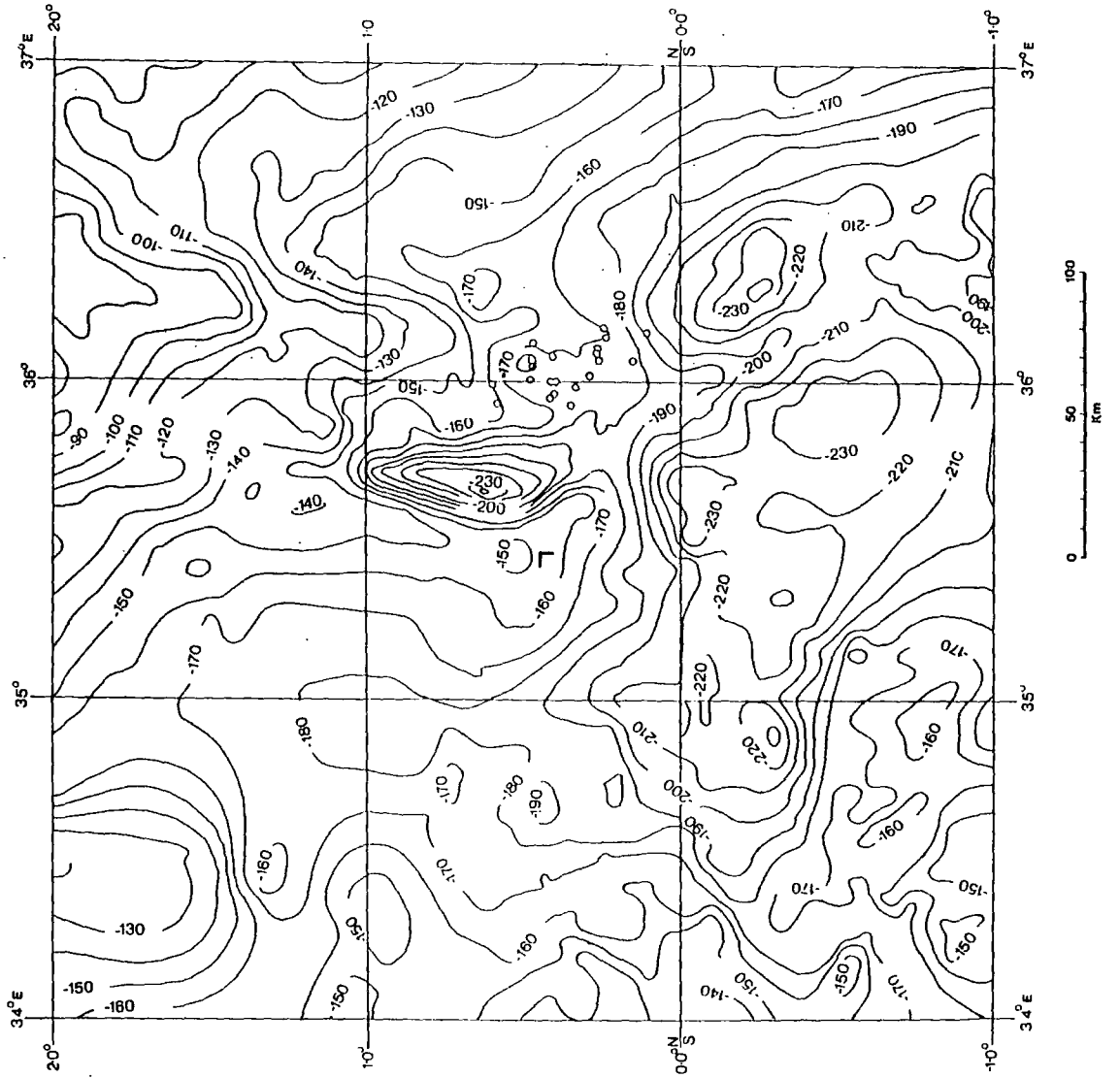

Fig. 4·6a: Location of epicentres of the immediate eastern local events in relation to the Bouguer anomaly map. Contour intervals are in mgals.

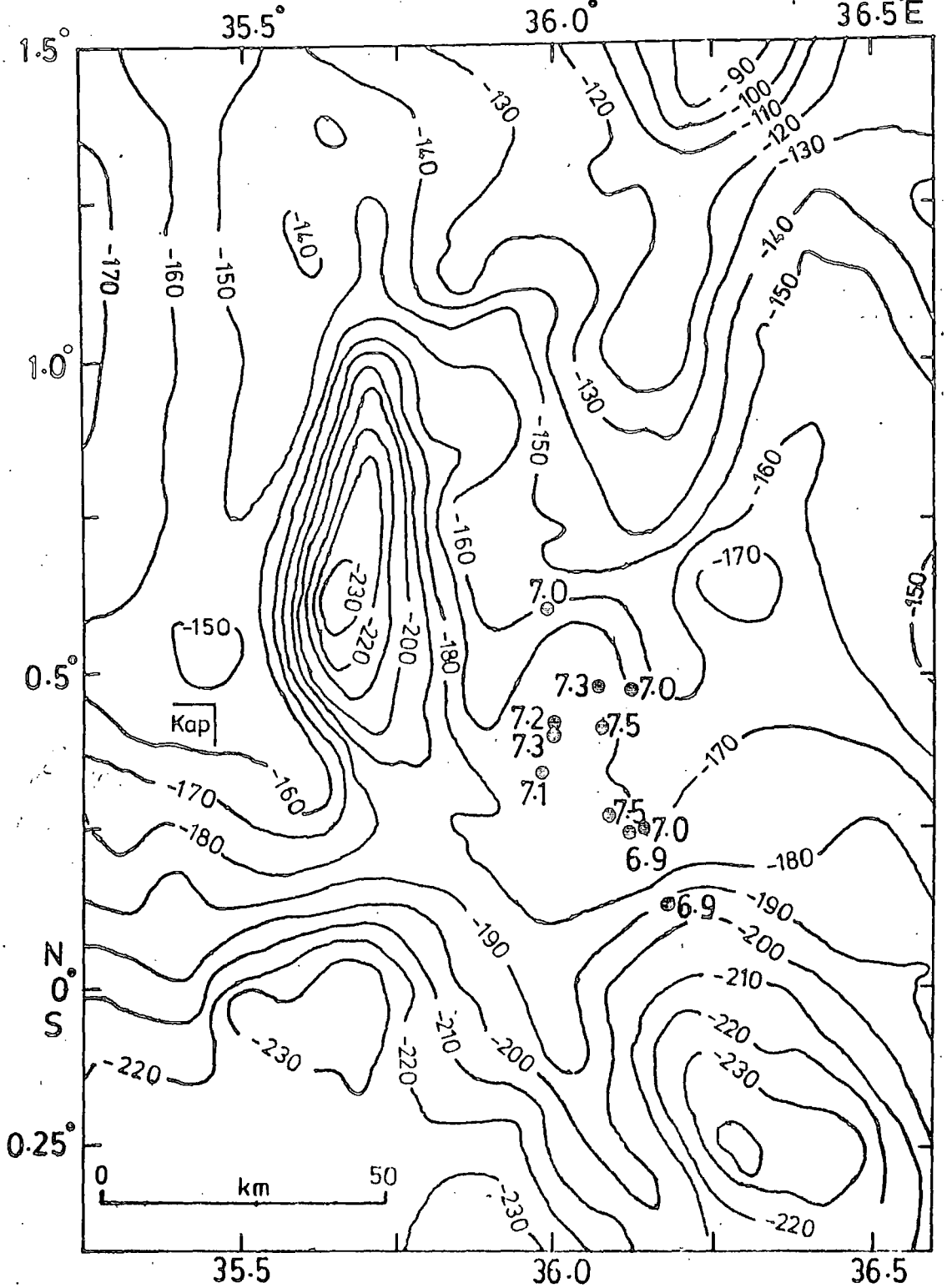

Fig 4·6b Location of some epicentres in relation to the Bouguer anomaly map of central part of the rift. Contour values are in mgals. Other figures represent event first arrival apparent velocities in km/s.

In fig. 4.7, the epicentres are located in relation to the zone of conductivity anomalies inferred from geomagnetic deep sounding data (Banks and Beamish, 1979). The epicentres are found to lie mostly within the zone in the central part of the rift beneath which melting is suggested at shallow crustal depths. This supports the argument for very shallow foci (see section 5.3).

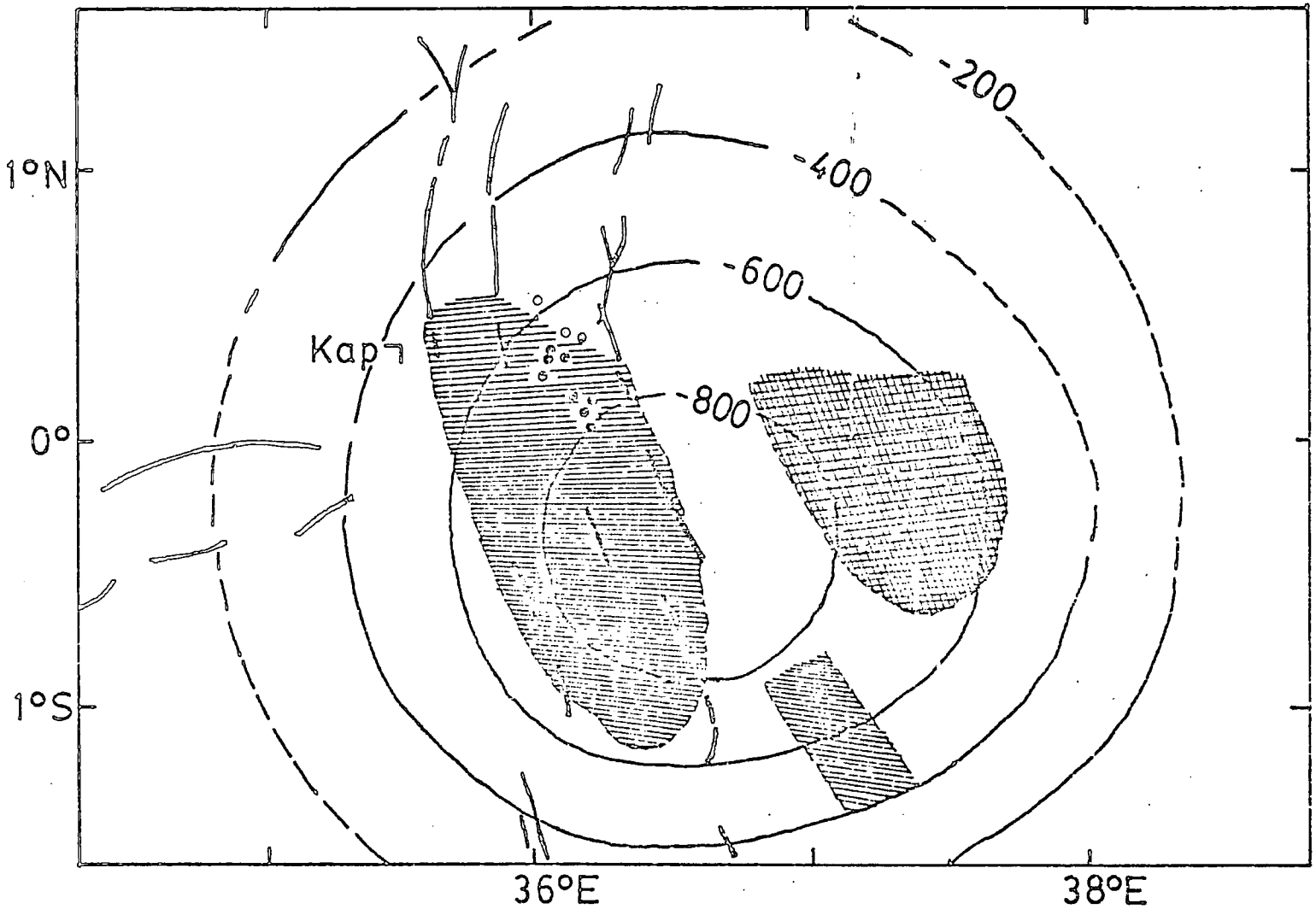

Fig 4.7: Location of epicentres (black circles) in relation to the conductivity anomalies (shaded). Cross-hatching indicates a deep conductor; the others are shallow. The contours are estimates of the long wavelength Bouguer anomaly specifically associated with the dome with values in μms^{-2}. Redrawn from Banks and Beamish (1979).

CHAPTER 5

INTERPRETATION OF CLOSE IN EASTERN RIFT DATA IN TERMS OF PLANE LAYERED MODELS.

5.1 Introduction.

Away from the rift zone Africa has a structure similar to that found in normal continental shield zones (Gumper and Pomeroy, 1970). These zones are characterised by thick crust and high crustal and sub-Moho velocities. In East Africa, this shield structure extends up to the western and probably eastern flanks of the Gregory rift (Maguire and Long, 1976; Herbert and Langston, 1985) in close proximity to the anomalous structure established to exist beneath the axial part of the rift floor (Searle, 1970; Baker and Wohlenberg, 1971; Maguire and Long, 1976; Savage and Long, 1985). Beneath the Gregory rift floor, available geological and geophysical data indicate that the lithosphere is extremely thinned (or ruptured?) and the upper mantle exhibits anomalously low values of density and seismic velocity. A steep boundary between the shield structure on the flanks and the anomalous rift structure is, therefore, suggested.

This chapter further investigates the structure of the crust/lithosphere beneath the Gregory rift at the latitude of about 0.5^{o}N under the constraints of available geological and geophysical data. For this interpretation we use the apparent velocity data from closein events located ,within the rift to the immediate east of Kaptagat.

5.1.1 The gravity starting model.

East-west Bouguer gravity profiles across East African plateau show a long wavelength negative anomaly over areas more

than about 1000 m in elevation with superimposed negative anomalies over the eastern and western rifts. The long wavelength anomaly has been interpreted as the effect of a body of low density asthenosphere material which has replaced normal upper mantle (Sowerbutts, 1969; Darracot et al., 1969; Khan and Mansfield, 1971; Baker and Wohlenberg, 1971; Fairhead, 1976). But the details of the models produced by these workers differ (see section 1.5.2 and fig. 1.6).

Over the axial part of the Gregory rift there is a positive ridge of short wavelength (40-80 km) low amplitude (30-60 mgal) anomaly superposed on the long wavelength Bouguer anomaly. This positive anomaly has been interpreted in terms of a dense basaltic mantle - derived crustal intrusion probably continuous with the low density asthenosphere material in the upper mantle. Estimates of the depth to the top surface of this crustal intrusion are given as about 2 km (Searle, 1970; Baker and Wohlenberg, 1971), 3.5 km (Fairhead, 1976) and 20 km (Khan and Mansfield, 1971) for latitudes 0^{o}, 1.1^{o}S and 1.0^{o}N respectively. The width of the intrusion within the crust is estimated as 6 km (Fairhead, 1976), 10 km (Baker and Wohlenberg, 1971) and 20 km (Searle, 1970).

The character of the axial positive anomaly varies along the length of the rift. Differences in estimates for the width and depth to the top surface of the crustal intrusion could, therefore, be due to different authors interpreting profiles at different latitudes. The thicknesses and densities of the lavas and sediments that lie beneath the rift floor may also vary along the length of the rift; this could partly explain the rather large estimate for the depth to the top of crustal

intrusion obtained by Khan and Mansfield (1971).

The preferred gravity model is that from Baker and Wohlenberg (1971) which is shown in fig. 5.1a. The anomalous region is shaded. This model agrees well with the seismic model obtained by Savage and Long (1985) for the Gregory rift at about the equator (see section 5.1.2).

5.1.2 The seismic starting model.

First arrival data from local earthquakes recorded at Kaptagat array station show that normal shield crust with normal sub-Moho velocities exist beneath the immediate western flank of the Gregory rift not farther than 50 km from the rift axis (Maguire and Long, 1976). The crust on the western flank is about 44 km thick and two layered with upper crustal, lower crustal and sub-Moho P-wave velocities of 5.8, 6.5 and 8.0 km/s respectively.

Analysis of teleseismic body and surface wave data recorded at Lwiro on the western flank and Nairobi on the eastern flank suggest that the crust beneath the two flanks of the Gregory rift are similar and shield type with an average thickness of about 40 km (Bonjer et al., 1970; Mueller and Bonjer, 1973; Herbert and Langston, 1985).

Basement rocks of velocity 5.7/5.8 km/s exist throughout the width of rift beneath volcanic sediments at about 0.5^{o}N (Swain et al, 1981; King et al. 1978). The thickness of the 5.8 km/s material is unknown but it is probably more than about 6 km. Beneath the axial zone of the Gregory rift, a high density mantle derived crustal intrusion is inferred from gravity data (see section 5.1.1). This high density intrusion

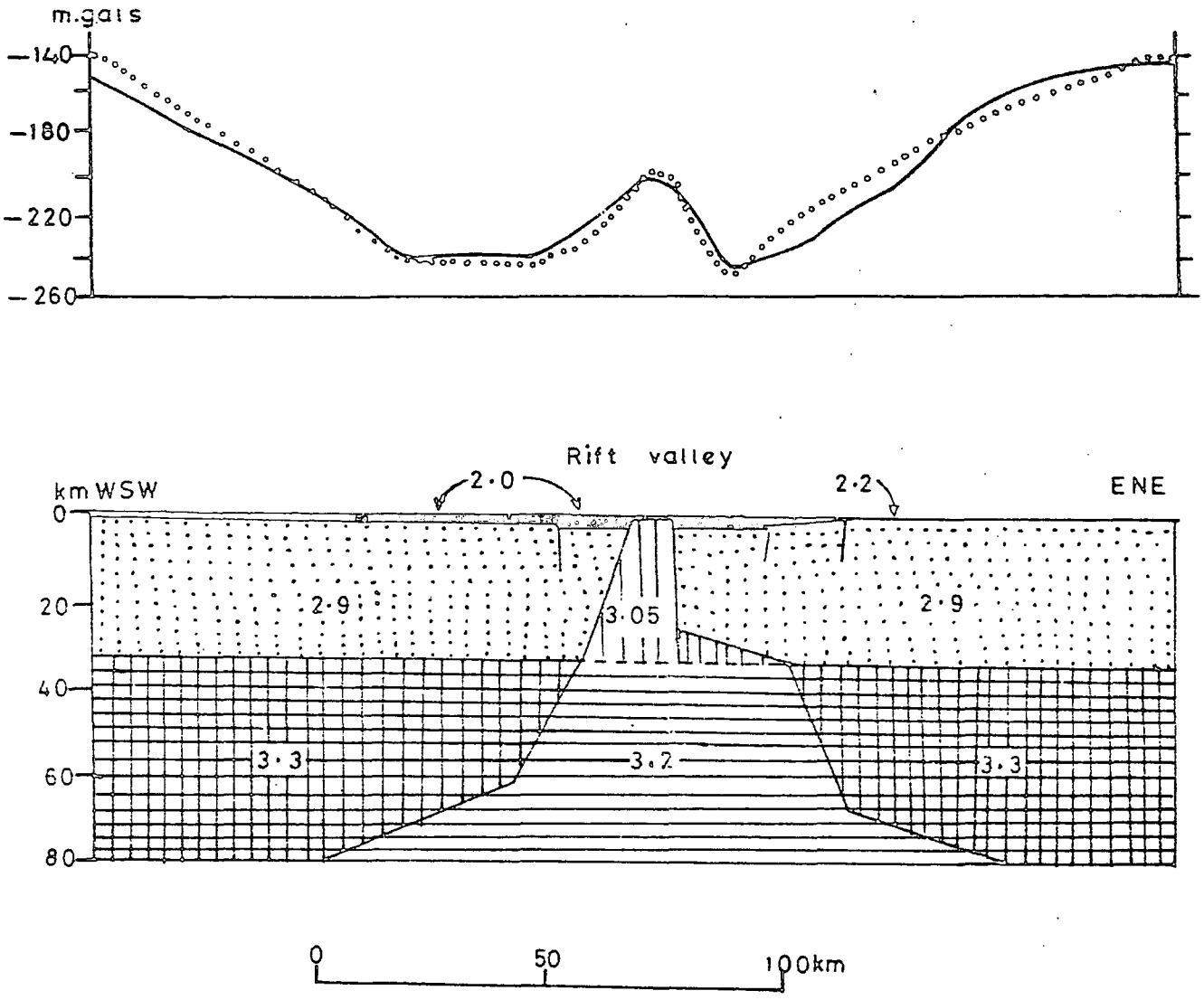

Fig.5.1a. Bouguer gravity profile and crustal model of the central Gregory rift (Baker and Wohlenberg, 1971).

would be expected to have higher seismic velocities than the intruded crustal rocks and hence its presence could be confirmed by seismic refraction data.

The refraction data of Griffiths et al. (1971) has been used to deduce a crustal model for the axial zone of the northern part of the Gregory rift. As has been discussed in section 1.4.4, the data were effectively unreversed. From shots in Lake Bogoria (Hannington), a "headwave" with velocity of 6.4 km/s was recorded whereas a 7.5 km/s "headwave" was recorded from shots in Lake Turkana (Rudolf) in a similar distance range. This observation suggests strong lateral variation in velocity and/or relatively large dips on the main refractor interface. The data could not, however, be interpreted in terms of a dipping refractor because it was inconsistent with large dips. The data was consequently interpreted in terms of a horizontal layer of material of velocity 6.4 km/s overlying a material of 7.5 km/s at a depth of about 20 km. A velocity of 6.4 km/s is definitely higher than normal for the upper crust of the shield type and establishment of the existence, within the upper crust, of material with such high velocity would support gravity interpretation of the positive axial gravity ridge. However, the refraction data of Griffiths et al. (1971) does not establish the existence of a 6.4 km/s material within the upper crust. The data can, therefore, not be used as a seismic evidence for the crustal intrusion inferred from gravity data but it is not inconsistent with the gravity data.

Maguire and Long (1976) used some first arrival seismic data from Kaptagat array station to derive a model for the crust beneath the Gregory rift at about 0.5^{o}N. They studied

rift events with P-S times less than about 15s and coming from the immediate east of Kaptagat. These events from similar azimuths and with similar P-S times showed two distinct statistically seperate apparent velocities of 7.9 $\pm$ 0.3 km/s and 7.1 $\pm$ 0.3 km/s. No firm explanation was given for the 7.9 km/s group of arrivals.

From the 7.1 km/s group of arrivals, they infer the existence of anomalous material (beneath the rift axis) whose true velocity is less than 7.5 km/s and probably greater than 7.1 km/s. This material may exist beneath a zone of 6.4 km/s material inferred from explosion data (Griffiths et al., 1971). No depth estimate for the top of the 7.1-7.5 km/s material was obtained from the data. But the data, however, strongly suggests that a steep structural boundary seperates the normal shield crust to the west from the anomalous rift structure to the east. The position and slope of the boundary was not determined from the data.

Savage and Long (1985) measured vertical teleseismic delay times for profiles across the Gregory rift near the equator and along a SE radius of the Kenya dome. Their mean rift model was based on data from stations along and across the rift between the equator and 1^{o}S.

For the section across the rift they observed significantly smaller delay times at the centre of the rift than at the edges. This observation was interpreted to indicate that anomalous mantle zone penetrates the crust to form an intrusion of relatively high velocity material along the rift axis. There was a clear correlation between delay time low and the axial Bouguer gravity high indicating that both are caused by the

same underlying structure.

The modelling assumes a uniform crustal structure exists both to the east and to the west of the rift as derived from Kaptagat data (Maguire and Long, 1976) and that the P-wave velocity for the anomalous zone at crustal depths is 7.5 kms^{-1} as recorded by Griffiths et al. (1971) along the rift axis to the north. With these reasonable assumptions, the width of the intrusion at the level of normal Moho was well defined at some 30 km. The delay time results, therefore, provide a further independent confirmation of the existence of the axial intrusion previously inferred from gravity and seismic data (Baker and Wohlenberg, 1971; Griffiths et al 1971). Although it is likely that there are lateral and vertical changes in velocity within and surrounding the anomalous mass, the data could not give these details.

Interpretation of data from a 300 km long seismic refraction line along the axis of the southern portion of the Gregory rift (from Lake Baringo to Lake Magadi) shows a variation of up to 4 km in the depth to the basement (Khan et al., 1987). It also shows that basement velocity increases from about 6.1 km/s at a depth of about 2 km to 6.25 km/s at 10 km depth. Material of velocity 6.35 km/s is inferred to exist between depths of about 10 and 15 km. Further details of this model have been discussed in section 1.7.4.

On this model (Khan et al., 1987), the average crustal velocity from the top of the basement to a depth of about 20 km is 6.34 km/s. This is comparable to the 6.4 km/s average velocity indicated by the data of Griffiths et al. (1971) for a similar depth range for the axial part of the northern portion of the rift. Such velocities for the upper crust are significantly

higher than the values (about 5.8 km/s) observed off the rift axis (Swain et al., 1981; Maguire and Long, 1976). The inferred high upper crustal velocities together with observed increase in velocity with depth are consistent with the theory that the rifting process is associated with some form of convected heat from below the lithosphere.

It is to be observed that the data of Khan et al.(1987), although more detailed, are in broad agreement with the results of Griffiths et al.(1971) especially with respect to average velocities in the upper crust. The difference in velocities obtained for the deeper structure suggests possible variations in structure along as well as across the rift.

Data from Swain et al.(1981), Maguire and Long (1976) and Savage and Long (1985) are from approximately the same E-W profile across the Gregory rift as the present data. They are not inconsistent with the data of Griffiths et al.(1971). In the present study, an average basement velocity of 5.8 km/s is initially adopted both within and outside the confines of the rift proper. The two dimensional seismic starting model for the crust in and around the Gregory rift near the equator is shown in fig. 5.1b.

In figure 5.1c the gravity model of Baker and Wohlenberg (1971) is compared with the seismic model of Savage and Long (1985); the top surface of the latter is shown by the dashed line. There is a broad agreement between the two models although the seismic model suggests a more restricted intrusion at Moho depths.

5.2 The data.

The epicentres of earthquakes part of whose records are used in the present study of the rift structure are shown by the black circles in fig. 4.5a. In the present analysis for the study of the rift structure we use data from local rift earth-

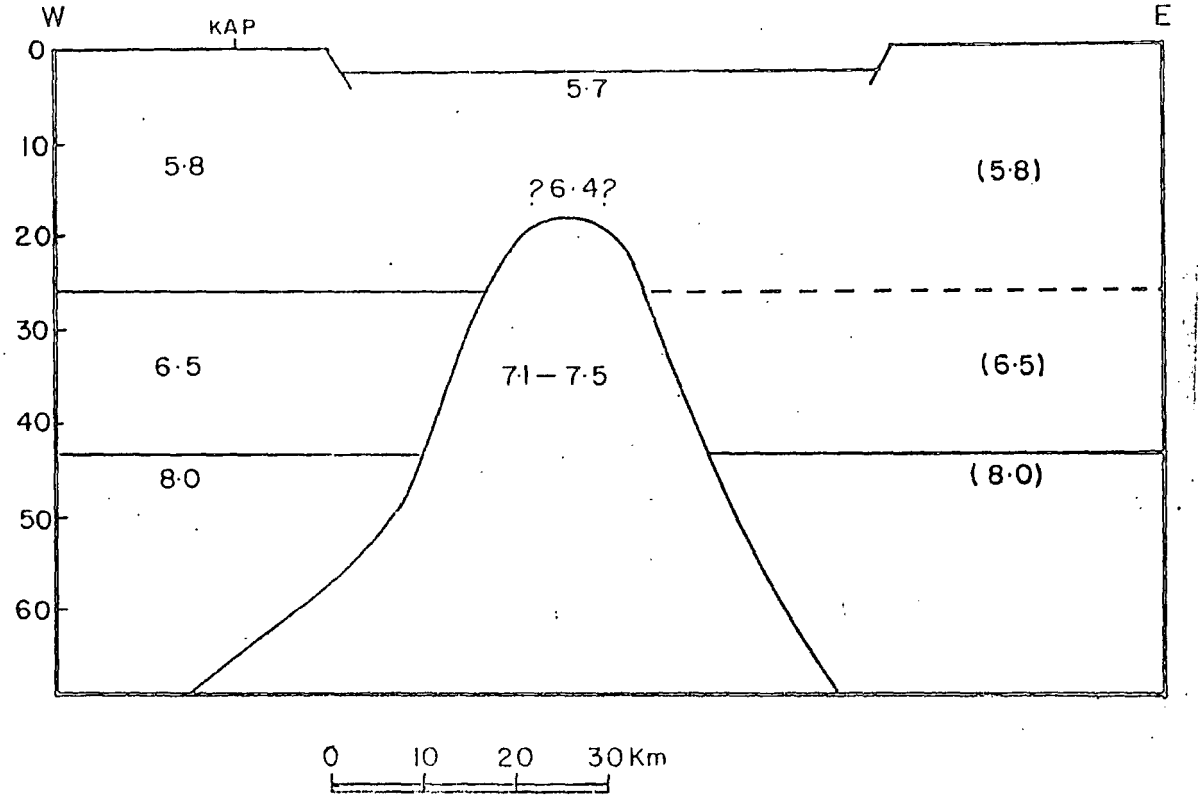

Fig. 5·1b: Seismic crustal model for the Gregory rift at the latitude of about 0·5°N. Depths are in km. and velocities in Km/s. (Maguire and Long, 1976; Griffiths et al; 1971; Swain et al; 1981; Savage and Long, 1985)

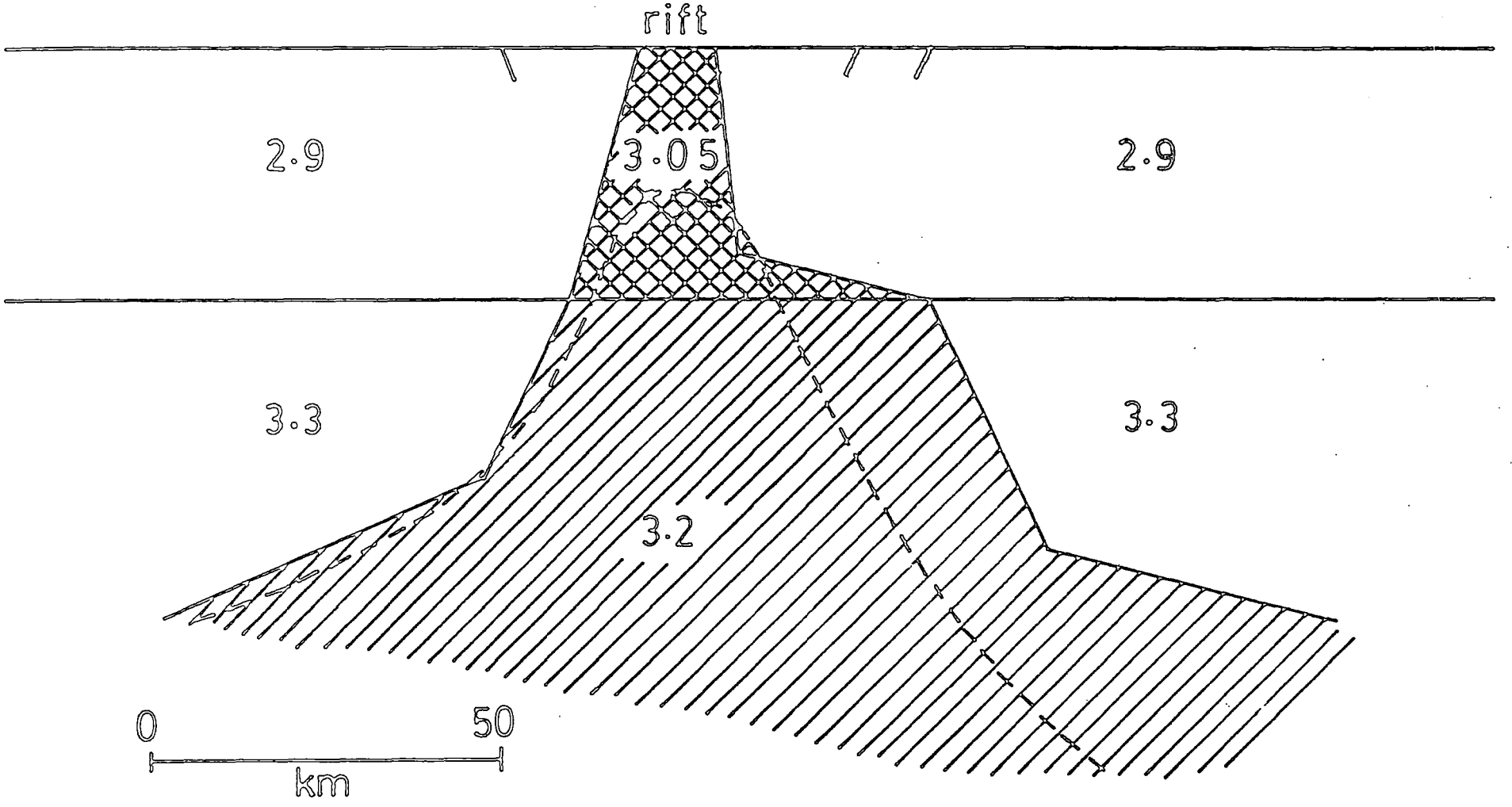

Fig. 5·1c : A gravity model from Baker and Wohlenberg (1971). For comparison, the top surface of the seismic model of Savage and Long (1985) is shown by the dashed line. Numbers are densities in g cm-3 .

quakes originating from the immediate east of Kaptagat. Ray paths from the more distant rift events to the north and south may not have sampled the rift structure. The epicentres of the immediate local closein eastern rift earthquakes in relation to the rift structure and to the Bouguer gravity map of the region are shown in fig. 5.2a and fig. 5.2b which are reproduced from fig. 4.5b and fig. 4.6b respectively.

These epicentres are located in a zone (within the wide axial Baringo trough lying between the Kamasia hills and Laikipia escarpment) where the axial positive Bouguer gravity anomaly appears flat (fig. 5.2b). In this region, basement rocks (density 2.7 g cm^{-3}) are overlain by over 3000 m of Miocene lavas and sediments (Chapman et al., 1978) whose densities are in the range 2.0 to 2.26 g cm^{-3} (Swain et al., 1981). These low density sediments (if not properly corrected for) may have the necessary density contrast to reasonably flatten the anomaly over the observed range of distance. The flat nature of the positive axial anomaly could also be explained by the geometry of the causative intrusion; it is consistent with an intrusion of approximately rectangular section whose top and bottom surfaces are nearly horizontal as suggested by Swain et al (1981).

5.2.1 Comparison with the data of Maguire and Long (1976).

Records for the present study are drawn from the same source as the records used to generate the data of Maguire and Long (1976). Their data set is shown in fig. 5.3a. For comparison, the present data is shown on the same scale in fig. 5.3b. We concentrate on the closein immediate eastern rift events for the study of the rift structure.

The apparent velocities observed in the present analysis

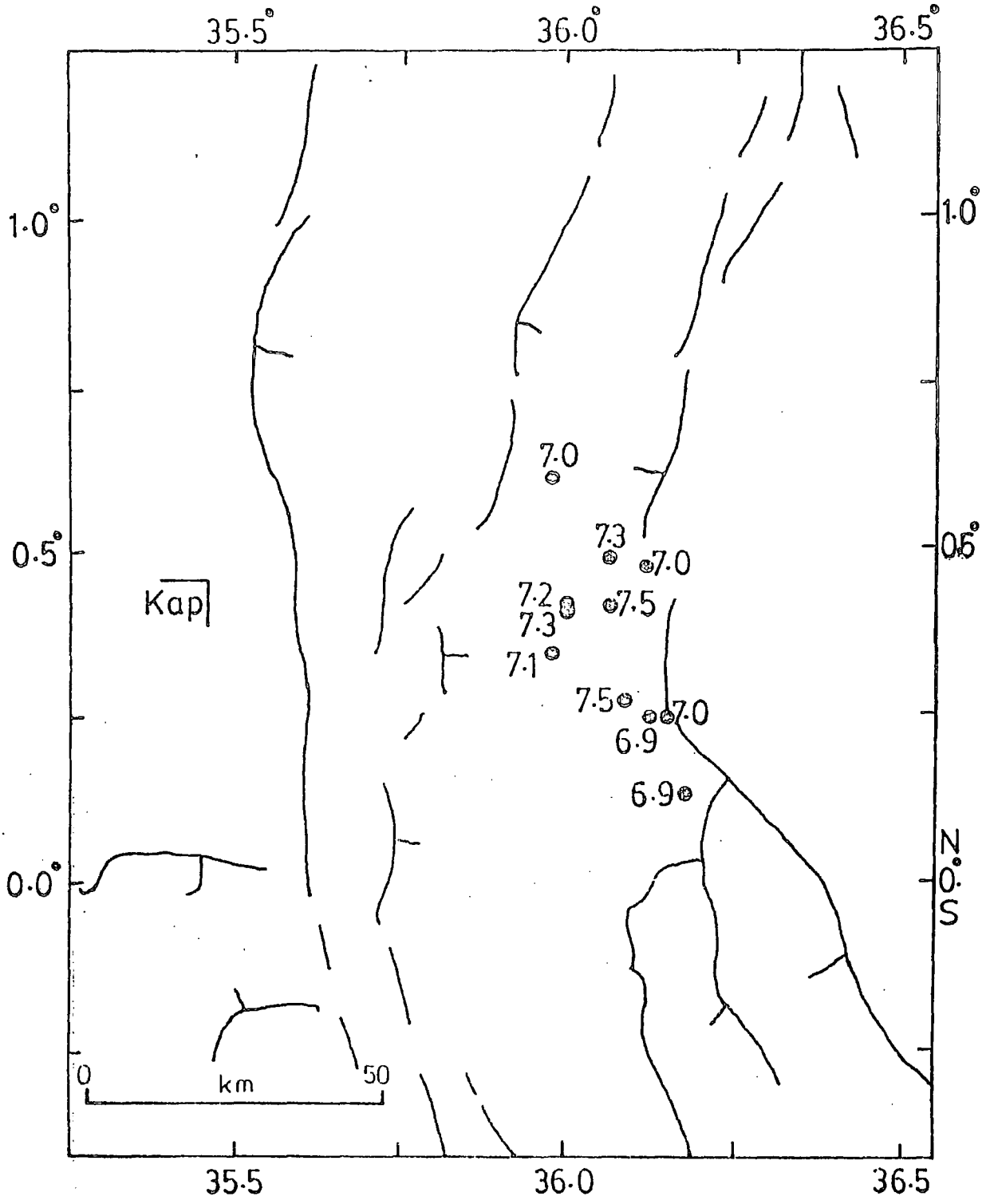

Fig 5.2a: Location of epicentres of local events to the immediate east of Kaptagat in relation to the rift structure. Figures indicate first arrival apparent velocities in km/s.

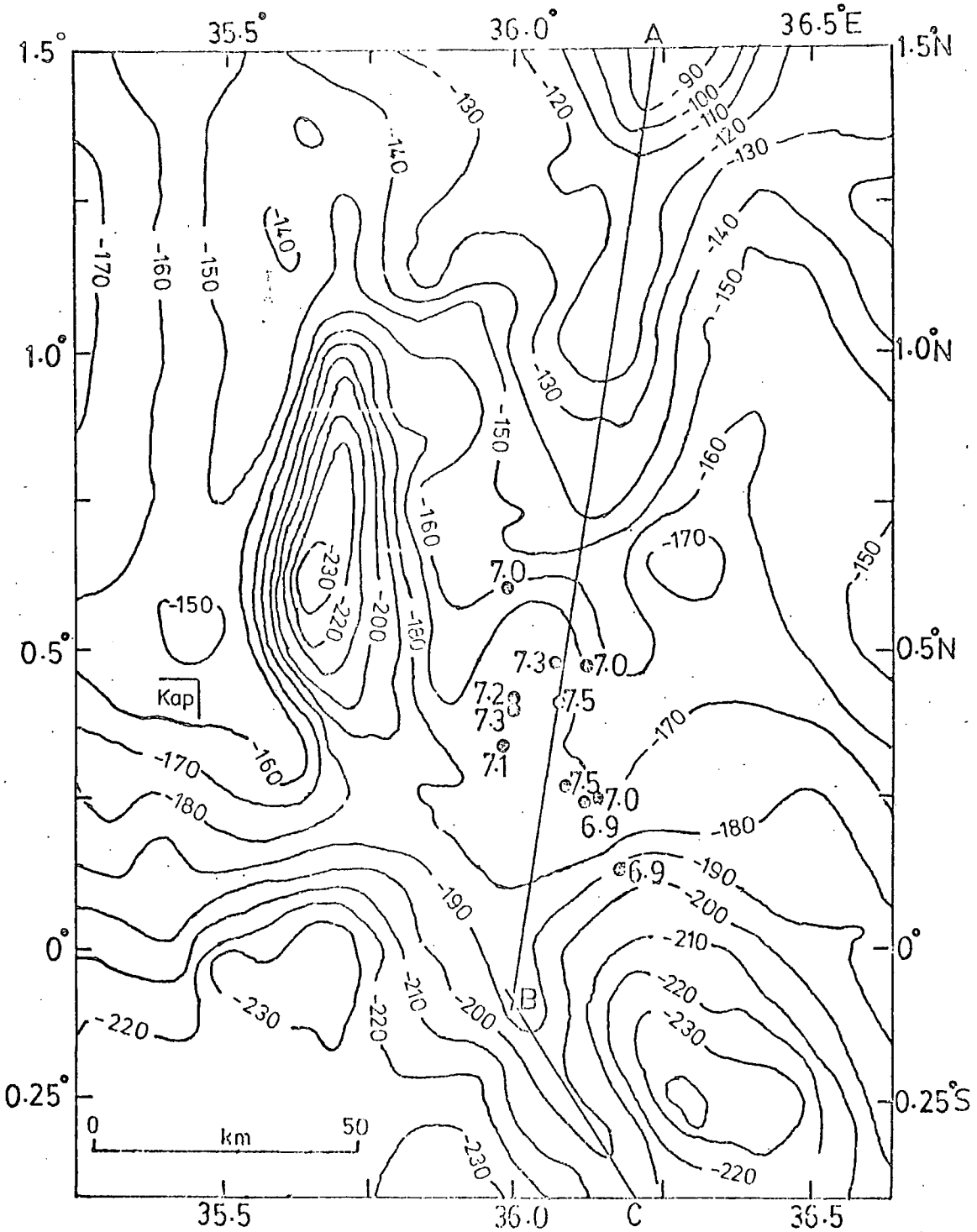

Fig 5·2b: Location of some epicentres in relation to the Bouguer anomaly map of central part of the rift. Contour values are in mgals. Other figures represent event first arrival apparent velocities in km/s.

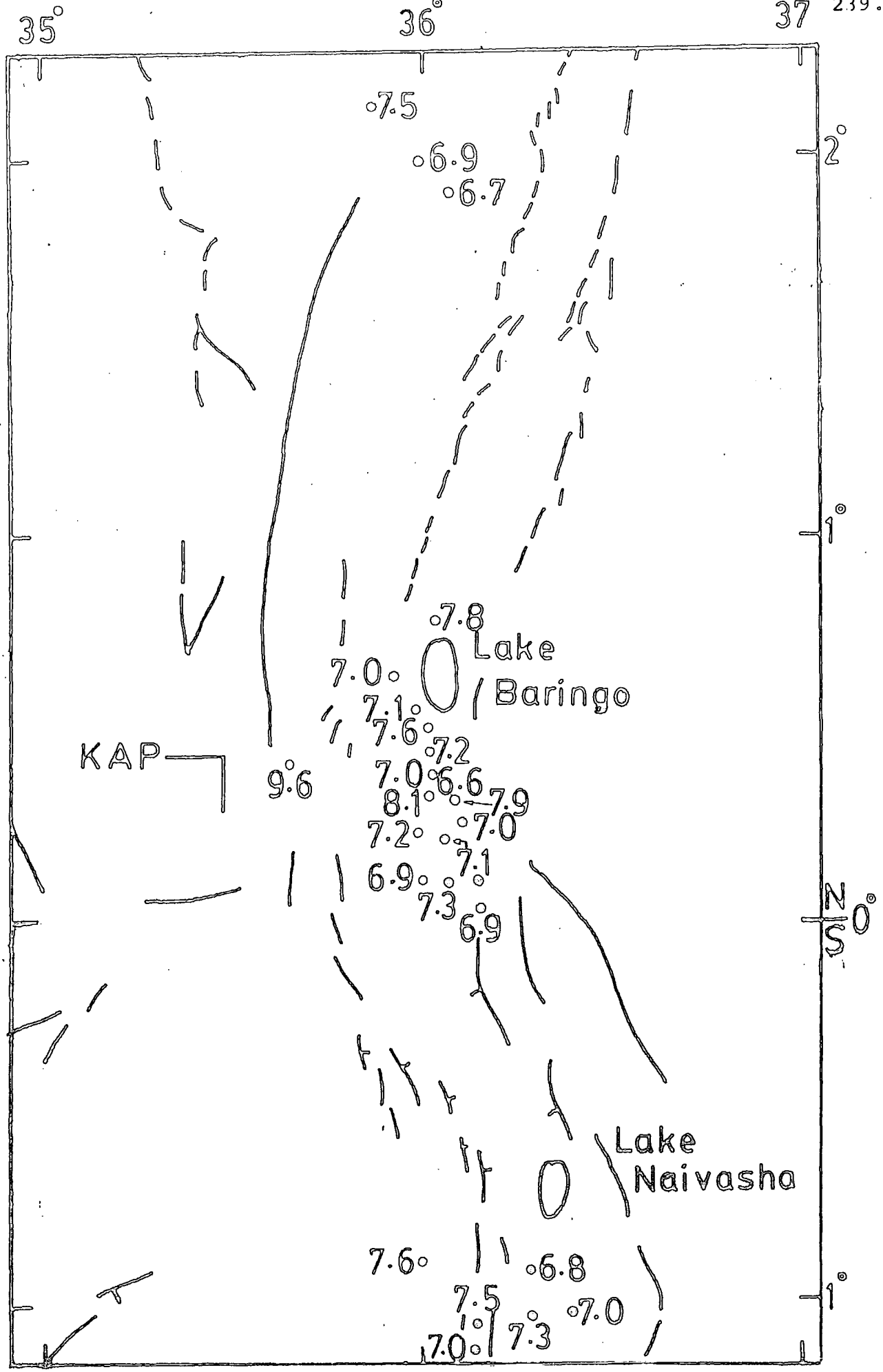

Fig. 5·3a: Epicentres of events (black circles) used by Maguire and Long (1976). Numbers are first arrival apparent velocities in km/s.

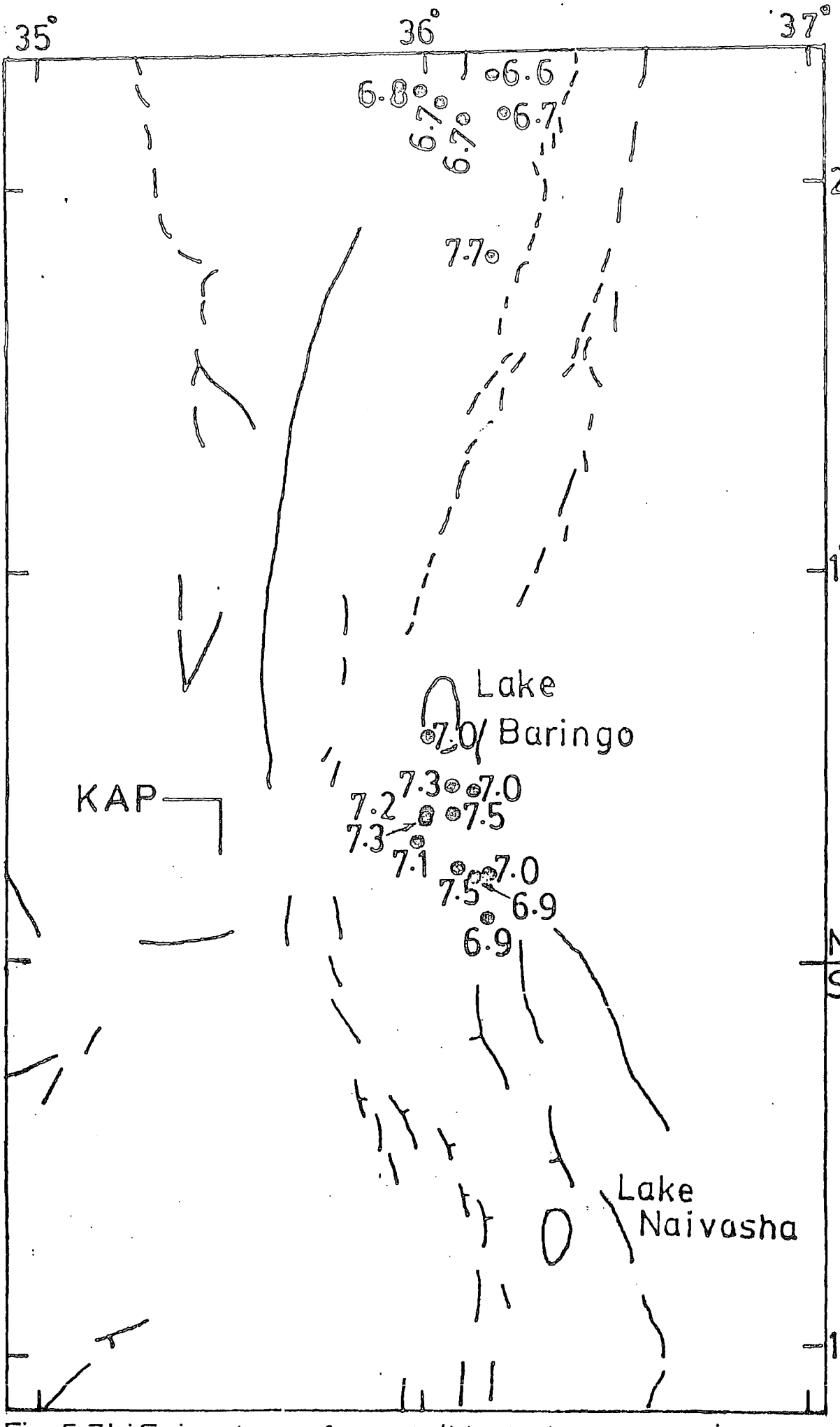

Fig. 5.3b: Epicentres of events (black circles) used in the present study. Numbers are first arrival apparent velocities in km/s.

are all in the range 6.9 - 7.5 km/s and the epicentres cover an azimuthal range 74° to 114°. The data of Maguire and Long (1976) cover about the same range of distance and an azimuthal range of about 58° to 122°; their measured apparent velocities are in the range 6.6 km/s to 8.1 km/s (fig. 5.3a). The events used by these authors may, however, be divided into two groups with mean velocities of 7.1 ± 0.3 km/s and 7.9 ± 0.3 km/s which are statistically seperate at the 99% confidence level. Four events with first arrival apparent velocities of 7.8, 7.8, 7.9 and 8.1 km/s make up their 7.9 ± 0.3 km/s group of events. The 7.9 km/s group of events is not observed in the present study where measured apparent velocities were all less than or equal to 7.5 km/s.

The two sets of data thus show higher than normal apparent velocities for small epicentral distances (about 60-70 km). One conspicuous difference between the two sets of data, however, is that apparent velocities greater than 7.5 km/s are not observed in the present data. It is necessary to find out if this difference is real or apparent.

One possible explanation for this difference is the improved precision of the present measurements. In the present study, only records that met the stringent requirements for velocity filtering were analysed. One requirement was that the seismograms must have a high signal to noise ratio. This requirement ensured high fidelity analogue to digital conversion without the need for frequency filtering prior to digitization.

Secondly, records with impulsive first arrival onsets (see fig. 4.1) were selected. On such seismograms, the direction of first motion was seen clearly and any inversion

before processing was carried out with confidence. There was also the requirement that the array record must have sufficient number of operating seismometers on each arm of the array to ensure improved resolution in apparent velocity and azimuth determinations.

These requirements were satisfied on only eleven local rift events to the immediate east of Kaptagat. The records of these events were subsequently analysed. With these restrictions, the measurement errors in the first arrival apparent velocity in this study had a 95% confidence limit of $\pm$ 0.2 km/s for most of the events. Only one event had a measurement error of up to $\pm$ 0.5 km/s in first arrival apparent velocity (see table 3.11). Maguire and Long (1976) claim a corresponding average measurement error of $\pm$ 0.5 km/s for 62% of the events. The rest had errors greater than $\pm$ 0.5 km/s but less than $\pm$ 1.0 km/s. The improved measurement precision of the present study may explain the fact that the 7.9 $\pm$ 0.3 km/s group of arrivals was not observed.

The present data covers a narrower azimuthal range (74^{o} to 114^{o}) than the data of Maguire and Long (58^{o} to 122^{o}). This may partly explain the difference in the ranges of measured apparent velocities. For example a 7.8 km/s observed by these authors (fig. 5.3a) is for an epicentre outside the range of azimuth covered in this study.

It was not possible to identify the particular events whose records were studied by Maguire and Long (1976). The present analysis may not, therefore, be looking at the same events studied by these authors. The four events from which they obtained first arrival apparent velocities in the range

7.8 to 8.1 km/s may not have been processed in this study.

To summarize, because of the improved precision of the present data, it is probable that the existence of the 7.9 km/s group of arrivals may be more apparent than real.

5.2.2 Velocity/P-X time relationship.

First arrival phase velocities (V) are plotted against P-X times (T) in fig. 5.4. The estimated measurement errors in V are indicated. Numbers against plotted points represent the corresponding first arrival measured apparent azimuths in degrees.

The linear correlation coefficient, r, between V and T calculated for the 11 observations is -0.434. To find out if there is a statistically significant linear relationship between V and T, this calculated value of r is tested against a null hypothesis $H_o (\rho \simeq o)$ using a t-statistic

$$t = r \sqrt{(n-2)/(1-r^2)}$$

with n-2 degrees of freedom (d.f.) and with ρ representing the population correlation coefficient. Because the alternative hypothesis is $H_a (\rho < o)$, one-tailed test is used. For the present data with 11 observations (i.e. 9 d.f.), the calculated value of t is -1.443. At the 5% level of significance, the table value of t for 9 d.f. is -1.833 which has a magnitude greater than that of the calculated t. The calculated t does not, therefore, lie within the critical or rejection region.

Hence the null hypothesis can not be rejected at the stated level of significance. There is, therefore, no significant linear relationship between first arrival apparent surface velocity and P-X time at the 95% confidence level.

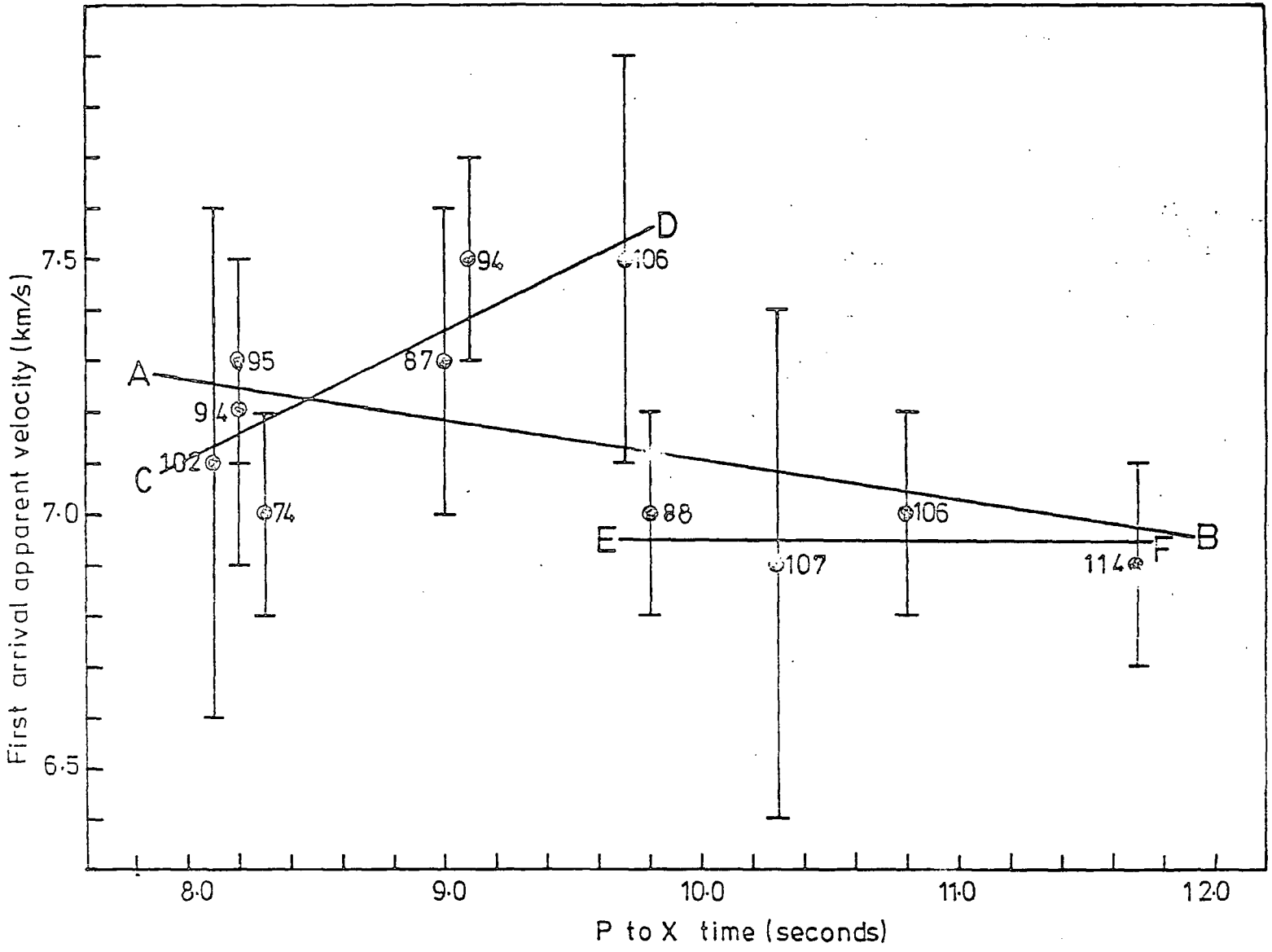

Fig. 5.4: Plot of first arrival apparent velocity against P-X time. Numbers are the corresponding first arrival azimuths in degrees.

The same conclusion is arrived at by considering the regression line (line AB of fig. 5.4) of V on T of the form

$$V = a + bT$$

where a and b are constants whose estimated values are 7.891 $\pm$ 1.162 km/s and -0.078 $\pm$ 0.123 km/s^2 respectively. Error estimates are 95% confidence limits. The error limits on slope are -0.201 and + 0.045 km/s^2; the value zero is contained within these limits thus confirming that there is no significant linear relationship between V and T for the whole set of 11 observations. The 95% confidence limits for the mean of these 11 first arrival apparent velocity measurements are 7.2 $\pm$ 0.2 km/s.

A closer inspection of fig. 5.4, however, shows that the data could be divided into two groups. The first group is for P-X times from 8.1s to 9.7s and contains seven events. In this range of P-X times, apparent surface velocity seems to increase with P-X time (line CD, fig. 5.4). The coefficient of linear correlation between V and T is 0.81. For 5 degrees of freedom this gives a calculated t-statistic of 3.06. The corresponding table value of t using a one-tailed test at 2.5% significance level is 2.57. This is smaller than the calculated value and so puts the calculated t within the critical/rejection region at 2.5% significance level. The null hypothesis can thus be rejected at this level. There is thus a significant linear relationship between V and T at the 95% significance level.

A straight line of best least squares fit to the data in this group has a slope of 0.25 $\pm$ 0.18 km/s^2 and an intercept

of 5.12 ± 1.59 km/s. Error estimates are 95% confidence limits. Limits on slope are 0.07 and 0.43 km/s^2 and do not enclose the value zero. This equivalently confirms significant linear relationship between velocity and P-X time. The mean first arrival velocity for events in this group is 7.3 ± 0.2 km/s at 95% confidence level.

The second group of events (4 observations) has P-X times from 9.8s to 11.7s. For this group, the correlation coefficient between V and T is -0.42. For 2 degrees of freedom, this gives a calculated t-statistic of -0.651. The corresponding table value of t for a one-tailed test at 2.5% significance level is -4.30 thus putting the calculated t not within the critical region. The null hypothesis can not be rejected at this level of significance. For this group of events, there is, therefore, no significant linear variation of velocity with P-X time at the 97.5% significance level. This conclusion is also confirmed by the line of best least squares fit (line EF) through the data. This line has a slope of -0.03 ± 0.19 km/s^2 and an intercept of 7.26 km/s. Error estimates are 95% confidence limits. The 95% confidence limits for the mean velocity in this group is 7.0 ± 0.1 km/s.

From fig. 5.4, line CD suggests that as P-X time increases from about 8.1s to 9.7s, the first arrival phase velocity increases from about 7.1 km/s to about 7.5 km/s. Line EF suggests that as P-X time increases from about 9.7s to 11.7s, the velocity remains constant at about 7.0 km/s. It will be shown later (section 5.7) that, taken together, lines CD and EF would suggest the existence of a layer in which seismic velocity increases with depth overlying a constant velocity

refractor.

5.2.3 Distance/azimuth relationship.

A plot of P-X time (T) against azimuth (θ) is shown in fig. 5.5. Numbers against plotted points represent measured first arrival phase velocities in km/s. We wish to find out if there is any significant linear relationship between azimuth and T (and hence distance).

The coefficient of linear correlation, r, between T and θ for the data of fig. 5.5 is 0.65 giving a calculated t value of 2.59 for 9 d.f. The table value of t for a one-tailed test and 9 d.f. at 2.5% level of significance is 2.262. The calculated t is thus located within the critical/rejection region and the null hypothesis of no significant linear relationship can be rejected at 0.025 level of significance. A significant linear variation of P-X time (and hence distance) with azimuth is thus established at 97.5% level of significance.

The estimate of r from the data of fig. 5.5 gives a disproportionately heavy weight to the last point with a T value of 11.7s. The value of r estimated for the other 10 observations is 0.51 and the corresponding calculated t is 1.68 for 8 d.f. Table value of t using a one-tailed test and 8 d.f. is 1.397 at 10% level of significance. This indicates that there is a significant linear relationship between distance and azimuth at the 90% level of significance.

A regression line of T on θ for the 11 observations has 95% confidence limits of 0.068 ± 0.061s deg^{-1} on slope and 2.63 ± 5.96s on intercept. This linear variation of distance with azimuth can be partly explained by the swing of the axial

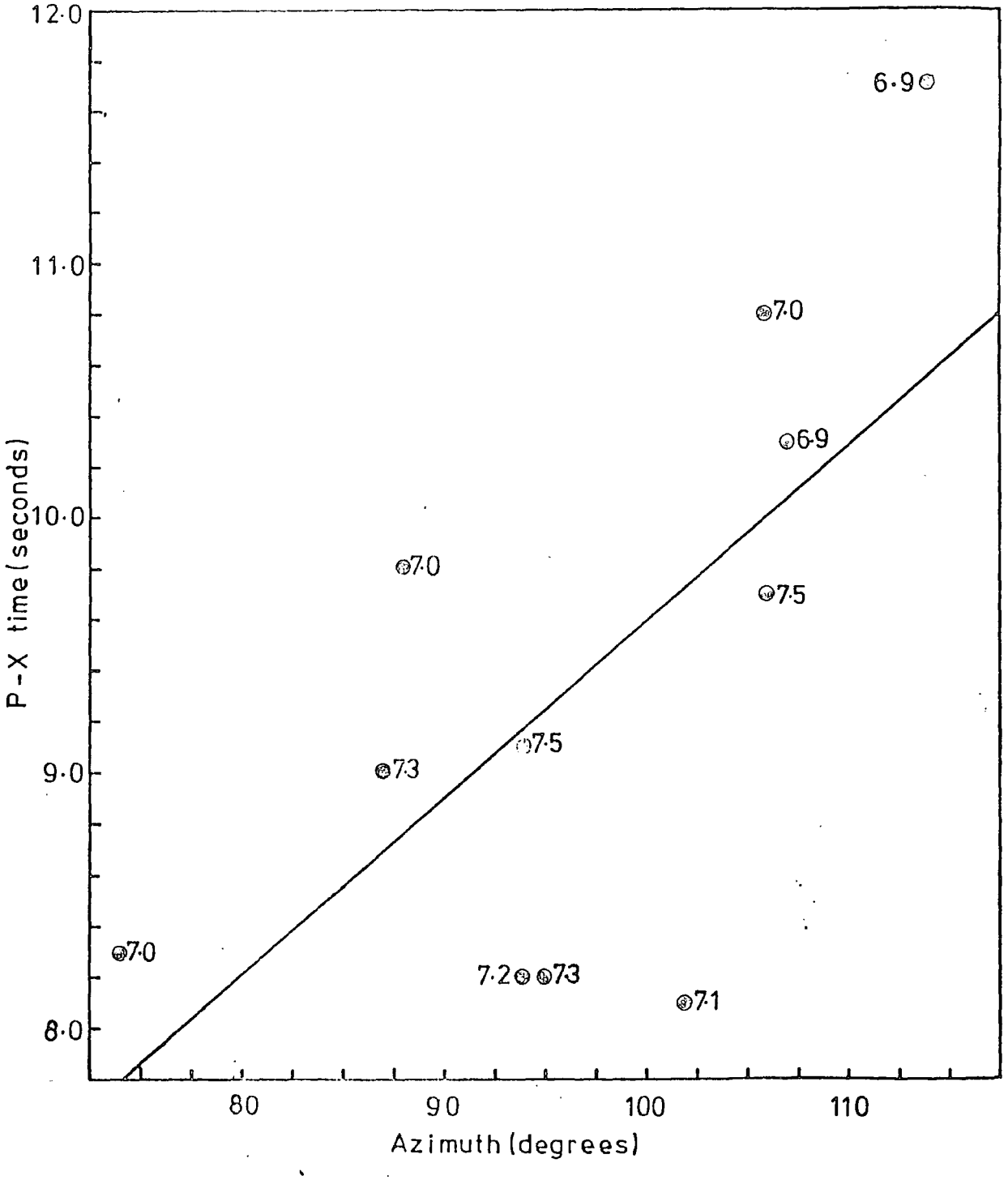

Fig 5·5: Event P-X time against first arrival azimuth. Figures are first arrival apparent velocities in km/s.

trough of the rift towards the east at the latitude of Kaptagat (see fig. 4.5b). The epicentres are located approximately within this trough with azimuth increasing from 74^{o} to 114^{o}.

2.4 Velocity/azimuth relationship.

In fig. 5.6a, measured first arrival apparent velocity, V, is plotted against azimuth, θ. The numbers against the plotted points are P-X times in seconds.

The linear correlation coefficient, r, between V and θ is -0.14; this gives a calculated t value (for 9 d.f.) of -0.41. From the tables the t statistic using a one-tailed test and 9.d.f. is -1.83 at the 0.05 level of significance. The calculated value of t is, therefore, clearly not within the critical/rejection region; the null hypothesis of no linear relationship between V and θ is accepted at the 95% level of significance. The 95% confidence limits for the slope of a straight line of best least squares fit to the data is 0.003 $\pm$ 0.014 km s^{-1} deg^{-1} which again confirms the suggestion of no significant linear relationship between V and θ since the limits include the value zero.

With the exception of one event from an azimuth of 106^{o}, all measured first arrival apparent velocities greater than or equal to 7.2 kms^{-1} are observed within the azimuthal range 87^{o} to 95^{o}. The spread of the data points in fig. 5.6a, therefore, suggests a sinusoidal relationship of the form

$$V = A + B \cos (\theta - \theta_{o})$$

where A, B and θ_{o} are constants. This equation is equivalent to a relation of the form

$$V = A + C \cos \theta + D \sin \theta$$

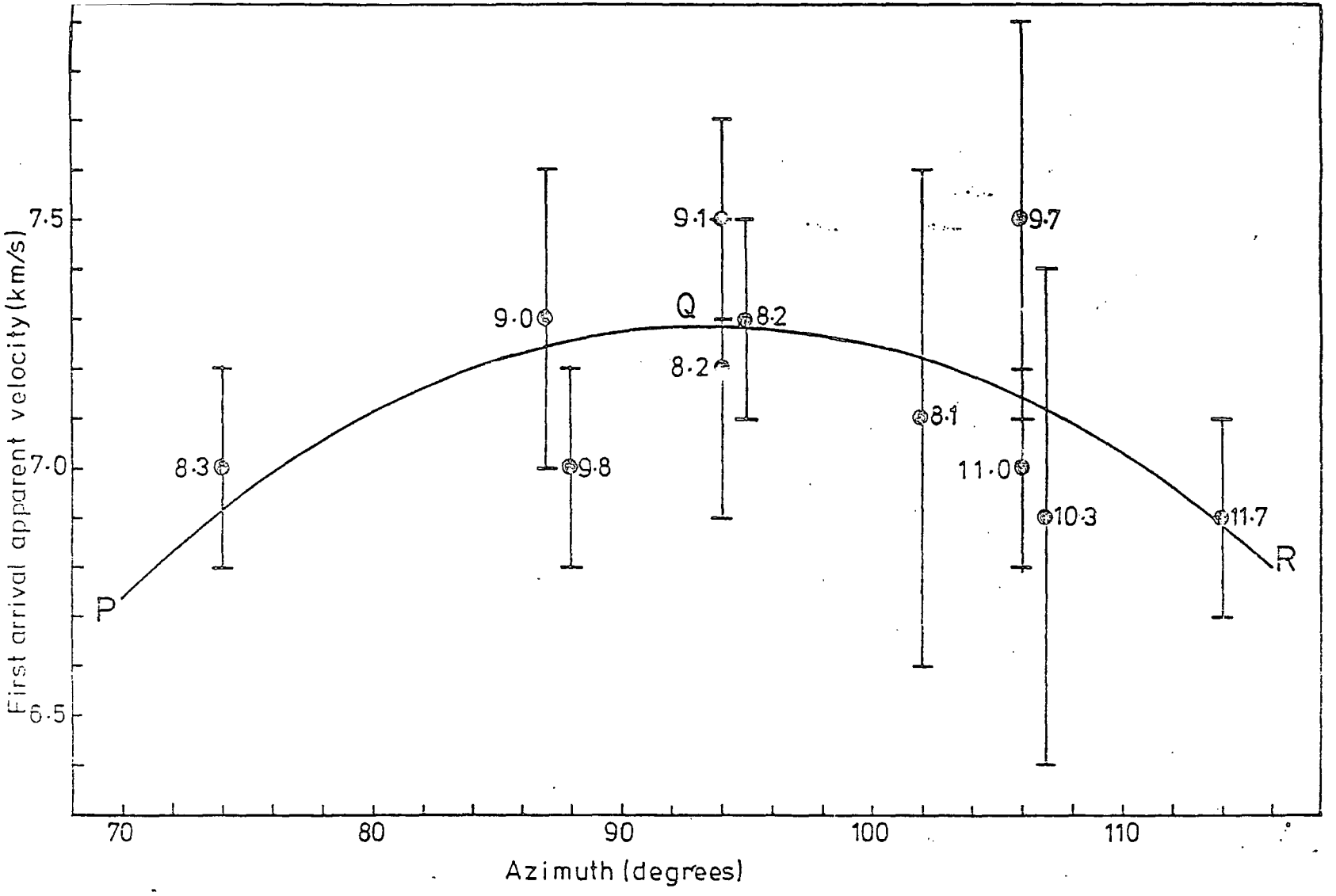

Fig 5·6a: Plot of first arrival apparent velocity against azimuth. Figures represent P-X times in seconds.

where C and D are other constants related to B and θ_o. For the data of fig. 5.6a, the multiple regression best least squares straight line of V upon sin θ and cos θ as independent variables gives estimates of 0.86 km/s for A, -0.41 ± 0.31 km/s for C and 6.42 ± 2.75 km/s for D. Limits are estimates of standard error. From the values of C and D, estimates of B and θ_o are obtained as 6.43 ± 2.74 km/s and about 94 ± 3^o respectively. This relationship, which is valid only within the range of distance and azimuth covered in the present data, is represented by the curve PQR in fig. 5.6a.

This sinusoidal variation of apparent velocity with azimuth shows that apparent velocity has a maximum value of about 7.3 km/s in a direction of about $N94^oE$ of Kaptagat which is a direction approximately normal to the rift profile at this latitude. It is, in fact, shown below that this maximum apparent velocity occurs along the rift axis.

In fig. 5.2b, the rift axis is taken as the line AB which represents the axis of the positive gravity high. Normal distances, x, of the epicentres from line AB and the corresponding apparent surface velocities, V, shown in table 5.1 are plotted in fig. 5.6b. The plot

Event number	Normal distance (x) of epicentre from the rift axis (km)	First arrival apparent surface velocity in km/s
1	-9.0	7.1
2	-8.2	7.2
3	-7.4	7.3
4	-12.3	7.0
5	-1.6	7.3
6	0.0	7.5
7	4.0	7.5
8	4.1	7.0
9	8.2	6.9
10	10.7	7.0
11	16.4	6.9

Table 5.1 Normal distances of epicentres measured from the rift axis, positive to the east and negative to the west.

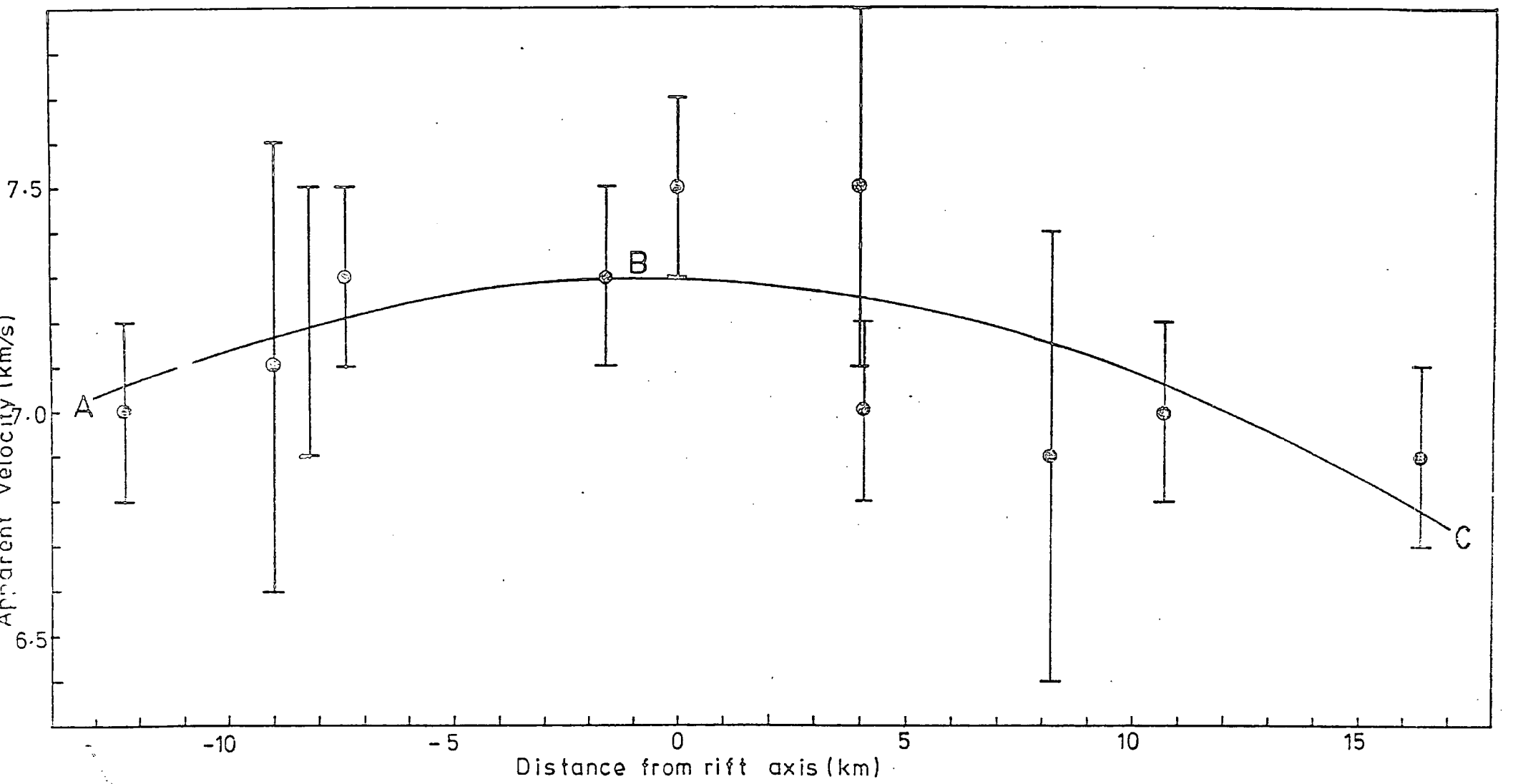

Fig 5·6b: Plot of first arrival apparent velocity against normal distance of epicentre from rift axis.

suggests a relationship of the form

$$V = a_o + a_1 x + a_2 x^2$$

where a_o, a_1 and a_2 are constants. For the best least squares curve (ABC in fig. 5.6b) a_o, a_1 and a_2 were found to have the values 7.289 km/s, -0.00273 ± 0.00667 s^{-1} and -0.00174 ± 0.00077 $km^{-1}s^{-1}$ respectively. Error estimates are standard errors. This relationship is, of course, applicable to the region covered by the data. It is evident from curve ABC that the maximum apparent velocity of about 7.3 km/s is obtained at the rift axis, that is where x is about zero.

The inferred variation of velocity with azimuth is consistent with the existence of a plane dipping refractor (dipping up towards the east) whose direction of maximum dip, as seen from Kaptagat, is about 94^o east of north. The decrease in apparent velocity to the north and south of this direction could be explained by a decrease of apparent dip towards these directions.

The variation of velocity with azimuth shows some symmetry with respect to the rift. The apparent velocity, as seen from Kaptagat, decreases to the north and to the south of a direction about normal to the rift axis at the latitude of Kaptagat. This could suggest attenuation of the possible causative intrusive body in these directions but could also have other alternative explanations.

5.2.5 Conclusions and inferences.

It has been shown (section 5.2.2) that for the data taken

as a whole, there is no significant linear relationship between apparent velocity and distance. This suggests that the first arrivals could be headwaves from a nearly horizontal boundary.

However, from fig. 5.4, the data could be fitted with lines CD and EF suggesting a distance range over which apparent velocity increases with distance followed by another range of distance over which apparent velocity remains constant. It will be shown later (section 5.7.3) that this data set could be explained in terms of a layer in which rock velocity increases with depth underlain by a constant velocity refractor. This is an oversimplified model since lateral as well as vertical variation in velocity seem more realistic. Such a realistic model may not, however, be constrained by the present data.

Significant linear relationship between distance and azimuth (section 5.2.3) suggests that the epicentres follow the trend and swing of the axial part of the rift to the south east at the latitude of Kaptagat (fig. 5.2a). This observation tends to support the suggestion that these are rift events most of which are probably located within the rift axis.

A possible sinusoidal relationship between apparent velocity and azimuth (section 5.2.4) suggests that apparent velocity has a maximum value of 7.3 $\pm$ 0.3 km/s at an azimuth of about 94^{o} from Kaptagat. The apparent velocity then decreases to about 6.9 km/s as azimuth changes by about 20^{o} on either side of 94^{o}. This observation could arise from a plane dipping refractor with the direction of maximum dip as seen from Kaptagat being at an azimuth of 94^{o}. This velocity/

azimuth relationship could also result from the attenuation of a possible causative intrusive body to the north and south of the central part of the rift axis. Other explanations are, of course, also possible.

5.3 Discussions on focal depth and the effect of shallow structures close to Kaptagat.

Assuming the crustal model of Maguire and Long (1976) extends to the whole region, rays can be traced back from Kaptagat using apparent velocity to determine the angle of the ray to the vertical under the station. Distances estimated from P-X times are used as path distances to locate foci on this model (fig. 5.7). It is found that all foci would locate below the intermediate boundary and above the Moho. The foci would all lie directly beneath the axial part of the rift (i.e. below AB in fig. 5.7) at depths ranging from about 31 km to 43 km.

Such large focal depths are unlikely beneath the central part of the Gregory rift where the epicentres in this study are located. Geological and geophysical evidence in support of much shallower foci have been discussed in section 4.5. It was shown that the epicentres are located within the axial part of the rift where heat flow, seismic, gravity and geomagnetic deep sounding data are all consistent with the existence of partial melts in rocks at depths of 5 to 20 km and probably nearer 5 km than 20 km. The inferred hot crustal zone of partial melt could not be expected to store enough strain energy to generate the observed tectonic earthquakes. Focal depths would, therefore, be expected to be limited to values

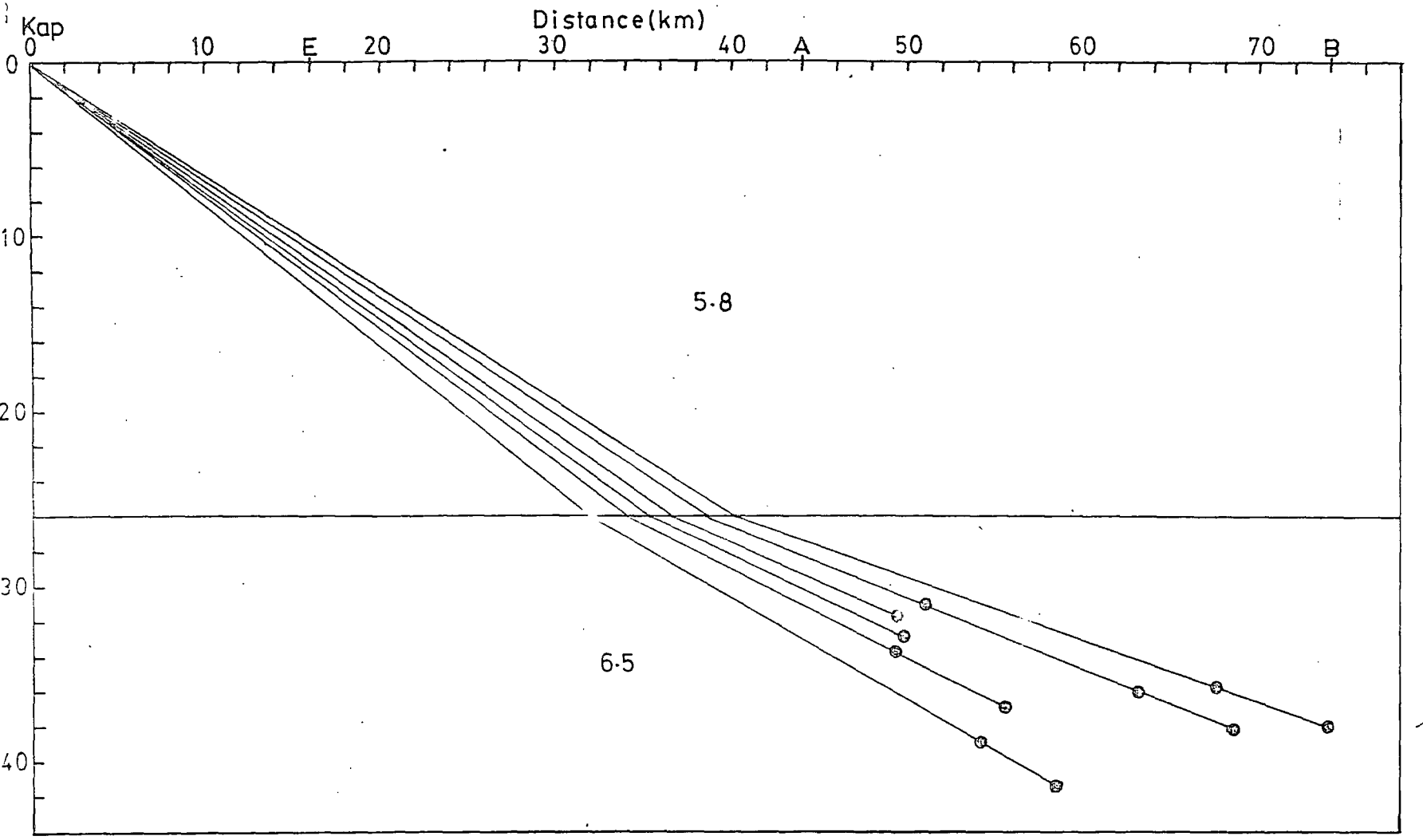

Fig 5.7: Epicentral distances plotted as ray path distances in the crustal model of Maguire and Long(1976).

less than about 20 km. For example most of the local events located within Lake Bogoria (Hannington) have focal depths not exceeding 14 km (Maguire et al., 1986). A most probable depth of about 5 km is estimated for the geothermal prospect areas near Lakes Bogoria and Naivasha (Hamilton et al., 1973) within the axial part of the rift. This appears to be supported by the analysis of second arrival data in this study (section 6.3.2) which suggests that focal depths could be of the order of 4 km.

From the foregoing, it is evident that focal depths of about 31 to 43 km for the survey area are highly improbable. The first arrivals are, therefore, unlikely to be direct waves coming in from the normal shield crust.

These arrivals are also unlikely to be headwaves from the intermediate layer of the normal shield crust. The observed average apparent velocity of 7.2 $\pm$ 0.2 km/s is significantly higher than the 6.5 $\pm$ 0.3 km/s estimated for the intermediate layer (Maguire and Long, 1976). Secondly, the observed distances for majority of the events in the present analysis fall below the critical distance for headwaves from the intermediate layer of the normal shield crust assuming realistic shallow focus. For example, in the azimuth range of about 94 $\pm$ 10^{o} there are six events whose estimated distances are within the range 59 to 73 km. Five of these have distances in the range 59 to 67 km. However, for normal sheild crust, the critical distance for headwaves from the intermediate layer decreases from 103 km through 83 km to 73 km as focal depth increases from 0 km through 10 km to 15 km. The observed arrivals are therefore unlikely to be headwaves from the intermediate layer or the Moho of a normal shield crust. The arrivals are also probably not reflections

from the normal shield crust because it is difficult to explain a situation where reflections come in as first arrivals preceding direct waves. The conclusion to be drawn from the discussions above is that the normal shield structure has been modified in a region somewhere to the east of Kaptagat.

But one of the arguments leading to this conclusion hinges on the unusually high first arrival apparent velocities observed in the region of study where foci are expected to be shallow. Swain et al. (1981) tried to explain these high apparent velocities not in terms of modification of the normal shield structure but as a result of bending of rays towards the vertical by lateral heterogeneity of very shallow structures in the vicinity of the station. These structures could have the effect of deflecting the incoming rays in such a way that they arrive Kaptagat at steep angles suggested by the observed high apparent velocities.

One such structure was suggested by Swain et al.(1981). These authors interpreted the seismic refraction data (Wilton, 1977) from a 50 km E-W line between Lake Baringo(B) and Chebloch Gorge(C) at about latitude 0.5^{o}N (fig. 5.8). Using this as control they interpreted an isostatic anomaly profile which includes the seismic line. For their interpretation (fig. 5.8) they used the Nafe-Drake (1963) relation between density and velocity to convert their measured velocities of 5.7 kms^{-1} (basement) and 2.35 kms^{-1} (Baringo sediments) to densities of 2.7 and 2.0 gcm^{-3} respectively. The Kaparaina basalts underlying the Baringo sediments and the Miocene - early Pliocene phonolite trachyte sequence were assigned

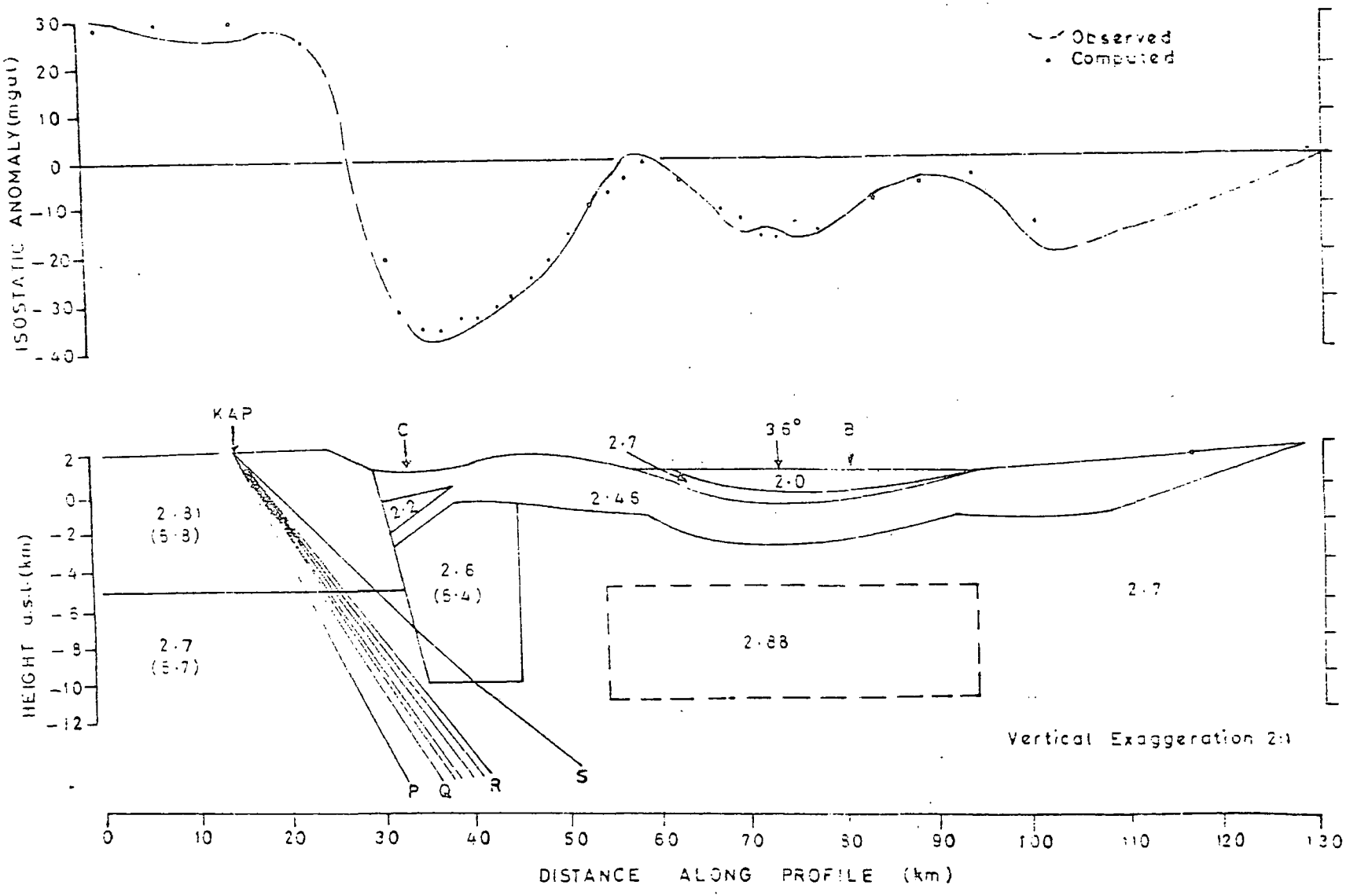

Fig. 5·8 : Two dimensional interpretation of gravity profile at about 0.5°N (Swain et al, 1981). Ray path coverage in the present study are shown.

densities of 2.7 and 2.46 gcm^{-3} respectively. For the basement west of Elgego fault, a density of 2.81 gcm^{-3} was adopted. Density information was obtained from previous referenced workers. These densities are shown in fig. 5.8.

Their gravity data required a low density (2.6 gcm^{-3}) material within the basement beneath the western Kamasia dip slope. The authors then suggest that this density contrast between the basement rocks on either side of the Elgeyo fault would result in contrast in seismic velocities across the fault face. The seismic contrast will, in turn, cause seismic rays to be deflected steeply upwards at the fault plane giving rise to the high apparent velocities observed at Kaptagat for the immediate local eastern rift events.

We have here used Nafe-Drake (1963) curve to convert the densities in the model of Swain et al. (1981) into seismic velocities (the numbers shown in brackets). For the basement west of Elgeyo fault, the established velocity of 5.8 ± 0.2 kms^{-1} (Maguire and Long, 1976) has been adopted.

The angle of emergence, θ, for a plane wave front arriving at Kaptagat is given by $\sin\theta = {}^{V}/V_a$ where V is the velocity of the basement rock immediately beneath the array station (i.e. 5.8 ± 0.2 kms^{-1}) and V_a is the observed phase velocity. The range of measured values of V_a is 6.9 ± 0.2 to 7.5 ± 0.2 kms^{-1} (estimates are 95% confidence limits.) Consequently the limits of V and V_a including the measurement errors are 5.6 to 6.0 kms^{-1} and 6.7 to 7.7 kms^{-1}, respectively. It follows that the limits suggested by the uncertainties in the measurements are defined by the extreme rays corresponding to ${}^{V}/V_a$ ratios of ${}^{5.6}/7.7$ and

$6.0/6.7$ respectively. The corresponding limiting angles of emergence at Kaptagat are about 47^{o} and 64^{o} respectively; the corresponding rays are represented by P and S in fig. 5.8. But the actual observed apparent velocities correspond to rays contained in the bundle QR.

None of the observed rays intersects the boundary demarcating the low density material introduced by Swain et al (1981) within the basement to explain their gravity data. The limiting ray S which cuts the low density body suffers a deviation of 4^{o} at the fault face and a further deviation of 9^{o}, in the same direction, at the base of the low density body. The resulting total deviation of 13^{o} gives rise to an increase in apparent velocity from 6.0 kms^{-1} to 6.5 kms^{-1}. A ray about half way between R and S just hits the low density body and suffers a deviation so that the angle of emergence decreases from about 74^{o} to about 61^{o} suggesting an increase in apparent velocity from about 6.0 kms^{-1} to 6.6 kms^{-1}. Our measured velocities are all in the range 6.9 ± 0.2 to 7.5 ± 0.2 kms^{-1} and can not, therefore, be explained by the refraction in the low density body as suggested by Swain et al. (1981).

The low density body could be made to intersect all the observed rays if the bottom surface were moved down to a depth of about 19 km or the ray paths crossed a region of increase of velocity with respect to depth. Current models of the shield crust have such an increase. A structure in which the low density body extends to a depth of about 19 km is unrealistic and untenable for this region; even if such a low density body existed the consequent decrease in density/velocity contrast would imply still smaller amounts of ray deviation.

It is important to note that the low density material suggested by Swain et al. (1981) in their gravity interpretation was not reflected in their seismic interpretation of the same profile. Gravity interpretation is non-unique and the details of their model depend heavily on densities determined from surface rocks.

It is, therefore, concluded that the observed first arrival phase velocities could not be fully explained by the presence lateral heterogeneity of shallow structures in the vicinity of Kaptagat. It has also been shown that the arrivals are unlikely to be reflections, direct waves or headwaves coming in from the normal shield crust. It is reasonable to conclude, therefore, that the structure of the crust has been modified in a region somewhere to the east of Kaptagat.

5.4 Interpretation of first arrival data in terms of plane layered models.

.4.1 Introduction.

It has been suggested (section 5.2.5) that the first arrival data could be interpreted as headwaves from a nearly horizontal refractor. Because of the sinusoidal variation of apparent velocity with azimuth, the data could also be interpreted in terms of headwaves from a plane dipping boundary. From fig. 5.4 and section 5.2.2, it was argued that the data could be explained in terms of a layer in which velocity increased with depth overlying a constant velocity refractor. Each of these possibilities would now be discussed in turn.

.2 Two layer plane model with horizontal boundary.

From fig. 5.3, it is shown that the linear variation of apparent velocity with P-X times (and hence distance) for the data set as a whole is not significant at the 95% level. These first arrivals could therefore be treated, to a first approximation, as headwaves from a horizontal refractor underlying a top layer of rock velocity 5.8 ± 0.2 km/s (Maguire and Long, 1976; Swain et al., 1981). In the present study, the measured first arrival apparent velocity has a mean value of 7.2 ± 0.2 km/s (error estimates are 95% confidence limits). This value of velocity can be taken as an estimate of the refractor velocity in the present two layer interpretation. With top and lower layer velocities of the model established, it is now necessary to estimate the depth, H, to the refracting boundary. Estimate of H depends on focal depth, h, which is not known precisely.

To estimate H we proceed as follows. Assuming the ray paths are all in the 5.8 km/s layer, rays are traced back from Kaotagat to the foci using distances estimated from P-X times as focal distances. The foci are located as shown by the black circles in fig. 5.9a. The open circles correspond to distance estimates based on identifying arrivals 'X' as surface waves. For the black circles, foci are found to lie in the depth range 34 to 48 km.

Since the arrivals are all being interpreted as head waves from shallow foci, the refracting boundary could not be deeper than the shallowest focus (about 34 km). If the refracting boundary were deeper than the shallowest focus, the arrival from that focus would become a direct wave contrary to the

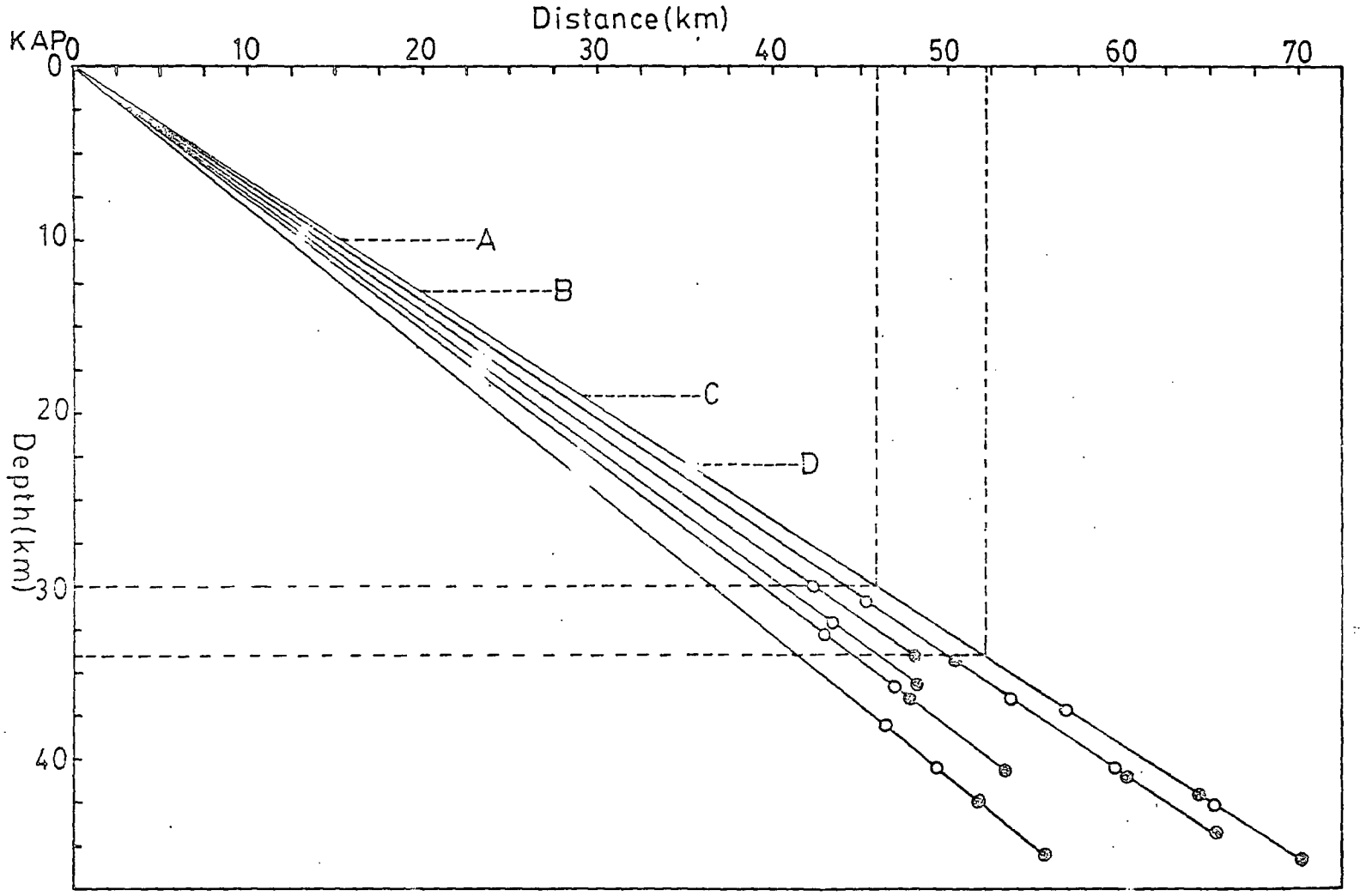

Fig 5.9a: Plot of hypocentral locations assuming the ray paths are all in a material of velocity 5.8 km/s.

proposition that all the arrivals are headwaves. It is, therefore, estimated that the depth to the refractor could not be greater than 34 km. At this maximum depth the refractor must extend to within 52 km east of Kaptagat or to within 37 km east of the Elgeyo escarpment bounding the rift to the west. From the open circles, the estimate of the maximum depth to the refractor is 30 km. At this depth the refractor extends to no farther than about 46 km from Kaptagat (fig. 5.9a).

To obtain a better control on estimate of maximum depth to the refractor, use is made of the fact that the arrivals are being interpreted as headwaves. The epicentral distances, Δ, deduced from P-X times must, therefore, all lie at or beyond the critical distance for headwaves from the refracting boundary at a depth H. For upper and lower layer model velocities of V_1 and V_2 and a focal depth h, this condition is fulfilled if

$$H \leq \frac{h}{2} + \frac{\Delta}{2V_1} \cdot (V_2^2 - V_1^2)^{\frac{1}{2}} \qquad \ldots\ldots \quad (5.1)$$

In the present analysis, the typical estimated epicentral distance in the east-west direction is about 60 km which is the mean distance for the four closest events. On substituting this value for Δ in equation (5.1) we obtain the dependence of maximum refractor depth, H_m, on focal depth, h. It is found that as focal depth increases from 0 to 20 km, the maximum refractor depth, H_m increases from 22 to 32 km. At a focal depth of 5 km, the maximum refractor depth is 25 km. If the 'X' arrivals were regarded as surface waves, the minimum estimated epicentral distance would be 54 km. This shows from equation (5.1)

that as focal depth increases from 0 to 20 km, H_m increases from 20 to 30 km. This estimate differs from the previous estimate by only 2 km. It should be pointed out that the minimum epicentral distance estimated in this study may be much larger than the actual critical distance for the model representing the real structure. The present limits calculated here for the maximum refractor depth H_m may be, therefore, probably overestimates.

Further control on estimate of H_m may be obtained from the fact that the arrivals under study are considered first arrival headwaves. The onset of these headwave arrivals must, therefore, precede direct waves onset in time. The observed distances must, therefore, all fall at or beyond the crossover distance for these two phases. This condition is satisfied if the refractor depth H satisfies the relation

$$H \leq \frac{h}{2} + \frac{V_1 V_2}{2(V_2^2 - V_1^2)^{\frac{1}{2}}} \left[\left(\frac{h^2+\Delta^2}{V_1} \right)^{\frac{1}{2}} - \frac{\Delta}{V_2} \right] \qquad \ldots\ldots (5.2)$$

Substituting the minimum estimated distance of 60 km and values of 5.8 km/s and 7.2 km/s for V_1 and V_2 in equation (5.2), the dependence of maximum refractor depth, H_m on focal depth is obtained (fig. 5.9b). It is found that as focal depth increased from 0 to 20 km, H_m increased from 10 km to 23 km. Lines A, B,C and D in fig. 5.9a give maximum values of refractor depth for focal depths of 0, 5, 15 and 20 km respectively. The corresponding estimate of H_m based on distances(Δ) estimated by identifying "X" arrivals as surface waves is found to increase from 9 km to 22 km as focal depth increased from 0 to 20 km. This shows that the correct identification of the

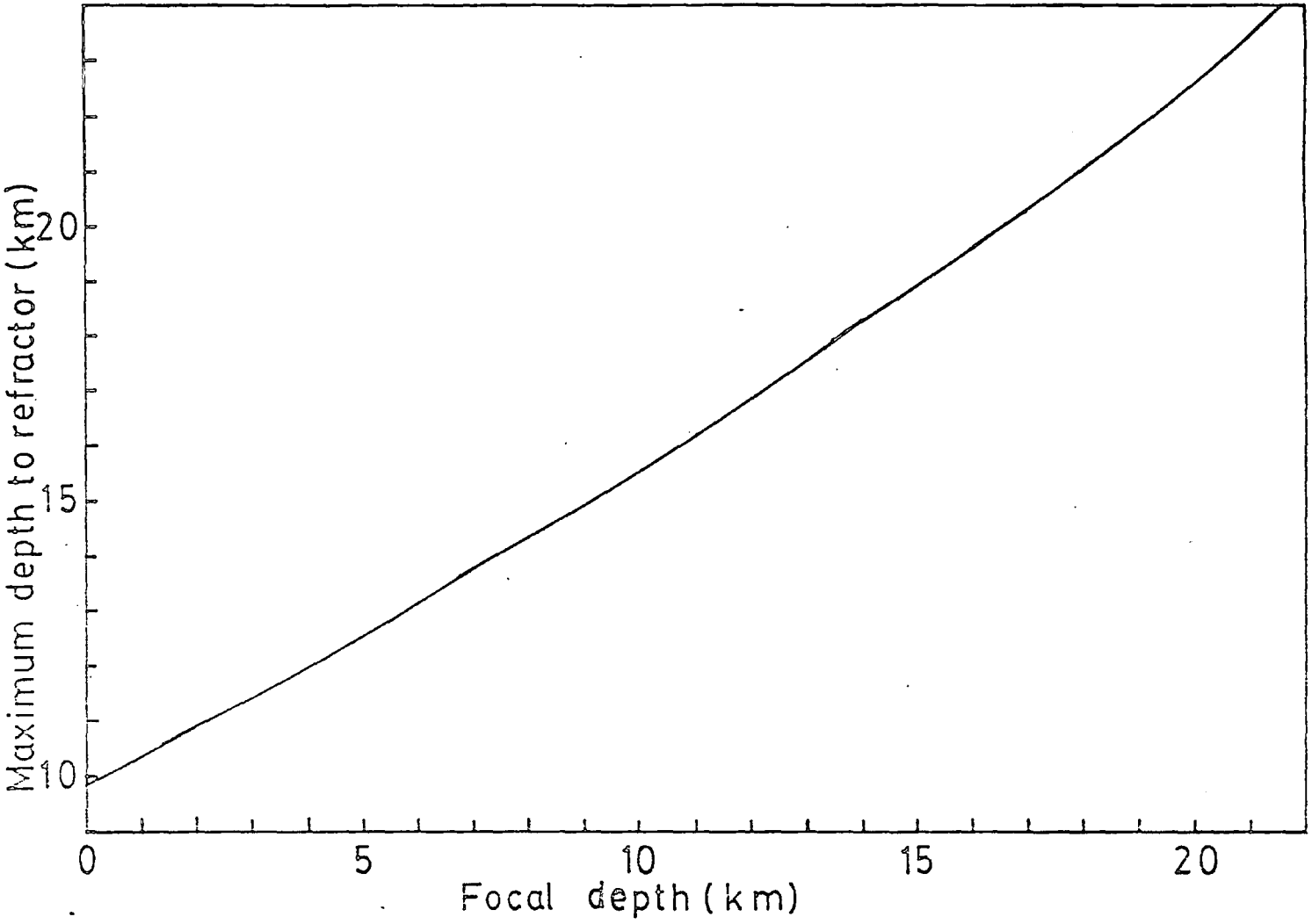

Fig 5.9b: Plot of maximum refractor depth, H_m against focal depth, h, for the two layer horizontal plane model.

phase of 'X' arrivals is not critical in estimating H_m.

At focal depth of 5 km, H_m is 13 km. At this value of H_m it is found (fig. 5.9a) that the refractor must extend west to at least within 20 km east of Kaptagat station, that is to within 5 km east of the western boundary fault of the rift. An error of 5 km in epicentral distance introduces an error of no more than 1 km in the estimate of H_m at a focal depth of 5 km.

A reasonable upper limit to the focal depth in the region of the present study is probably about 15 km (see discussions in sections 4.5 and 5.3). At this focal depth, the maximum depth to the refractor in the model is about 19 km (line C in fig. 5.9a). At this focal depth, the refractor must extend to within 35 km east of the station or 20 km east of the Elgeyo escarpment.

In the discussions above, estimates of the maximum depth to the refractor have been made. Available data could be used to estimate the minimum depth to the refractor. Explosion refraction data show that at the latitude of Kaptagat, basement rocks with P-wave velocity of 5.7/5.8 km/s exist beneath the entire width of the rift floor to a depth of at least 6 km for points along a 50 km E-W profile extending from Chebloch gorge to Lake Baringo (Swain et al, 1981). This is consistent with the observation that basement rocks outcrop in some locations within this part of the Gregory rift (Chapman et al., 1978).

The seismic profile of Swain and others (1981) is contained within the azimuthal range 76° to 83° from Kaptagat and

covers a distance range of 21 km to 67 km from Kaptagat. The present data set covers an azimuthal range 74^{o} to 114^{o} with six of the eleven epicentres, located within an azimuthal range 74^{o} to 95^{o}. Epicentral distances in this study are in the range 59 km to 84 km (with east-west component of distance in the range 58 to 75 km) from Kaptagat. The two surveys thus overlap to an appreciable extent and it is reasonable to assume that they sample the same structure.

Hence the minimum depth to the refractor in the two-layer plane horizontal model proposed here will be taken as 6 km. At this value of refractor depth, the refractor would extend westwards to within 11 km east of Kaptagat or upto 4 km west of the Elgeyo fault.

To provide a rough check on the order of magnitude of the estimates for the refractor depth, measured P-X times were used as P-S times (t) noting, however, that P-X times over-estimates P-S times (t) and hence H.

By considering the P-S times, t, for headwave arrivals, the depth H to the horizontal refracting boundary in our two-layer model is given by

$$H = \tfrac{1}{2}h + \frac{V_1 V_2}{2\sqrt{V_2^2 - V_1^2}} \left\{ \frac{t}{R-1} - \frac{\Delta}{V_2} \right\} .$$

The sumbols retain their already defined meanings. Regarding

measured P-X times as t and taking distances estimated from P-X times as Δ, the expression above was used to calculate a value for H from each of the 11 measured times. It was found that calculated values of H ranged from 15.9 to 20.1 km with a mean of 17 ± 1 km (error estimate is standard deviation). This is of the same order of magnitude as the estimates given above and in particular agrees very well with H_m estimated for a focal depth of 10 km.

To summarize, it is restated that the estimate of maximum depth to the refractor depends on the focal depth. The maximum depth to the refractor increases from about 10 to 23 km as focal depth increases from 0 to 20 km (fig. 5.9b). The minimum depth to the refractor is estimated at about 6 km. It follows, therefore, from fig. 5.9b, that at a focal depth of 5 km the refractor would lie in the depth range 6 km to 13 km. For a focal depth of 10 km the depth range for the refractor would be 6 km to 16 km.

Gently dipping boundary

The last section assumed a horizontal interface. We now consider the possibility of a gentle dip on that interface. Consider a plane refracting boundary (fig. 5.9c) dipping down (with dip α) from the rift axis towards Kaptagat and let the boundary seperate rock layers of P-wave velocities V_1 and V_2. Let the ray approaching Kaptagat station make an angle, e, with the vertical at the station. If the measured apparent velocity is V, then

$$e = \mathrm{Sin}^{-1}\left(\frac{V_1}{V}\right)$$

and

$$\alpha = e - \mathrm{Sin}^{-1}\left(\frac{V_1}{V_2}\right).$$

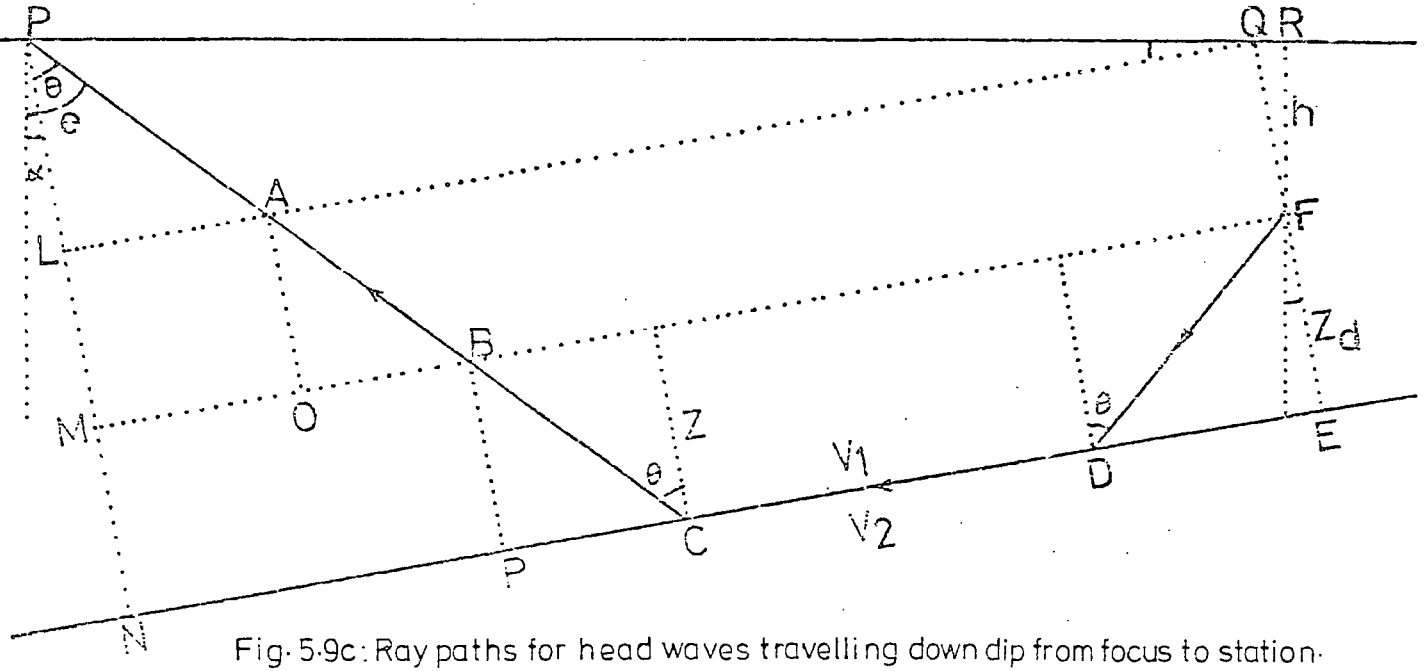

Fig. 5.9c: Ray paths for head waves travelling down dip from focus to station.

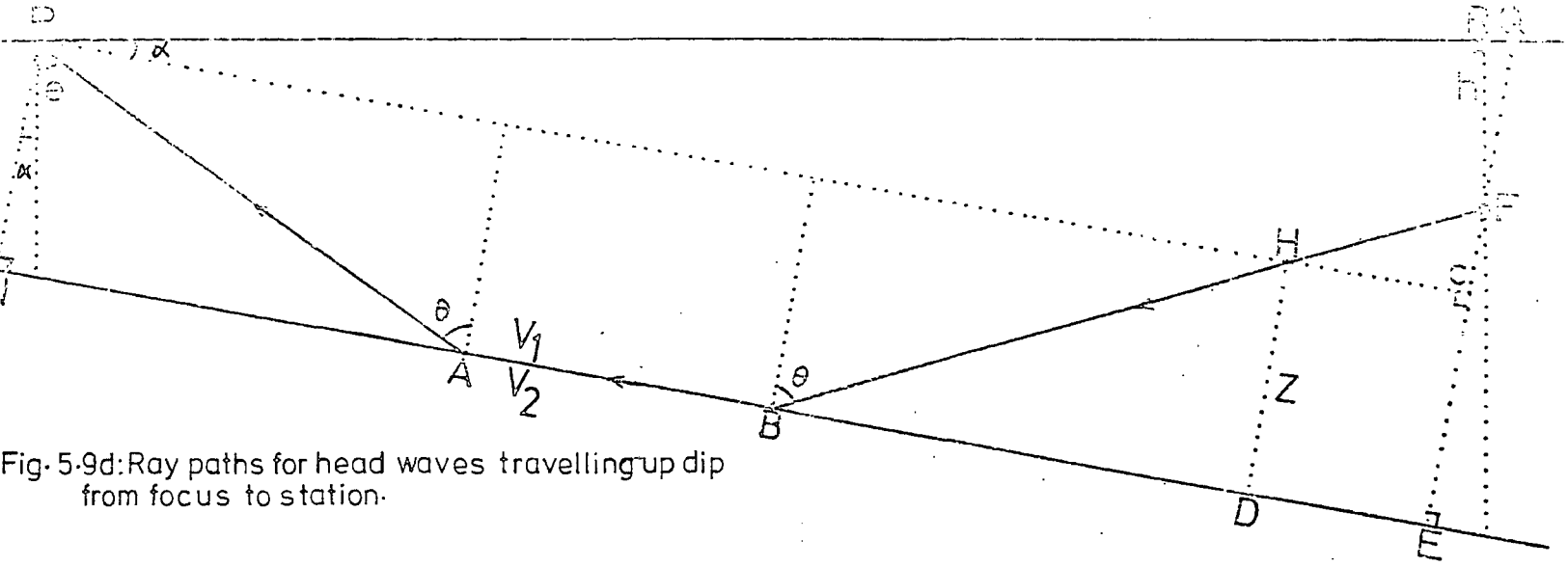

Fig. 5.9d: Ray paths for head waves travelling up dip from focus to station.

In the present study (with V_1 = 5.8 km/s), e increases from 50.6° to 57.2° as V decreases from 7.5 to 6.9 km/s. The mean value of V is 7.2 km/s corresponding to a mean value of 53.7° for e. Values of the dip α as a function of V_2 are shown in fig. 5.10 for V_2 in the range 5.9 to 8.6 km/s and with e fixed at 53.7°.

From fig. 5.10, it is found that all refractor velocities (V_2) equal to or greater than 5.9 km/s could give the observed mean value of e = 53.7° provided the corresponding refractor dips are as given in that figure. It is found that as V_2 increased from 5.9 to 7.2 km/s, the corresponding refractor dip up west from the rift axis decreased from 26° to 0°.

For refractor velocities greater than 7.2 km/s the data is consistent with a refractor dipping up from Kaptagat towards the rift axis. In this case, as the refractor velocity increased above 7.2 km/s, the dip increased from 0° to no more than about 11° for refractor velocity of 8.6 km/s. If we associate the refracting interface with the upper surface of the intrusive zone, such gentle dip would not be inconsistent with gravity and seismic data which indicate that the mantle derived crustal intrusion shallows towards the rift axis. Refractor velocities above about 7.1 km/s would, therefore, seem probable and are supported by the explosion data of Griffiths et al. (1971).

These authors shot a long refraction profile along the rift axis from Lake Turkana (Rudolf) in the north to Lake Bogoria (Hannington) in the south. They observed a maximum velocity of 7.5 km/s although their 367 km profile was long enough to detect an 8.0 km/s refractor if such material existed

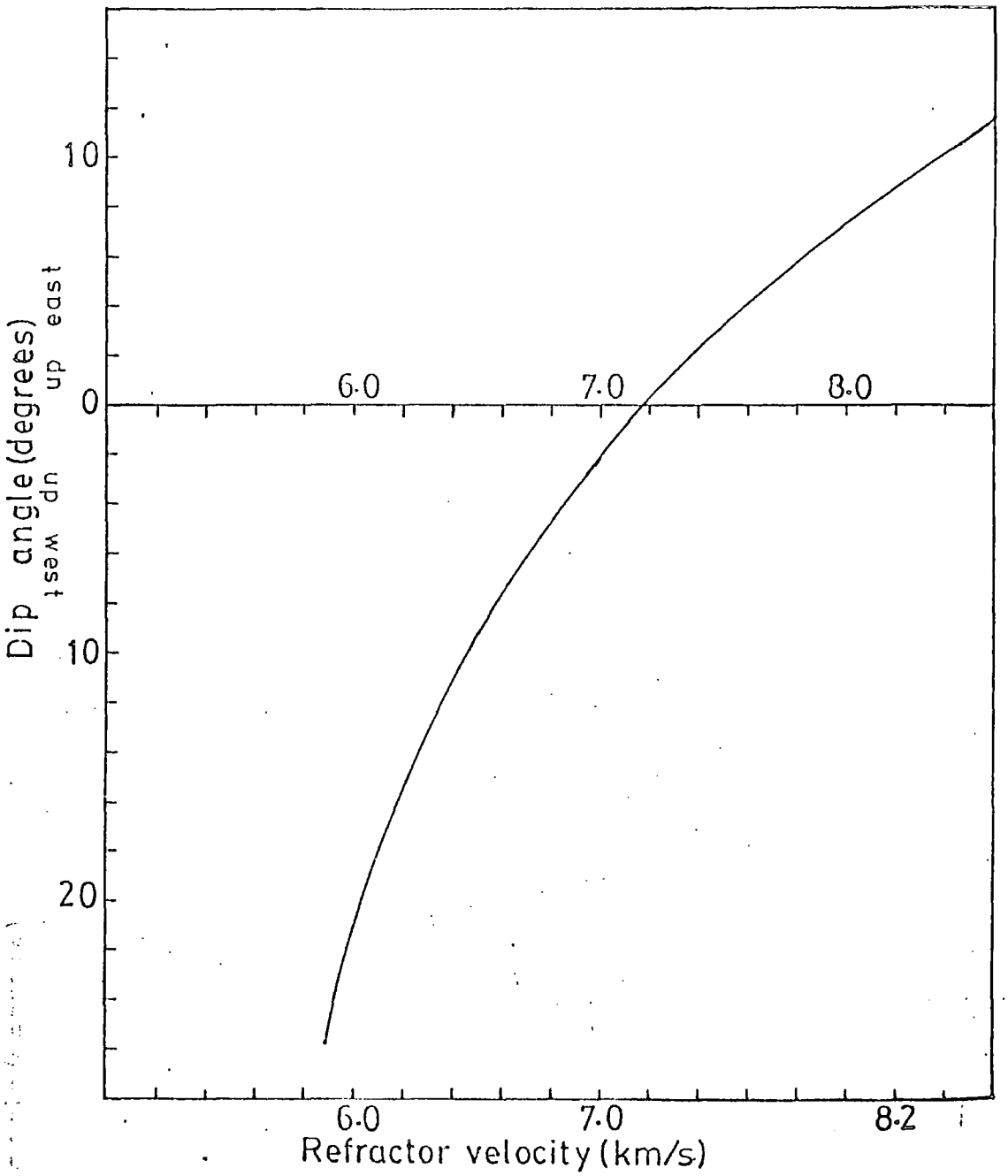

Fig 5.10: Plot of refractor velocity against refractor dip consistent with mean apparent velocity of 7·2 km/s.

within the axial zone of the rift. From a 300 km long seismic refraction profile along the axis of the southern portion of the Gregory rift (with end shot points at Lakes Baringo and Magadi), a maximum rock velocity of 7.6 km/s was observed at a depth of about 35 km (Khan et al., 1987). These observations suggest that, in our simple two layer model for the rift, refractor velocities greater than about 7.5 km/s are improbable.

The existence of material with such anamalous velocities in the region of the present study is supported by slowness and delay time teleseismic data (Long and Backhouse,1976). Their data is consistent with the existence of a low velocity material whose upper crustal part could have velocity in the range 7.1-7.5 km/s. The material is steep sided and extends to a depth of about 160 km beneath the normal crustal material on the western flanks of the Gregory rift at the latitude of Kaptagat. The authors assumed a mean velocity of 7.3 km/s for the body to explain their data.

Similar anomalous P wave velocities have also been reported in some other Cainozoic continental rifts and in Iceland. In Iceland a basaltic layer with P-wave velocity of 6.7 km/s is found to overlie a 7.4 km/s refractor at a depth of about 17.8 km (Bath, 1960). Palmason (1971) has shown that a 6.4 km/s layer overlies a 7.2 km/s layer at a depth in the range 8-16 km in different parts of Iceland. The refractor with a velocity of about 6.5 km/s has been found all over Iceland (Palmason, 1971) and the depth to its too surface is estimated at about 3-4 km (Zverev et al., 1980). It is thus evident that beneath both Iceland and the central part of the Gregory rift, rock velocities greater than about 7.5 km/s have not been observed.

Beneath most Cainozoic continental rift zones, these anomalous velocities have also been observed. On the basis of wide angle reflections and refractions, Cook et al.(1979) proposed a lower crustal replacement model for the axis of the central part of the Rio Grande rift. The model consists of an upper crust (6.0 km/s) overlying a lower crustal layer (6.5 km/s) and a basal crustal layer with a velocity of 7.4 km/s at a depth of 25 km. But for the same region, the crustal model based on a refraction profile (Olsen et al., 1979) indicates a crustal depth of 34 km and P_n velocities of 7.6-7.8 km/s. A review of the work of Soviet investigators shows that P_n velocities near the central part of the Baikal rift appears anomalous with values about 7.6 to 7.7 km/s (Olsen, 1983.).

From the foregoing discussions, it would appear that 7.8 km/s is a reasonable estimate for the maximum velocity, V_2, allowed for the refractor in the two layer plane model proposed here for the region of the present study. From fig. 5.10 it is found that for refractor velocities V_2 above 7.2 km/s, the refractor would dip up/towards the rift from Kaptagat axis. As V_2 increases from 7.2 to 7.8 km/s this dip, α, increases from 0^o to about 6^o. Hence the maximum dip, α_m, allowed on the boundary for updip towards the rift axis would be taken as about 6^o. Even if the maximum allowed V_2 had the unlikely high value of 8.0 km/s, α_m would only change to about 7^o. From the estimate of α_m as 6^o, the depth and the disposition of the refractor in relation to the rift were determined as shown below.

The travel time, t_d, for headwaves travelling downdip from source F (fig. 5.9c) to Kaptagat can be shown (appendix D) to be

$$t_d = \frac{1}{V_1} \{\Delta \text{Sine} + 2z_d \text{ Cos } (e-\alpha) + h \text{ Cose}\} \quad \ldots\ldots \quad (5.3)$$

where z_d is the length of the normal from focus to the plane refractor and h is focal depth. The corresponding travel time, t_{pg}, for direct waves from focus to Kaptagat is given by

$$t_{pg} = \frac{1}{V_1} (\Delta^2 + h^2)^{\frac{1}{2}} \quad \ldots\ldots \quad (5.4)$$

Since the arrivals under consideration are being interpreted as headwave first arrivals, t_d must be less than t_{pg} and this condition is satisfied if

$$Z_d \leq \{\frac{(\Delta^2+h^2)^{\frac{1}{2}} - \Delta \text{Sine} - h \text{ Cose}\}}{2\text{Cos}(e-\alpha)} \quad \ldots. \quad (5.5)$$

If the maximum value of z_d is designated D, then the maximum vertical depth, H, from epicentre to the refractor is

$$H = h + D/\text{Cos}\alpha \quad \ldots\ldots \quad (5.6)$$

In this analysis events located within the azimuthal range $94 \pm 5^{\circ}$ (in which the maximum apparent velocities are observed) are at an average distance of about 60 km from Kaptagat. Ray paths from such events would be expected to have sampled more of the rift structure than other ray paths. The mean value of e has been obtained as 53.7° and the maximum allowed dip α_m is 6°. On substituting these values of Δ, e and α_m into equations (5.5) and (5.6), a relation between H and h for the average distance of 60 km was obtained and plotted (curve A of fig. 5.11). It is found that as focal depths increased

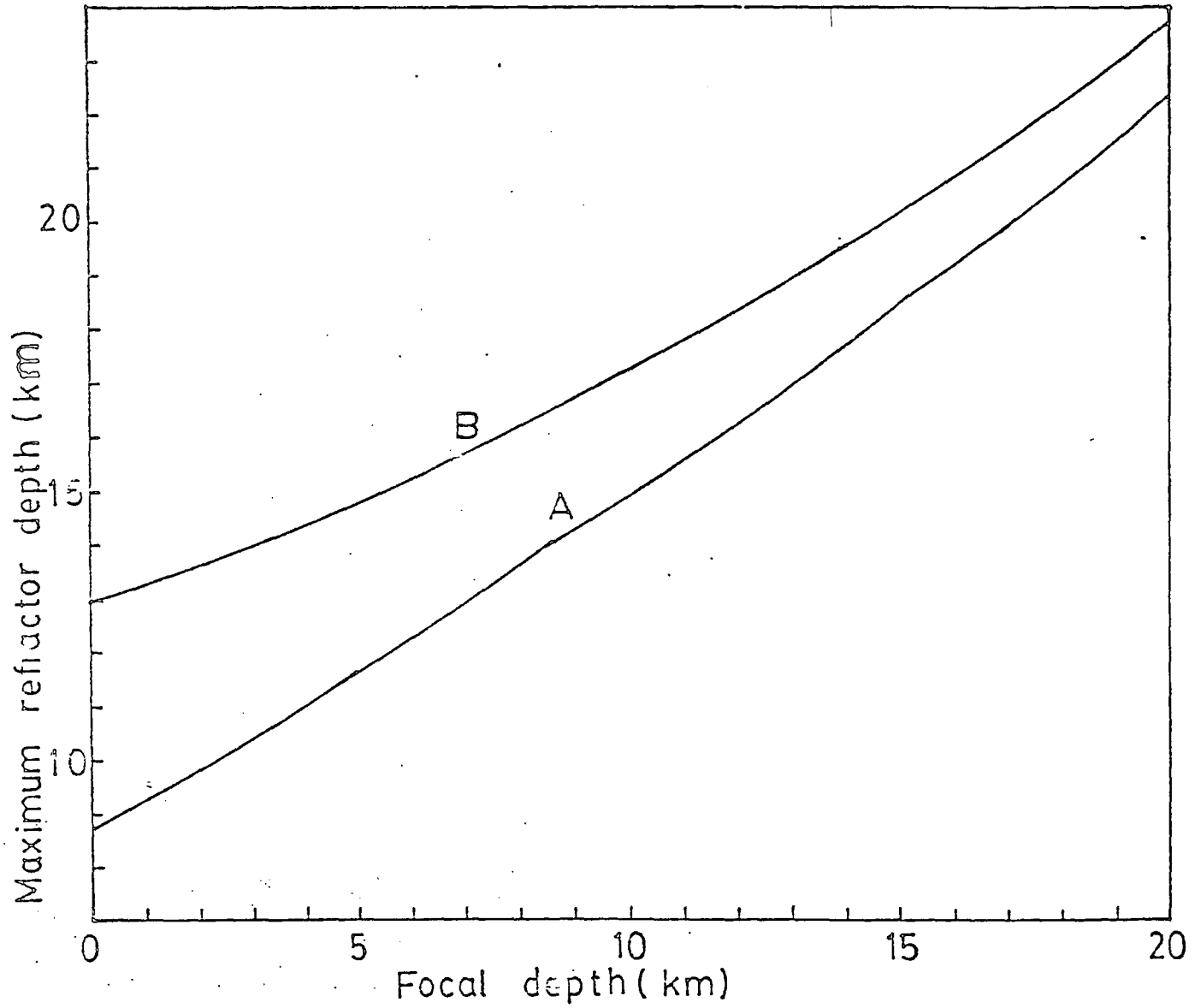

Fig 5·11: Maximum vertical depth of the refractor beneath the epicentre plotted against focal depth. Curve A is for a dip of 6° on the

from 0 to 20 km, H increased from about 9 km to about 22 km.

The disposition of the refractor for some values of h are shown in fig. 5.12a. Line OB corresponds to the mean measured apparent velocity of 7.2 km/s giving an angle of emergence of 53.7°. Lines OA and OC give the range of data coverage (6.9-7.5 km/s) and correspond to values of 50.6° and 57.2° respectively for e. For focal depths of 0,5,10, 15 and 20 km, the maximum vertical depth, H, from epicentre to the plane of the refractor would be about 9,12,15,18 and 22 km respectively. At these focal depths the refractor would extend west to horizontal distances of not more than about 18,21,25,29 and 34 km respectively east of Kaptagat. It follows, therefore, that the refractor would extend west to no more than about 3,6,10,14 and 19 km respectively east of the Elgeyo fault bounding the rift to the west; at these western limiting points the depths to the refractor would be about 13,16,18,21 and 25 km respectively.

An increase/decrease of about 10 km in distance, Δ, about the average distance of 60 km would result in an increase/decrease of less than 2 km in the corresponding estimate of H. This will, in turn, lead to an increase/ decrease of not more than about 4 km in the estimate of the maximum horizontal distance east of the western boundary fault (of the Gregory rift) at which the refractor could be located.

From the discussions in section 5.3, foci are expected to be shallow in the axial part of the rift where the epicentres are most probably located. Focal depths greater than about 10-15 km would seem unlikely. A most probable focal

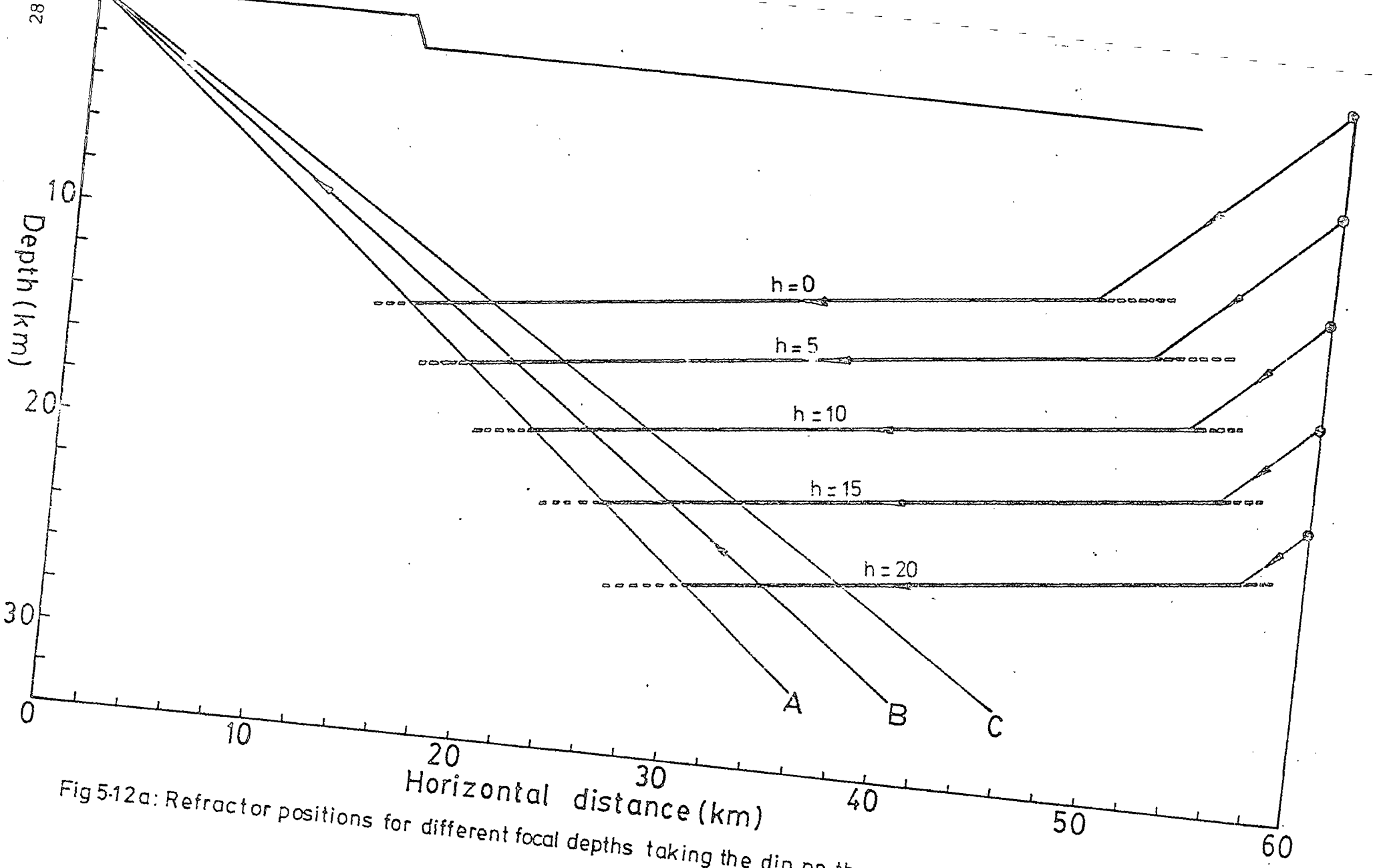

Fig 5-12a: Refractor positions for different focal depths taking the dip on the refractor as 6° up towards the east.

depth would be in the range 5-10 km; this would, in turn, imply that the western or Kaptagat end of the refractor would extend to within a distance of not more than about 6-10 km east of the Elgeyo fault at refractor depths of about 16-18 km. These results were deduced using the maximum allowed dip, α, of 6^{o}. For smaller values of α, smaller values of refractor depths and lateral displacements east of Kaptagat would be obtained.

We next consider the possibility of an eastward dip on the interface down from Kaptagat towards the rift axis. From fig. 5.10, the present data could be satisfied for refractor velocities in the range 5.9 to 7.1 km/s provided the corresponding dips on the interface were in the range about 26^{o} to 1^{o}. If we associate the refracting interface with the upper surface of the crustal intrusion suggested by gravity and seismic data (Baker and Wohlenberg, 1971; Savage and Long, 1985), large dips down towards the rift axis would be unlikely. Such large dips would suggest that the crustal intrusion deepens towards the axial part of the rift. This suggestion which also implies lower than normal crustal velocities contradicts the established interpretation of the axial positive Bouguer anomaly as due to the presence of dense mantle derived crustal intrusion shallowing towards the rift axis.

The region of study is within the rift which is characterised by higher than normal crustal velocities. The refractor velocity is therefore very unlikely to be less than the mid-crustal velocity of 6.5 km/s established for the normal shield crust adacent to the rift (Maguire and Long, 1976).

A reasonable estimate for the minimum acceptable refractor velocity would thus be 6.5 km/s. The present data will be satisfied if a refractor with that velocity has a dip of about 9^{o} from Kaptagat down towards the rift axis. The maximum dip allowed in this direction would thus be 9^{o}. As in the preceding paragraphs, the possible disposition of the refractor (with its dip down east) as a function of focal depth will now be determined.

From fig. 5.9d the travel times, t_u, for headwaves travelling up dip from focus to the surface at Kaptagat station can be shown (appendix D) to be given by

$$t_u = \frac{1}{V_1} \{ \Delta \text{Sine} + 2z_u \cos(e + \alpha) + h \cos e \} \quad \ldots \quad (5.7)$$

where z_u is the length of the normal from the focus to the plane of the interface. The condition that these headwaves come in as first arrivals preceding direct wave onset in time can be shown to be

$$z_u \leq \frac{\{(\Delta^2 + h^2)^{\frac{1}{2}} - \Delta \sin e - h \cos e\}}{2 \cos(e + \alpha)} \quad \ldots \quad (5.8)$$

Equation (5.8) gives the maximum value of z_u, say U, as a function of focal depth, h. From U, the maximum vertical depth, H, to the refractor beneath the epicentre is estimated from the relation

$$H = h + U/\cos\alpha \quad \ldots \quad (5.9)$$

In the present discussion, e, Δ and α have the values 53.7^{o}, 60 km and 9^{o} respectively. By substituting for α, e and Δ in equations (5.8) and (5.9), H is estimated as a function of h (curve B of fig. 5.11). As focal depth is increased from 0 to 20 km, the vertical depth from the epicentre to the plane of

the refractor increases from about 13 km to about 23 km. The corresponding dispositions of the interface with respect to the rift are shown in fig. 5.12b for focal depths of 0,5,10, 15 and 20 km respectively.

It is found from fig. 5.12b that as the focal depth increases from 0 to 20 km, the maximum horizontal distance from Kaptagat (eastwards) to the interface increases from about 5 km to about 23 km (i.e. from about 10 km west to about 8 km east of the Elgeyo fault). The corresponding vertical depths to the interface at these inferred western limit of the refractor for focal depths of 0,5,10,15 and 20 km are found to be 4,7,9,12 and 16 km respectively. For the most probable focal depth of 5-10 km, the interface would extend westwards to at least 6 to 3 km west of the Elgeyo fault and at depths of 7 to 9 km (fig.5.12b). An uncertainty of about 10 km in distance at the distance of 60 km would result in an uncertainty of about 3 km in estimate of westward lateral extension of interface and about 3 km in depth estimate.

From the above discussions, an updip of the 5.8/6.5 km/s refractor (Maguire and Long, 1976) from the rift axis to the west could explain the mean apparent velocity of 7.2 $\pm$ 0.2 km/s observed at Kaptagat. But the thickness of the upper crustal layer becomes unacceptably small unless unacceptably large focal depths were assumed (fig. 5.12b). For focal depths less than about 10 km, the crustal intrusion proposed here extends well beyond the western margin of the Gregory rift where the existence of normal shield crust has been firmly established by seismic data (Maguire and Long, 1976). In that region, the model proposed here for the region does not also agree with the gravity data (Baker and Wohlenberg, 1971) which suggest a crustal

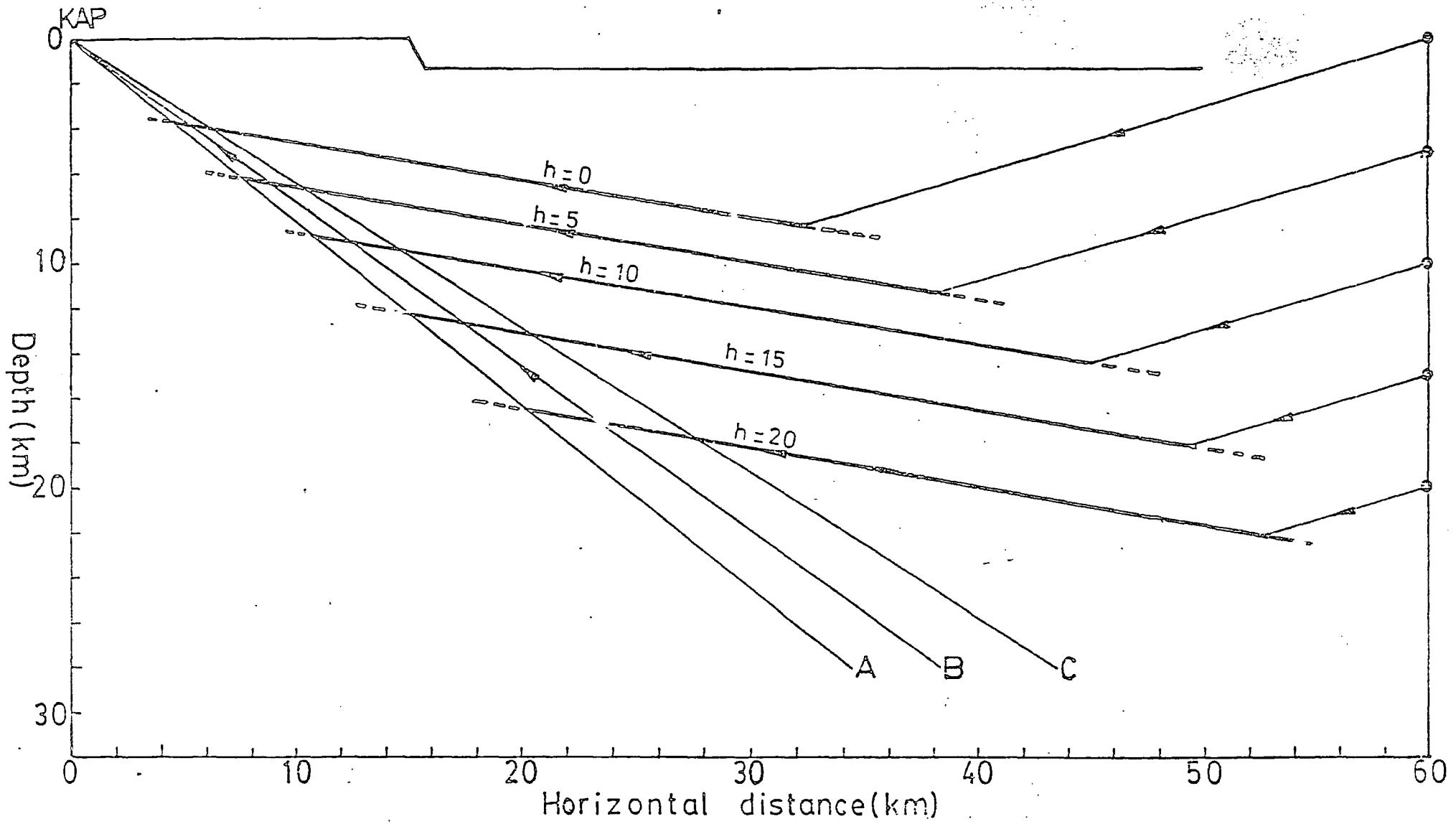

Fig 5·12b: Positions of the 5·8/6·5 km/s interface for different focal depths assuming the dip on the interface is 9° up towards the west.

intrustion of much smaller width limited to the inner graben.

5.5 The effect of a steep dip on the boundary.

Gravity and seismic data strongly suggest that within the Gregory rift zone, at about the latitude of Kaptagat, a steep boundary seperates the normal shield type crust to the west (Maguire and Long, 1976) from the anomalous rift structure to the east (Baker and Wohlenberg, 1971; Savage and Long, 1985). We now discuss the possibility that ray paths in present study may have sampled such a steep interface. Although the problem is a three dimensional one, the present data can only support a two dimensional interpretation.

Consider a steep plane refracting boundary AB dipping at an angle α and seperating two rock layers of P wave velocities V_1 and V_2 (fig. 5.13). If the angle of emergence for the ray at Kaptagat is e, then the angle of refraction, θ, in the second medium is given by

$$\theta = \mathrm{Sin}^{-1} \left(\frac{V_2}{V_1} \mathrm{Sin}(\alpha - e)\right) \qquad \ldots\ldots \quad (5.10)$$

We assume that V_1 has the value 5.8 km/s (Maguire and Long,1976) and study the deviation of the ray at the interface for realistic values of V_2. As the ray strikes the boundary, the ray path suffers a deviation D in the vertical plane containing the ray and the normal to the refracting interface where the deviation is given by

$$D = \theta - \alpha + e \qquad \ldots\ldots \quad (5.11)$$

From equations (5.10) and (5.11), D could be calculated for values of refractor velocity V_2 from 5.9 to 8.0 km/s for given values of dip, α. In fig. 5.14, D is plotted against V_2 for dip angle α increasing from 10° to 130° in steps of 10°.

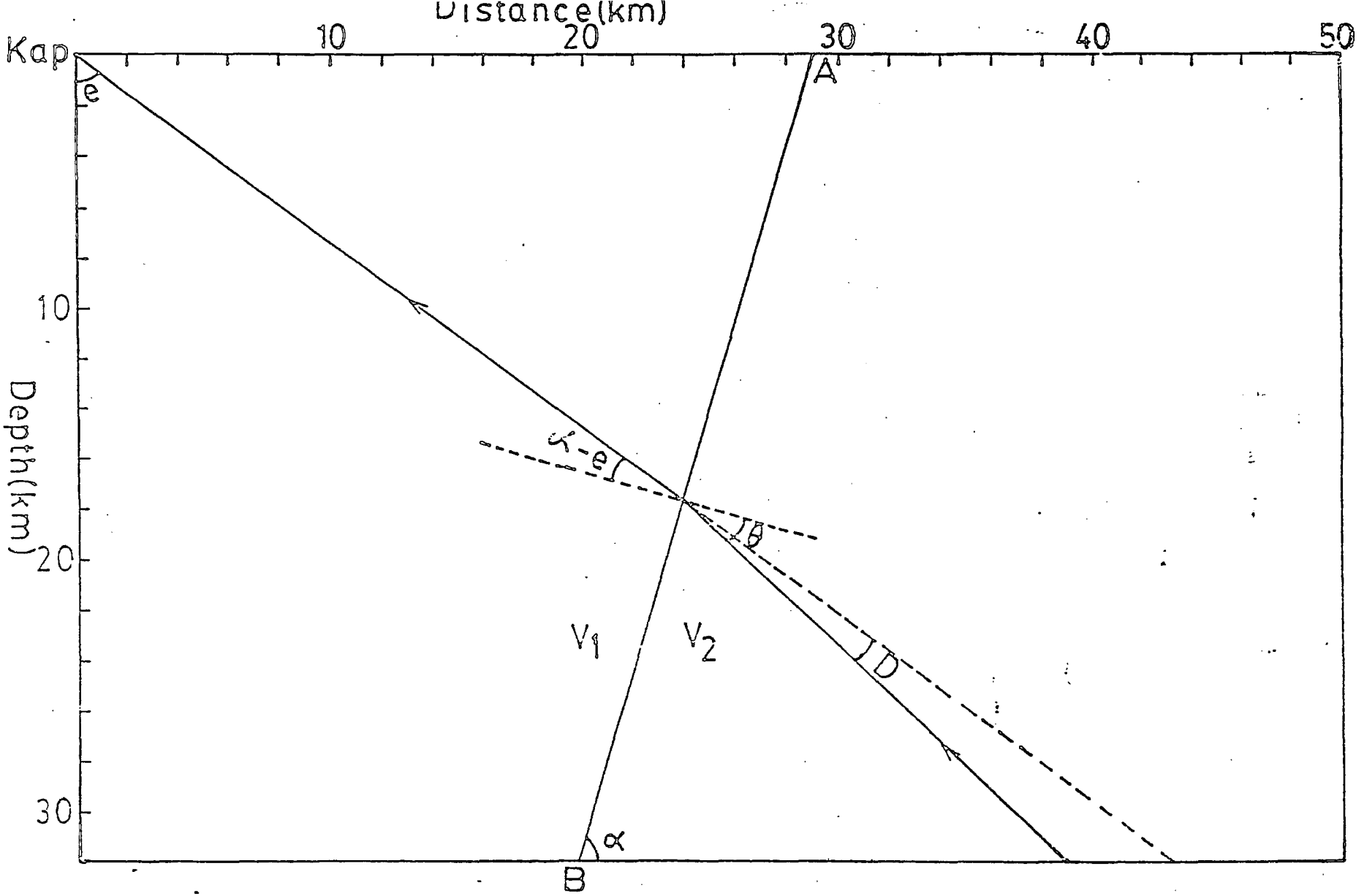

Fig 5-13: Diagram to illustrate the deviation of a ray to Kaptagat as it encounters a steep plane boundary between materials of velocities V_1 and V_2.

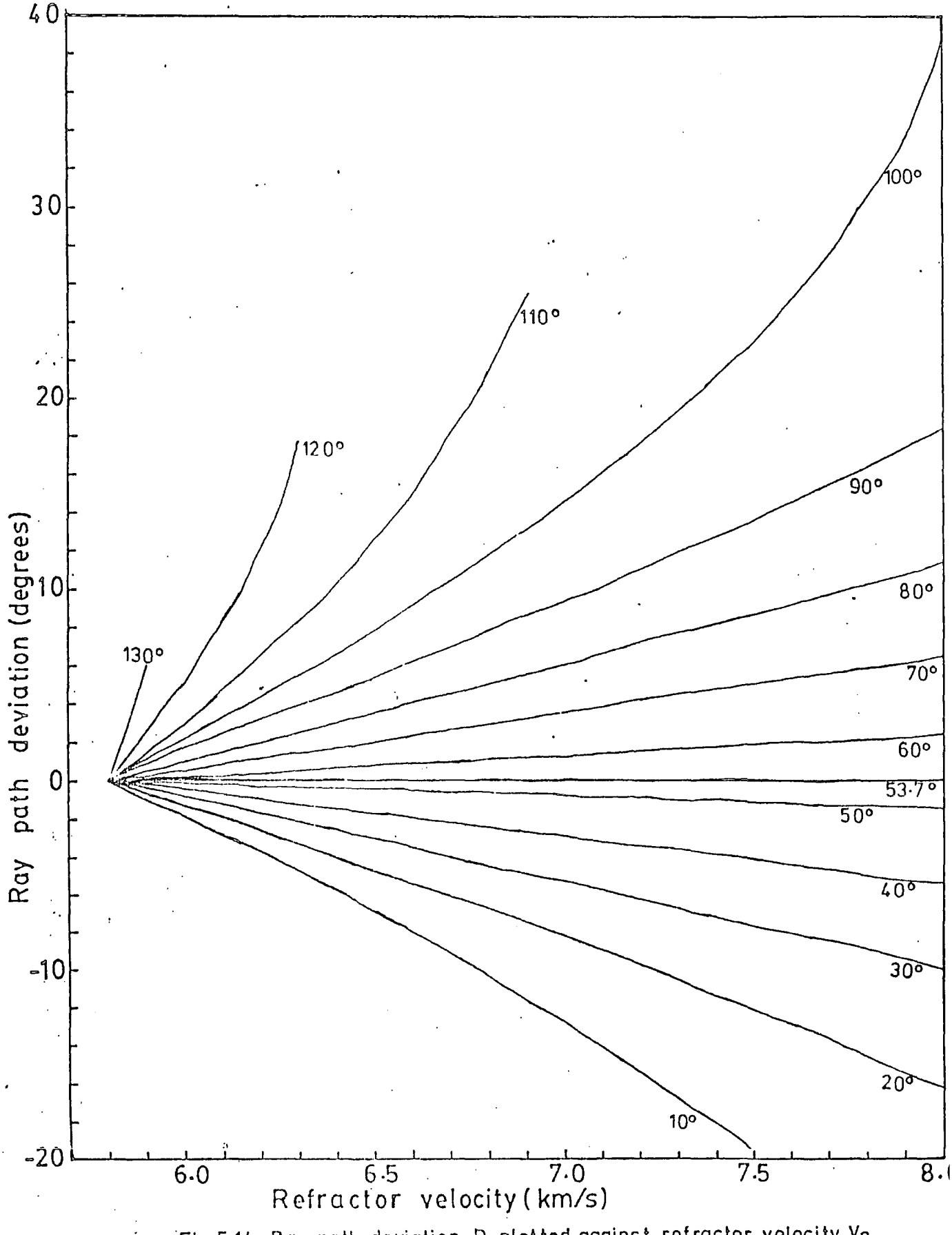

Fig 5·14 : Ray path deviation, D, plotted against refractor velocity, V_2 for different angles of dip.

For a ray starting at Kaptagat and striking the boundary, an effective deviation vertically downwards in the second medium is regarded as positive while a deviation vertically upwards is negative. From this plot, it is found that for dips greater than 53.7^{o}, the ray paths are deviated vertically down for all V_2 greater than 5.8 km/s. Such downward deviation of the ray path would suggest that for the distances (about 60-80 km) observed in this study, the focal depths would be greater than about 43 km. But such large depths of focus are not consistent with available geological and geophysical data (see section 5.5.3). Dips of more than about 54^{o} are, therefore, unlikely unless the rays subsequently encounter nearly horizontal refractor on their path and are then deflected upwards or that the rays encounter, in the second layer, material in which the velocity increases with depth.

If the dip on the boundary is about 54^{o}, the rays are normal to the refracting boundary and are undeviated for all values of V_2. Interfaces with about this value of dip would, therefore, not be confidently detected by the present data. It has, however been argued that such large dips imply unacceptably large focal depths and are, therefore, inconsistent with the present data.

For dips less than about 54^{o}, the ray paths suffer upward deviations from their original directions in the vertical plane defined by the rays and the normal to the dipping refractor. Such a deviation is in the right direction to lead to shallower and acceptable focal depths. But the magnitude of the deviation produced may be insufficient to guarrantee reasonably shallow foci in the short distances involved.

If we take 7.9 km/s as the maximum allowed refractor velocity V_2 (see section 5.3), it is found from fig. 5.14 that the maximum upward deviation decreases from about 25^{o} to about 1^{o} as the dip, α, increased from about 10^{o} to about 50^{o}. Assume, in the extremely unlikely situation, that the refractor intersects the ray just before but very close to Kaptagat. The calculated maximum deviations for dips of 10^{o}, 20^{o}, 30^{o}, 40^{o} and 50^{o} occur when V_2 has the maximum allowed value of 7.8 km/s and would lead to focal depths of about 12, 23, 28, 36 and 42 km respectively. These estimates of focal depth would be increased as the interface moved east away from Kaptagat. Since foci deeper than about 15 km are unlikely beneath the part of the rift under study, dips of more than about 10^{o} are inconsistent with the present data. This observation is in agreement with the discussions in section 5.3.

To summarise, we state that steep dips are inconsistent with the present data. It would thus appear that the data is sampling a nearly horizontal top surface of a possible intracrustal intrusion or a gently dipping mid-crustal interface in the shield crust. The data does not seem to have sampled the steep boundary inferred to seperate normal structure to the east.

5.6 Lateral variation in velocity.

The crustal zone of partial melt indicated beneath the Gregory rift (Banks and Beamish, 1979; Rooney and Hutton, 1977)

coincides with the trend of the positive Bouguer anomaly observed over the axial part of the rift (Searle, 1970; Baker and Wohlenberg, 1971). Quarternary volcanoes and hot springs are mostly confined to the zone of this axial positive anomaly which is also associated with very high heat flow values (Crane and O'Connel, 1983; Morgan, 1983). These observations strongly suggest that the crust, within this zone, may be intruded by hot dense mantle derived basaltic rock which may at present, be cooling.

The temperature of this inferred intrusive body may be expected to decrease from the centre outwards. If the mineralogical composition of the cooling rock mass is assumed uniform, then the density, and hence, the seismic velocity would increase from the centre out towards the contact with the host rock. As a result there would be gradational lateral variation of density/velocity within the intrusion. Seismic rays would, therefore, be refracted not only in a vertical plane but also in a horizontal plane. This type of structure could give rise to the observed P-X time/apparent velocity relationship indicated by line CD in fig. 5.4.

The observed increase in apparent velocity from about 7.1 km/s to 7.5 km/s as P-X time increased from about 8.1 s to 9.7 s could be partly explained (qualitatively) as due to gradual lateral increase in rock velocity of an intrusive body from its hot centre towards the cooler outer parts. P-X time of 8.1 s corresponds to a distance of about 59 km (to the east of Kaptagat) which falls within the axial zone of rift. The data suggests, therefore, that the rock velocity

within such intrusive body would increase from the hot central part to the cooler outer parts extending up to about 12 km from the centre. The boundary between this dyke like body and the normal shield crust would be expected to be steep because of change in mineralogical composition. The problem as presented above requires three dimensional interpretation which could not be supported by the present data. No such interpretation is attempted here.

5.7 Vertical variation in velocity.

.7.1 Introduction.

It has been suggested (section 5.2.2) that the data set in fig. 5.4 could be divided into two groups represented by lines CD and EF respectively. It was shown that for the first group (line CD) there is a significant linear increase in measured first arrival apparent velocity with P-X time (and hence distance). The slope of the regression line of apparent velocity on P-X time for the first group is 0.25 $\pm$ 0.18 km/s^2; this slope suggests an average horizontal gradient of about 0.031 km/s per kilometre over the distance of about 12 km corresponding to a change in P-X time from 8.1 s to 9.7 s.

For events in the second group (line EF of fig. 5.4) there is no significant linear variation of velocity with P-X time at the 95% significance level. The 95% confidence limits for measured phase velocities in this group are 7.0 $\pm$ 0.1 km/s. The complete data (fig. 5.4) taken as a whole, therefore, suggests the existence of a layer in which velocity

increases with depth overlying a nearly horizontal refractor of constant velocity.

To illustrate the validity of this suggestion we consider the simple case in which rock velocity, V, is a linear function of depth, Z, given by

$$V = V_o + kZ \tag{5.12}$$

where V_o is the rock velocity at top of layer and k is a constant. The travel time t for rays in such layer is given (Dobrin, 1976) by

$$t = (2/k)\sinh^{-1}(kx/2V_o) \tag{5.13}$$

where x is the horizontal distance from source to detector. The apparent velocity, V_a, is obtained by differenting x with respect to t in equation (5.13):

$$V_a = \frac{dx}{dt} = V_o \cosh(\sinh^{-1}(kx/2V_o)) \tag{5.14}$$

The rate of change of apparent velocity V_a with distance x is then given by

$$\frac{dV_a}{dx} = k^2 x/(4 \cosh(\sinh^{-1}(kx/2V_o))). \tag{5.15}$$

The numerator and denominator of the expression in equation (5.15) are positive for all positive values of x. Hence $\frac{dV_a}{dx}$ is positive indicating that V_a increases as x increases. For such a layer, therefore, apparent velocity would increase with distance from the source.

In this analysis, ray paths from all foci converge at Kaptagat and are completely reversible. In other words, if all the sources are located at Kaptagat, the rays will reverse

their paths and pass through their respective foci. The implication of this and the preceding discussion is that apparent velocity would increase with increasing distance from Kaptagat if the velocity of the subsurface material increased linearly with depth. The two groups of data put together would suggest that below the layer in which velocity increased with depth, there is a high speed horizontal refractor whose true rock velocity is probably not less than about 7.0 km/s. If there is appreciable dip on the refractor, the true rock velocity will be greater than this value.

Geological and geophysical data indicate that the crust beneath the Gregory rift is intruded by dense basaltic material derived from the mantle. The concentration of this high density basic material present would increase with depth and give rise to increase in density/seismic velocity with depth. A model in which velocity increases with depth is thus plausible. A ray tracing program was used to obtain one such model consistent with the present data.

5.7.2 The ray tracing program.

The program used (RTO1 and its later modification SEIS 83) was that originally written by I. Psencik and subsequently modified by V. Cerveny. The English version has been updated at Durham to make use of NUMAC graphic subroutine library PLOTSYS. The program is designed for the computation of rays of seismic waves which arrive at a number of receivers distributed along the earth's surface. It handles two-dimensional laterally inhomogeneous models with curved interfaces.

The program uses ray-tracing theory, in which the path of each ray is calculated in terms of the distance and direction travelled by the ray during successive, small time-steps. Each ray path is therefore defined by a series of short, straight line segments, whose length and direction are controlled by the local seismic velocity distribution. Normally, each segment represents the same travel time. If, however, the ray reaches an interface before the end of a time step, then that ray segment is automatically truncated at the interface and the time step shortened accordingly. A new time-step is then started for the reflected or refracted ray after it has left the interface.

The velocity structure within the model is specified in two ways. In the first mode, the model may be divided into layers using a set of interfaces across which sharp velocity jumps occur. Secondly, the model may be divided up using a series of horizontal and vertical grid lines, thus allowing the introduction of horizontal and vertical velocity gradients. Interfaces may be specified by their x and z coordinates or directly as a function of x and z. The simultaneous use of interfaces and grid lines allows for great flexibility in specifying velocity distributions. Approximation of velocity distribution inside individual layers is carried out by cubic spline interpolation, linear interpolation between insovelocity interfaces, or by piece-wise bilinear interpolation. The program package SEIS 83 includes programs for the preparation of data for velocity model (SMOOTH), to compute synthetic seismograms (SYNTPL) and to plot rays, travel-time and amplitude-distance curves (RAYPLOT) or synthetic

seismograms (SEISPLOT).

Input to the program includes control indices, model parameters and depth of source, h. The control indices control the behaviour of the rays at interfaces (i.e. whether reflection or refraction) and the mode used for generating the velocity distribution (whether by a mesh or through an analytical function). Pure head waves are not considered in the program. The model parameters are described by a block of cards which give information about interfaces, mesh lines, velocities and source coordinates within the model. Horizontal distance, x, from the source to observation point is determined by the angle (with the x-axis) at which the given ray is projected from the source. This angle (measured in radians) is taken as positive below the x-axis and negative above. The initial angle taken is such that all the rays that can emerge at the surface are calculated from the given increment in the initial angle and the number of rays to be shot out.

Results from the computations are displayed in the form of plotter and line printer outputs. The plotter output includes a ray diagram and a reduced time-distance plot. Amongst other information, the line printer output consists of the input data for the model and a table of results from successful rays (i.e. rays that succeed in completing the required trajectories). These results give the epicentral distance x, the travel time and the amplitude (when required) of each ray.

5.7.3 Interpretation in terms of uniform increase in velocity.

Savage and Long (1985) have derived a structural model for the central part of the Gregory rift at about the latitude of Kaptagat (fig. 1.7). We may assume that the epicentres in the present study are all within the axial part of the rift and that focal depths are of the order of 5-10 km. Then ray tracing (using program RT01) shows that the rays sampling the 7.5 km/s material in this model are mostly refracted downwards and do not come up to the surface (fig. 5.15) unless they encounter a region in which velocity increases with depth. However, if the top surface of the model were planar, nearly horizontal and had a much wider lateral extent, headwave arrivals could be observed at epicentral distances in the range 60-80 km (see section 5.4.2). The critical distance for such headwaves decreases from about 49 km to about 30 km as focal depth increases from 0 to 15 km. In the present section, we attempt to derive a model (consistent with the data) in which velocity increases with depth.

The rays in the present data arrive Kaptagat at steep angles of emergence. For these rays from probably shallow foci to emerge at the surface within the observed short distance range at angles of emergence in the range 54 ± 3^{o}, the ray paths would be expected to show definite upward concavity. This, in turn, would suggest that the rays may have sampled a region in which velocity increases with depth as discussed in section 5.7.1. In the present section, the data will be interpreted in terms of a two dimensional horizontally layered model in which a constant velocity layer overlies a layer in

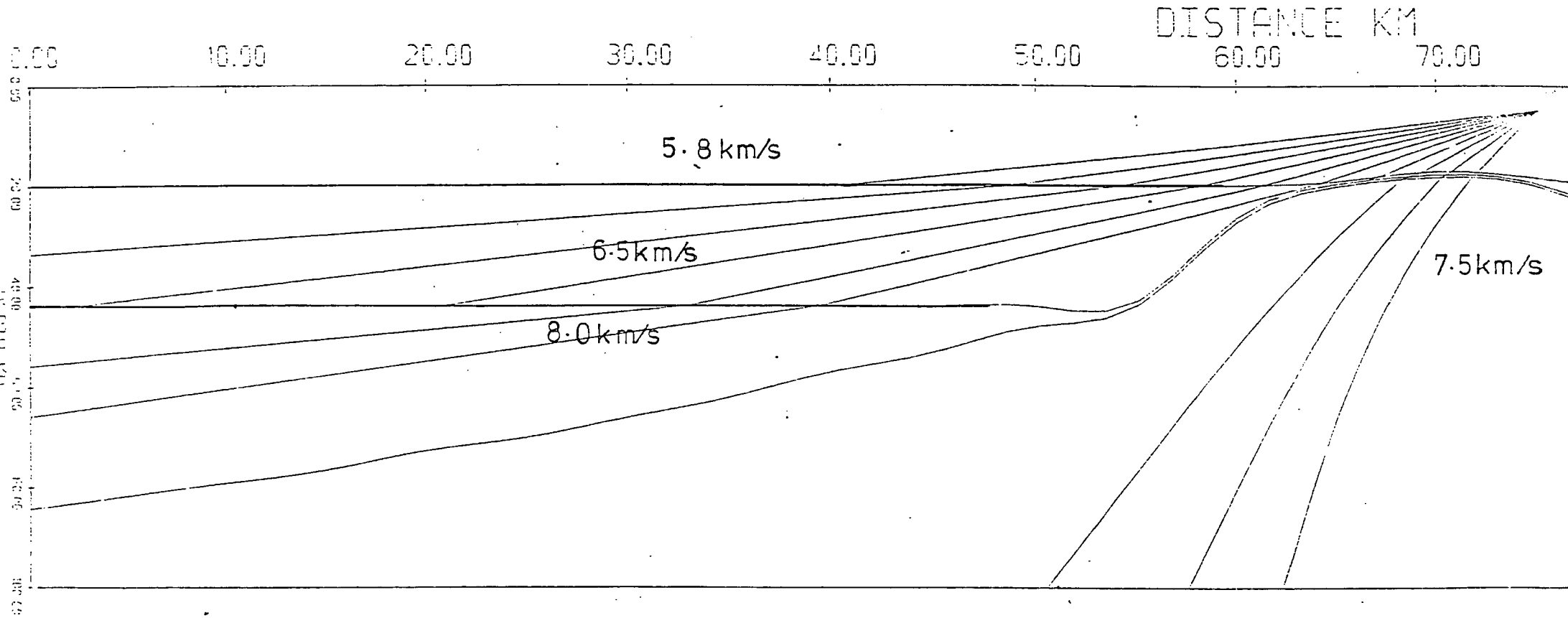

Fig. 5.15: Ray tracing (using RT01) through the lithospheric model of Savage and Long (1985). Rays (from a shallow focus) sampling the 7.5 km/s material are mostly refracted downwards and do not emerge at the surface.

which there is uniform increase in velocity with depth. Such a model will be constrained by some conclusions/inferences reached in our earlier discussions. Focal depths must be small - less than about 10-15 km. A constant velocity of 5.8 km/s (Maguire and Long, 1976; Swain et al, 1981) will be adopted for the top few kilometres of the crust beneath the rift floor and beyond. In addition, the layer in which velocity increases with depth (according to equation 5.12) would be terminated by a constant velocity refractor or in a region of sudden change in velocity gradient. Here V_o in equation 5.12 is the velocity with in the basement rocks of velocity 5.8 km/s.

The modelling involves estimating the probable values of basement thickness, the velocity gradient, the thickness of the layer in which velocity increases uniformly with depth and the velocity of the refractor at the base of this intermediate layer. The ray tracing program (RT01/SFIS83) discussed in section 5.7.2 was used in a trial and error manner to obtain estimates of these parameters. Any acceptable model must be able to explain the first arrival apparent velocities (in the range 6.9-7.5 km/s) observed at Kaptagat station.

In the modelling a typical initial angle from the source was about 2.20 radians. Increment in initial angle depended on increment in source-receiver distance and the number of receiver positions. Interfaces were taken as plane and horizontal and were specified by the x and z coordinates of points selected on them. Velocities above and below each interface were stipulated at selected points along the interface. The program then used linear interpolation to establish other

points on the interface and the velocity at each point of the model.

A range of velocity gradients was tried and values of about 0.15 to 0.20 s^{-1} were found to explain the data adequately. The thickness of the upper crustal layer (velocity 5.8 km/s) was estimated at about 10 km. The underlying layer of uniform increase of velocity with depth had estimated thickness of about 10 km. In the interpretation no fixed value was assumed for focal depth.

The proposed model with the corresponding ray diagrams and reduced travel time plot for a focal depth of 9 km is shown in fig.5.16. In the top layer a slight velocity gradient (0.01 s^{-1}) was introduced. In the second layer velocity increased from 6.0 km/s to 7.5 km/s as depth increased from 10 km to 20 km. Just below the 20 km interface the velocity was taken as 7.6 km/s. Fig. 5.16 a and b show ray diagrams and the reduced travel time curve (reducing velocity 6.0 km/s) for direct waves. Similar plots for the reflections from the 10 km interface are shown in fig. 5.16c and d. Fig. 5.16e and f show the corresponding plots for diving waves sampling the intermediate layer and the reflections from the 20 km interface which are of main interest in the present study.

On the plotter outputs (and also on the line printer outputs) from program SFIS83 source and receiver horizontal positions were measured from an arbitrary zero at the left end of the plotting space. Source-receiver horizontal distance, Δ, was obtained as the difference between their respective positions.

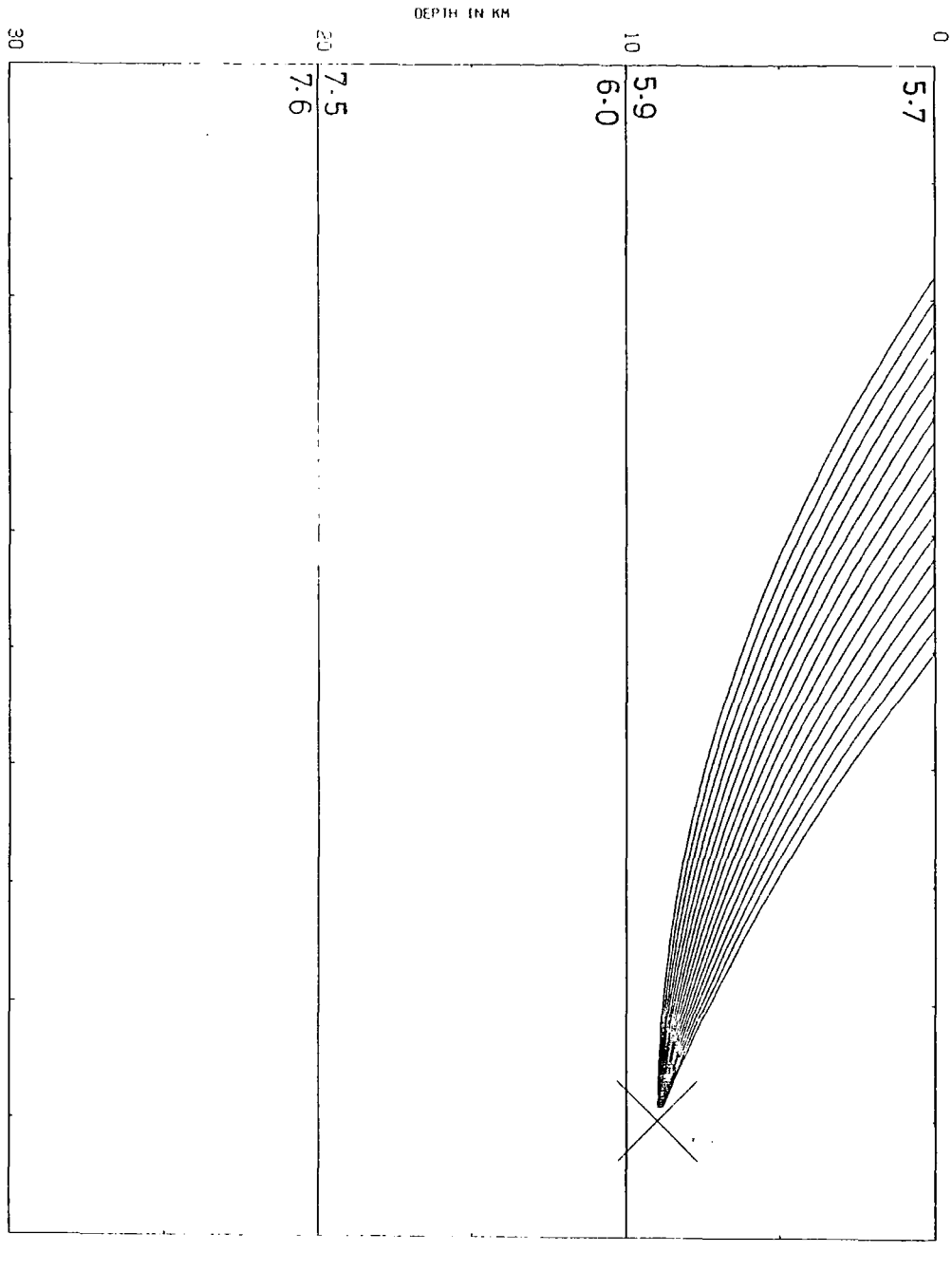

Fig. 5.16a: Ray diagram for direct waves. Model velocities in km/s.

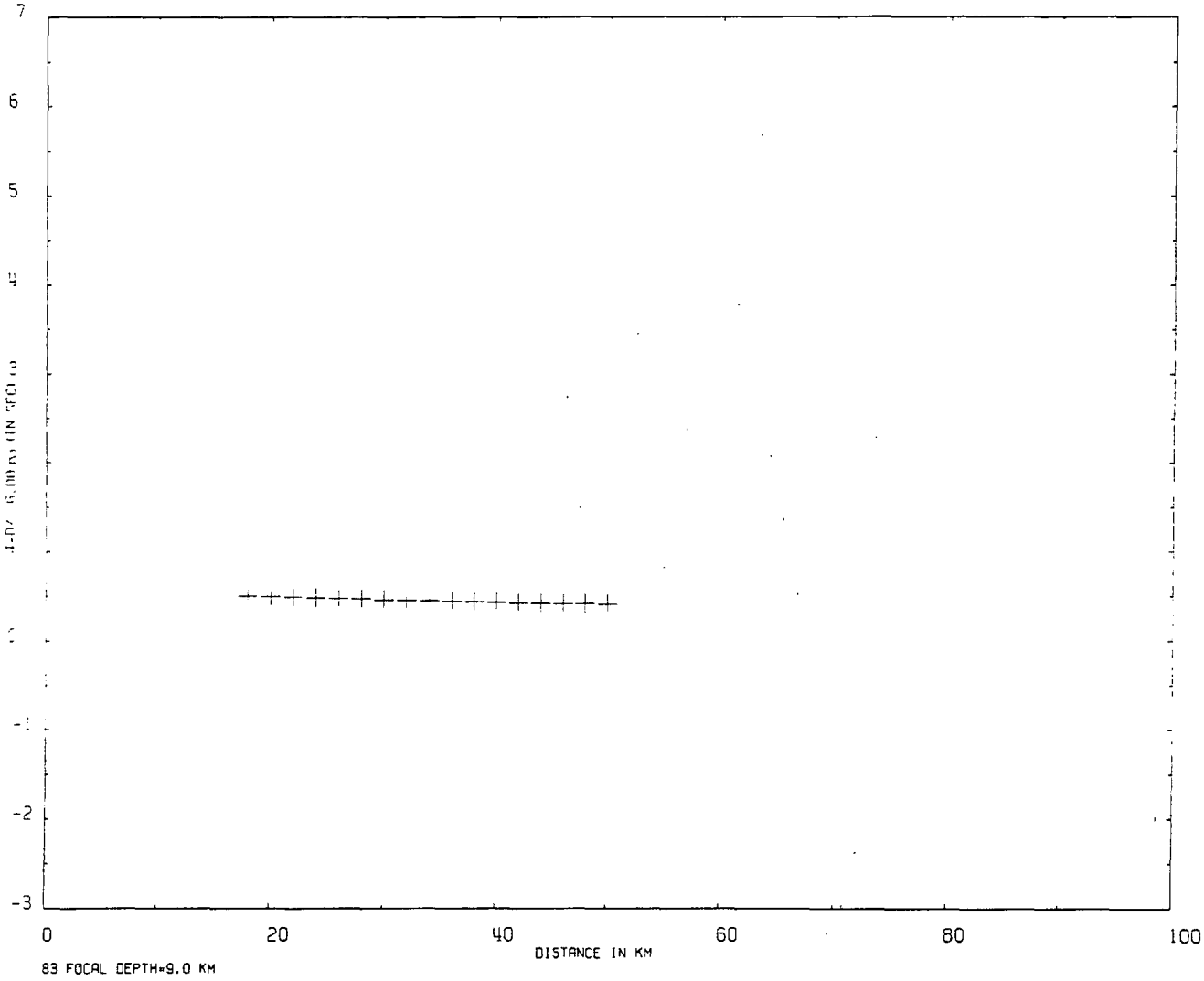

Fig. 5.16b: Reduced travel time plot for the direct waves shown in fig. 5.16a.

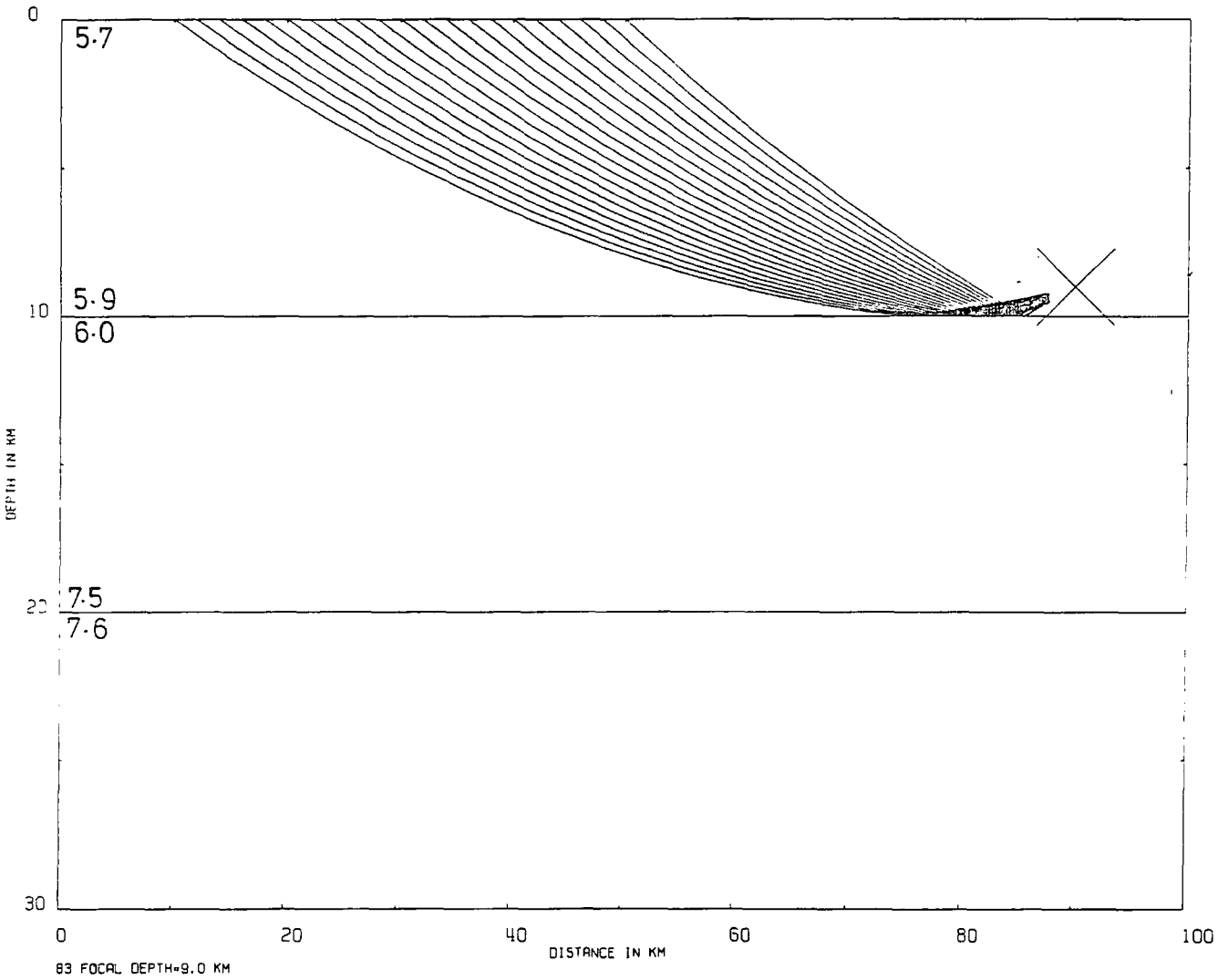

Fig-5-16c: Ray diagram for reflections from the interface at depth of 10 km. Model velocities in km/s.

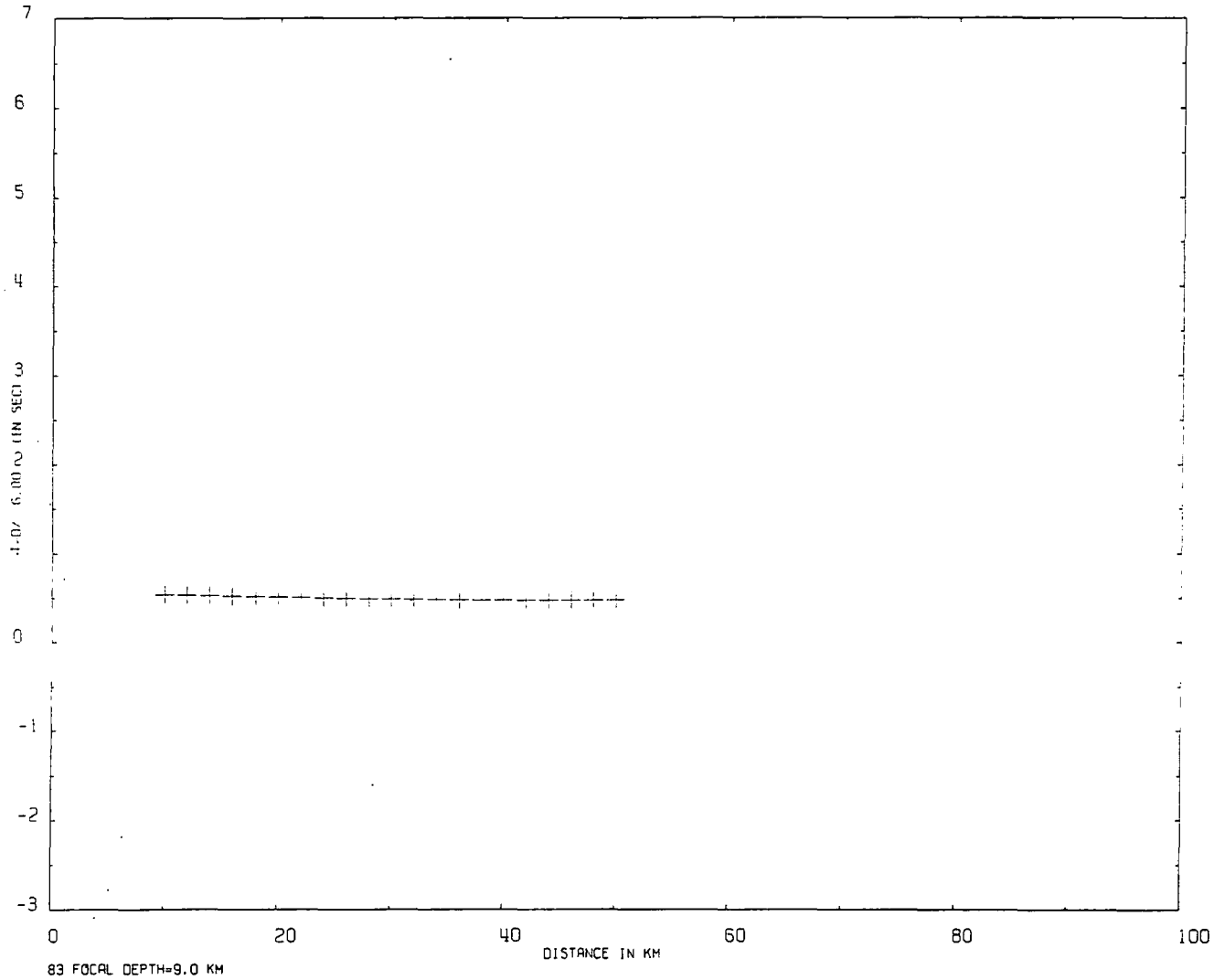

Fig-5.16d: Reduced travel time plot for the reflections shown in fig-5.16c.

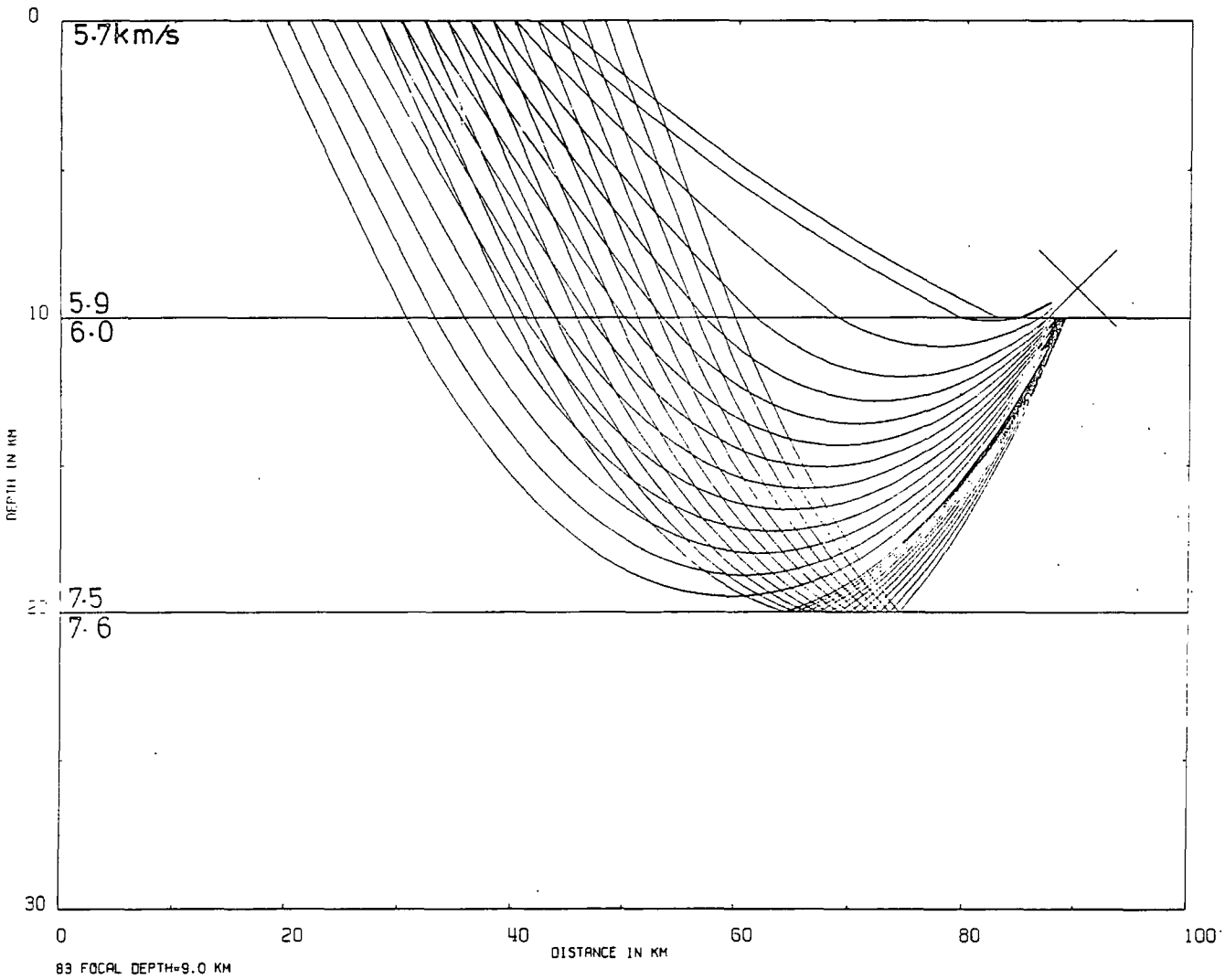

Fig. 5·16e: Ray diagram for diving waves sampling the intermediate layer of uniform increase in velocity with depth. Also shown are reflections from the 20km interface.

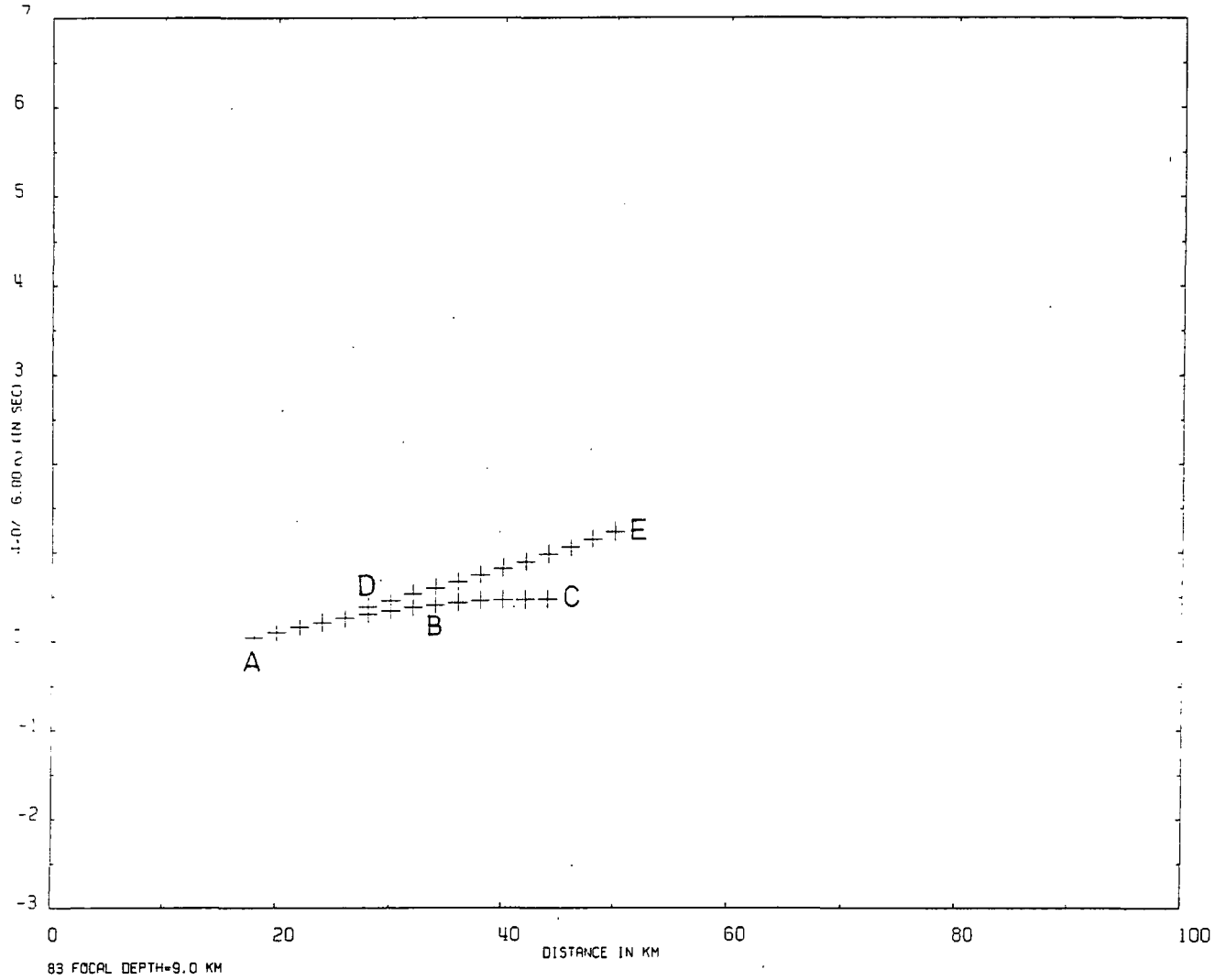

Fig. 5-16f: Reduced travel time plot for the diving waves and reflections shown in fig. 5-16e.

In the input data, the source position was put at about 90-100 km and the initial angles taken so that the receivers were located west of the source. Of main interest in the present study is the source-detector horizontal distance in the range about 60 to 80 km which would correspond to the observed range of distance to Kaptagat.

A portion of the line printer output corresponding to fig. 5.16 is shown on table 5.1. The information on this output includes the input data and the results of the computations for the direct wave (code -111), reflections from the first interface (code 1211) and waves that have sampled the second layer (code 141221). Within the output for each of these phases, the nominal receiver position is shown in the first column. The second and the third columns contain the x and z coordinates of the receiver positions actually used in the computations. The computed travel time is shown in the fourth column.

To confirm that the proposed model is consistent with the present data, it is necessary to show that the rays from a source within the model would arrive the position of Kaptagat (epicentral distance about 60-80 km) at the right angle of emergence to give the observed first arrival apparent velocities (6.9-7.5,km/s). To show this, we use the ray diagram/reduced travel time curve in fig. 5.16e/f and the corresponding line printer output in table 5.2. The reduced time-distance curve (fig. 5.16f) splits into two branches. The steeper branch DE containing 12 points and covering a distance range of 40-62 km, has greater value of travel time (for the same distance) than

```
 4     3     2     1
  0.0          0.0          0.0          0.0          0.0          0.0          0.0          0.0          0.0          0
  0.0         10.00000      0.0          0.0          0.0          0.0          0.0          0.0          0.0          0
  0.0         20.00000      0.0          0.0          0.0          0.0          0.0          0.0          0.0          0
  0.0         30.00000      0.0          0.0          0.0          0.0          0.0          0.0          0.0          0
 0   0   0   0
  0.0          0.0          0.0
  0.0          0.0          0.0          0.0          0.0          0.0          0.0
  1  21   1   3   2   0  -0   0   0   1   0   0   0  50   1   7   8   0
 10.00000     2.00000
 90.00000     9.00000      -0.0          0.0          0.0          0.0          0.0          0.0
  0.20000     3.14000     -0.01570      1.57300      3.14000      0.15700      4.71000      0.00100
-1   1   1

 INT.CODE          E X T E R N A L    C O D E
                    1   -1   1   1

 10.00000    17.99751      0.0          12.50252     0.0          3.143221     71.999       0.22555E-0
 20.00000    20.00000      0.0          11.16277     0.0          3.140174     69.992       0.22505E-0
 22.00000    21.99996      0.0          11.15624     0.0          3.156246     68.013       0.22388E-0
 24.00000    23.99265      0.0          11.14999     0.0          3.141599     66.021       0.22446E-0
 26.00000    25.99144      0.0          11.14420     0.0          3.171219     64.024       0.22541E-0
 28.00000    27.99142      0.0          11.13886     0.0          3.179000     62.041       0.22625E-0
 30.00000    29.99262      0.0          11.13395     0.0          3.187355     60.054       0.22714E-0
 32.00000    31.99510      0.0          11.12950     0.0          3.195721     58.077       0.22814E-0
 34.00000    33.99917      0.0           7.78116     0.0          3.204521     56.110       0.22915E-0
 36.00000    35.99836      0.0           7.44104     0.0          3.213771     54.143       0.23037E-0
 38.00000    37.99156      0.0           7.10274     0.0          3.223406     52.171       0.23157E-0
 40.00000    39.99861      0.0           7.76519     0.0          3.233586     50.211       0.23290E-0
 42.00000    41.99600      0.0           7.42577     0.0          3.244197     48.259       0.23443E-0
 44.00000    44.00053      0.0           7.08727     0.0          3.255579     46.297       0.23597E-0
 46.00000    46.00255      0.0           7.74955     0.0          3.267552     44.347       0.23772E-0
 48.00000    48.00134      0.0           7.41238     0.0          3.280502     42.402       0.23965E-0
 50.00000    50.00000      0.0           7.07590     0.0          3.293998     40.459       0.24184E-0
 1   2   1   1

 INT.CODE          E X T E R N A L    C O D E
                    2   1   2   1   1

 10.00000     9.99762      0.0          13.86391     0.0          3.049549     139.458      0.11644E-0
 12.00000    11.99997      0.0          13.53044     0.0          3.047222     139.077      0.11624E-0
 14.00000    13.99955      0.0          13.19644     0.0          3.044860     138.614      0.11600E-0
 16.00000    15.99857      0.0          12.85407     0.0          3.041654     137.904      0.11567E-0
 18.00000    17.99754      0.0          12.51107     0.0          3.033374     136.721      0.11500E-0
 20.00000    19.99654      0.0          12.17705     0.0          3.023432     135.229      0.11420E-0
 22.00000    21.99551      0.0          11.84303     0.0          3.030557     133.744      0.11494E-0
 24.00000    23.99450      0.0          11.50903     0.0          3.025987     132.758      0.11447E-0
 26.00000    25.99357      0.0          11.17552     0.0          3.021096     131.708      0.11397E-0
 28.00000    27.99271      0.0          10.84271     0.0          3.015600     130.520      0.11341E-0
 30.00000    29.99264      0.0          10.51071     0.0          3.009675     129.245      0.11280E-0
 32.00000    31.99279      0.0          10.17960     0.0          3.003241     127.860      0.11214E-0
 34.00000    33.99418      0.0           9.84951     0.0          2.996191     126.347      0.11142E-0
 36.00000    35.99947      0.0           9.52055     0.0          2.988360     124.658      0.11062E-0
 38.00000    37.99920      0.0           9.19285     0.0          2.979697     122.793      0.10973E-0
 40.00000    39.99933      0.0           8.86655     0.0          2.970256     120.761      0.10876E-0
 42.00000    41.99929      0.0           8.54174     0.0          2.960163     118.586      0.10772E-0
 44.00000    44.00000      0.0           8.21874     0.0          2.950091     116.414      0.10668E-0
 46.00000    46.00047      0.0           7.90740     0.0          2.939429     114.120      0.10558E-0

 48.00000    48.00024      0.0           7.47145     0.0          2.926940     111.434      0.10430E-0
 50.00000    50.00000      0.0           7.13493     0.0          2.913325     108.513      0.10293E-0
 1   4   1   2   2   1

 INT.CODE          E X T E R N A L    C O D E
                    3   1   4   1   2   2   1

            65.30180     10.00000      4.19882      3.0592260361   9   2 50      CRITICAL RAY
 44.00000   43.99864      0.0           2.14576     0.0          2.938653     94.240       0.26042E-0
 42.00000   42.00391      0.0           2.47103     0.0          2.928516     97.546       0.25491E-0
 40.00000   40.00014      0.0           2.80018     0.0          2.945617     100.150      0.24911E-0
 38.00000   37.99171      0.0           3.12443     0.0          2.773004     99.631       0.25031E-0
 36.00000   35.99962      0.0           3.43549     0.0          2.726393     96.333       0.24921E-0
 34.00000   33.99854      0.0           3.74429     0.0          2.683514     91.716       0.24271E-0
 32.00000   32.00005      0.0           4.04772     0.0          2.655741     86.537       0.23731E-0
 30.00000   30.00124      0.0           4.34891     0.0          2.636058     81.999       0.23221E-0
 28.00000   28.00244      0.0           4.64915     0.0          2.623227     77.507       0.22721E-0
 26.00000   26.00328      0.0           4.94922     0.0          2.615750     73.006       0.22176E-0
 24.00000   24.00344      0.0           5.24978     0.0          2.612484     68.584       0.21629E-0
 22.00000   22.00249      0.0           5.55144     0.0          2.612744     64.301       0.21099E-0
 20.00000   19.99913      0.0           5.85506     0.0          2.616506     60.195       0.20595E-0
 18.00000   17.99401      0.0           6.16151     0.0          2.624251     56.295       0.20126E-0
 16.00000   15.98771      0.0           6.47161     0.0          2.636021     52.622       0.19697E-0
 14.00000   13.98102      0.0           6.78618     0.0          2.651761     49.191       0.19312E-0
 12.00000   11.97477      0.0           7.10606     0.0          2.671838     46.014       0.18975E-0
 10.00000    9.97000      0.0           7.43213     0.0          2.696553     43.104       0.18688E-0
  8.00000    7.96800      0.0           7.76535     0.0          2.727393     40.475       0.18455E-0
  6.00000    5.97000      0.0           8.10677     0.0          2.765914     38.142       0.18278E-0
  4.00000    3.97600      0.0           8.45752     0.0          2.814000     36.123       0.18161E-0
  2.00000    1.98400      0.0           8.81882     0.0          2.874000     34.438       0.18107E-0
  0.00000    0.00000      0.0           9.19200     0.0          2.950000     33.111       0.18120E-0
 0   0
```

Table 5.2 A portion of the print output from the program SEIS 83 applied to the model of fig. 5.16.

the other branch ABC and corresponds to rays that have been reflected from the 20 km interface. This reflected phase is, however, unlikely to come in with appreciable amplitude because of the small velocity contrast across the 20 km interface. The branch ABC covering a distance range of 46-72 km corresponds to diving waves that have sampled the material between 10 and 20 km depths without hitting the 20 km interface.

Plotted points on the segment DE appear to be approximately colinear and the straight line of best least squares fit through the 12 points has a slope, m, of 0.0371 s/km. If the epicentral distance and the corresponding travel time are Δ and t respectively, then it follows from fig. 5.16f that

$$m = (t - \frac{\Delta}{6})/(90-\Delta).$$

Hence the apparent velocity, $\frac{d\Delta}{dt}$, can be obtained as

$$\frac{d\Delta}{dt} = \frac{1}{(\frac{1}{6} - m)}$$

On substituting the value 0.0371 s/km for m, the average apparent velocity for this phase was obtained as 7.72 km/s. Similar treatment to the outputs from the model for focal depths of 0 and 5 km result in computed average apparent velocities of about 7.58 km/s and 7.69 km/s respectively for comparative range of distance.

Segment ABC can be divided into two parts, AB and BC. The part BC with six points appears approximately parallel to the distance axis thus suggesting an average apparent velocity close to 6.0 km/s in the indicated distance range (46 to 54 km). A straight line of best least squares fit to these 6 data points gives an average apparent velocity of 6.24 km/s. The rays

corresponding to these points have sampled only the top parts of the second layer. The part AB (with nine points) which covers the range of 60 to 72 km is clearly inclined at an appreciable angle to the distance axis. The straight line of best least squares fit to the 9 points of AB has a slope of 0.14s/km implying an average apparent velocity of 7.14 km/s for this phase. Similar output from the same model but with the source at a depth of 5 km shows that this phase (the diving waves) has a mean apparent velocity of about 7.07 km/s in the distance range 65-75 km. These values compare very well with the mean first arrival apparent velocity of 7.2 $\pm$ 0.2 km/s observed at Kaptagat for about the same range of distance.

To show how apparent velocity of the diving waves in the proposed model varies with distance, use was made of the source-detector distance, Δ, and the corresponding computed travel times, t in table 5.3. This table, extracted from table 5.2, shows Δ, and the corresponding t, at distance intervals of about 2 km for the diving waves. The apparent velocity, V, midway between two adjacent receiver positions was obtained by dividing the difference in distances (about 2 km) by the difference in travel times. The apparent velocity so obtained was plotted against distance (fig. 5.17). The line of best least squares fit to the plotted points was found to be of the form

$$V = (0.055 \pm 0.003)\Delta + 3.508.$$

This relationship implies that apparent velocity would increase from about 6.8 to 7.5 km/s as distance increased from 60 km to 72 km. In the present data, epicentral distances to Kaptagat are mainly within this range of distance. Furthermore,

Table 5.3: Values of apparent velocity V estimated for the diving waves from the model of fig. 5.16 for various distances, Δ, and times, t.

Distance (km)	Travel time (s)	Apparent velocity (km/s)
50	8.80016	
		6.168
52	9.12443	
		6.430
54	9.43548	
		6.466
56	9.74479	
		6.600
58	10.04779	
		6.710
60	10.34582	
		6.818
62	10.63915	
		6.923
64	10.92802	
		7.034
66	11.21234	
		7.026
68	11.49701	
		7.264
70	11.77235	
		7.364
72	12.04392	

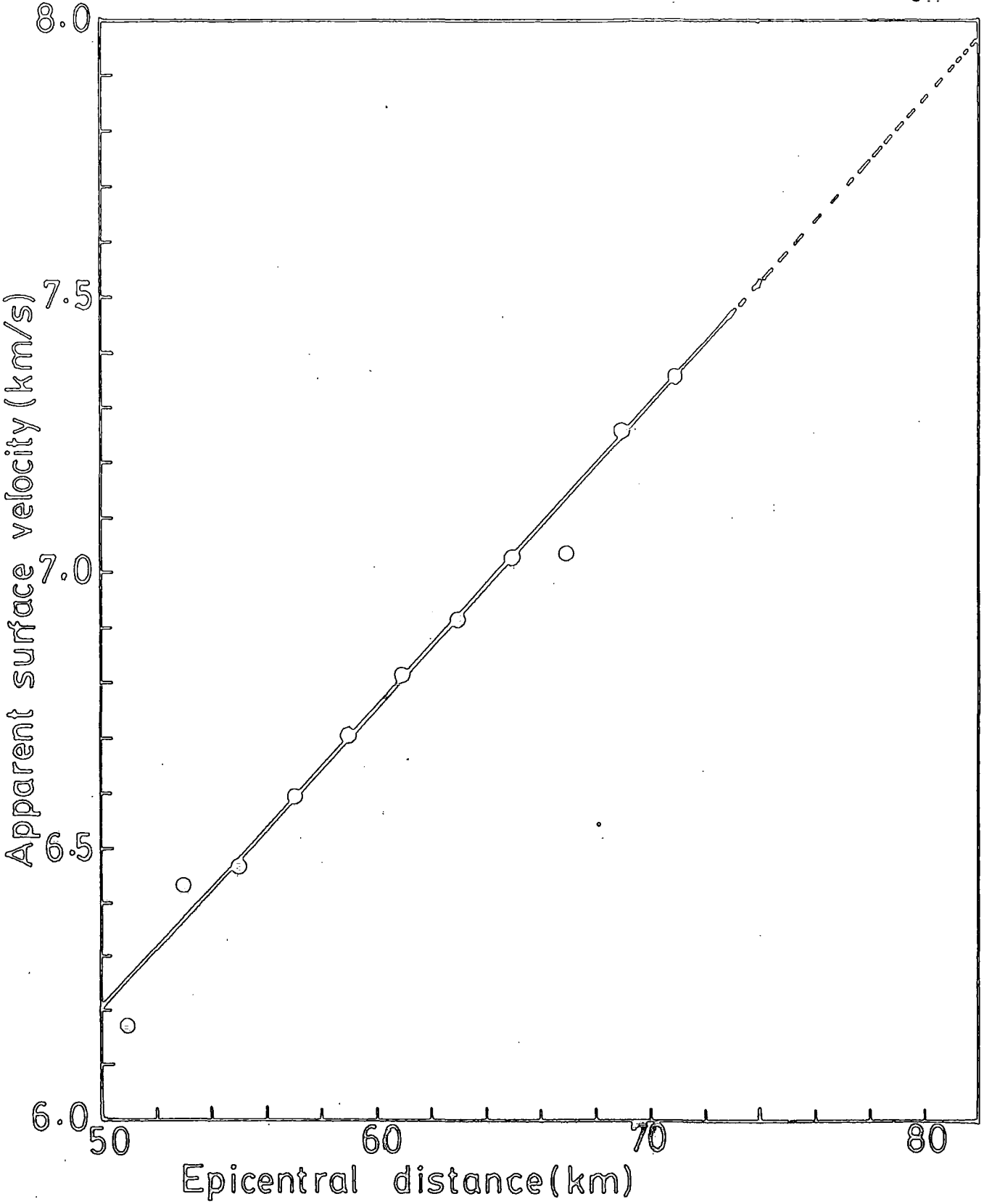

Fig 5.17: Apparent surface velocities derived from the travel times calculated for the model of fig 5.16 are plotted against epicentral distances assuming an average focal depth of 9km.

the first arrival apparent velocities (6.9-7.5 km/s) observed at Kaptagat station are also in excellent agreement with the range of values computed above from the model. The first arrival data is, thus, adequately explained by the proposed model which is, therefore, a possible model.

This simple model is summarised in fig. 5.16e. We may assume an average distance of epicentres in the east-west direction to be about 60 km. Then from fig. 5.16e, it is easily seen that the intermediate layer of uniform increase in velocity with depth is not further than about 13 to 14 km to the east from Kaptagat. This implies that that layer extends west to about the western bounding fault of the Gregory rift.

This model explains the data satisfactorily and suggests that higher velocities appear higher in the crust than would be expected for a normal shield crust. Increase in velocity up to 7.5 kms^{-1} at 20 km depth probably indicates crustal intrusion of multiple dykes. Velocity increase with depth at crustal levels has also been reported by Khan et al.(1987) for the axial part of southern portion of the Gregory rift. These observations suggest multiple dyke injection as a possible driving mechanism for the rifting process.

5.7.4 Summary.

Ray tracing through the crustal model of Savage and Long (1985) shows that rays from shallow rift events associated with the present data would be deviated downwards and would not come up to the surface at the distance of Kaptagat. It is argued that for the rays to emerge at the surface at Kaptagat, a structure including a horizontal/gently dipping interface or a structure in which velocity increases with depth is

required.

The two layer model with horizontal interface derived in sections 5.4.2 suggest the presence of a top layer of P-wave velosity 5.8 km/s. This is underlain at a depth of not more than about 16 km by a material of velocity 7.2 km/s assuming an average focal depth of 10 km for the region. An increase/decrease of 5 km in this estimate of mean focal depth increases/decreases the maximum refractor depth estimate by about 3 km. Hence, for mean focal depths of 5, 10 and 15 km, the corresponding estimated maximum depths to the 5.8/7.2 km/s refracting interface would be 13, 16 and 19 km respectively. In this region, focal depths are not known accurately but are most probablyiin the range 5-15 km.

In fig. 5.18 the positions (A, B and C) of the refracting interface for mean focal depths of 5, 10 and 15 km respectively are superposed on the structural model of Savage and Long (1985). The corresponding refraction ray paths from foci to Kaptagat are shown for a typical epicentral distance of 60 km. It is desirable to obtain an estimate of the minimum lateral extent of the top surface of the refractor consistent with the present data. This estimate depends on knowledge of focal depth and epicentral distance.

Typical distance in this study is about 60 km in the east-west direction with an uncertainty of about $\pm$10 km. At this typical distance, rays can be traced back from Kaptagat to the appropriate focus for each of the refracting interfaces at depths of 13, 16 and 19 km (fig. 5.18). The portion of each of the refracting interfaces at levels A, B and C contained between the slant ray paths estimate the corresponding horizontal lateral

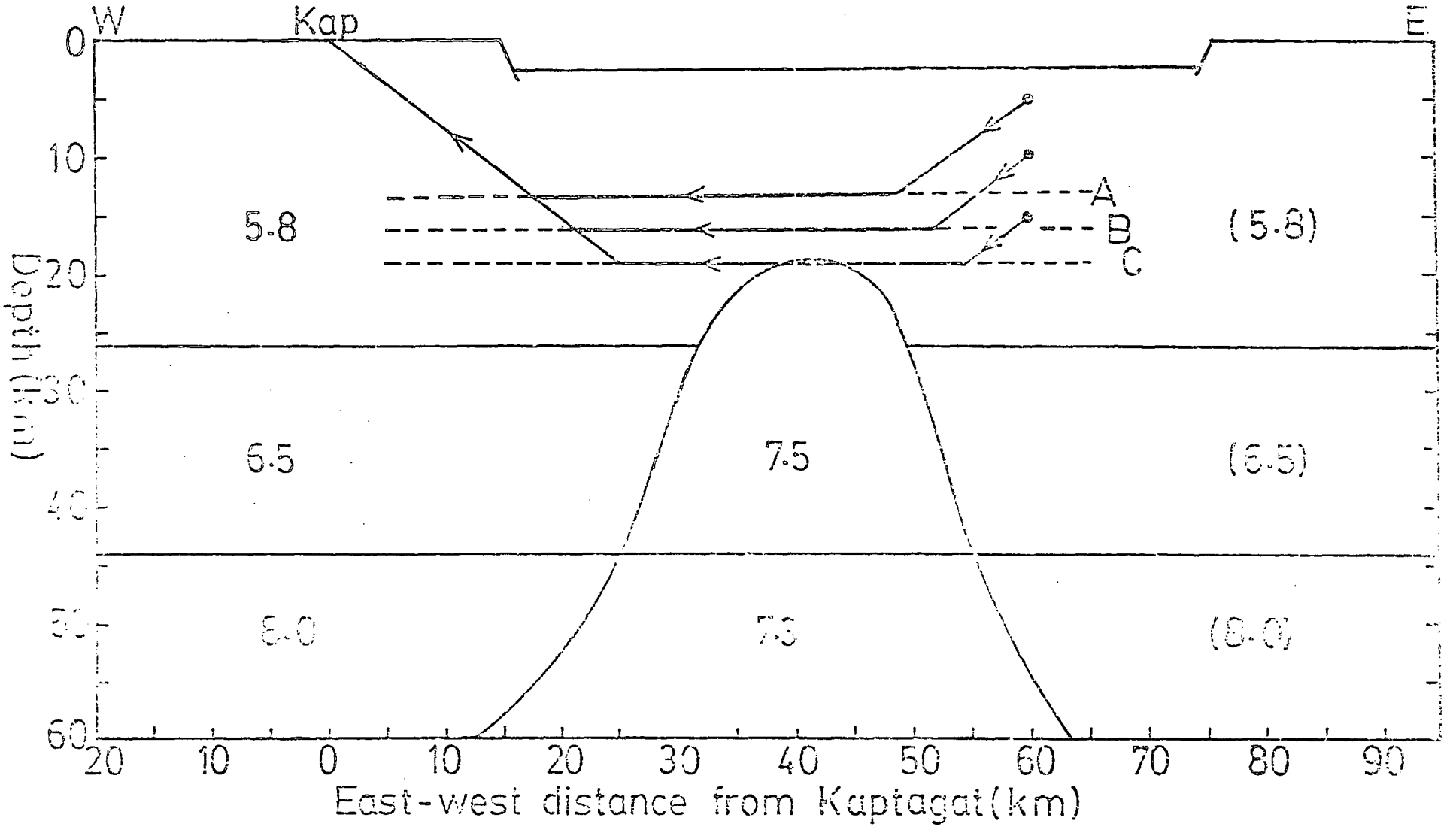

Fig 5-18: The positions A, B and C of the 5-8/7-2 refracting interface (assuming mean focal depths of 5, 10 and 15 km respectively) are superposed on the structural model from Savage and Long (1985). Ray paths are indicated by arrows and numbers are P-wave velocities in km/s.

extent of the refractor at the appropriate level. From this, the minimum horizontal lateral extent of the top surface of the refractor is estimated as about 31, 30 and 30 km respectively for focal depths of 5, 10 and 15 km. The mean estimate of the minimum lateral extent of the top of the refractor is thus about 30 km. An increase/decrease of 10 km in distance estimate about the distance of 60 km increases/decreases the estimate of minimum lateral extent by about 10 km.

The east-west component of distance of epicentres from Kaptagat covers the range about 60-74 km. If we adopt a mean focal depth of 10 km for the region of study, the maximum depth to the 7.2 km/s refractor would thus be about 16 km with a minimum lateral extent of about 30 km. It was suggested in section 4.6 that the estimates of distances may have exaggerated the true distances. If estimated distances are greater than true distances by about 10 km, the minimum lateral extent estimated for the top surface of the refractor would be about 20 km.

In section 5.4.3, the data was explained in terms of a two layer model with a plane gently dipping interface. A maximum dip of 6^{o} (corresponding to refractor velocity of 7.8 km/s) from Kaptagat up towards the rift axis is allowed by the data. At this value of dip, the minimum westward horizontal extent of the refractor for given focal depths is given by the intersection of the inferred plane refracting interface with the western limiting ray path, A (fig. 5.12a). It is observed from this figure that for a typical epicentral distance of about 60 km and for focal depths of 0,5,10,15 and 20 km, the maximum vertical depths from the epicentre to the interface are estimated as 9,12,15,18 and 22 km respectively. Consequently, the infer-

red western ends of the refractor would then be at maximum vertical depths of 13,16,18,21 and 25 km respectively (fig. 5.12a). The horizontal offsets of these points from Kaptagat have about the same magnitudes as the corresponding offsets in the case of horizontal interface. The maximum vertical depth estimates obtained in the case of gentle dip (6^{o} up from Kaptagat towards the rift axis) are therefore, about 2 km higher than the corresponding estimates for zero dip.

For interface dipping up from Kaptagat towards the rift axis, refractor velocities beneath the study area are unlikely to be as high as 7.8 km/s. Dips as high as 6^{o} in this direction are, therefore, unlikely. Differences in depth estimates, for horizontal and this gently dipping interface could, consequently, be within the error limits in estimate of depths. This suggests that there may, therefore, be no significant difference in depth estimates from this model and the model assuming horizontal interface. However, the two layer model with horizontal interface is better constrained by the data than the two layer model with a dipping interface.

In section 5.7.3, the model shown in fig. 5.16e was also found consistent with the data. In this model, a 10 km thick top horizontal layer with average velocity of 5.8 km/s overlies an intermediate layer about 10 km thick. In the intermediate layer velocity increases uniformly from 6.0 km/s at 10 km depth to 7.5 km/s at a depth of 20 km. The intermediate layer, in turn, overlies a constant velocity refractor (velocity about 7.6 km/s). Assuming a typical epicentral distance of 60 km and a mean focal depth of 9 km, the intermediate layer is found to extend west to as far as the Elgeyo fault, the western boundary

fault of the rift. This model suggests, like the two layer model with horizontal interface, that higher velocities appear higher in the crust than would be expected for a nomal shield crust. Increase in velocity with depth within the crustal zone of the axial part of the southern portion of the Gregory rift has also been reported by Khan et al.(1987). Increase in velocity up to 7.5 km/s at 20 km depth probably indicates crustal intrusion of multiple dykes.

CHAPTER 6

INTERPRETATION OF SECOND ARRIVAL DATA

.1 Introduction.

In section 5.4, data from first arrivals were interpreted in terms of a model consisting of two uniform plane layers seperated by a plane horizontal/dipping interface. In section 5.7, these same data were interpreted in terms of a model consisting of a top horizontal uniform velocity layer overlying an intermediate layer in which velocity increases with depth which is, in turn, underlain by a uniform velocity refractor. In the present chapter, attempts will be made to show how consistent the second arrival data are with these models.

The apparent velocities, azimuths and onset times of later arrivals were determined with lower precision than those of the first arrivals. One of the main reasons for this lower precision is signal interference. Several phases may arrive at the same station at about the same time. These arrivals could superpose in such a way that the velocity filtering technique may not be able to seperate them adequately in terms of apparent velocity, azimuth and time. The resulting composite signal may, therefore, have measured apparent velocity/azimuth different from the true event apparent velocity/azimuth of any of the single phases.

As suggested by the response contour given in fig. 3.3, the process of velocity filtering could also, under certain conditions, generate non existent arrivals. In selecting second arrivals for interpretation, it is, therefore, important

to proceed with caution. In this study, attempt was made to relate the arrivals spotted by velocity filtering with the arrivals seen on single seismograms. It will be noted, however, that at the short distances involved in this study, what looks like a single arrival on a seismogram may, in fact, be two or more arrivals. With practice, however, it is possible, on a single seismogram, to identify the onsets of such arrivals by the changes in curvature, frequency and amplitude of the waveform.

For interpretation, use was made of later arrivals which have about the same azimuth as the corresponding first arrivals. Later arrivals whose azimuths are significantly different from those of the first arrivals may have resulted from different sources and/or from lateral variations in velocity. Adequate handing of such arrivals, would, of necessity, require three dimensional interpretation which can not be supported by the present data. The data for the later as well as for the first arrivals are shown in fig. 3.31. Only a few of the later arrivals indicated in fig. 3.31 could be identified and used in this study. The problems created by signal interference would be expected to increase with time into the record. Later arrivals close, in time, to the first arrivals were, therefore, used in the interpretation because such arrivals were expected to give more reliable results.

.2 Guides to the identification of some later arrival phases.

.1 Introduction.

To be able to use a particular phase for interpretation, that phase must first be identified. The discussions given

below are designed to provide some useful guide in the identification of prominent phases by their measured apparent velocities, azimuths and relative onset times assuming a plausible model.

6.2.2 Direct waves.

Following the discussions in section 5.4, consider a two layer structure with a horizontal interface at a depth H of 20 km. Let the top and lower layers have uniform velocities V_1 and V_2 whose values will, from earlier discussions, be taken as 5.8 km/s and 7.2 km/s respectively. Then the expression for apparent velocity V_a, of direct waves from a source at a distance Δ and depth h is given by

$$V_a = \frac{V_1}{\Delta}\sqrt{(\Delta^2 + h^2)}$$

From this expression, apparent velocity for direct waves was calculated and plotted as a function of focal depth at distances of 40, 50, 60, 70 and 80 km respectively (fig.6.1a). From this plot it is found that apparent velocities for direct waves for the observed distances between 50 and 80 km are all within the range 5.80 to 6.25 km/s if only focal depths in the range 0 to 20 km are considered. It is also found that for a given focal depth, the apparent velocity increases with a decrease in distance.

It is also useful to calculate the expected travel times of direct waves in relation to the first arrivals assumed to be headwaves. Travel times of direct waves as function of focal depth, h, are plotted as curve A in fig. 6.1b for a distance of 60 km. Also plotted (for the

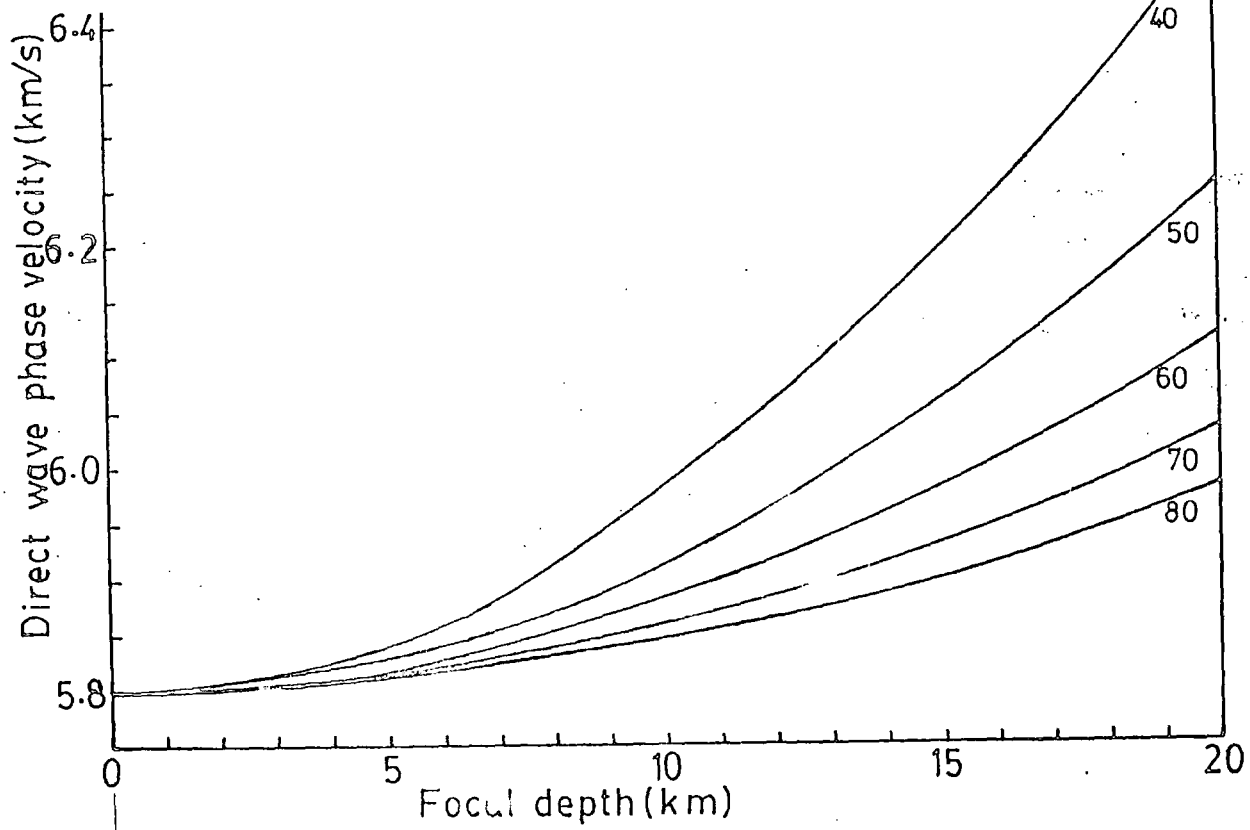

Fig 6·1a: Theoretical apparent velocity for direct waves in a material of velocity 5·8 km/s plotted against focal depth for epicentral distances of 40, 50, 60, 70 and 80 km respectively.

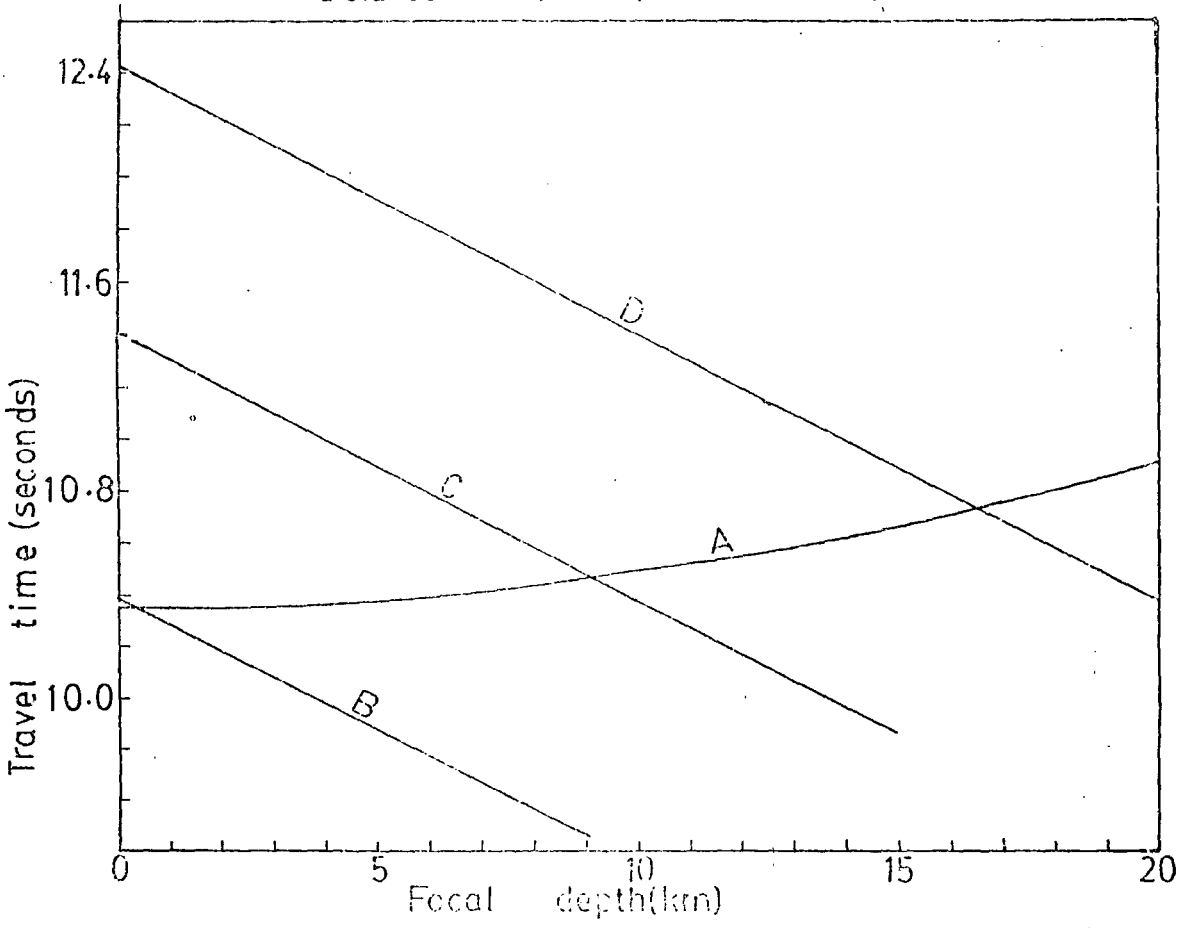

Fig 6·1b: Plot of travel time against focal depth for direct waves(A) and for head waves from horizontal interfaces at depths of 10, 15 and 20 km (B, C and D) respectively assuming epicentral distance of 60 km.

same distance in this figure are travel times of headwaves from a refractor at depths H of 10, 15 and 20 km which are shown as curves B, C and D respectively.

From fig. 6.1b, it is evident that at a distance of 60 km and for refractor depth of 20 km, headwaves precede direct waves and could be first arrivals only for all focal depths greater than about 17 km. At this value of refractor depth, the difference, t, between the onset times of headwaves and direct waves increases from 0 to about 0.50 s as h increases from 17 to 20 km. Such large focal depths are, however, unlikely in the region of present study. If the refractor depth is 15 km, the head waves could be first arrivals only for focal depths greater than about 9 km; in this case the difference, t, in onset times of the two arrivals would increase from 0 to about 0.80s as focal depth increased from 9 to about 15 km.

For refractor depth of 10 km, headwaves could be first arrivals for all focal depths up to about 10 km. Difference in onset times would in this case be expected to increase from 0 to about 1.00s as h increased from 0 to about 10 km. To summarize, the direct waves would be expected to come in with apparent veolcities in the range 5.80 to 6.11 km/s and with a time delay of up to about +1.00s with respect to the first arrival headwaves if a typical distance of 60 km is considered. This is summarized in the table given below.

Interface depth H(km)	Range of focal depth, h (km)	Range of step out time, t (seconds)	Range of apparent velocity V_a (km/s)
10	0-10	0.00-1.00	5.80-5.88
15	9-15	0.00-0.80	5.86-5.98
20	17-20	0.00-0.50	6.00-6.11

If the top layer velocity was actually lower/higher than the 5.8 km/s assumed above, the computed values of V_a would be correspondingly lower/higher than the values stated above.

6.2.3 Wide angle reflections.

The expression for the apparent velocity of wide angle reflections from the horizontal interface at depth of H is given by

$$V_a = \frac{V_1}{\Delta}\sqrt{\Delta^2 + (2H-h)^2}.$$

For Δ in the range 50 to 80 km, this expression shows that the apparent velocity for reflections from an interface at 20 km depth would be in the range 7.43 to 6.00 km/s for focal depths between 0 and 19 km. For a fixed value of refractor depth, H, apparent velocity for these reflections increases with decreasing distance, Δ; and for a fixed value of Δ, apparent velocity increases with increase in H.

If the 20 km thick top uniform horizontal layer of velocity 5.8 km/s overlies a 7.2 km/s layer, the critical distance for headwaves from the interface would decrease from about 54 km to about 29 km if focal depth were increased from 0 to 19 km. The distances of about 50-80 km observed in this study thus fall beyond the critical distance for such headwaves within the stated range of h. The difference, t, between the onset times of the wide angle reflections and the headwaves from the same interface at depth H is given by

$$t = \frac{\sqrt{\Delta^2 + (2H-h)^2}}{V_1} - \frac{\Delta}{V_2} - \frac{(2H-h)\sqrt{V_2^2 - V_1^2}}{V_1 V_2} \quad \ldots (6.1)$$

To illustrate, apparent velocity, V_a of the wide angle reflections is plotted against focal depth, h for interface depths of 10, 15 and 20 km respectively at an epicentral distance Δ of 60 km (fig. 6.2a). As before, top and lower layer velocities were adopted as 5.8 km/s and 7.2 km/s respectively. Differences in onset times, t, between the wide angle reflections and the headwaves from the interface is plotted against focal depth for interface depths of 10, 15 and 20 km respectively at epicentral distance of 60 km (fig. 6.2b). The head wave onset precede the wide angle reflections in time in the models illustrated in fig. 6.2. Relevant guiding information from fig. 6.2a and b are summarized below in tabular form for a distance of 60 km.

Interface depth H(km)	Range of focal depth(km)	Range of step out time, t(s)	Range of apparent velocity (km/s)
5	0-5	1.13-1.54	5.82-5.88
10	0-10	0.53-1.06	5.88-6.11
15	0-15	0.17-0.80	5.98-6.48
20	0-20	0.01-0.53	6.21-6.97

Comparing direct waves and wide angle reflections, it is to be noted that there may be appreciable overlap in their onset times. The wide angle reflections are expected to come in with slightly higher apparent velocities but the magnitude of the error involved in measuring second arrival apparent velocities may be as large or even larger than the expected difference in the measured apparent velocities of these two phases. It is, therefore, possible to misidentify a wide

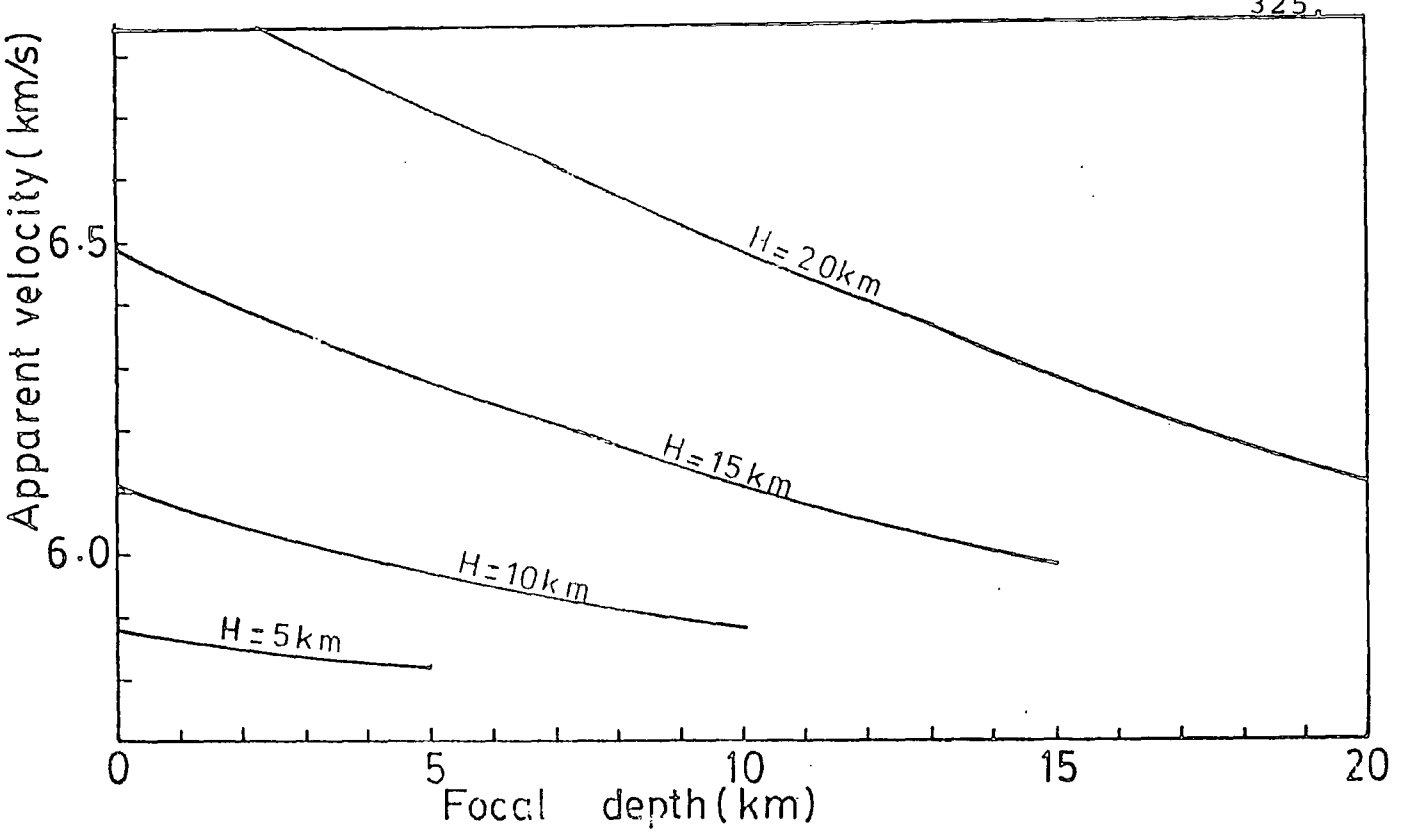

Fig 6·2a : Plot of apparent velocity of wide angle reflections against focal depth for reflector depths, H, of 10, 15 and 20 km respectively at an epicentral distance of 60 km.

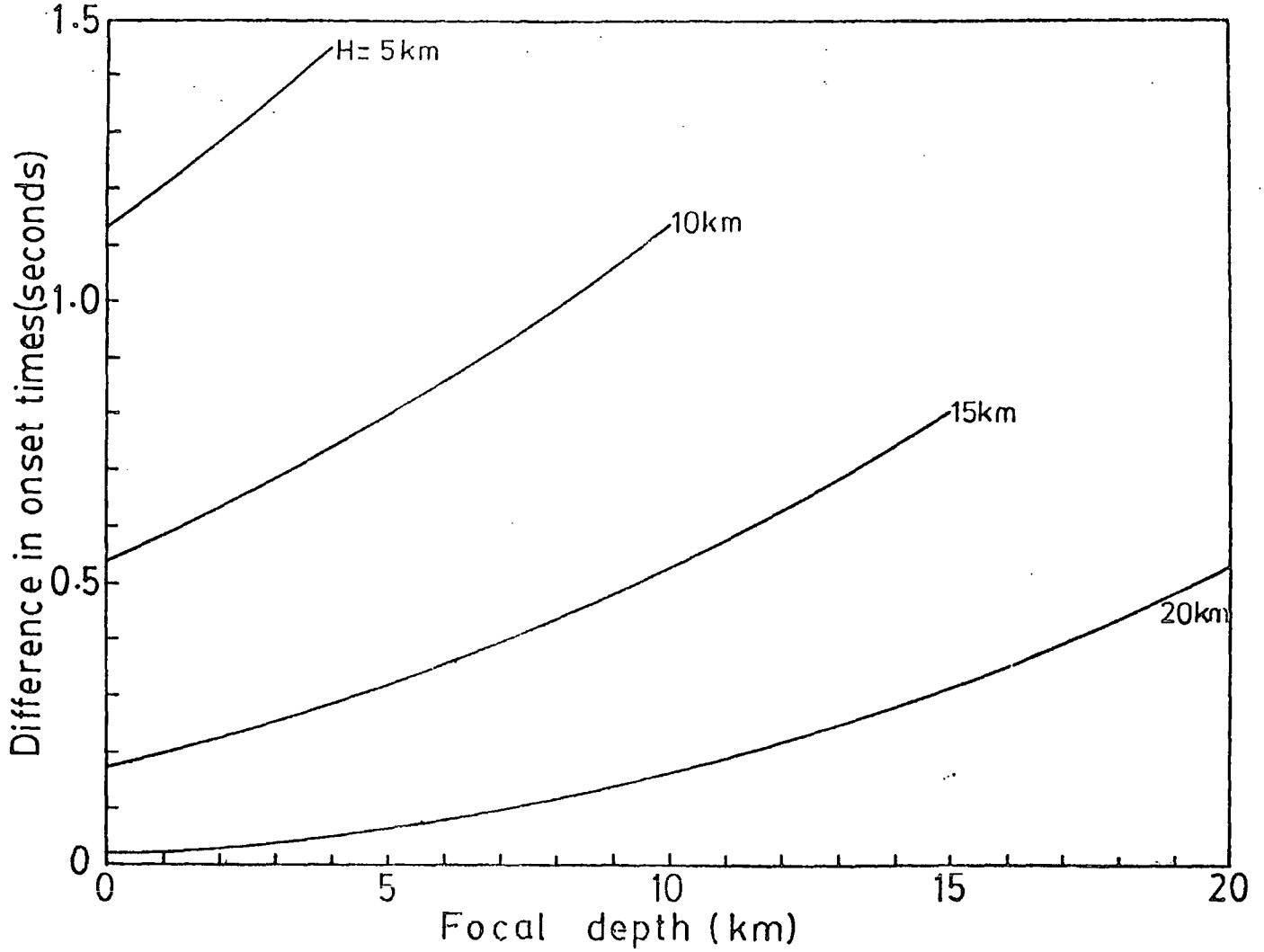

Fig 6·2b: Plot of the difference, t, between the onset times of head waves and wide angle reflections from the same interface at depths, H, of 10, 15 and 20 km respectively assuming epicentral distance of 60 km.

angle reflection as a direct wave and vice virsa.

6.2.4 A multiple reflection phase.

Apart from direct waves, head waves and wide angle reflections discussed above, some multiple reflections could have enough energy to be well recorded. To illustrate we may consider the two layer case with a horizontal interface at a depth H. If the depth of the source is h ($h < H$), epicentral distance Δ and upper layer velocity V_1, we may obtain expressions for apparent velocity, V_a, and time off-set, t, from first arrival onset, for a multiple reflection arrival involving two reflections at the interface and one reflection at the surface, the first reflection occuring at the interface. The expressions for t and V_a are

$$t = \frac{\sqrt{\Delta^2 + (4H-h)^2}}{V_1} - \frac{\Delta}{V_2} - (2H-h)\left(\frac{1}{V_1^2} - \frac{1}{V_2^2}\right)^{\frac{1}{2}} \qquad \ldots (6.2)$$

$$V_a = \frac{V_1}{\Delta}\sqrt{\Delta^2 + (4H-h)^2}$$

To be able to identify such multiple reflections (if they exist) on the data for second arrivals (fig. 3.31), it is necessary to estimate the possible ranges of values for their apparent velocities and travel times with respect to those of first arrivals assuming different depths, H, in the model. These estimates were obtained for an epicentral distance of 60 km which is typical in the present study. Average values of 5.8 km/s and 7.2 km/s were adopted for V_1 and V_2 respectively.

With the epicentral distance Δ fixed at 60 km, apparent velocity, V_a, of the specified multiple reflection was calculated and plotted against the depth, H, to the reflecting interface at each of the focal depths 5, 10, 15 and 20 km (fig. 6.3a). For the same fixed distance of 60 km, the step out time, t, between the onsets of the headwaves and the multiple reflection from the same interface at depth H was plotted against H for focal depths of 5, 10, 15 and 20 km (fig. 6.3b). In both plots it was assumed that the focus was above the reflecting/refracting interface.

From fig. 6.3a and b, it is found that for focal depths of 5 and 10 km and interface depth of 13km, the step out time, t, has an average value of about 2.70s while V_a covers the range 7.04 to 7.39 km/s. At a refractor depth of 16 km, the value of t is about 3.33s while V_a has values in the range 7.48 to 8.14 km/s for focal depths in the range 5-15 km. If the depth to the refractor is 20 km, then t covers the range 4.36-4.66s. while V_a covers the range 8.56-9.28 km/s assuming focal depths in the range 5-15 km. Apparent velocities in the range 5.80-6.10 km/s and step out time values of about 1.80s would be expected from a refractor at a depth of about 6 km for focal depths shallower than this depth. These computed values are summarized in the table below.

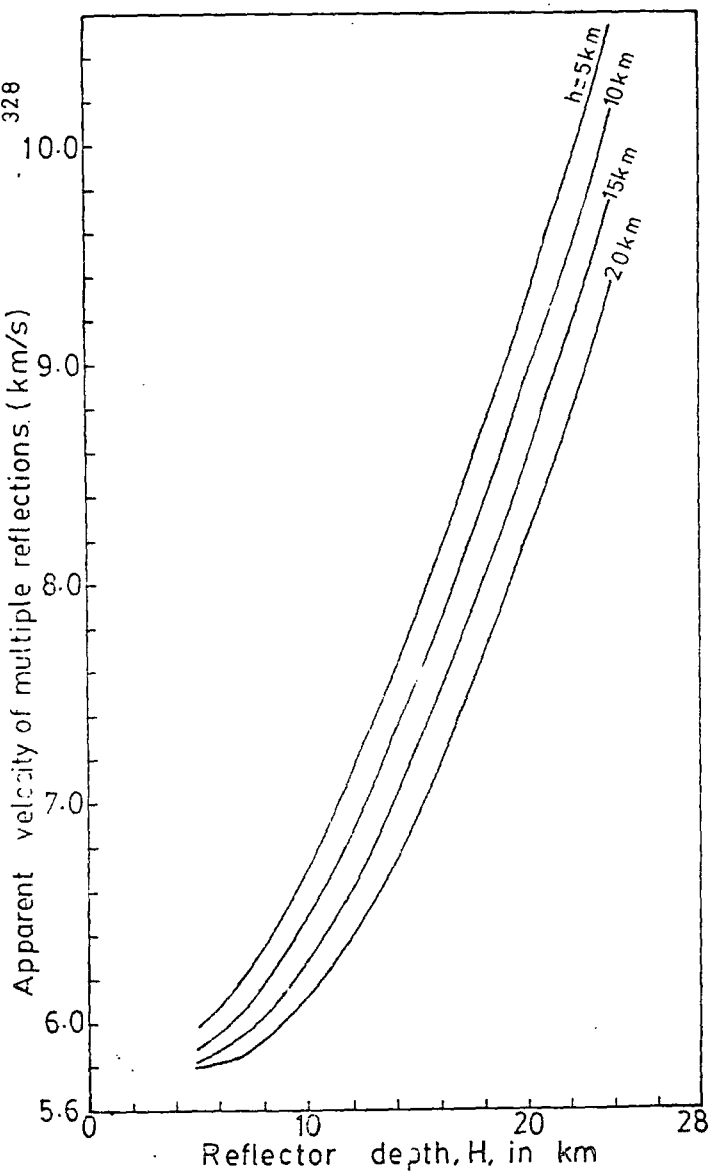

Fig 6·3a: Plot of apparent velocity of multiple reflections (of the type described in section 6·2·4) against reflector depth, H, for focal depths, h, of 5, 10, 15 and 20 km respectively.

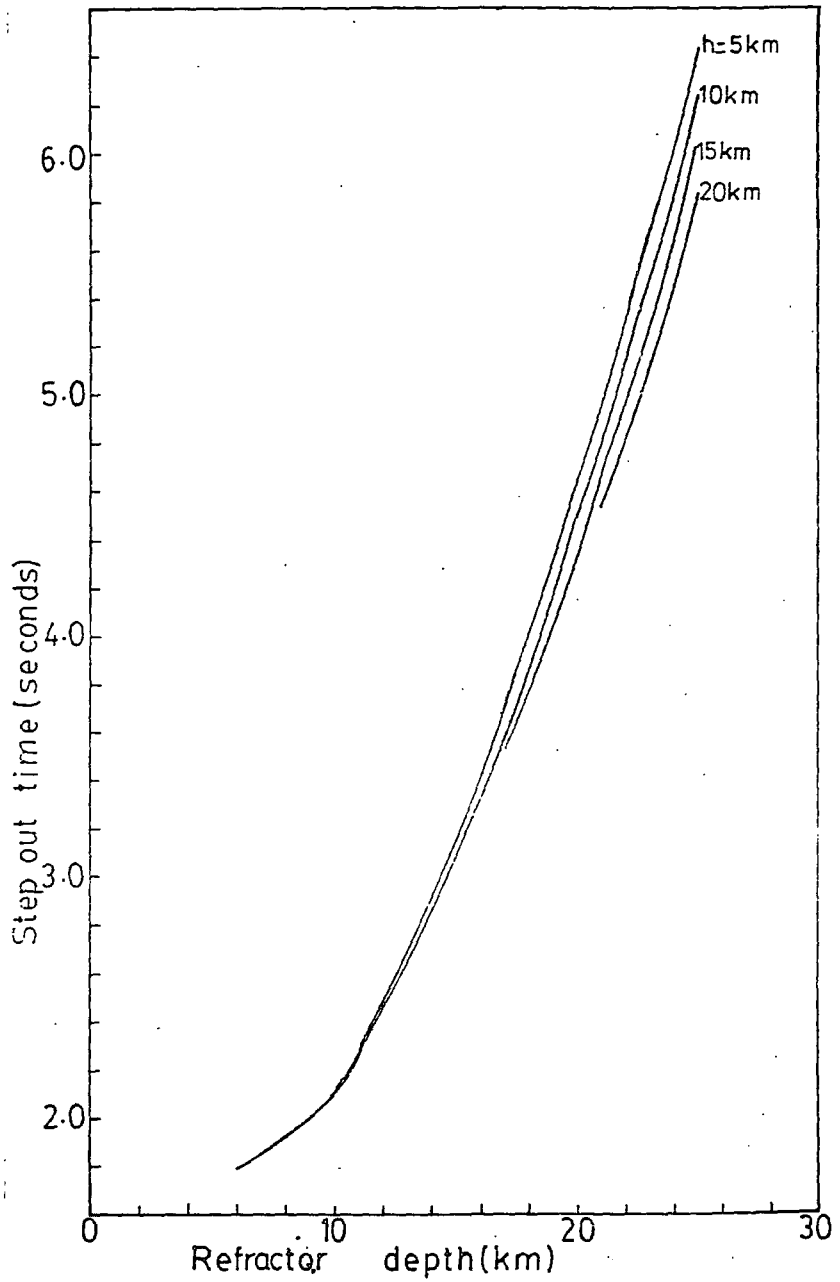

Fig 6·3b: Plot of the difference, t, between the onset times of head waves and multiple reflections (described in section 6·2·4) against interface depth, H, for focal depths of 5, 10, 15 and 20 km.

Interface depth H(km)	Estimated mean step out time (seconds)	Range of apparent velocity(km/s)
6	1.80	5.80-6.10
13	2.70	7.04-7.39
16	3.33	7.48-8.14
20	4.51	8.56-9.28

In general, for given values of H and h, V_a decreases with increase in Δ. And for given values of Δ and h, V_a increases with increase in H.

From the foregoing discussions, it is obvious that for a given model and a given distance, Δ, the apparent velocity and relative onset time of a given phase both depend on focal depth. This may explain why the phases shown in fig. 3.31 are not easily correlated from one event to the other across the record. It is also to be noted that expected phase velocities and travel times of different phases show some overlap mainly because of variations in focal depth. This would create some difficulty in unambiguously identifying arrivals by their measured apparent veolcities and relative onset times. However, relative amplitudes and consistency of data from all arrivals for one event could help resolve this problem. Estimates of the parameters of phases discussed in this section were used as a general guide in identifying some of the phases indicated in fig. 3.31 and subsequently used in the interpretation.

6.3 Refractor depth estimates from some identified phases.

In this section, with the discussions in section 6.2 as guide, some phases indicated in fig. 3.31 are identified and used to estimate depths to the reflector/refractor in a two layer model with horizontal interface. It is to be

noted, that because of interference problems, measured values of apparent velocity and azimuth may, under certain conditions, be anomalous. But observed relative onset times are probably more reliable and will be used in computations. We now discuss phases suspected to be direct waves, wide angle reflections, multiple reflections and refracted reflections.

6.3.1 The 5.8 km/s arrivals.

Velocity filtered records (fig. 3.31) for events 1,2, 3,5,6,7,8,9,10 and 11 show some phases marked 'C', having apparent velocities of about 5.8 km/s and coming in at about one second after the first arrivals. In this section, an investigation is carried out to see how well the data from these arrivals agree with the two layer horizontal model derived in section 5.4. The measured parameters of these 5.8 km/s arrivals are shown in table 6.1.

The amplitude of these arrivals relative to the corresponding first arrivals averages about 0.40. This, combined with their measured apparent velocities of about 5.8 km/s and the discussions in section 6.2.2 would suggest that these arrivals could be direct waves, P_g, from near surface foci. Assuming a two layer model with horizontal interface, these arrivals are here being interpreted as direct waves in an attempt to estimate the depth H to the refracting interface generating the first arrivals. The expression for the refractor depth is obtained from equation (6.1) as

$$H = \frac{h}{2} + \left\{ \frac{(\Delta^2 + h^2)^{\frac{1}{2}}}{V_1} - \frac{\Delta}{V_2} - t \right\} \frac{V_1 V_2}{2(V_2^2 - V_1^2)^{\frac{1}{2}}}$$

Event number	Distance Δ (km)	First arrival		5.8 km/s arrival		Difference in onset times (s)	Refractor depth H from direct wave interpretation (km)		
		Azimuth (degrees)	Apparent velocity (km/s)	Azimuth (degrees)	Apparent velocity (km/s)		For h = 5 km	For h = 10 km	For h = 15 km
2	60	94	7.2	100	5.8	1.20	6.6	9.7	13.0
3	60	95	7.3	104	5.8	1.20	7.1	10.1	13.4
5	67	87	7.3	88	5.8	1.50	6.8	9.8	13.0
6	67	94	7.5	78	5.6	1.38	9.5	12.4	15.6
7	72	105	7.5	101	5.8	0.00	15.5	18.4	21.6
8	73	88	7.0	84	5.8	0.90	9.2	12.1	15.4
10	82	106	7.0	110	5.8	0.80	11.0	13.9	17.1
11	88	114	6.9	114	6.0	0.50	13.1	16.0	19.2
1	59	102	7.1	86	5.6	0.80	7.5	10.5	13.7
9	77	107	6.9	114	5.8	0.64	10.5	13.5	16.6

Table 6.1. Estimates of refractor depth based on interpreting the 5.8 km/s arrivals as direct waves and at focal depths of 5, 10 and 15 km.

where t is the stepout time between the onsets of the first arrival assumed to be headwaves and the 5.8 km/s arrival. As before, V_1 and V_2 are top and lower layer velocities, h is the focal depth of source and Δ the epicentral distance measured for each event. Focal depth is unknown and is expected to vary from one event to another probably in the range about 0 to 15 km. It is, therefore, necessary to see how the choice of focal depth affects estimates of H.

For each of the events, one value of H was estimated for each of the focal depths of 5, 10 and 15 km. The actual observed apparent velocity for each 5.8 km/s arrival was taken as V_1 while the corresponding event first arrival apparent velocity was taken as V_2. These quantities were combined with the measured stepout times, t, to estimate the refractor depth H from the equation given above. Of particular interest is event number 7 for which the 7.5 km/s and 5.8 km/s phases arrive the station at about the same time as indicated in fig. 6.4. The results from all events are shown in table 6.1. It is found from the 10 events that the mean values of H for focal depths of 5, 10 and 15 km are 10 $\pm$ 3, 13 $\pm$ 3 and 16 $\pm$ 3 km respectively. Error estimates are standard deviations.

It is useful to consider the uncertainty in the estimate of refractor depth H due to an error in the measured distance Δ. To illustrate this we may use event number 3 for which the measured stepout time is 1.2s. For this event at an epicentral distance of 60 km, fig. 6.5 shows the calculated refractor depths assuming various distances in the range 30 to 100 km and a focal depth of 5.0 km. The diagram shows that at the distance of 60 km and for focal depth of 5 km, an error of $\pm$ 10 km in distance

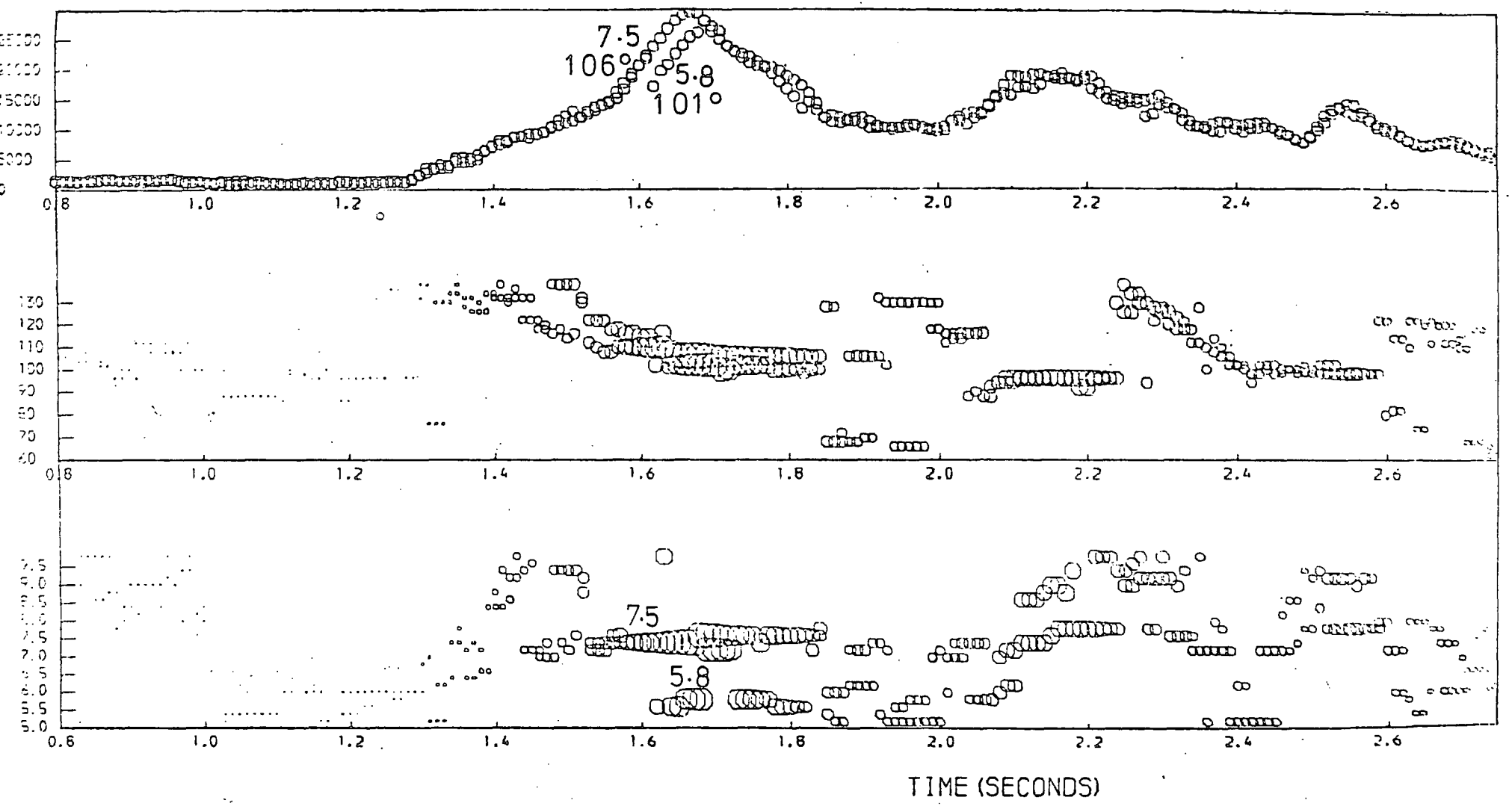

Fig·6·4: Plot output from program VFIL applied to event number 7· A phase with apparent velocity of about 5·8 km/s arrives the station at about the same time as the first arrival with velocity of 7·5 km/s·

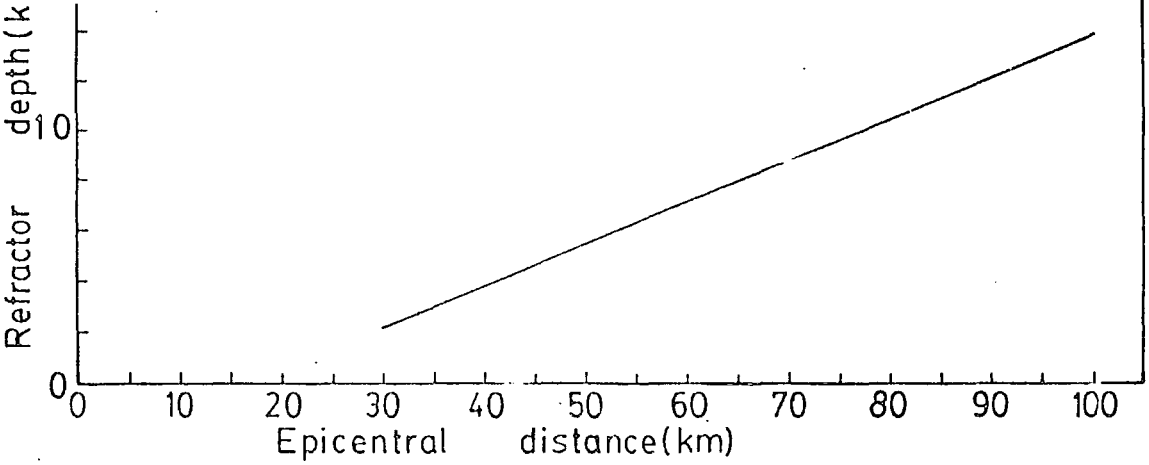

Fig 6·5 : Values of refractor depth, H, calculated from the difference of 1·20s [illegible] and head waves assuming a focal depth of 5km and [illegible] epicentral distance for distances in the range 30 to 100 km.

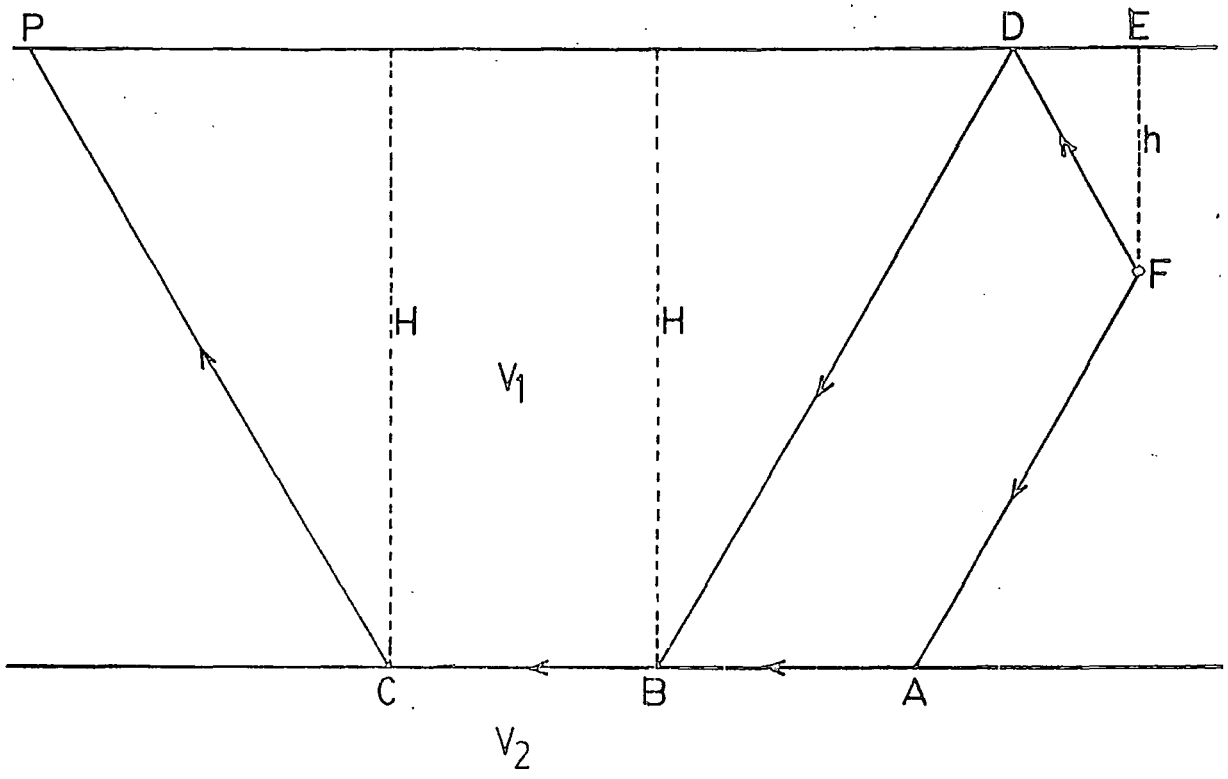

Fig 6·6: Ray paths (arrowed) illustrating refracted reflections in a simple two layer structure with plane interface.

introduces an error of about $\pm$ 2 km in H. From discussions in section 4.6, the error in distance at the distance of about 60 km is about $\pm$ 10 km.

In section 5.4.2, estimated maximum depths to the refracting interface in a two layer horizontal model were established as 13 km, 16 km and 19 km assuming focal depths of 5 km, 10 km and 15 km respectively. These values compare very well with the corresponding mean depth estimates of 10 km, 13 km and 16 km obtained in this section for the same refractor depth.

6.3.2 Refracted reflections?

Coming within less than about one second after the first arrivals are some phases (marked 'b' in fig. 3.31) whose measured apparent velocities are approximately equal to those of the corresponding first arrivals. Because these arrivals come very close to the first arrivals and because their phase velocities are approximately equal to those of the corresponding first arrivals, they may be considered as refracted reflections of the type represented by the path FDBCP in fig. 6.6. DF represents the surface. FABCP is the ray path for headwaves from the interface ABC.

The travel time for the headwave path FABCP is

$$t_1 = \frac{\Delta}{V_2} + (2H-h)\left(\frac{1}{V_1^2} - \frac{1}{V_2^2}\right)^{\frac{1}{2}}$$

For the path FDBCP, the travel time t_2 can be shown to be

$$t_2 = \frac{\Delta}{V_2} + (2H + h)\left(\frac{1}{V_1^2} - \frac{1}{V_2^2}\right)^{\frac{1}{2}}$$

The other symbols have meanings indicated in previous discussions.

The difference, t, in travel times between the first arrival and 'b' is thus given by

$$t = \frac{2h\sqrt{V_2^2 - V_1^2}}{V_1 V_2}$$

For a given model, this time difference, t, depends only on h and is independent of distance Δ. Measured values of t for events 1, 4, 5, 6, 7, 8, 9, 10 and 11 extracted from fig. 3.31 are shown in the fourth column of table 6.2 and were substituted in the equation above to estimate focal depths of these events. The mean value of t is 0.84 $\pm$ 0.29s (estimate is standard deviation).

To estimate the focal depth for a given event, the value 5.8 km/s was adopted for V_1 and the observed first arrival apparent velocity for that event was adopted as V_2. The focal depth, h, was calculated for each event from the corresponding values of t and V_2 shown in table 6.2; the results are shown in the fifth column of that table. The mean focal depth from the 9 measurements was 4.2 $\pm$ 1.5 km (error estimate is standard deviation). This result suggests that variation in focal depth is small within the region of study. It also suggests that 5 km may be a reasonable average focal depth within this part of the rift.

6.3.3 Wide angle reflections.

From the discussions in section 6.2.3, measured apparent velocities, azimuths and relative onset times were used to identify arrivals likely to be wide angle reflections. These arrivals are labelled 'w' in fig. 3.31.

Event number	First arrival apparent velocity (km/s)	Apparent velocity of phase 'b' (km/s)	Difference between the onset times of 'a' and 'b' (seconds)	Focal depth h (km)
1	7.1	7.0	0.36	1.8
4	7.0	7.0	1.00	5.2
5	7.3	7.4	0.90	4.3
6	7.5	7.4	0.92	4.2
7	7.5	7.8	0.88	4.0
8	7.0	7.4	1.40	7.2
9	6.9	7.0	0.80	4.3
10	7.0	7.0	0.50	2.6
11	6.9	7.0	0.80	4.1

Table 6.2. Stepout times between the first arrivals and the phase 'b' and the calculated focal depths.

Preference was given to arrivals coming in at about the same azimuth as the corresponding first arrival. As a guide, it was noted that the wide angle reflections lag the direct waves in time. In a few cases, some arrivals already considered as direct waves were also considered here as wide angle reflections. In section 3.4.4, it was shown that signal interference could give rise to anomalous apparent velocities and azimuths for later arrivals. Onset times are, however, not similarly affected. In this analysis, observed apparent velocities for later arrivals were used as a guide to phase identification while computations on depths were based entirely on relative time measurements. It must also be emphasized that there is some element of subjective judgement in the selection and identification of later arrival phases.

For each of the events listed in table 6.3, equation 6.1 was solved for the interface depth H using trial and error method. In this equation t was taken as the step out time between the first arrival and the phase "w" interpreted here as wide angle reflections. V_1 was adopted as the measured phase velocity of the corresponding "5.8 km/s arrival" and V_2 was taken as the corresponding observed event first arrival apparent velocity. Estimates of the interface depth H were made for each event assuming focal depths of 5 and 10 km as shown in table 6.3. From the 6th and 7th columns of table 6.3, it is found that the mean reflector/refractor depth estimates at focal depths of 5 km and 10 km are 8 $\pm$ 2 km and 10 $\pm$ 2 km respectively. Error estimates are standard deviations. These results are consistent with the results of section 6.3.2 and with the first arrival data.

Event number	Epicentral distance, Δ (km)	First arrival apparent velocity (km/s)	Apparent velocity of arrival marked 'w' (km/s)	Step out time, t, between 'w' and first arrival onsets (seconds)	Refractor depth (km)	
					For h = 5 km	For h = 10 km
1	59	7.1	6.5	1.03	9.1	11.6
2	60	7.2	5.8	1.20	7.0	9.5
3	60	7.3	5.8	1.20	7.0	9.5
4	61	7.0	7.0	1.00	7.4	9.9
5	67	7.3	6.6	1.80	5.5	8.0
7	72	7.5	6.2	1.80	7.8	10.3
8	73	7.0	7.4	1.40	9.1	11.6
9	77	6.9	6.0	1.40	6.8	9.3
10	81	7.0	6.4	1.10	10.7	13.2
11	88	6.9	6.0	1.60	7.4	9.9

Table 6.3. Parameters of the phase marked 'w' in fig. 3.31 and identified here as wide angle reflections. Reflector depth estimates in the last two columns were made from these parameters.

6.3.4 A multiple reflection phase

We next consider multiple reflections of the type discussed in section 6.2.4 with two reflections at the interface at depth H and one reflection at the surface, the first reflection occuring at the interface. Apparent velocity and relative time estimates discussed in section 6.2.4 were used as guide in identifying phases that could possibly have such propagation path. The identified phases are labelled 'm' in fig. 3.31.

The apparent velocities and step out times, t (relative to first arrival onset) for these phases are shown in table 6.4 for eight events. Equation 6.3 was solved for H by trial and error method from the data for each event. Values for V_1 and V_2 were adopted as discussed in section 6.3.3. Estimates of interface depth H assuming a focal depth of 5 km are shown in the last column of table 6.4. The mean value of H obtained from this table is 11 $\pm$ 2 km (error estimate is standard deviation). It was found that estimates of H at focal depths of 5 and 10 km did not differ significantly.

It is doubtful if this phase has been correctly identified. The interface depth is, therefore, probably estimated with less confidence than in the cases of direct waves and wide angle reflections.

6.4 Summary

To be able to identify the phases of selected later arrivals with confidence, knowledge of the model, the focal depth and the epicentral distance is required. Estimates of distances and focal depths were made in chapter 4. It was shown that distances for events now under consideration were

Event number	Epicentral distance, Δ (km)	First arrival apparent velocity (km/s)	Apparent velocity of arrival marked 'm' (km/s)	Step out time, t, between 'm' and first arrival onsets (seconds)	Reflector depth, H assuming h = 5 km (km)
1	59	7.1	8.0	3.08	14.0
2	60	7.2	6.6	2.30	11.2
4	61	7.0	7.4	2.00	10.2
5	67	7.3	5.8	2.40	11.0
7	72	7.5	6.2	2.78	12.0
10	81	7.0	6.4	2.38	11.8
11	88	6.9	6.6	2.20	10.4
3	60	7.3	6.6	2.26	10.5

Table 6.4. Parameters of the phase marked 'm' in fig. 3.31 and interpreted here as multiple reflections of the type described in sections 6.2.3 and 6.3.4. Reflector depth estimates in the last column were made from these parameters.

estimated to within about ± 10 km. It was not possible, however, to quantify the uncertainty in the estimates of focal depth although discussions in section 6.3.2 and other geophysical/ geological data suggest that depths of focus are unlikely to be greater than about 15 km within the survey area. First arrival apparent velocities and azimuths were measured with high accuracy and were used to derive plane layered models in chapter 5.

The parameters of later arrivals may have been determined with lower accuracy for various reasons. Interference effects (see section 3.4.4) may give rise to anomalous values of measured apparent surface velocity and azimuth of these later arrivals. This would make the use of the magnitude of these measured parameters as aid to phase identification unreliable. The thickness and the nature of the volcanics overlying the basement in the study are not known with reasonable accuracy. It is possible that some reflections/refractions from these volcanics could have been identified as coming from deeper levels.

In the light of these and other uncertainties, it is clear that the second arrival interpretation serve only as a support to the model derived from first arrival data. However, the phases here identified as direct waves and wide angle reflections are more reliable than the others because they give apparent velocities close to those predicted by the model derived from the first arrival data.

In this chapter, second arrival data have been used to confirm and refine the estimate of depth to the 5.8/7.2 km/s interface in the two layer model with uniform velocities derived

from first arrival data in chapter 5. The first and second arrival data are now interpreted in terms of two layer model with a horizontal interface at a depth of 13 $\pm$ 5 km (fig. 6.7). The top and lower layer velocities are 5.8 $\pm$ 0.2 km/s and 7.2 $\pm$ 0.2 km/s respectively. The depth estimate assumes a mean focal depth of 10 km. An increase/decrease of 5 km in focal depth introduces an increase/decrease of about 3 km in the resulting estimate of interface depth. It is suggested that the data has sampled the top surface of a mantle derived crustal intrusion. The exact lateral extent of the top surface of this inferred intrusion is not established by the present data although a minimum lateral extent of about 30 km is suggested.

The second arrival data has also been shown to be consistent with the model of fig. 5.16e redrawn here as fig. 6.8. This model comprises a 10 km thick upper horizontal layer of velocity 5.8 km/s underlain by a 10 km thick intermediate layer in which velocity increases from 6.1 km/s at a depth of 10 km to 7.5 km/s at 20 km depth. This is,in turn, underlain by a 7.6 km/s refractor. The 5.8 km/s top layer is associated with the phases identified as P_g and having apparent velocities of about 5.8 km/s. The first arrivals observed in the present data (with apparent velocities in the range 6.9-7.5 km/s) may be identified as diving waves sampling the greater part of the intermediate layer.

The increase in velocity with depth can be associated with penetrative injection of multiple dykes from below. This, in turn, suggests that the rifting process is probably caused by such asthenospheric intrustions. The model of fig. 6.8 is thus a very plausible and realistic model for this part of the rift, and is preferred to the model of fig. 6.7.

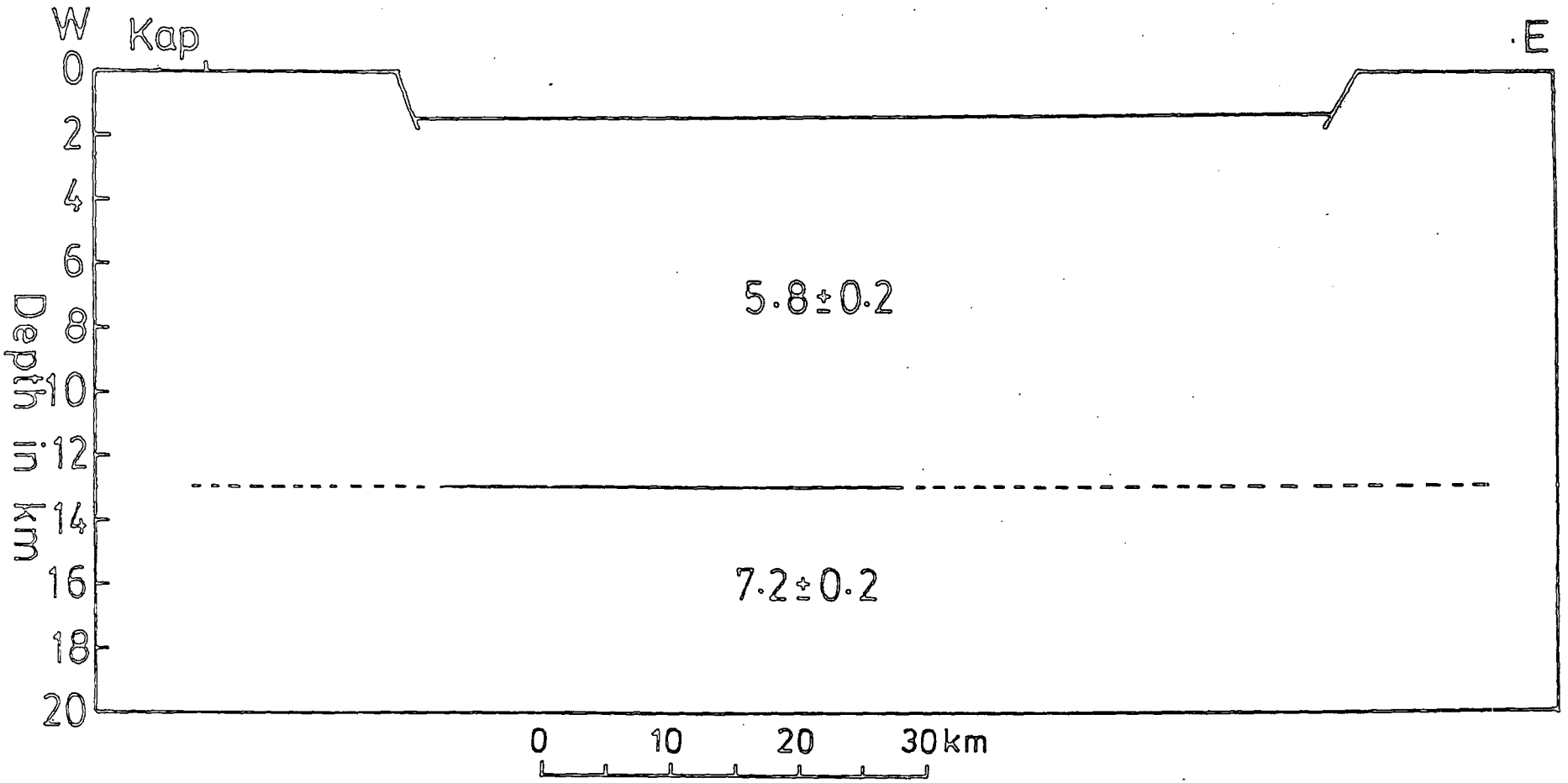

Fig. 6.7 : The two layer model consistent with the first and later arrival data. Layer velocities are shown in km/s. The depth to the interface is 13±5km.

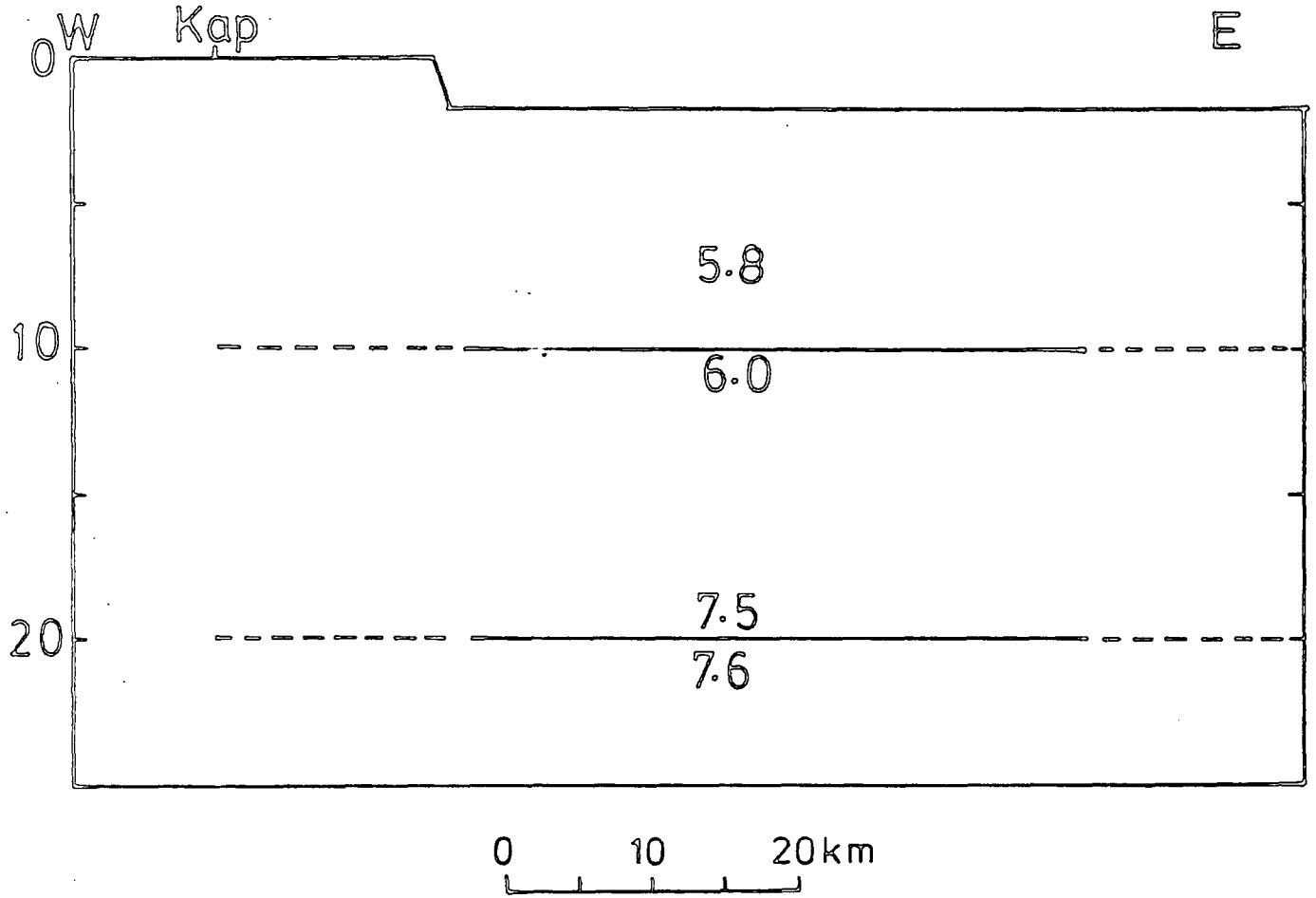

Fig. 6.8: The three layer model consistent with the data. Velocities are shown in km/s and depths in km.

CHAPTER 7

DISCUSSION AND CONCLUSIONS

7.1 The preferred model compared with previous models

The present data have been used to derive models for the structure of the lithosphere beneath the Gregory rift at about 0.5°N latitude. The data have been interpreted in terms of a two layer model with horizontal interface (section 5.4.2), in terms of a two layer model with gently dipping interface (section 5.4.3) and in terms of a three layer model with linear increase of velocity with depth in the intermediate layer (section 5.7.3).

The model including a layer of uniform increase in velocity with depth (fig. 7.1a) and the simple two layer model (fig.7.1b) both explain the data adequately. For the two layer model, assuming a mean focal depth of 10 km for the region under study, the depth to the interface is estimated as 13 $\pm$ 5 km. At this focal depth, an increase/decrease of about 5 km in focal depth introduces an increase/decrease of about 3 km in the estimate of refractor depth. The estimated minimum lateral extent of the top surface of the 7.2 km/s material consistent with the present data is about 30 km. If, as suggested in section 5.7.4, the typical distance used in this study, had been overestimated by about 10 km, the correct estimate of minimum width would be reduced from 30 km to about 20 km. The estimate of 30 km is significantly larger than about 10 km suggested by gravity data (Baker and Wohlenberg, 1971). The boundary (expected steep and sharp) between the normal shield crust to the west of Kaptagat and the rift structure to the east could not be defined by the present data.

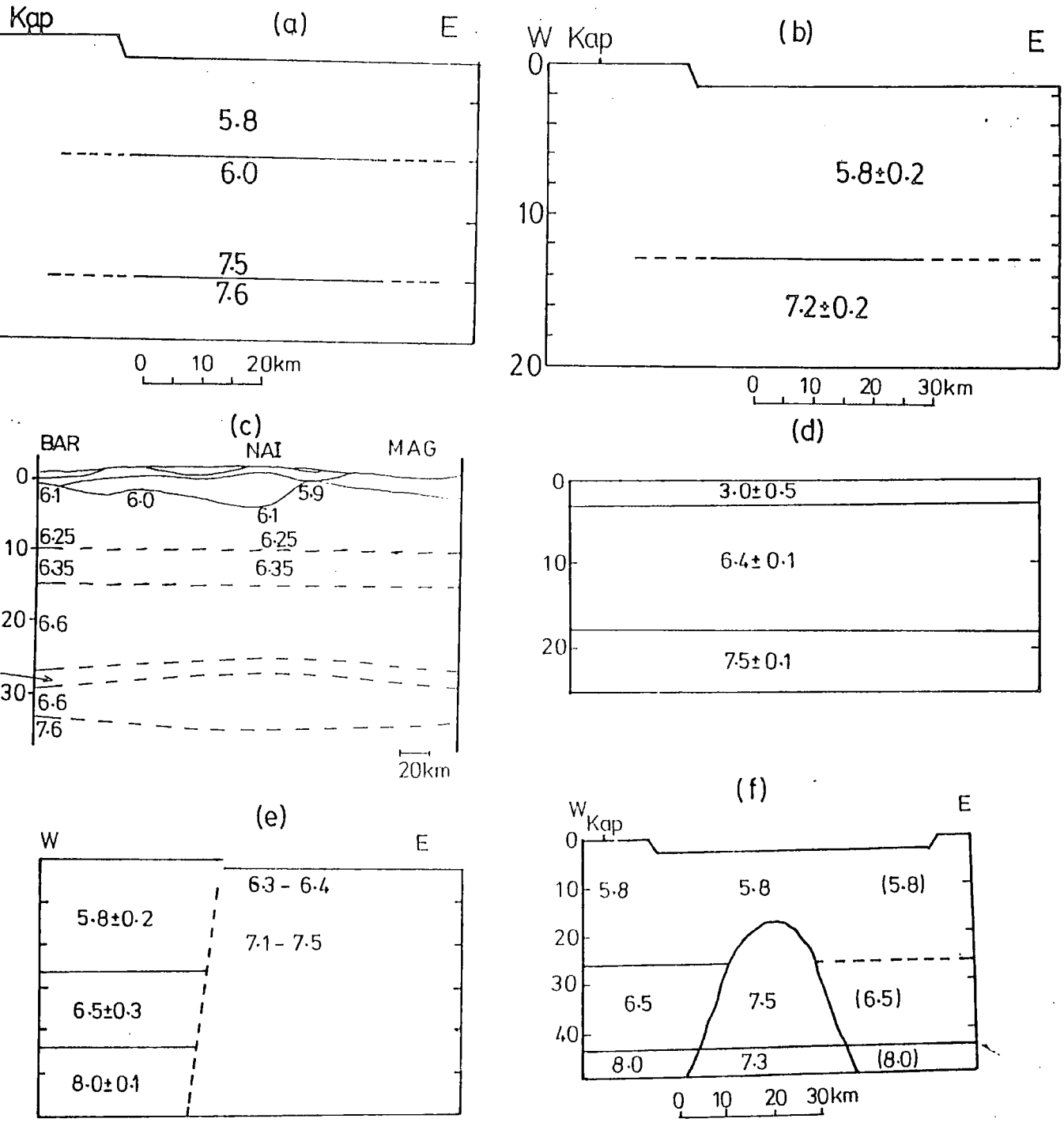

Fig 7·1 : Comparison of structural models (a) and (b) derived in this study with some other previous models (c) to (f) for the Gregory rift : (c) Khan and others, 1987; (d) Griffiths et al., 1971; (e) Maguire and Long, 1976; (f) Savage and Long, 1976. Depths are in km and P-wave velocities in km/s.

The preferred model (fig. 7.1a) has a 10 km thick top layer of velocity 5.8 km/s underlain by an intermediate layer in which velocity increases from 6.0 km/s at 10 km depth to 7.5 km/s at a depth of 20 km. This is, in turn, underlain by a 7.6 km/s refractor. This model, like the model of Khan et al. (fig. 7.1c), suggests multiple dyke injection or diapirism as the primary cause of rifting. This is a very plausible model and appears more realistic than the model of fig. 7.1b although the former requires more data for better definition.

The model of Khan et al.(1987) for the axial part of the southern portion of the Gregory rift is shown in fig. 7.1c. In this model basement velocity increases from about 6.1 kms^{-1} at about 2 km depth to 6.25 kms^{-1} at 10 km depth. Like the models of fig. 7.1a and b, this model indicates higher average upper crustal velocity than would be expected for normal shield structure. Like the model of fig. 7.1a, the model shown in fig. 7.1c shows velocity increase with depth indicative of asthenospheric diapirism. In many other respects the model of Khan et al.(1987) seem to differ from the models derived in this present study and the model of Griffiths et al.(1971) for the axial part of the northern section of the rift (fig. 7.1d). These differences could be explained. The model of fig. 7.1c was derived from a N-S axial profile while the models of fig. 7.1a and b were derived from an E-W profile across the rift at about $0.5^{o}N$. It is, therefore, probable, as suggested by Khan et al.(1987), that the crustal structure beneath the rift varies along and across the rift.

A lithospheric model for the axial part of the northern Gregory rift (fig. 7.1d) derived from explosion refraction data (Griffiths et al., 1971) was discussed in section 1.5.4.

In this model, the existence of the 6.4 km/s material was suggested by gravity data with no independent confirmation from the refraction data of Griffiths et al.(1971).

In the present study, the 6.4 km/s material has also not been observed although its existence is not inconsistent with the data. But the 7.5 km/s material of Griffiths et al.(1971) and the 7.2 km/s material suggested by the two layer model from present data most probably refer to the same crustal intrusion.

The Griffiths' line was oriented approximately north-south along the rift axis while the present data sampled the structure along an approximately east-west profile at about 0.5^{o}N. Any difference in velocities measured in these two directions could be due to a northward dip on the refracting interface as suggested by Long and Backhouse (1976).

Maguire and Long (1976), using first arrival data from records similar to those used in the present study, established that anomalous material with true velocity in the range 7.1-7.5 km/s exists beneath the axis of the Gregory rift at the latitude of Kaptagat (fig. 7.1e). They suggested that this may lie beneath a 6.4 km/s material of Griffiths et al. (1971). But Maguire and Long (1976) did not estimate the depth to and the width of the top surface of the 7.1-7.5 material. Their data assumed (but did not confirm) the existence of the 6.4 km/s material. If this assumption is removed, it is evident that their model is in broad agreement with the simple two plane layer model (fig. 7.1b) derived in the present study. The present data has, however, given estimates for the depth to and the minimum lateral extent of the top surface of what is probably the same material as the top of their 7.1-7.5 km/s material and which corresponds to the 7.2 km/s refractor in

the present analysis.

Like the present data, the seismic profile of Swain et al.(1981) at about 0.5°N did not confirm the presence of the 6.4 km/s material. But their gravity data along the seismic profile suggests that such a material may exist as an intrusion within the basement. The lateral extent of the top surface of their inferred intrusion is estimated to be about 20-35 km; this estimate is of the same order of magnitude as the corresponding estimate for the two layer model (fig. 7.1b) derived here.

It is probable that what is being interpreted in the present study as 7.2 km/s refractor is the same as the basement intrusion suggested by the combined seismic and gravity data of Swain et al.(1981) although their estimate of the depth to its top surface (about 7 km) appears smaller than the corresponding estimate of about 13 km from the present data.

The observed variation in the lateral extent and the depth to top surface of the inferred intrusion obtained by various gravity data may be real but could also be caused by the unknown variations in the thickness and density of the basement cover. Until the work of Khan et al.(1987), the thickness and density of the sediments/volcanics above the basement were not well known; from this work it is now known that the thickness and velocity of the sediment/volcanics for the axial part of southern portion of the rift vary with latitude along the trend of the rift axis. If proper corrections are not made for this variation, differences in gravity model, as observed above, may result even when the deeper structure itself does not change with latitude. More small

scale seismic refraction/reflection experiments designed to determine basement depth and velocity (and density) of superficial material along the existing and future gravity profiles along and across the rift zone will help in obtaining unique gravity models for the sub volcanic structure beneath the rift zone.

The seismic model from Savage and Long (1985) for the central part of the Gregory rift close to the equator and just south of the present survey area is shown in fig.7.1f. This model has a curved upper surface. The present data could, however, only support interpretations involving plane interfaces. The 7.5 km/s material in fig. 7.1f which was originally suggested by Griffiths et al.(1971) for the part of the axis north of the present study area is as suggested above, probably, the same as the 7.2 km/s material in the present model.

Depth to the top surface of the crustal intrusion in fig. 7.1f is about 20 km while the corresponding depth estimate to the top of probably the same intrusion in fig. 7.1b is 13 $\pm$ 5 km. The two depth estimates are, therefore, not significantly different. It will be emphasized, however, that while the teleseismic data are capable of giving broad details of structure at upper mantle depths, such data are not normally suitable for detailed description of the geometry of the top surface of small scale intrusions within the crust.

There may be differences in detail between the present models and other previous models and also between the previous models themselves. But there is a broad agreement between the present models and other models in support of the observation that the structure of the crust/lithosphere beneath the Gregory

rift is essentially different from that of normal shield structure observed outside the rift zone. Data from Khan et al.(1987) suggests crustal thickness of about 35 km but anomalous crustal and "Moho" velocities. Most other models including those derived in this study (fig.7.1a and b) are consistent with extreme thinning of the crust/lithosphere beneath the Gregory rift. Furthermore, velocity increase with depth as observed in the present study (fig. 7.1a) probably results from multiple dyke injection from below the lithosphere. This intrusion will, in turn, provide the driving mechanism for the rifting process.

7.2 Some limitations of the present data.

.2.1 Uncertainties in the estimates of focal depth and distance.

The local earthquakes whose seismograms were analysed in the present work were not recorded at other stations outside the array. Consequently both the epicentral distances, focal depths and onset times of recorded phases had to be measured from the array seismograms themselves. But accurate determination of epicentral distance and focal depth requires a prior knowledge of the seismic model of the crust/lithosphere, which, of course, is initially unknown and is, in fact, the main object of the study. The use of the same seismograms for both structural modelling and the estimation of the earthquake source parameters inevitably involves wider assumptions than could be tolerated in the interpretation of data from controlled seismic experiments.

Particularly disturbing is the uncertainty in the estimate of focal depths of events. This uncertainty, in turn,

affects the estimates of interface depths in any plausible model. In the present data, focal depths could not be determined unambiguously and the estimates of epicentral distances were based on phases ('X') whose identity could not be ascertained uniquely. However, constraints from other geological/geophysical data were used to narrow the limits for the estimates of these source parameters.

It is obvious that the details of the shallow structure (seismic) beneath the rift zone can only be obtained from controlled refraction/reflection experiments similar to KRISP85 (Khan et al., 1987). E-W seismic profiles across the rift at different latitudes are particularly important for studying the variation of crustal/lithospheric structure along the rift. This can be supported by the recordings of local earthquakes using suitable mobile station networks.

3.2.2 Application of velocity/azimuth filtering technique to records from local earthquakes.

Velocity filtering had traditionally been developed and successfully applied to the study of teleseismic events where recorded phases are normally well seperated from one another in time. Its use in the study of local earthquake records has not been equally well reported. This is possibly because, in the case of local events, many phases often arrive the station partially superposed or seperated by times too small for these phases to be confidently resolved by velocity filtering. This interference problem (discussed in section 3.4.4) could result in measured apparent velocities and azimuths which may be significantly different from their true values.

Identification of later arrival phases on the basis of such measured values could therefore some times be misleading. To achieve more reliable identification of second arrival phases in this study, the peaks indicated on the velocity filter outputs were, therefore, as far as possible, reconciled with the corresponding phases seen on the single seismograms. It was observed that prominent phases including P_g and some reflections could be easily identified with confidence on both records. Although interference could some times produce anomalous values of measured apparent velocity and azimuth for some second arrival phases, the relative onset times for such arrivals are not normally affected. Interpretation of such arrivals was, therefore, in this study based on measured relative onset times while estimated velocity values were used mainly to aid phase identification.

7.2.3 The volcanic/sedimentary cover.

The effects of lavas and sediments overlying the basement along the profile of the present data have been ignored in the present analysis. These lavas and sediments are expected to have velocities significantly lower than normal crustal velocities. However, their thicknesses and velocities along present profile are not known accurately although some estimates have been reported for various parts of the rift zone.

King (1978) suggests a total thickness of about 5.5 km for the rift trough southwards from Lake Baringo. A maximum thickness of about 3000 m is estimated in the northern part of the Kamasia area (Chapman et al., 1978). A seismic profile

along the southern portion of the rift axis indicates that depth to basement is about 2 km beneath Susua and Lake Baringo and about 6 km beneath Lake Naivasha (Khan et al., 1987). All these estimates are for basement cover within the axial part of the rift which may be a very narrow belt.

Of more relevance to the present analysis is the variation in the thickness of volcanic/sedimentary cover along an E-W line crossing the rift at the latitude of Kaptagat. Interpretation of a 50 km E-W reversed refraction line between Lake Baringo and Chebloch gorge indicates a 2.0-3.5 km thickness of 3.7 km/s volcanics overlying a 5.7-5.8 km/s material thought to be crystalline basement (Swain et al., 1981). There is reasonable over lap between this profile and the profile of the present data. It was shown, in section 2.2, that the thickness of the volcanics beneath Kaptagat station is about 150-200 m which is negligible compared with thickness of the basement cover within the rift trough. Estimates of depths to interfaces (within the rift) obtained in this study would, therefore, have to be increased by about 2 km to take account of the difference in the thicknesses of the basement cover beneath Kaptagat and the rift trough.

The presence of the volcanics and sediments which have considerably lower velocities than crustal rocks would be expected to influence the values of onset times measured from the records. This, however, will not have adverse effect on the present data which measures only relative onset times. Moreover, most of the useful rays arriving Kaptagat where basement cover is negligible may not have sample significant part of the low velocity sediments/volcanics.

7.3 The present study and theories of rift formation

The theories for the formation of continental rifts discussed in chapter 1 fall into one or the other of the two broad mechanisms - active or passive (Sengor and Burke, 1978). Specific theories discussed within these two broad categories include the following: (a) lithospheric plate motion over mantle hot spots or plumes, (b) membrane tectonic theory, (c) lithospheric stretching mechanism and (d) the perturbation and upward movement of the lithosphere/asthenosphere boundary. The present data together with other available data could be used to establish which of these mechanisms offers the most satisfactory explanation for the formation of the Gregory rift in particular and the Eastern rift in general.

Geophysical data show that the lithosphere beneath the Gregory rift zone (and indeed the whole of the Eastern rift zone) is underlain by low density/low velocity and relatively hot asthenosphere with significant partial melt fraction. From this and other studies, it is shown that this asthenospheric material shallows beneath the rift axis indicating enhanced thinning of the lithosphere. Geological data (Bailey, 1983; Wendlandt, 1982) support the theory that lithospheric thinning and subsequent rifting in East Africa are explicable from a source of heat in upwelling mantle below the lithosphere (Gass et al., 1978; Gass, 1970,1972; Bott, 1981). The convected heat gives rise to thermal perturbation of and upward migration of the asthenosphere/lithosphere boundary. From the present data, this active mechanism is preferred to the others as the most viable explanation for the formation of the Gregory rift and other

continental rifts.

The essential features of this mechanism are given by Bott (1981). Diagrams illustrating three main stages in the process, together with Bott's captions, are shown in fig. 7.2. Bott's explanations are, in essence, similar to those of Gass (1972). The present stage of development in the Gregory rift is very close to stage c suggesting severe lithospheric thinning of the lithosphere but no crustal disruption in agreement with geological data (King, 1978).

This theory of thermal perturbation of and the upward migration of the lithosphere-asthenosphere boundary is due primarily to convection of heat into the rift zones by ascending magma. The theory adequately explains domal uplift and the observed evolution of volcanism from strongly alkaline basalts to transitional basalts and tholeiites. The stress system resulting from the combined effect of topographic load of the uplifted region and the upthrust caused by the underlying low density upper mantle is sufficient to cause rifting. Clay models of Cloos (1939) and finite element analysis of Neugebauer (1978, 1981) show that the nature and finite extent of the Gregory rift can also be explained as due to rifting in the resulting domed structure.

The membrane tectonic theory argues that the East African Rift system was produced by membrane stresses in the lithosphere developed in response to the rapid latitude change experienced by East Africa during the late Cretaceous and Tertiary. The theory explains the major features associated with the Gregory rift. As observed, the rift developed in the central part (which should be under tension)

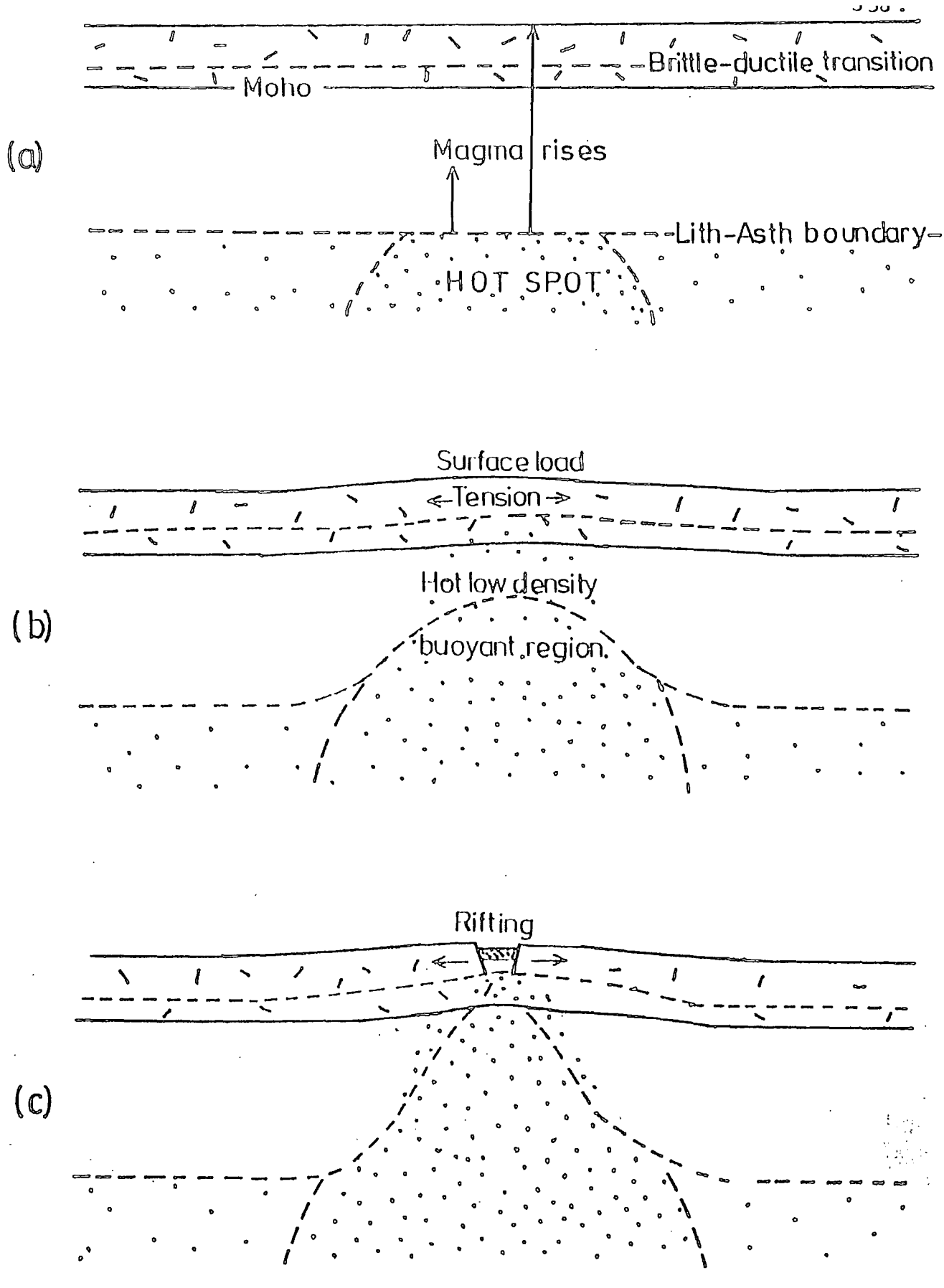

Fig. 7.2 : Stages in the development of a domed and rifted structure: (a) Hot spot forms below the continental lithosphere by upwelling from the deeper parts of the mantle. (b) The continental lithosphere becomes heated and thinned, with consequent isostatic uplift and development of tensile stress system in the upper crust. (c) Graben formation starts when the tensile stresses become sufficiently large. (From Bott, 1981).

of the African plate moving north towards the equator. This direction of plate motion, in turn, explains the observed southward migration of rifting and accompanying volcanism. The nature and finite extent of the rift are also explained. But the extension across the Red Sea and the Gulf of Aden is too much to be explained by the membrane tectonic theory.

The preferred model from the present data (fig. 7.1a) shows an increase in velocity with depth within the crust. Evidence of such velocity variation is an evidence for multiple dyke penetration from below. This, in turn, is an evidence for the mechanism of the upward migration of the mantle material. The present data is, therefore, consistent with other data in supporting the theory that rifting within the Gregory rift zone (and in deed the whole of the East African rift zone) is caused primarily by thermal perturbation of and upward migration of the lithosphere/asthenosphere boundary. This active mechanism could be aided by one or more of the other mechanisms. But before active spreading can take place within the Eastern rift, the seperate magma regions below the Ethiopian and Kenya domes must be linked. It will, therefore, be useful to investigate the extent to which these regions are linked at depth.

7.4 Suggestions for further research

From empirical linear relationships between delay time, station elevation and Bouguer gravity anomaly, Fairhead and Reeves (1977) have produced a map of lithospheric thickness for Africa. This map reveals a zone of thinning coincident with the rift system, from Ethiopia through Kenya and

Tanzania to Angola. The thinning is most pronounced beneath the rift valleys. Volcanism and high heat flow are all associated with zones of lithospheric thinning which may be future sites of lithospheric rupture.

Nearly all the different stages of continental rifting have been recognized within the Eastern rift. The sequence of development seems to evolve from incipient rifting in Southern Africa progressing northwards to a region of block faulting in Tanzania. This advances to major rift development in Kenya with volcanics on the rift shoulders and along the rift floor. Further north, there is increasing valcanism through the Ethiopian rift culminating in sea-floor spreading and the development of a fully oceanic region in the Gulf of Aden.

These observations suggest an imminent/eventual break up of the African continent along the Eastern rift zone. To investigate this suggestion, further studies of the crust and the upper mantle beneath the Gregory rift and other parts of the Eastern rift zone are required to ascertain the variation of lithospheric thinning along the trend of the rift zone.

7.4.1 The crust.

From seismic data it has been established that the crust on the western flank of the Gregory Rift is of the normal shield type (Maguire and Long, 1976). It will be useful to confirm the suggestion that a similar normal shield crustal structure exists beneath the eastern flank and beyond. Most current upper mantle models for the Gregory Rift zone (from seismic and gravity data) assume that the western and eastern

flanks sit on the same type of crust. This assumption should be tested by acquiring fresh and better refined seismic and gravity data for further elucidation of the crustal structure within and outside the rift zone. Such experiment should also be able to define the positions of the boundaries between the normal shield structure to the west (and also to the east) and the rift structure in between.

Long range controlled refraction profiles (with close station spacing) along and at right angles to the rift axis are required for these studies. Khan et al.(1987) have already interpreted one such profile approximately 300 km long along the axis of the southern portion of the Gregory rift from Lake Baringo to Lake Magadi. Their interpretation (fig. 7.1c) appears to differ significantly from the model of Griffiths et al.(1971) for a 367 km long seismic refraction profile along the axis of the northern part of the rift between Lake Turkana and Lake Bogoria (Hannington) (fig. 7.1d).

The difference between these interpretations could be due to differences in crustal structure along the rift. It could also be due to differences in quality and quantity of data. It is important to resolve this difference. To this end it will be useful to carry out another long range controlled seismic experiment along the profile originally shot by Griffiths et al.(1971) in the manner of KRISP85.

Other long range refraction profiles parallel to but outside the rift axis are required. Also required is a series of east-west controlled refraction/reflection profiles at right angles to the rift axis at different latitudes. This will help study the variation of crustal structure along and across the rift axis. Such east-west profile (although rather short) has

been shot across the rift axis at about 1°S latitude (Khan et al., 1987). But the data from this profile has not been interpreted probably because of poor record quality. Within the rift zone, it will be useful to have controlled small scale reflection experiments to complement refraction data in elucidating crustal structure. Data from controlled seismic experiments should be supplemented with mobile network records of local/regional earthquakes.

Both the reflection and refraction data should be aimed also at determining the spacial variation of the thicknesses and velocities of the volcanics/sediments overlying the basement within the rift zone. This information will be of immense use in reinterpreting more reliably, already existing and the yet to be acquired gravity data for the elucidation of the rift structure. The limits of what can be done depends, of course, on the available funds.

It will be helpful if fresh gravity measurements are made along all the seismic profiles suggested above. Attempt at more precise determination of densities of near surface rocks can then be made and fresh gravity models obtained. The combined gravity and seismic data should aim at studying the variation of crustal/lithospheric thinning along the trend of the rift axis thereby shedding more light on the debate about the imminent break up of the African continent along the rift zone.

7.4.2 The upper mantle

A knowledge of the detailed structure of the crust in and around the rift zone that will result from the implementation of the discussions in section 7.4.1 will help in the

derivation of a more accurate and realistic model for the structure of the upper mantle and below. Knowledge of the structure of the crust and upper mantle within the rift zone will help in the understanding of processes responsible for the formation of the Gregory rift and other continental rifts. This will, in turn, help establish whether the rift system is at the closing stages of a stalled evolution or is marking the initiation of an episode of lithospheric spreading.

It is, for example important to establish to what extent the Kenya and Ethiopian domes are linked at depth. For such investigation, new refined and better controlled regional seismic and gravity data are required. Teleseismic delay time data from mobile network of independent stations could be used to define the upper mantle structure in the region beneath and between the Kenya and Ethiopian domes. Further information on slowness anomalies should also be obtained by having small aperture seismic arrays included within the mobile network. The array aperture should be small because of the expected rapid lateral variations in structure within the rift zone. In principle, it should be useful to supplement above delay time and slowness data with fresh regional data from controlled seismic reflection and refraction data if cost permits.

It is also necessary to reinterpret currently available local and regional gravity data within the rift zone and to add new data. Reinterpretation should be carried out only after accurate and reliable values of thicknesses and densities/velocities of the superficial volcanics/sediments within and outside the rift zone must have been determined. These enlarged data would further elucidate the upper mantle structure especially in the region between the Kenya and Ethiopian domes.

The combined crustal and upper mantle study should unambiguously define the variation of the position and the depth and lateral extent of the crustal intrusion inferred from gravity data along the trend of the rift and with respect to visible rift structures. The link between this intrusion and any feeder from below should also be established.

7.5 Conclusions.

In chapter 1 a review of previous geological and geophysical studies of the crust and the upper mantle within the Eastern rift zone was given with emphasis on the Gregory rift. These studies reveal the evolution of the Gregory Rift and suggest possible theories for the formation of this and other continental rifts.

Chapter 2 discusses the collection of data from the small aperture Kaptagat array station located at about 0.5N in Northern Kenya. Chapter 3 describes the theory, performance and problems of the velocity filtering technique used in processing the data. Data from local rift events to the immediate east and south west and from more distant rift events to the north and south of Kaptagat were processed using programs developed for the CTL Modular 1 computer and the University of Durham IBM 360/370 computer. The resulting data used for interpretation were in the form of apparent velocities and azimuths of first and later arrival phases. The first arrival data were determined with a high degree of accuracy. Interpretation in the present study was based only on data from closein eastern local rift events since ray paths from these events must definitely have sampled the rift structure better than ray paths from other events further to the north and south.

In chapter 4, probable values of focal depth in the region of study were discussed. On the strength of available geological and geophysical data it is argued that depths of focus greater than about 15-20 km are unlikely within the Gregory rift zone. Average focal depth of about 5-10 km appears realistic. A prominent arrival on the records, designated 'X' arrival was used in estimating epicentral distances. An empirical curve for converting P-X times to epicentral distances of events was derived. Using this curve, measured P-X times were subsequently converted to epicentral distances for realistic focal depths. These distances were combined with the corresponding measured azimuths to locate the event epicentres. The epicentres thus located were observed to lie mostly within the axial trough of the Gregory rift.

Interpretation of the first arrival data was carried out in chapter 5. These data were first interpreted in terms of a two layer model with a horizontal interface. The top and lower layer velocities consistent with the data were as 5.8 km/s and 7.2 km/s respectively. The maximum depth to the refracting interface was estimated as about 16 km if a mean focal depth of 10 km were assumed. An increase/decrease of 5 km in focal depth increases/decreases this maximum refractor depth estimate by about 3 km. From other geophysical data the minimum depth to the refractor was estimated at about 6 km.

The first arrival data is also consistent with a two layer model with a gently dipping plane interface dipping from Kaptagat up towards the rift axis at an angle of no more than about 6°. On this model, estimates of the depth to the Kaptagat end or minimum westward limit of the refractor are

not significantly different from the corresponding depth estimates from the two layer model with a horizontal interface discussed above.

The data is inconsistent with a steeply dipping boundary. This implies that the present data has not sampled the steep boundary suggested to seperate the normal shield crust to the west of Kaptagat from the anomalous rift structure to the east.

In chapter 5, it was shown that the first arrival data could also be explained in terms of a three layer horizontal model with top and middle layers each about 10 km thick. The top layer has a uniform velocity of 5.8 km/s. In the middle layer velocity increased from 6.0 km/s at a depth of 10 km to 7.5 km/s at a depth of 20 km. The intermediate layer overlies a 7.6 km/s refractor. This model is also consistent with second arrival data discussed in chapter 6 and is preferred to the simple two layer model.

In chapter 6, the depth to the interface in the two layer model was further constrained and refined by the second arrival data. The resulting refined two layer model consists of two uniform horizontal layers with upper and lower layer velocities of 5.8 ± 0.2 km/s and 7.2 ± 0.2 km/s respectively. The depth to the refracting interface was estimated at 13 ± 5 km. The minimum lateral extent of the top surface of the 7.2 km/s refractor was estimated as about 20-30 km.

The preferred model (fig. 7.1a) has been discussed above. This model includes an intermediate layer in which velocity increases uniformly with depth as shown in fig. 7.1a. This velocity increase with depth is evidence for multiple dyke penetration from below. This, in turn, is evidence for the mechanism of upward migration of the mantle material from below.

A velocity of about 7.5 km/s at a depth of about 20 km suggests extreme thinning of the crust. A similar conclusion is reached from the simple two layer model.

Extreme thinning of the crust/lithosphere beneath the Gregory rift at about 0.5°N latitude is, therefore, inferred from the present study. The models derived here are consistent with the theory that rifting is primarily caused by upward migration of the lithosphere/asthenosphere boundary. This thermal upwelling is driven by gravitational instability of the less dense and hotter asthenosphere under the more dense mantle lithosphere. Lithospheric tension induced by the resultant isostatic crustal uparching gives rise to graben formation. In the process, magma and volatiles, if available, are injected along the axis of the graben. But before active spreading can take place within the Eastern rift zone, the seperate magma regions beneath the Ethiopian and Kenya domes must be linked.

APPENDIX A

THE VELOCITY FILTER PROGRAM FOR MOD1 COMPUTER

This program was written for use on Mod1 computer in a specialised language called SERAC (seismic record analysis compiler). The present form is adapted from an original program written by Forth (1975) and later modified by Armour (1977).

In the form presented here, the program processes array data of events recorded on 8 channel magnetic tapes and produces a plot, on an X-Y plotter, of a series of correlator functions for one azimuth and a range of velocities. Input data to the program include azimuth and the 8 channel array record which has previously been transferred from tape to disc file. The program can, of course, easily be modified to handle up to 16 channel array data as input.

APPENDIX A

```
72;
;
SPR;
AZIMUTH;
ASK;
ADD;159;104;
SPR;
FILEN;
ASK;

CALL;58;

LIN;;18;;
INS;K;159;
EVA;TBP=0;
INP;K;;1,2,3,4,5,6,7,8;1,2,3,4,5,6,7,8;
WEI;8;.02;54;
OUT;;;1,2,3;54,61,62;
ADD;62,63;62;
IF;TBP<10;
IGOTO;10;
ELSE;

CALL;58;

18DO;A,B,D;5.0,5.0,1.0;0.5,0.5,0.8;10.0,10.0,9.0;
INS;C;159;
EVA;TBP=0;

CALL;58;

INPUT;C;;1,2,3,4,5,6,7,8;
1,2,3,4,5,6,7,8;
STACK;1,2,3,4,5;A;E;50;
STACK;6,7,8,9,10;B;E;51;
MUL;50,51,50;
    60,60,51;
    50,51,71;
IF;C(.71,0) <0;
SUB;71;70;71;
SQRT;71;71;
SUB;71;70;9;
GOTO;33;
ELSE;
SQRT;71;9;
INT;9;.20;52;
WEI;52;.1;53;
ADD;53,103;54;
ADD;62,63;62;
OUT;0;;1,2,3;54,61,62;
IF;TBP>11;
GOTO;42;
ELSE;
IGOTO;22;
SPR;
;
CPR;100,104;
CONT;
```

APPENDIX A contd.

```
DO;H;1.0;0.8;9.0;

CALL;58;

EVA;TBP=0;
INP;;;1;99;
ADD;62,63;62;
OUT;;;1,2,3;107,61,62;
IF;TBP<10;
IGOTO;48;
ELSE;
SPR;
;
CPR;107;
CONT;
FGOTO;1;;



58SET;50,51,52,53,60,61,62,63,70;
    0,  0,  0, 0,.1,10,0,.01,0;

DO;90;0;.01;1;
SET;9,12;,;
SET;1,2,3,4,5,6,7,8;,,,,,,,;
INP;;;1;91;
OUT;;;1,2,3,4,5,6;50,51,53,54,61,62;
IGOTO;59;
CONT;

SET;61;-10;
RETURN;
END;
```

```
45;
;
SPR;
FILEN;
ASK;
INS;C;159;
SET;19,20,21;6.28,4.0,0.5;
SET;22,23,24;0.4,1.45,5.0;
EVA;TBP=0;
CALL;31;
CALL;34;
IF;TBP<0.50;
IGOTO;7;
ELSE;
DO;A;0;0.01;0.5;
MUL;19,30;20,100;30,31;
EVA;C(.41,0)=C(.24,0)*SINC(.31,0);
SUB;22;23;33;
DIV;33;21;34;
MUL;34;100;35;
ADD;35,22;36;
EVA;C(.51,0)=COSC(.36,0)/SINC(.36,0);
MUL;41;51;60;
WEI;60;1.0;61;
DEL;61,61,61,61,61,61,61,61,61,61;0,1,2,3,4,5,6,7,8,9,10;
CALL;34;
CONT;
EVA;C(1.06,0)=TBP+8.0;
CALL;31;
CALL;34;
IF;TBP<C(1.06,0);
IGOTO;26;
ELSE;
SET;1,2,3,4,5,6,7,8;0,0,0,0,0,0,0,0;
SET;9,10;0,0;
RETURN;

OUT;0;0;1,2,3,4,5,6,7,8,9,10;1,2,3,4,5,6,7,8,9,10;
OUT;C;0;1,2,3,4,5,6,7,8,9,10;1,2,3,4,5,6,7,8,9,10;
RETURN;
END;
```

APPENDIX C

(a) Program TREAD

This program reads tapes written on Modular 1 computer. These tapes take the form of a continuous string of digits multiplexed in blocks of 8 or 16. In this study 8 tracks were used. Reading the tape involves demultiplexing and producing as output an 8 channel array record for velocity/azimuth filtering using the program VFIL on NUMAC general purpose IBM 360/370 computer.

(b) Program VFIL

This program calculates the correlator functions at given time points along the array record as functions of apparent velocity and azimuth. The input data include starting, final and incremental values of velocity, azimuth and time (i.e. sample number along the record). Also required as input are the time window for smoothing the correlator function and the number of correlator peaks required.

Then at each time point along the record, the program computes the correlator functions in the given velocity-azimuth space. These computed values are smoothed and arranged in descending order of magnitude so that a specified number of these peaks can be printed and/or plotted.

```
      C          PROGRAM  TREAD:
      C THIS PROGRAM READS TAPE WRITTEN ON MODULAR ONE COMPUTER
      C POSITON TAPE TO THE BEGINNING OF THE FIRST FILE
            INTEGER*2 SAMP(256), LEN
            DIMENSION CH(?,3000),ID(?),DC(8)
            LEN=?
            CALL CNTRL('POSL=*?*',LEN,1)
            KPOS=1
            CALL RSEE(,,0)
            READ(5,358)DUMF
        358 FORMAT(?0X,I1?)
            NFILE = DUMF - KPOS
            CALL SKIP(NFILE,0,1)
            NSAM=0
      C
      C   THE FIRST BLOCK CONTAINS HEADER INFO
      C    AND ABOUT 0.27SEC OF DATA IF RECORDED AT
      C    SAMPLING RATE OF 100SAMPLES PER SECOND
      C*   THE FIRST BLOCK IS THEREFORE READ AND IGNORED
      C
            READ(1,33)SAMP
      C
      C    THE SECOND AND SUBSEQUENT BLOCKS ARE READ AND USED
      C
      C    EACH BLOCK CONTAINS 256 STRINGS REPRESENTING 32 SAMPLES
      C    OF 8 CHANNEL INFORMATION. THE FIRST STRING OF EACH BLOCK BELO
      C    TO THE LAST SAMPLE OF THE PREVIOUOS BLOCK
      30    READ(1,33,END=49)SAMP
      33    FORMAT(1?A2,1?3A2)
            DO 41 I=1,32
            NSAM=NSAM+1
            IF(NSAM.GT.3000)GOTO 49
            DO 35 J=1,?
            IPOS=8*(I-1)+J
            K=SAMP(IPOS)
            CH(J,NSAM)=FLOAT(K)
      35    CONTINUE
      41    CONTINUE
            GOTO 50
      49    NSAM=NSAM-3?
      C
      C    REARRANGE CH ARRAY IN REQUIRED ORDER AND
      C    CALCULATE DC OFFSETS
            DO 43 I=1,?
            DC(I)=0.0
      43    CONTINUE
      50    DO 55 I=1,NSAM
            CH(1,I)=CH(1,I+1)
            TEMP=CH(1,I)
            DO 53 J=1,7
            CH(J,I)=CH(J+1,I)
      53    DC(J)=DC(J)+CH(J,1)
            CH(8,I)=TEMP
            DC(8)=DC(?)+TEMP
      55    CONTINUE
      C
      C    REMOVE DC OFFSETS
      C

ting of TREAD at 12:00:46 on AUG 2?, 1985 for CCid=GP02

            DO 57 I=1,?
            DC(I)=DC(I)/FLOAT(NSAM)
      57    CONTINUE
            DO 58 I=1,NSAM
            DO 58 J=1,?
            CH(J,I)=CH(J,I)-DC(J)
      58    CONTINUE
            K = NSAM+1
            DO 60 I = K,3000
            DO 60 J = 1,?
            CH(J,I) = 0.0
      60    CONTINUE
            WRITE(6,?0)((CH(J,I),J=1,?),I=1,NSAM)
      90    FORMAT(?F10.?)
            STOP
            END
```

```
C      PROGRAM  VEIL  : J.U.CHUKUDEBELU
C  THIS PROGRAM DETERMINES VELOCITY AND AZIMUTH AT EACH TIME POINT
C ALONG A SINGLE SEISMIC CHANNEL. THESE SIGNAL PARAMETERS CORRESPOND
C TO MAXIMUM CORRELATION AT EACH POINT.
C
C INPUT DATA ARE PIT COORDINATES, STARTING AND TERMINAL VELOCITIES
C AND AZIMUTHS, SAMPLING RATE AND INTEGRATION WINDOW
C CHANNEL DATA IS READ FROM CH ARRAY STORED IN DISC FILE
C
      DIMENSION CH(8,2000), TAP(100,200), SP(2000), TAPMX(2000), DC(8)
      DIMENSION VEL(2000), AZM(2000), IO(8,100), V(100)
      DIMENSION X(8), Y(8), SMTAP(100,200)
      COMMON /DEL/ V, NV, SR, X, Y, NPIT
      DIMENSION CORR(1000), VELCTY(1000), AZMUTH(1000)
      COMMON VELCTY, AZMUTH, CORR, NPEAK, TI, F2
      COMMON /P1/ VSTAT, VEND, AZSTAT, AZEND, TSTAT, TEND
      DTOR = ATAN(1.0) / 45.0
C
C
C READ IN CONTROL DATA
      READ (5,10) AZSTAT, AZEND, AZSTEP, VSTAT, VEND, VSTEP, SR, WD
      READ (5,20) NPIT, NR, NY, MX, IP, ISTEP, NPEAK, MPEAK
      READ (5,10) X
      READ (5,10) Y
      READ (5,30) NEVENT, NTAPE, NFILE, NSAM, CM, FR
      READ (1,10) ((CH(I,J),I=1,NPIT),J=1,NSAM)
   10 FORMAT (8F10.3)
   20 FORMAT (8I10)
   30 FORMAT (4I10, 2F10.1)
      WRITE (6,40) NEVENT, NTAPE, NFILE
   40 FORMAT ('1', 14X, 'EVENTNO=', I5, /14X, 'TAPENO=', I3, /14X, 'FILEN
     1', I3)
      WRITE (6,50) IP, ISTEP, WD, NPEAK
   50 FORMAT ('0', 15X, 'IP=', I5, 'SAMPS', /16X, 'ISTEP=', I5, 1X, 'SA
     1PS'/16X, 'INT. WINDOW = ', F3.2, 2X, 'SECONDS', /16X, 'NPEAK = ',
     2I3)
      WRITE (6,60)
   60 FORMAT ('0', 35X, 'START', 3X, 'TERMINAL', 2X, 'INCREMENT')
      WRITE (6,70) VSTAT, VEND, VSTEP, AZSTAT, AZEND, AZSTEP
   70 FORMAT ('0', 15X, 'VELOCITY (KM/S)', 3(3X,F7.2), /16X, 'AZIMUTH (
     1EGS)', 3(4X,F7.2))
      WRITE (6,80)
   80 FORMAT (1H1, 17X, 'SP    VELOCITY  AZIMUTH     CORREL'/)
C SET POINTER TO A REQUIRED ELEMENT(TIME) ALONG CH ARRAY AND
C CONVERT TIME WINDOW TO INTEGRAL NUMBER OF SAMPLES
      L=IP
      NRP1 = NR + 1
      NCH = NR + NY
      M = IP
      NWD = IFIX(SR*WD) / 2 * 2 + 1
      NAZ = IFIX((AZEND - AZSTAT)/AZSTEP) + 1
      NV = IFIX((VEND - VSTAT)/VSTEP) + 1
      TSTAT = (FLOAT(IP)) / SR
      TEND = (FLOAT(MX)) / SR
      TSTEP = (FLOAT(ISTEP)) / SR
      TI = TSTAT
      F1 = FR / 2.0
      F2 = FR - 0.1
      F3 = F1 + 0.3
      KP = 1

      CALL PAPLR(1)
      CALL CSPACE(0.0, FR, 0.0, 1.0)
      CALL PSPACE(0.0, FR, 0.0, 1.0)
      CALL MAP(0.0, F2, 0.0, 1.0)
      CALL PLOTCS(F1, 0.03, 'TIME(SECONDS)', 13)
      CALL CTRORI(1.0)
      CALL PLOTCS(0.02, 0.10, 'VELOCITY(KM/S)', 14)
      CALL PLOTCS(0.02, 0.40, 'AZIMUTH(DEG)', 12)
      CALL PLOTCS(0.02, 0.75, 'CORREL', 6)
      CALL CTRORI(0.0)
      CALL PSPACE(0.1, F2, 0.1, 0.3)
      CALL MAP(TSTAT, TEND, VSTAT, VEND)
      CALL AXES
      CALL PSPACE(0.1, F2, 0.4, 0.6)
      CALL MAP(TSTAT, TEND, AZSTAT, AZEND)
```

```
      CALL AXES
      CALL PSPACE(0.1, .2, 0.7, 0.9)
      CALL MAP(TSTAT, TEND, 0.0, CM)
      CALL AXES
C INITIALIZE TAP ARRAY TO ZERO
C
   90 DO 110 I = 1, NAZ
        DO 100 J = 1, NV
          TAP(J,I) = 0.0
  100   CONTINUE
  110 CONTINUE
C CREATE ARRAY OF VELOCITIES
      VDUM = VSTAT
      DO 120 IV = 1, NV
        V(IV) = VDUM
        VDUM = VDUM + VSTEP
  120 CONTINUE
C
CCCC
CCCC START LOOP TO CALCULATE TAP ARRAY FOR GIVEN RANGES OF
CCCC AZIMUTH AND VELOCITY. INTEGRATION IS OVER A SQUARE WINDOW
C
      AZDUM = AZSTAT
  130 DO 180 IAZ = 1, NAZ
        AZ = DTOR * AZDUM
        AZDUM = AZDUM + AZSTEP
        CALL DELAY(M, AZ, ID)
C
C
        DO 170 IV = 1, NV
C
C--START LOOP TO SUM OVER NUMBER OF SAMPLES CORRESPONDING TO TIME WINDO
C
          DO 160 I = 1, NWD
            R = 0.0
            YY = 0.0
C
CCC SUM RED ARM
C
            DO 140 J = 1, NR
              R = R + CH(J,ID(J,IV) + I)
  140       CONTINUE
C SUM YELLOW ARM
            DO 150 J = NRP1, NCH
              YY = YY + CH(J,ID(J,IV) + I)

  150       CONTINUE
C
CCC TAKE SQRT OF R*YY WITH THE SIGN PRESERVED
C
            RY = R * YY
            ROOTRY = SQRT(ABS(RY))
            ROOTRY = SIGN(ROOTRY,RY)
C
CCCCC FOR ONE VELOCITY AND ONE AZIMUTH COMBINATION,
CCCCC ONE TAP VALUE IS RETURNED
C
            TAP(IV,IAZ) = TAP(IV,IAZ) + ROOTRY
  160     CONTINUE
  170   CONTINUE
  180 CONTINUE
C* SMOOTH OUT CORRELATION VALUES IN TAP ARRAY AND OUTPUT TO SMTAP ARRAY
C THE FOUR ELEMENTS OF SMTAP ARRAY AT THE FOUR CORNERS
C OF THE FIELD ARE NOT SMOOTHED
  190 NVM1 = NV - 1
      NAZM1 = NAZ - 1
C
CCC INITIALIZE SMTAP ARRAY TO ZERO
CCC
      DO 210 I = 1, NAZ
        DO 200 J = 1, NV
          SMTAP(I,J) = 0.0
  200   CONTINUE
  210 CONTINUE
      SMTAP(1,1) = TAP(1,1)
      SMTAP(NV,1) = TAP(NV,1)
      SMTAP(1,NAZ) = TAP(1,NAZ)
      SMTAP(NV,NAZ) = TAP(NV,NAZ)
      DO 230 J = 2, NAZM1
```

```
      DO 220 I = 2, NVM1
        SMTAP(I,J) = (TAP(I,J - 1) + TAP(I,J + 1) + TAP(I - 1,J) +
     1    TAP(I + 1,J) + 6.0*TAP(I,J)) / 10.0
  220   CONTINUE
  230 CONTINUE
      DO 250 I = 1, NV, NVM1
        DO 240 J = 2, NAZM1
        SMTAP(I,J) = (TAP(I,J - 1) + TAP(I,J + 1) + 6.0*TAP(I,J)) /
     1  0
  240   CONTINUE
  250 CONTINUE
      DO 270 J = 1, NAZ, NAZM1
        DO 260 I = 2, NVM1
        SMTAP(I,J) = (TAP(I - 1,J) + TAP(I + 1,J) + 6.0*TAP(I,J)) /
     1  0
  260   CONTINUE
  270 CONTINUE
C FOR FULL RANGES OF VELOCITY AND AZIMUTH, SMTAP ARRAY
C HOLDS NV*NAZ VALUES. DETERMINE THE PEAKS IN THESE VALUES
C ANY PEAKS FROM OUTER ONE ROW AND ONE COLUMN TO THE EDGES OF THE
C FIELD ARE NOT CONSIDERED
      NAZM1 = NAZ - 1
      NVM1 = NV - 1
      WRITE (6,280) L
  280 FORMAT (1H0, I6)
      L=L+ISTEP
      KC = 0

      DO 330 J = 2, NAZM1
        DO 320 I = 2, NVM1
          VAL = SMTAP(I,J)
          JM1 = J - 1
          JP1 = J + 1
          IM1 = I - 1
          IP1 = I + 1
          NP = 3 * 3
          JC = 0
          DO 310 J1 = JM1, JP1
            DO 300 I1 = IM1, IP1
              IF (VAL .LT. SMTAP(I1,J1)) GO TO 300
              JC = JC + 1
  300       CONTINUE
  310     CONTINUE
          IF (VAL .LT. 0.0) GO TO 320
          IF (JC .NE. NP) GO TO 320
          KC = KC + 1
          IVV = I
          JAZ = J
          VELCTY(KC) = V(IVV)
          AZMUTH(KC) = AZSTAT + (JAZ - 1) * AZSTEP
          CORR(KC) = SMTAP(IVV,JAZ)
  320   CONTINUE
  330 CONTINUE
C SET UNUSED LOCATIONS OF CORR, VELCTY, AZMUTH ARRAYS TO ZERO
C
      KCP1 = KC + 1
      DO 340 I = KCP1, 1000
        CORR(I) = 0.0
        VELCTY(I) = 0.0
        AZMUTH(I) = 0.0
  340 CONTINUE
C
      KCK=KC
      IF (KC .EQ. 0) GO TO 370
      CALL SORT(KC)
      IF(KC.LE.MPEAK) GO TO 350
      KC = MPEAK
  350 CALL PLOT(KC, CM)
      IF(KCK.LE.MPEAK) GO TO 355
      KC=MPEAK
      GO TO 357
  355 KC=KCK
  357 WRITE (6,360) (VELCTY(I),AZMUTH(I),CORR(I),I=1,KC)
  360 FORMAT (20X, 2F10.2, 5X, F10.2)
C
```

```
C  AZIMUTH IN THE FIELD
C INCLUDING THE EDGES
  370     CMAX = 0.0
          DO 390 I = 1, NAZ
            DO 380 J = 1, NV
              IF (SMTAP(J,I) .LE. CMAX) GO TO 380
              CMAX = SMTAP(J,I)
              IMX = I
              JMX = J
  380       CONTINUE
  390     CONTINUE
          TAPMX(KP) = CMAX

          VEL(KP) = V(JMX)
          AZM(KP) = AZSTAT + (IMX - 1) * AZSTEP
          SP(KP) = CH(1,M + NWD/2)
          WRITE (6,400) SP(KP), VEL(KP), AZM(KP), TAPMX(KP)
  400     FORMAT (1H , 10X, 3F10.2, 3X, F10.2)
          KP = KP + 1
          TI = TI + TSTEP
          M = M + ISTEP
          IF (M .GT. MX) GO TO 410
          GO TO 90
  410     CONTINUE
          CALL PSPACE(0.1, F2, 0.1, 0.9)
          CALL BORDER
          CALL PSPACE(0.1, F2, 0.0, 1.0)
          CALL CSPACE(0.0, F2, 0.0, 1.0)
          CALL MAP(0.1, F2, 0.0, 1.0)
          CALL CTRMAG(10)
          CALL PLOTCS(F1, 0.99, 'NEVENT = ', 9)
          CALL TYPENI(NEVENT)
          CALL PLOTCS(F1, 0.96, 'ISTEP = ', 8)
          CALL TYPENI(ISTEP)
          CALL TYPECS(' SAMPS', 6)
          CALL PLOTCS(F1, 0.93, 'VSTEP = ', 8)
          CALL TYPENF(VSTEP, 2)
          CALL TYPECS(' KM/S', 5)
          CALL PLOTCS(F3, 0.99, 'AZSTEP = ', 9)
          CALL TYPENF(AZSTEP, 2)
          CALL TYPECS(' DEG', 4)
          CALL PLOTCS(F3, 0.95, 'NPEAK = ', 8)
          CALL TYPENI(NPEAK)
          CALL TYPECS(' PEAKS', 6)
          CALL CTRMAG(20)
          CALL GPEND
          STOP
          END
C
CC SUBROUTINE DELAY CALCULATES DELAYS IN WHOLE NUMBERS OF SAMPLES
CC FOR A GIVEN AZIMUTH OVER THE GIVEN RANGE OF VELOCITY
CC
C
          SUBROUTINE DELAY(M, AZ, ID)
          DIMENSION X(8), Y(8), ID(8,100), V(100)
          COMMON /VEL/ V, NV, SP, X, Y, NPIT
C START DO LOOP TO COMPUTE TIME DELAYS IN WHOLE NUMBER OF SAMPLES
C
          DO 40 IV = 1, NV
            IDMIN = 32000
            DO 10 I = 1, NPIT
              TIV = -(Y(I)*COS(AZ) + X(I)*SIN(AZ)) / V(IV)
              ID(I,IV) = IFIX(TIV*SP + 0.5)
              IF (ID(I,IV) .LT. IDMIN) IDMIN = ID(I,IV)
   10       CONTINUE
   20       IADD = M - IDMIN
            DO 30 I = 1, NPIT
              ID(I,IV) = ID(I,IV) + IADD
   30       CONTINUE
   40     CONTINUE
          RETURN
          END
C SUBROUTINE 'SORT' SORTS NC ELEMENTS OF CORR ARRAY IN DESCENDING
C ORDER OF MAGNITUDE. FOR EACH ELEMENT OF CORR, THE CORRESPONDING
C VALUES OF VELOCITY AND AZIMUTH ARE ATTACHED
CCCC
```

```
      SUBROUTINE SORT(KC)
      DIMENSION CORR(1000), VELCTY(1000), AZMUTH(1000)
      COMMON VELCTY, AZMUTH, CORR, NPEAK, TI, F2
      KCM1 = KC - 1
      DO 20 I = 1, KCM1
        IP1 = I + 1
        DO 10 J = IP1, KC
          IF (CORR(I) .GE. CORR(J)) GO TO 10
          TEMP = CORR(I)
          CORR(I) = CORR(J)
          CORR(J) = TEMP
          TEMP = VELCTY(I)
          VELCTY(I) = VELCTY(J)
          VELCTY(J) = TEMP
          TEMP = AZMUTH(I)
          AZMUTH(I) = AZMUTH(J)
          AZMUTH(J) = TEMP
   10   CONTINUE
   20 CONTINUE
      RETURN
      END
C
C
C
C  SUBROUTINE "PLOT" PLOTS UP TO NPEAK VALUES
C OFVELOCITY,AZIMUTH,CORRELATION IN THE FIELD
C
      SUBROUTINE PLOT(KC, CM)
      DIMENSION T(2000)
      DIMENSION CORR(1000), VELCTY(1000), AZMUTH(1000)
      COMMON VELCTY, AZMUTH, CORR, NPEAK, TI, F2
      COMMON /P1/ VSTAT, VEND, AZSTAT, AZEND, TSTAT, TEND
      SF = CM / 50.0
      CALL PSPACE(0.1, F2, 0.1, 0.3)
      CALL MAP(TSTAT, TEND, VSTAT, VEND)
      CALL CTRSET(4)
      DO 10 I = 1, KC
        CALL CTRMAG(IFIX(CORR(I)/SF))
        Y = VELCTY(I)
        CALL PLOTNC(TI, Y, 54)
   10 CONTINUE
      CALL PSPACE(0.1, F2, 0.4, 0.6)
      CALL MAP(TSTAT, TEND, AZSTAT, AZEND)
      DO 20 I = 1, KC
        CALL CTRMAG(IFIX(CORR(I)/SF))
        Y = AZMUTH(I)
        CALL PLOTNC(TI, Y, 54)
   20 CONTINUE
      CALL PSPACE(0.1, F2, 0.7, 0.9)
      CALL MAP(TSTAT, TEND, 0.0, CM)
      DO 30 I = 1, KC
        CALL CTRMAG(20)
        Y = CORR(I)
        CALL PLOTNC(TI, Y, 54)
   30 CONTINUE

      CALL CTRSET(1)
      RETURN
      END
```

APPENDIX D

EXPRESSIONS FOR TRAVEL TIMES OF HEAD WAVES FROM A PLANE DIPPING INTERFACE IN A TWO LAYER MEDIUM

(a) Travel time, t_d, from focus downdip to Kaptagat.

Let the plane interface (fig. 5.9c) dip down from focus, F, towards Kaptagat(P) at an angle α . Let θ be the critical angle for head waves from this interface and Z_d the length of the normal from F to the interface. Let the focal depth be h and the epicentral distance, PR, be Δ . The upper and lower layer velocities are taken as V_1 and V_2 respectively.

Then, using the concept of delay time, the travel time, t_d, for head waves travelling down from focus to P is given by

$$t_d = \frac{NE}{V_2} + \frac{EHCos\theta}{V_1} + \frac{Z_d Cos\theta}{V_1}$$

$$= \frac{(\Delta - htan\alpha)Cos\alpha}{V_2} + \frac{((\Delta - htan\alpha)sin\alpha + \frac{h}{Cos\alpha} + Z_d)Cos\theta}{V_1}$$

$$+ \frac{Z_d Cos\theta}{V_1}$$

$$t_d = \frac{\Delta Cos\alpha}{V_2} + \frac{\Delta sin\alpha Cos\theta}{V_1} + \frac{htan\alpha Cos\theta}{V_2} - \frac{htan\alpha sin\alpha Cos\theta}{V_1}$$

$$+ \frac{hCos\theta}{V_1 Cos\alpha} + \frac{2Z_d Cos\theta}{V_1}$$

$$= \frac{\Delta}{V_1}\left(\frac{V_1 Cos\alpha + sin\alpha Cos\theta}{V_2}\right) - \frac{h}{V_1}\left(\frac{V_1 tan\alpha Cos\alpha + tan\alpha Sin\alpha Cos\theta}{V_2}\right.$$

$$\left. - \frac{Cos\theta}{Cos\alpha}\right) + \frac{2Z_d Cos\theta}{V_1}$$

$$= \frac{\Delta}{V_1}(\sin\theta\cos\alpha + \sin\alpha\cos\theta) - \frac{h}{V_1}(\sin\theta\tan\alpha\cos\alpha + \tan\alpha\sin\alpha\cos\theta - \frac{\cos\theta}{\cos\alpha}) + \frac{2Z_d\cos\theta}{V_1}$$

$$= \frac{\Delta}{V_1}\sin(\theta+\alpha) - \frac{h}{V_1}(\sin\theta\sin\alpha + \frac{\sin^2\alpha\cos\theta}{\cos\alpha} - \frac{\cos\theta}{\cos\alpha}) + \frac{2Z_d\cos\theta}{V_1}$$

$$t_d = \frac{\Delta}{V_1}\sin(\theta+\alpha) - \frac{h}{V_1}((\sin\theta\sin\alpha + \frac{\cos\theta}{\cos\alpha}(\sin^2\alpha - 1)) + \frac{2Z_d\cos\theta}{V_1}$$

$$= \frac{\Delta}{V_1}\sin(\theta+\alpha) - \frac{h}{V_1}(\sin\theta\sin\alpha - \frac{\cos\theta\cos^2\alpha}{\cos\alpha}) + \frac{2Z_d\cos\theta}{V_1}$$

$$= \frac{1}{V_1}(\Delta\sin(\theta+\alpha) + h\cos(\theta+\alpha) + 2Z_d\cos\theta)$$

But from fig. 5.9c, the angle of emergence, e, is given by

$$e = \theta + \alpha$$

$$\therefore t_d = \frac{1}{V_1}(\Delta\sin e + h\cos e + 2Z_d\cos(e-\alpha))$$

(b) Travel time, t_u, from focus updip to Kaptagat station.

From fig. 5.9d, using delay time concept,

$$t_u = \frac{NE}{V_2} + \frac{PH\cos\theta}{V_1} + \frac{Z_u\cos\theta}{V_1}$$

$$= \frac{NE}{V_2} + \frac{(Z_u - FC)}{V_1}\cos\theta + \frac{Z_u\cos\theta}{V_1}$$

where FC = QC-QF and Z_u is the length of the normal from F to the interface HE.

$$\therefore t_u = \frac{(\Delta + h\tan\alpha)\cos\alpha}{V_2} + \left(\frac{Z_u-(\Delta + h\tan\alpha)\sin\alpha}{V_1} + \frac{h}{\cos\alpha}\right)\cos\theta + \frac{Z_u\cos\theta}{V_1}$$

$$= \frac{(\Delta + h\tan\alpha)(\cos\alpha\sin\theta-\sin\alpha\cos\theta)}{V_1} + \frac{2Z_u\cos\theta}{V_1} \quad \frac{h\cos\theta}{\cos\alpha}$$

$$= \frac{(\Delta + h\tan\alpha)\sin(\theta-\alpha)}{V_1} + \frac{2Z_u\cos\theta}{V_1} + \frac{h\cos\theta}{V_1\cos\alpha}$$

But from fig. 5.9d, $\theta = e + \alpha$.

$$\therefore t_u = \frac{1}{V_1}\left(\Delta\sin e + \frac{h}{\cos\alpha}(\sin\alpha\sin e + \cos(e+\alpha)) + 2Z_u\cos(e+\alpha)\right.$$

$$\therefore t_u = \frac{1}{V_1}\left(\Delta\sin e + h\cos e + 2Z_u\cos(e+\alpha)\right)$$

REFERENCES

ANDERSON, D.L., 1965. Recent evidence concerning the structure and composition of the earth's mantle, Phys. Chem. of the Earth, 6, 1-31.

ARTYUSHKOV, E.V., 1973. Stresses in the lithosphere caused by crustal thickness inhomogeneities, J. Geophys. Res., 78, 7675-7708.

BACKHOUSE, R.W., 1972. Upper mantle structure using P-wave data from an East African array station, Ph.D. thesis, University of Durham.

BAILEY, D.K., 1983. The chemical and thermal evolution of rifts, Tectonophysics, 94, 585-597.

BAKER, B.H., MOHR, P.A. and WILLIAMS, L.A., 1972. Geology of the eastern rift system of Africa, Geol. Soc. Am. Special Paper No. 136.

BAKER, G.H. and WOHLENBERG, J., 1971. Structure and evolution of the Kenya rift valley, Nature, 229, 538-542.

BANKS, R.J. and BEAMISH, D., 1979. Melting in the crust and upper mantle beneath the Kenya rift: evidence from geomagnetic deep sounding experiments, Jl geol. Soc. Lond., 136, 225-233.

BANKS, R.J. and OTTEY, P., 1974. Geomagnetic deep sounding in and around the Kenya rift valley, Geophys. J.R. astr. Soc., 36, 321-335.

BATH, M. 1960. Crustal structure of Iceland, J. Geophys. Res., 65, 1793-1806.

BEAMISH, D., 1977. The mapping of induced currents around the Kenya rift: a comparison of techniques, Geophys. J.R. astr. Soc., 50, 311-332.

BERRY, M.J. and WEST, G.F., 1966. Reflected and headwave amplitudes in a medium of several layers, In: Steinhart, J.S. and Smith, T.J. (eds.). The earth beneath the continents, Am. Geophys. Union Mono. 10, 464-481.

BIRTILL, J.W. and WHITEWAY, F.E., 1965. The application of phased arrays to the analysis of seismic body waves, Phil. Trans. R. Soc. Lond., 258A, 421-493.

BLOCH, S., HALES, A.L. and LANDISMAN, M., 1969. Velocities in the crust and upper mantle of southern Africa from multimode surface wave dispersion, Bull. seism. Soc. Am., 59, 1599-1629.

BONJER, K.P., FUCHS, K. and WOHLENBERG, J., 1970. Crustal structure of the East African rift system from spectral response ratios of long period body waves, Zeitschrift fur Geophysik, 36, 287-297.

BOTT, M.H.P., 1965. Formation of ocean ridges, Nature, Lond., 207, 840-843.

BOTT, M.H.P., 1971. The interior of the earth, Edward Arnold, London.

BOTT, M.H.P., 1976. Formation of sedimentary basins of graben type by extension of the continental crust, Tectonophysics, 73, 1-8.

BOTT, M.H.P., 1981. Crustal doming and the mechanism of continental rifting, Tectonophysics, 73, 1-8.

BOTT, M.H.P. and KUSZNIR, N.J., 1979. Stress distributions associated with compensated plateau uplift structures with application to the continental splitting mechanism, Geophys. J.R. astr. Soc., 56, 451-459.

BOTT, M.H.P. and KUSZNIR, N.J., 1984. The origin of tectonic stress in the lithosphere, Tectonophysics, 105, 1-13.

BOTT, M.H.P. and MITHEN, D.P., 1981. Mechanism of graben formation and sources of causative stress, Abstracts, Conference on the processes of planetary rifting, Lunar Planet. Inst. Contrib. No. 457, 11-12.

BOTT, M.H.P. and MITHEN, D.P., 1983. Mechanism of graben formation - the wedge subsidence hypothesis, Tectonophysics, 94, 11-22.

BRAILE, L.W. and SMITH, R.B., 1975. Guide to the interpretation of crustal refraction profiles, Geophys. J.R. astr. Soc., 40, 145-176.

BRUNE, J. and DORMAN, J., 1963. Seismic waves and earth structure in the Canadian shield, Bull. seism. Soc. A., 53, 167-210.

BULLARD, E.C., 1936. Gravity measurements in East Africa, Phil. Trans. R. Soc. Lond., 253, 445-531.

BUNGUM, H. and HUSEBYE, E.S., 1971. Errors in time delay measurements, Applied Geophysics, 91, 56-70.

BURKE, K.C. and WILSON, J.T., 1976. Hot spots on the earth's surface,
Scientific American, 235(2), 46-57.

CAHEN, L. and SNELLING, N.J., 1966. The geochronology of equatorial Africa,
North-Holland Publ. Co., Amsterdam.

CAPON, J., GREENFIELD, R.J. and KOLKER, R.J., 1967. Multi-dimensional maximum likelyhood processing of a large aperture seismic array,
Proc. IEEE, 55, 192-211.

CARPENTER, E.W., 1965. An historial review of seismometer array development,
Proc. IEEE, 53(12), 1816-1821.

CERVENY, V., 1966. On the dynamic properties of reflected and head waves in the n-layered earth's crust,
Geophys. J. R. astr. Soc., 11, 139-147.

CERVENY, V. and RAVINDRA, R., 1971. Theory of seismic headwaves,
University of Toronto Press.

CHAPMAN, G.R., LIPPARD, S.J. and MARTYN, J.E., 1978. The stratigraphy and structure of the Kamasia range, Kenya rift valley,
J. geol. Soc. London, 135, 265-281.

CHAPMAN, D.S. and POLLACK, H.N., 1975. Heatflow and incipient rifting in the central African plateau,
Nature, Lond., 256, 28-30.

CHEN, W. and MOLNAR, P., 1983. Focal depth of intraplate earthquakes and their implications for the thermal and mechanical properties of the lithosphere,
J. Geophys. Res., 88, 4183-4214.

CLEARY, J.R., WRIGHT, C. and MUIRHEAD, K.J., 1968. The effects of local structure upon measurements of the travel time gradient at Warramunga array,
Geophys. J.R. astr. Soc., 16, 21-29.

CLOOS, H., 1939. Hebung-Spathung-Vulkanismus,
Geol. Rundsch., 30, 405-527.

CLOWES, R.M., KANASEWICH, E.R. and CUMMING, G.L., 1968. Deep crustal seismic reflections at near vertical incidence,
Geophysics, 33, 441-451.

COOK, F.A., McCULLARD, D.B., DECKER, E.R. and SMITH, S.B., 1979. Crustal structure and evolution of the southern Rio Grande rift,
In: Riecker, E.R., (ed.), Rio Grande rift: tectonics and magmatism, Am. Geophys, Union, 195-208.

CRANE, K. and O'CONNELL, S., 1983. The distribution and implications of heat flow from the Gregory rift in Kenya, Tectonophysics, 94, 253-275.

CROUGH, S.T., 1983. Rifts and swells: geophysical constraints on casuality, Tectonophysics, 94, 23-37.

DAHLHEIM, H.A., DAVIS, P.M. and ACHAUER, U., 1986. Deep velocity structure beneath the East African rift and waveform analysis using teleseismic events, EOS, 67, 1103.

DARRACOTT, B.W., FAIRHEAD, J.D. And GIRDLER, R.W., 1972. Gravity and magnetic surveys in northern Tanzania and southern Kenya, Tectonophysics, 15, 131-141.

DAVIES, D., KELLY, E.J. and FILSON, J.R., 1971. Vespa process for the analysis of seismic signals, Nature Phys. Sci., 232, 8-13.

ELDER, J.W., 1966. Penetrative convection, its role in volcanism, Bull. Vulc., 29, 327-343.

FAIRHEAD, J.D., 1976. The structure of the lithosphere beneath the eastern rift, East Africa; deduced from gravity studies, Tectonophysics, 30, 269-298.

FAIRHEAD, J.D. and GIRDLER, R.W., 1969. How far does the rift system extend through Africa? Nature, 221, 1018-1020.

FAIRHEAD,J.D. and GIRDLER, R.W., 1971. The seismicity of Africa, Geophys. J. R. astr. Soc., 24, 271-301.

FARRELL, E.J., 1971. Sensor array processing with channel recursive bayes techniques, Geophysics, 36, 822-834.

FORBES, C.B., OBENCHAIN, R. and SWAIN, R.J., 1965. The LASA sensing system design, installation and operation, Proc. IEEE, 53, 1834-1843.

FORSYTH, D. And UYEDA, S., 1975. On the relative importance of the driving forces of plate motion, Geophys. J.R. astr. Soc., 43, 163-200.

FORTH, P.A., 1975. The structure of the upper mantle beneath East Africa, Ph.D. thesis, University of Durham.

FREETH, S.J., 1980. Can membrane tectonics be used to explain the breakup of plates?
In: Davies, P.A. and Runcorn, S.K. (eds.), Mechanisms of continental drift and plate tectonics, pp. 135-149.

GANE, P.G., ATKINS, A.R., SELLSCHOP, J.P.F. and SELIGMAN, P., 1956. Crustal structure in the Transvaal,
Bull. seism. Soc. Am., 46, 293-316.

GASS, I.G., 1970. The evolution of volcanism in the junction area of the Red Sea, Gulf of Aden and Ethiopian rifts,
Phil. Trans. R. Soc. Lond. Series A, 267, 369-381.

GASS, I.G., 1972. The role of magmatic processes in continental rifting and sea floor spreading,
Fourth Tomkeieff Memorial lecture, Geology Department, University of Newcastle upon Tyne.

GASS, I.G., CHAPMAN, D.S., POLLACK, H.N. and THORPE, R.S., 1978. Geological and geophysical parameters of mid-plate volcanism,
Phil. Trans. R. Soc. Lond., 288A, 581-587.

GIRDLER, R.W., FAIRHEAD, J.D., SEARLE, R.C. and SOWERBUTTS, W.T.C., 1969. The evolution of rifting in Africa,
Nature, 224, 1178-1182.

GOLES, G.G., 1975. Depths of origin of Kenya basalts and implications for the Gregory rift,
Nature Lond., 225, 391-393.

GREEN, D.H. and RINGWOOD, A.E., 1969. The origin of basalt magmas,
In: Hart, P.J. (ed.), The earth's crust and upper mantle,
Am. Geophys. Union Mono. 13, 489-495.

GRIFFITHS, D.H., KING, R.F., KHAN, M.A. and BLUNDELL, D.J., 1971. Seismic refraction line in the Gregory rift,
Nature, Phys. Sci., 229, 69-71.

GUMPER, F. and POMEROY, P.W., 1970. Seismic wave velocities and earth structure for the African continent,
Bull. seism. Soc. Am., 60, 651-668.

HAMILTON, R.M., SMITH, B.E. and KNAPP, F., 1973. Earthquakes in geothermal areas near Lakes Naivasha and Hannington, Kenya,
U.S. Department of Interior, Geological Survey Report prepared under contract No. CON90/71 for the U.N.

HALES, A.L. and SACKS, I.S., 1959. Evidence for an intermediate layer from crustal structure studies in Eastern Transvaal,
Geophys. J.R. astr. Soc., 2, 15-33.

HEISKANEN, W.A. and VENING MEINESZ, F.A., 1958. The earth and its gravity field,
Published by McGraw-Hill Book Company, Inc.

HERBERT, L. and LANGSTON, C.A., 1985. Crustal thickness estimate at AAE (Addis-Ababa, Ethipia) and NAI (Nairobi, Kenys) using telsdeismic P-wave conversions,
Tectonophysics, 111, 297-327.

JEFFREYS, H., 1970. The earth, its origin, history and Physical constitution,
Cambridge University Press.

JENNINGS, D.J., 1964. Geology of the Kapsabet plateau area,
Geol. Surv. Kenya Report No. 63.

JIRACEK, G.R., GUSTAFSON, E.P. and MITCHELL, P.S., 1983. Magnetotelluric results opposing magma origin of crustal conductors in the Rio Grande rift,
Tectonophysics, 94, 299-326.

KANASEWICH, E.R., HEMMINGS, C.D. and ALPASLAN, T., 1973. Nth root stack non linear multichannel filter,
Geophys., 38(2), 327-338.

KEEN, C.E., 1985. The dynamics of rifting: deformation of the lithosphere by active and passive driving forces,
Geophys. J.R. astr. Soc., 80, 95-120.

KEY, F.A., 1967. Signal generated noise recorded at the Eskdalemuir seismometer array station,
Bull. seism. Soc. Am., 57, 27-37.

KHAN, M.A. and others (KRISP working group), 1987. Structure of the Kenya rift from seismic refraction,
Nature, 325, 239-242.

KHAN, M.A. and MANSFIELD, J., 1971. Gravity measurements in the Gregory rift.
Nature, Phys. Sci., 229, 72-75.

KING, B.C., 1970. Vulcanicity and rift tectonics in East Africa,
In: Clifford, T.N. and Gass, I.C.(eds.), African magmatism and tectonics.
Oliver and Boyd, Edinburgh p. 263-283.

KING, B.C., 1978. Structural and volcanic evolution of the Gregory rift,
In: Bishop, W.W.(ed.), Geological background to fossil man.
Scottish Academic Press, Edinburgh.

KING, B.C, and CHAPMAN, G.R., 1972. Volcanism of the Kenya rift valley,
Phil. Trans. R. Soc. Lond. Series A, 271, 185-208.

KING, D.W., MEREU, R.F. and MUIRHEAD, K.J., 1973. The measurement of apparent velocity and azimuth using adaptive processing techniques on data from Warramunga seismic array,
Geophys. J.R. astr. Soc., 35, 137-167.

KNOPOFF, L. and SCHLUE, J.W., 1972. Rayleigh wave phase velocities for the path Addis-Ababa-Nairobi,
Tectonophysics, 15, 157-163.

LOCOSS, R.T., 1975. Review of some techniques for array processing,
In: Beauchamp, K.G.(ed.), Exploitation of seismograph networks.
Noordhoff International Publishing, Leiden, The Netherlands.

LACOSS, R.T., KELLY, E.J. and Toksoz, M.N., 1969. Estimation of seismic noise structure using arrays,
Geophysics, 34, 21-38.

LAUGHTON, A.S., 1966. The gulf of Aden in relation to the Red Sea and the Afar depression of Ethiopia,
In: The world rift system - UMC symposium: Canada Geol. Survey Paper 66-14 p. 78-97.

LE BAS, M.J., 1971. Per-alkaline volcanism, crustal swelling and rifting,
Nature, 230, 85-87.

LOGATCHEV, N.A., BELOUSSOV, V.V. and MILLANOVSKY, E.E., 1972. East African rift development,
Tectonophysics, 15, 71-81.

LOGATCHEV, N.A., ZORIN, Y.A. and ROGOZHINA, V.A., 1983. Baikal rift : active or passive? - comparison of the Baikal and Kenya rift zones,
Tectonophysics, 94, 223-240.

LONG, R.E., 1968. Temporary seismic array stations,
Geophys. J.R. astr. Soc., 16, 37-45.

LONG, R.E., 1986. Lithospheric anomalies beneath the central Kenya rift,
EOS, 67, 1103.

LONG, R.E. and BACKHOUSE, R.W., 1976. The structure of the western flank of the Gregory rift. Part II. The mantle,
Geophys. J.R. astr. Soc., 44, 677-688.

MACK, H., 1969. Nature of short period P-wave signal variations at LASA,
J. Geophys. Res., 74(12), 3161-3170.

MAGUIRE, P.K.H., 1974. The crustal structure of East Africa through earthquake seismology,
Ph.D. thesis, University of Durham.

MAGUIRE, P.K.H., COOKE, P.A.V., LAFFOLEY, N.A. and EVANS, J.R., 1986. Earthquake recording in the central part of the Kenya rift valley,
EOS, 67, 1103.

MAGUIRE, P.K.H. and LONG, R.E., 1976. The structure of the western flank of the Gregory rift (Kenya). Part I. The crust,
Geophys. J.R. astr. Soc., 44, 661-675.

MARESCHAL, J., 1983. Mechanism of uplift preceding rifting, Tectonophysics, 94, 51-66.

McCALL, G.J.H., 1967. Geology of Nakuru-Thomson's Falls-Lake Hannington area.
Geol. Surv. Kenya Report No. 78.

McCALL, G.J.H., 1968. The five caldera volcanoes of the central rift valley, Kenya,
Geol. Soc. Lond. Proc. No. 1647, 54-59.

McKENZIE, D., 1978. Some remarks on the development of sedimentary basins,
Earth Planet. Sci. Lett., 40, 25-32.

McKENZIE, D.P., DAVIES, D. and MOLNAR, P., 1970. Plate tectonics of the Red Sea and East Africa,
Nature, 226, 243-248.

MOHR, P.A., 1967. The Ethiopian rift system,
Bull. Geophys. Obs. Addis Ababa, No. 11, 1-65.

MOLNAR, P. and AGGARWALL, Y.P., 1971. A microearthquake survey in Kenya,
Bull. Seism. Soc. A.m, 61, 195-201.

MOLNAR, P. and OLIVER, J., 1969. Lateral variations of attenuation in the upper mantle and discontinuities in the lithosphere,
J. Geophys. Res., 74, 2648-2682.

MORGAN, W.J., 1971. Convection plumes in the lower mantle,
Nature, 230, 42-43.

MORGAN, P., 1983. Constraints on rift thermal processes from heat flow and uplift,
Tectonophysics, 94, 277-298.

MOUGENOT, D., REQ, M., VIRLOGEUX, P. and LEPVRIER, C., 1986. Seaward extension of East African rift.
Nature, Lond., 321, 599-603.

MUELLER, S. and BONJER, K.P., 1973. Average structure of the crust and upper mantle in East Africa,
Tectonophysics, 20, 283-293.

MUIRHEAD, K.J., 1968. Eliminating false alarms when detecting events automatically,
Nature, 217, 533-534.

MUIRHEAD, K.J. and RAM, A., 1976. The N-th root processing applied to seismic array data, Geophys. J.R. astr. Soc., 47, 197-210.

MURRAY, C.G., 1970. Magma genesis and heat flow: Differences between mid ocean ridges and African rift valleys, Earth Planet. Sci. Lett., 9, 34-38.

NAFE, J.E. and DRAKE, C.L., 1963. Physical properties of marine sediments, In: Hill, M.N.(ed), The Sea, 3, 794-815. Interscience Publishers.

NEUGEBAUER, H.J., 1978. Crustal doming and mechanism of rifting, part I: rift formation, Tectonophysics, 45, 159-186.

NEUGEBAUER, H.J., 1983. Mechanical aspects of continental rifsting, Tectonophysics, 94, 91-108.

NEUGEBAUER, H.J. and TEMME, P., 1981. Crustal uplift and the propagation of failure zones, Tectonophysics, 73, 33-51.

OLIVER, J. and ISACKS, B., 1967. Deep earthquake zones, anomalous structures in the upper mantle and the lithosphere, J. Geophys. Res., 72, 4259-4275.

OLSEN, K.H., 1983. The role of seismic refraction data for studies of the origin and evolution of continental rifts, Tectonophysics, 94, 349-370.

OLSEN, K.H., KELLER, G.R. and STEWART, J.N., 1979. Crustal structure along the Rio Grande rift from seismic refraction profiles, In: Riecker, R.E. (ed.), Rio Grande rift: Tectonics and magmatism, American Geophysical Union.

OXBURGH, E.R., 1978. Rifting in East Africa and large scale tectonic processes, In: Bishop, W.W. (ed.), Geological background to fossil man. Scottish Academic Press, Edinburgh, p. 1-18.

OXBURGH, E.R. and TURCOTTE, D.L., 1974. Membrane tectonics and the East African rift, Earth Planet. Sci. Lett., 22, 133-140.

PALMASON, G., 1971. Crustal structure of Iceland from explosion seismology, Soc. Sci. Islandica, Rit.

RAM, A. and MEREU, R.F., 1975. A comparison of the adaptive processing techniques with the Nth root beam forming methods,
Geophys. J.R. astr. Soc., 42, 653-670.

RICHTER, C.F., 1958. Elementary seismology,
W.H. Freeman and Company, San Francisco.

ROONEY, D. and HUTTON, V.R.S., 1977. A magnetotelluric and magnetovariational study of the Gregory rift valley, Kenya,
Geophys. J. R. astr. Soc., 51, 91-119.

RYKOUNOV, L.N., SEDOV, V.V., SAVRINA, L.A. and BOURMIN, V.J.U., 1972. Study of microearthquakes in the rift zones of East Africa,
Tectonophysics, 12, 123-130.

SAGGERSON, E.P. and BAKER, B.H., 1965. Post-Jurassic erosion surfaces in eastern Kenya and their deformation in relation to rift structure,
Q.J. geol. Soc. Lond., 121, 51-72.

SAVAGE, J.E.G., 1979. A seismic investigation of the lithosphere of the Gregory rift,
Ph.D. thesis, University of Durham.

SAVAGE, J.E.G. and LONG, R.E., 1985. Lithospheric structure beneath the Kenya dome,
Geophys. J.R. astr. Soc., 82, 461-477.

SENGOR, A.M.C. and BURKE, K., 1978. Relative timing of rifting and volcanism on earth and its tectonic implications,
Geophys. Res. Lett., 5, 419-421.

SEARLE, R,C., 1970. Evidence from gravity anomalies for thinning of the lithosphere beneath the rift valley in Kenya,
Geophys. J.R. astr. Soc., 21, 13-31.

SHACKLETON, R.M., 1978. Structural development of the East African rift system,
In: Bishop, W.W.(ed.), Geological background to fossil man. Scottish Academic Press, Edinburgh.

SOLOMON, S.C., SLEEP, N.H. and RICHARDSON, R.M., 1975. On the forces driving plate tectonics: inferences from absolute plate velocities and intraplate stress,
Geophys. J.R. astr. Soc., 42, 769-801.

SOMERS, H. and MANCHEE, E.B., 1966. Selectivity of the Yellowknife seismic array,
Geophys. J.R. astr. Soc., 10, 401-412.

SOWERBUTTS, W.T.C., 1969. Crustal structure of the East African plateau and rift valleys from gravity measurements,
Nature, Lond., 223, 143-146.

SUNDARALINGAM, K., 1971. A seismic investigation of the crust and upper mantle of East Africa,
Ph.D. thesis, University of Durham.

SWAIN, C.J., KHAN, M.A., WILTON, T.J., MAGUIRE, P.K.H. and GRIFFITHS, D.H., 1981. Seismic and gravity surveys in the Lake Baringo-Tugen Hills area, Kenya rift valley,
J. geol. Soc. London, 138, 93-102.

SYKES, L.R. and LANDISMAN, M., 1964. The seismicity of East Africa, the Gulf of Aden and the Arabian and Red Seas,
Bull. seism. Soc. Am., 54, 1927-1940.

THOMPSON, A.O. and DODSON, R.G., 1963. Geology of the Naivasha area, Kenya,
Geol. Surv. Kenya Report No. 55.

TURCOTTE, D.L., 1974. Membrane tectonics,
Geophys. J.R. astr. Soc., 36, 33-42.

TURCOTTE, D.L. and EMERMAN, S.H., 1983. Mechanisms of active and passive rifting,
Tectonophysics, 94, 39-50.

TURCOTTE, D.L. and OXBURGH, E.R., 1973. Mid-plate tectonics,
Nature, 244, 337-339.

TURCOTTE, D.L., and OXBURGH, E.R., 1976. Stress accumulation in the lithosphere,
Tectonophysics, 35, 185-199.

WENDLANDT, R.F. and MORGAN, P., 1982. Lithospheric thinning associated with rifting in East Africa,
Nature, 298, 734-736.

WHITTEWAY, F.E., 1965. The recording and analysis of seismic body waves using linear cross arrays,
The Radio and Electronic Engineer, 29(1), 33-46.

WILLIAMS, L.A.J., 1969. Volcanic associations in the Gregory rift valley, East Africa,
Nature, 224, 61-64.

WILLIAMS, L.A.J., 1972. The Kenya rift volcanics: a note on volumes and chemical compositions,
Tectonophysics, 15, 83-96.

WILLIAMS, L.A.J., 1978. Character of quaternary volcanism in the Gregory rift valley, In: Bishop, W.W.(ed.), Geological background to fossil man, pp. 55-69. Scottish Academic Press, Edinburgh.

WILLMORE, P.L., HALES, A.L. and GANE, P.G., 1952. Seismic investigation of crustal structure in the Western Transvaal, Bull. seism. Soc. Am., 42, 53-80.

WILSON, J.T., 1963. A possible origin of the Hawaiian islands, Can. J. Phys., 41, 863-870.

WILTON, T.J., 1977. KRISP 1975. Seismic profiles within the Gregory rift valley, Kenya, (Abstract), Geophys. J.R. astr. Soc., 49, 287.

ZVEREZ, S.M., LITVINENKO, I.V., PALMASON, G., YAROSHEVSKAYA, G.A. and OSOKIN, N.N., 1980. A seismic crustal study of the axial rift zone in south-west Iceland, J. Geophys., 47, 202-210.